NONDESTRUCTIVE MONITORING OF THE VARIATIONS IN MICROSTRUCTURE AND RESIDUAL STRESS IN CARBURIZED STEELS

A THESIS SUBMITTED TO
THE GRADUATE SCHOOL OF NATURAL AND APPLIED SCIENCES
OF
MIDDLE EAST TECHNICAL UNIVERSITY

BY

HÜSEYİN HIZLI

IN PARTIAL FULFILLMENT OF THE REQUIREMENTS
FOR
THE DEGREE OF MASTER OF SCIENCE
IN
METALLURGICAL AND MATERIALS ENGINEERING

SEPTEMBER 2016

Approval of the thesis:

NONDESTRUCTIVE MONITORING OF THE VARIATIONS IN MICROSTRUCTURE AND RESIDUAL STRESS IN CARBURIZED STEELS

submitted by **HÜSEYİN HIZLI** in partial fulfillment of the requirements for the degree of **Master of Science in Metallurgical and Materials Engineering Department, Middle East Technical University** by,

Prof. Dr. Gülbin Dural Ünver ________________
Dean, Graduate School of **Natural and Applied Sciences**

Prof. Dr. C. Hakan Gür ________________
Head of Department, **Metallurgical Materials Engineering**

Prof. Dr. C. Hakan Gür ________________
Supervisor, **Metallurgical and Materials Engineering, METU**

Examining Committee Members:

Prof. Dr. A. Bülent Doyum ________________
Mechanical Engineering Department, METU

Prof. Dr. C. Hakan Gür ________________
Metallurgical and Materials Engineering Department, METU

Prof. Dr. Bilgehan Ögel ________________
Metallurgical and Materials Engineering Department, METU

Assist. Prof. Dr. Caner Şimşir ________________
Manufacturing Engineering Department, Atılım University

Assist. Prof. Dr. Mert Efe ________________
Metallurgical and Materials Engineering Department, METU

Date: 21.09.2016

I hereby declare that all information in this document has been obtained and presented in accordance with academic rules and ethical conduct. I also declare that, as required by these rules and conduct, I have fully cited and referenced all material and results that are not original to this work.

Name, Last Name : Hüseyin HIZLI

Signature :

ABSTRACT

NONDESTRUCTIVE MONITORING OF THE VARIATIONS IN MICROSTRUCTURE AND RESIDUAL STRESS IN CARBURIZED STEELS

Hızlı, Hüseyin
M.Sc., Department of Metallurgical and Materials Engineering
Supervisor: Prof. Dr. C. Hakan GÜR

September 2016, 178 pages

Service life and performance of the case-hardened machine parts are greatly dependent on the residual stress state in the surface layers which directly affects the fatigue behavior. Recently, all industrial sectors have been requested for a fast and non-destructive determination of residual stress. This study aims to monitor the variations in surface residual stress distributions in the carburized 19CrNi5H steels by means of non-destructive and semi-destructive measurement techniques, Magnetic Barkhausen Noise (MBN), X-Ray Diffraction (XRD), and Electronic Speckle Pattern Interferometry (ESPI) assisted hole drilling. Microstructural investigation by optical and scanning electron microscopy, hardness measurements, and spectroscopy analysis were also conducted. To comprehend the differences in the residual stress distributions, various samples were prepared by applying different duration of carburizing and tempering temperatures. Residual stress measurements carried out by XRD and ESPI assisted hole drilling showed that the compressive residual stress state exists for the case-hardened samples throughout the case depth regions, and the magnitude of the compressive residual stress decreases as the tempering temperature increases. MBN measurements showed that the BN activity increases with decreasing carburization time and increasing tempering temperature. It was concluded that MBN technique could be used to measure the surface residual stress distributions with a proper calibration operation.

Keywords: Carburizing, Residual Stress, Non-destructive Evaluation, Magnetic Barkhausen Noise Technique, X-ray Diffraction, ESPI, Hole Drilling

ÖZ

SEMENTE EDİLMİŞ ÇELİKLERDE İÇYAPI VE KALINTI GERİLİMDEKİ DEĞİŞİMLERİN TAHRİBATSIZ YÖNTEMLERLE TESPİT EDİLMESİ

Hızlı, Hüseyin
Yüksek Lisans, Metalurji ve Malzeme Mühendisliği Bölümü
Tez Yöneticisi: Prof. Dr. C. Hakan GÜR

Eylül 2016, 178 sayfa

Yüzeyi sertleştirilmiş makine parçalarının kullanım ömrü ve performansı büyük ölçüde parçanın yüzeyinde oluşan ve yorulma davranışını doğrudan etkileyen kalıntı gerilim durumuna bağlıdır. Son zamanlarda, tüm endüstriyel sektörler için kalıntı gerilimlerin hızlı ve tahribatsız bir şekilde belirlenmesi önem kazanmıştır. Bu çalışma sementasyon ısıl işlemi uygulanmış 19CrNi5H çeliklerindeki artık gerilim dağılımlarının tahribatsız ve yarı tahribatsız yöntemler kullanılarak ölçümünü amaçlamaktadır. Bu çalışma süresince Manyetik Barkhausen Gürültüsü (MBN), X-ışınları kırınımı (XRD) ve Elektronik Benek Desen Girişim Ölçümü (ESPI) yardımı ile delik delme teknikleri kullanılmıştır. Artık gerilim ölçümlerinin yanı sıra, optik ve taramalı elektron mikroskobu kullanılarak içyapı analizi, sertlik ölçümleri ve spektroskopi analizi gerçekleştirilmiştir. Sementasyon işleminin kalıntı gerilim dağılımları üzerindeki etkisini anlayabilmek için, farklı sertleşme derinliğine sahip ve farklı sıcaklıklarda menevişlenmiş numuneler hazırlanmıştır. XRD ve ESPI metotları kullanılarak yapılan kalıntı gerilim ölçümleri, sertleşme derinliği boyunca baskı kalıntı gerilimlerinin oluştuğunu ve baskı kalıntı gerilime büyüklüğünün menevişleme sıcaklığındaki artış ile düştüğünü göstermektedir. MBN ölçüm sonuçları, Barkhausen Gürültüsünün sementasyon süresindeki azalış ve menevişleme sıcaklığındaki artış ile arttığını göstermektedir. Yapılan bu çalışma sonrası uygun bir kalibrasyon ile MBN tekniğinin sementasyon sonrası oluşan yüzey kalıntı gerilimlerinin ölçümünde kullanılabilir olduğu sonucuna varılmıştır.

Anahtar Kelimeler: Sementasyon, Kalıntı Gerilim, Tahribatsız Muayene, Manyetik Barkhausen Gürültüsü Yöntemi, X-ışınları Kırınımı, ESPI, Delik delme

To my family and people who are reading this page....

ACKNOWLEDGMENTS

I would like to thank my supervisor Prof. Dr. C. Hakan Gür for their constant support, guidance, and friendship. It was a great honor to work with him for the last three years, and our cooperation highly influenced my academic and worldview. I would also like to thank Assistant Prof. Dr. Caner Şimşir, Assistant Prof. Dr. Kemal Davut and Dr. İbrahim Çam for their support and guidance.

I am very thankful to my colleagues from Welding Technology and Non-destructive Testing Research/Application Center for their support and valuable help. In addition, I am more than grateful for those from the Metal Forming Center of Excellence, Atilim University (MFCE). They have given me the opportunity to conduct my experiments. It was so great to work with them.

Many people were with me in these three years. They defined me; they made me who I am; they are real owners of this work. It is not possible to write down why each of them is important to me and this job because it will take more space than the work itself. I am very grateful to all people I know during my research assistantship in METU-WTNDT, they changed me deeply: my vision towards life, happiness, and friendship. I am very lucky to have them all. So I will just give names of some of them; H. İlker Yelbay, Orcan Kolankaya, Seyhan Çamlıgüney, Tuğçe Kaleli, and the others. I would also like to thank you Ebru Arslan, Emin Tamer et al. I give my special gratitude for Zeynep Öztürk and Yahya Tunç from MFCE for always helping me from the start of my Master Degree and being more than a friend to me.

Lastly, sincerest thanks to each of my family members and Yeliz Yurdakan for supporting and believing in me all the way through my academic life.

TABLE OF CONTENTS

ABSTRACT v

ÖZ vii

ACKNOWLEDGMENTS x

TABLE OF CONTENTS xi

LIST OF TABLES xv

LIST OF FIGURES xvi

NOMENCLATURE xxi

CHAPTERS

1 INTRODUCTION 1

- 1.1 Introduction to the Heat Treatment 1
  - 1.1.1 Theory of Carburizing 2
  - 1.1.2 Methods of Carburizing 5
- 1.2 Residual Stress Phenomenon 18
  - 1.2.1 Background and Definition 18
  - 1.2.2 Residual Stress Formation 20
  - 1.2.3 Effects of Residual Stress on the Operating Performance 24
  - 1.2.4 Residual Stress Measurement Methods 25
- 1.3 Theory of Magnetic Barkhausen Noise Method 26
  - 1.3.1 Principles of Magnetism 26
  - 1.3.2 The Fundamentals of Barkhausen Noise 31
  - 1.3.3 Factors Influencing Barkhausen Noise 36
- 1.4 Theory of X-Ray Diffraction Stress Measurement Method 44
  - 1.4.1 X-Ray Diffraction Principles 44

1.4.2 Strain and Stress Measurement ... 46
1.4.3 Selection of X-ray Radiation ... 54
1.4.4 Measurement Parameters ... 56
1.4.5 Potential Sources of Measurement Uncertainties ... 56
1.4.6 Advantages and Disadvantages ... 57

1.5 Theory of ESPI Hole-Drilling Stress Measurement Method ... 57
1.5.1 Principle of ESPI System ... 58
1.5.2 Stress Analysis Technique by ESPI System ... 60
1.5.3 Potential Errors and Uncertainties of ESPI System ... 64
1.5.4 Advantages and Disadvantages of the ESPI System ... 66

1.6 Literature Survey ... 66
1.6.1 Studies Based on Magnetic Barkhausen Noise Method ... 67
1.6.2 Studies Based on X-ray Diffraction Method ... 69
1.6.3 Studies Based on ESPI Hole-Drilling Stress Measurement Method ... 73

1.7 The Aim of Study ... 77

2 EXPERIMENTAL PROCEDURE ... 79

2.1 Material Selection ... 79

2.2 Heat Treatment ... 80

2.3 Magnetic Barkhausen Noise Method ... 83
2.3.1 Specimen Preparation ... 83
2.3.2 Device Information and System Settings ... 83
2.3.3 Test Parameters ... 84

2.4 X-Ray Diffraction Method ... 85
2.4.1 Specimen Preparation ... 85
2.4.2 Device Information and System Settings ... 85
2.4.3 Test Parameters ... 87

2.5 ESPI Hole-Drilling Method ... 88
2.5.1 Specimen Preparation ... 88
2.5.2 Device Information and System Settings ... 89

2.5.3 Test Parameters 90

2.6 Microstructure – Hardness – Spectral Analysis 91

3 RESULTS AND DISCUSSION 93

3.1 Microstructure – Hardness – Spectral Analysis Results 93
3.1.1 Microstructural Characterization 94
3.1.2 Retained Austenite Measurement 100
3.1.3 Hardness Measurement 103
3.1.4 Optical Emission Spectrometer Analysis Results 105

3.2 X-Ray Diffraction Measurement Results 107

3.3 Magnetic Barkhausen Noise Measurement Results 115
3.3.1 Parameter Optimization 115
3.3.2 Rollscan Results 120
3.3.3 µScan Measurement Results 124

3.4 ESPI Hole-Drilling Measurement Results 132

3.5 Comparison of the Three Residual Stress Measurement Methods 143

4 CONCLUSION 147

4.1 General Conclusions 147

4.2 Recommendations for Further Studies 149

REFERENCES 151

APPENDICES

A. SCANNING ELECTRON MICROSCOPE IMAGES 163

B. CORRELATION BETWEEN XRD and MBN METHODS 169
B.1 8hrs Carburized Steel Samples 169
B.2 10hrs Carburized Steel Samples 170

C. ESPI FRINGE PATTERNS 171
C.1 Fringe Patterns of the 8hrs Carburized Sample 171
C.1.1 180°C Tempered Sample 171
C.1.2 240°C Tempered Sample 172

C.1.3 600°C Tempered Sample 173
C.2 Fringe Patterns of the 10hrs Carburized Sample 174
C.2.1 240°C Tempered Sample 174
C.2.2 600°C Tempered Sample 175
C.3 Fringe Patterns of the 13hrs Carburized Sample 176
C.3.1 180°C Tempered Sample 176
C.3.2 240°C Tempered Sample 177
C.3.3 600°C Tempered Sample 178

LIST OF TABLES

TABLES

Table 1.1-1 Typical composition for a solid carburizing [60] 6

Table 1.1-2 Compositions of liquid carburizing baths in wt% [60]............................. 9

Table 1.4-1 Recommended test parameters for steels [8] 55

Table 1.6-1 Calculated stress σ_{xx} for measured α= 24° and percentage error for Δα=±2° [62] 74

Table 1.6-2 Effect of drilling speed on the residual stress measurement [62]........... 75

Table 2.1-1 Mechanical properties and chemical composition of sample 80

Table 3.1-1 Diffraction angle, integral intensities, and R-values of γ-Fe and α-Fe. 101

Table 3.1-2 Calculated volume percent of retained austenite 102

Table 3.1-3 Calculated retained austenite content in carburized 19CrNi5H samples 102

Table 3.1-4 Average hardness (HV1) of the carburized samples 103

Table 3.2-1 Average residual stress values for martensite phase with the three different phi angle in carburized 19CrNi5H steel sample.. 108

Table 3.2-2 Average residual stress values for austenite phase in carburized steel sample 112

Table 3.3-1 Average root mean square values of the MBN measurement 121

Table 3.3-2 Coercivity and Remanence values obtained from magnetic hysteresis curve of carburized 19CrNi5H steel 127

LIST OF FIGURES

FIGURES

Figure 1.1–1 Solubility of carbon in austenite for some carburizing grade steels [65] 3

Figure 1.1–2 Actual and approximate carbon content during carburizing [65] 5

Figure 1.1–3 Relationship carbon dioxide content and carbon potential for endothermic gas from methane [60] 14

Figure 1.1–4 Relationship dew point and carbon potential for endothermic gas from methane [60] 15

Figure 1.2–1 Schematic diagram of the cross-section of a sheet of toughened glass showing how residual stresses can exist in the absence of an external load [6] 19

Figure 1.2–2 Residual stresses arise from misfits either between different regions or between phases within material: types of macro and micro residual stress [6] 20

Figure 1.2–3 Temperatures and stresses of surface and core during quenching of carburized steel as a function of log t [1] 22

Figure 1.2–4 Temperatures and stresses of surface and core during quenching of carburized steel when martensitic transformations start in the surface [1] 23

Figure 1.3–1 A periodic table showing the type of magnetic behavior of each element at room temperature [14] 27

Figure 1.3–2 Elongation of a ferromagnetic object in the direction of an applied magnetic field [14] 28

Figure 1.3–3 a) Alignment of individual atomic moments, b) Division into magnetic domains with antiparallel domain magnetizations [14] 29

Figure 1.3–4 Magnetic domain walls containing varying orientation of magnetic moment [32] 30

Figure 1.3–5 Diagram showing examples of 90° domain wall and 180° domain wall [35] 31

Figure 1.3–6 a) Hysteresis curve with large magnification produced by alternating the applied magnetic field as a function of magnetic flux density b) Hysteresis curve for magnetically soft (I) and magnetically hard material (II) [35] 33

Figure 1.3–7 Schematic diagram of a Barkhausen noise measurement system [41] . 34

Figure 1.3–8 A typical Barkhausen noise signal with bursts 35

Figure 1.3–9 A change in the magnetoelastic signal level with respect to applied stress [28] 38

Figure 1.3–10 Barkhausen noise response to tensile and compressive stress [28] 40

Figure 1.3–11 The RMS value of the BN signal as a function of applied magnetic field with different microstructures [77] ... 43

Figure 1.4–1 Radiation diffraction within a crystal structure [4] ... 45

Figure 1.4–2 Schematic of diffraction emanating from an atomic array in an (a) unstrained state and (b) under tensile strain due to an applied load [4] ... 46

Figure 1.4–3 Definition of the laboratory coordinate system L_i, simple coordinate system S_i, and the angles ϕ, ψ [6] ... 47

Figure 1.4–4 Plots of regular (a, b) and oscillatory $d_{\phi\psi}$ versus $\sin^2\psi$ data [6] ... 48

Figure 1.4–5 A d(311) versus $\sin^2\psi$ plot for a shot peened 5056-O aluminum alloy [7] ... 52

Figure 1.5–1 The ESPI measurement system set-up [7] ... 59

Figure 1.5–2 Example of speckle pattern of unprocessed image (left) and processed image (right) by computer software ... 60

Figure 1.5–3 Typical fringe counting path [11] ... 63

Figure 1.6–1 Residual stress distribution across the thickness of hardened and case-hardened steel plates [45] ... 70

Figure 1.6–2 a) Influence of case-hardening depth (CHD) on the distribution of longitudinal residual stresses [45], b) depth profile of tangential residual stress with different case-hardening depths [47] ... 71

Figure 1.6–3 Residual stress distributions in identical carburized cylinders with different diameters [50] ... 72

Figure 1.6–4 a) Effect of quenchant temperature on the residual stress state, b) Effect of tempering on the residual stress state [58] ... 73

Figure 1.6–5 Variation of the percentage difference in the calculated σ_{XX} with the hole depth in correspondence of an error with respect to measured angle [62] ... 74

Figure 1.6–6 Comparison of the measured (ESPI) and calculated (FEM) residual stress distribution [63] ... 75

Figure 1.6–7 Comparison of the residual hoop stress measured by ESPI and XRD methods [67] ... 76

Figure 2.2–1 Nomenclature for coding of the samples ... 81

Figure 2.2–2 Typical carburizing cycle for 19CrNi5 steel ... 82

Figure 2.3–1 Magnetic Barkhausen Noise device and the sensor used ... 84

Figure 2.4–1 XStress 3000 G2/G2R residual stress measurement system ... 86

Figure 2.4–2 Seifert XRD 3003 PTS system ... 87

Figure 2.4–3 Detector arc in modified χ mode [7] ... 88

Figure 2.5–1 Prism® residual stress measurement system ... 89

Figure 2.6–1 Zig-zag pattern adopted for hardness measurements ... 91

Figure 3.1–1 CCT and TTT (right) diagram for 19CrNi5H steel [100] 94

Figure 3.1–2 Optical (left) and SEM (right) micrographs of the normalized 19CrNi5H steel: 500X and 5000X magnification, respectively 95

Figure 3.1–3 Optical micrographs for case-hardened 19CrNi5H steel (900°C/8 hrs): 1000X magnification 97

Figure 3.1–4 Optical micrographs for case-hardened 19CrNi5H steel (900°C/10hrs): 1000X magnification 98

Figure 3.1–5 Optical micrographs for case-hardened 19CrNi5H steel (900°C/13hrs): 1000X magnification 99

Figure 3.1–6 XRD pattern of the case-hardened 19CrNi5H steel (900°C/13 hrs): as-quenched 101

Figure 3.1–7 Effect of the carburizing time at 900°C on the hardness depth profile of the 19CrNi5H steel 104

Figure 3.1–8 Effect of the carburizing time at 900°C on the depth profile of the percent carbon in the 19CrNi5H steel 105

Figure 3.1–9 Hardness versus percent carbon for carburized 19CrNi5H steel (900°C/13hrs): as-quenched 106

Figure 3.2–1 A linear graph of d vs. $sin^2\psi$ fitted to diffraction data of $\Phi=0°$ for carburized 19CrNi5H (800°C/8hrs): as-quenched 107

Figure 3.2–2 Effect of tempering on the surface residual stress of the carburized 19CrNi5H steel (900°C/8hrs) 109

Figure 3.2–3 Effect of tempering on the surface residual stress of the carburized 19CrNi5H steel (900°C/10hrs) 110

Figure 3.2–4 Effect of tempering on the surface residual stress of the carburized 19CrNi5H steel (900°C/13hrs) 111

Figure 3.2–5 Effect of tempering on the surface residual stress of the carburized 19CrNi5H steel for 8hrs, 10hrs, and 13hrs 112

Figure 3.2–6 Residual stress depth profile obtained by XRD method for carburized 19CrNi5H steel (900°C/8hrs): as-quenched 114

Figure 3.2–7 Residual stress depth profile obtained by XRD method for carburized 19CrNi5H steel (900°C/13hrs): as-quenched 114

Figure 3.2–8 Effect of the tempering temperature on the depth profile of the residual stresses in the carburized 19CrNi5H steel (900°C/13hrs) 115

Figure 3.3–1 Pearson's correlation for 160 MBN measurements on the carburized samples 116

Figure 3.3–2 Sensitivity Index values of 160 MBN measurements on the carburized samples 117

Figure 3.3–3 Validity index values of 160 MBN measurements on the carburized samples 118

Figure 3.3–4 Calculated score values for parameter optimization of the MBN measurement 119

Figure 3.3–5 Effect of tempering temperature on the average RMS values of Barkhausen Noise for carburized 19CrNi5H steel (900°C/8hrs) 122

Figure 3.3–6 Effect of tempering on the average RMS values of Barkhausen Noise for carburized 19CrNi5H steel (900°C/10hrs) 122

Figure 3.3–7 Effect of tempering on the average RMS values of Barkhausen Noise for carburized 19CrNi5H steel (900°C/13hrs) 123

Figure 3.3–8 Effect of tempering and carburizing time on the average RMS values of Barkhausen noise emission of the samples carburized at 900°C for different periods 124

Figure 3.3–9 The relative RMS voltage as a function of relative magnetic field strength for the normalized and carburized 19CrNi5H samples 126

Figure 3.3–10 Magnetic hysteresis curve for the normalized 19CrNi5H steel 128

Figure 3.3–11 Magnetic hysteresis curve for the carburized and tempered 19CrNi5H steel 129

Figure 3.3–12 Magnetic hysteresis curves for the carburized samples (900°C/13hrs) 130

Figure 3.3–13 Correlation between residual stress and RMS values for carburized 19CrNi5H (900°/13hrs) 132

Figure 3.4–1 ESPI assisted hole-drilling measurement points 132

Figure 3.4–2 Fringe pattern of normalized 19CrNi5H steel (880°C/3 hrs) 134

Figure 3.4–3 Depth profile of the residual stress state obtained by ESPI assisted hole-drilling (after normalizing) 135

Figure 3.4–4 Fringe pattern of the carburized 19CrNi5H steel (900°C/8hrs): as-quenched 136

Figure 3.4–5 Depth profile of the residual stress state obtained by ESPI assisted hole-drilling (900°C/8hrs carburizing): as-quenched 138

Figure 3.4–6 Effect of the tempering temperature on the depth profile of the residual stress state obtained by ESPI assisted hole-drilling (900°C/8hrs carburizing) 138

Figure 3.4–7 Fringe pattern of the carburized 19CrNi5H steel (900°C/10hrs): T180 139

Figure 3.4–8 Effect of the tempering temperature on the depth profile of the residual stress state obtained by ESPI assisted hole-drilling (900°C/10hrs) 140

Figure 3.4–9 Fringe pattern of the carburized 19CrNi5H steel (900°C/13hrs): as-quenched 141

Figure 3.4–10 Effect of the tempering temperature on the depth profile of the residual stress state obtained by ESPI assisted hole-drilling (900°C/13hrs) 142

Figure 3.4–11 Effect of the carburizing time on the residual stress state of the 19CrNi5H steel......143

Figure 3.5–1 Comparison of the residual stress depth profiles obtained by XRD and ESPI techniques for the carburized 19CrNi5H steel (900°C/13hrs): 180°C tempered......144

Figure 3.5–2 Barkhausen Noise response to the residual stress......145

Figure A–1 SEM micrographs of carburized steel sample (900°C/8hrs): as-quenched core (upper left), as-quenched core (upper right) and 180°C tempered case (below left) and core (below right)......163

Figure A–2 SEM micrographs of carburized steel sample (900°C/8hrs): 240°C tempered core (upper left), as-quenched core (upper right) and 600°C tempered case (below left) and core (below right)......164

Figure A–3 SEM micrographs of carburized steel sample (900°C/10hrs)......165

Figure A–4 SEM micrographs of carburized steel sample (900°C/13hrs): as-quenched core (upper left), as-quenched core (upper right) and 180°C tempered case (below left) and core (below right)......166

Figure A–5 SEM micrographs of carburized steel sample (900°C/13hrs): 240°C tempered core (upper left), as-quenched core (upper right) and 600°C tempered case (below left) and core (below right)......167

Figure A–6 Correlation between residual stress and RMS values for carburized 19CrNi5H (900°/8hrs)......169

Figure A–7 Correlation between residual stress and RMS values for carburized 19CrNi5H (900°/10hrs)......170

Figure A–8 Fringe pattern of the carburized 19CrNi5H steel (900°C/8hrs): 180°C Tempered......171

Figure A–9 Fringe pattern of the carburized 19CrNi5H steel (900°C/8hrs): 240°C Tempered......172

Figure A–10 Fringe pattern of the carburized 19CrNi5H steel (900°C/8hrs): 600°C Tempered......173

Figure A–11 Fringe pattern of the carburized 19CrNi5H steel (900°C/10hrs): 240°C Tempered......174

Figure A–12 Fringe pattern of the carburized 19CrNi5H steel (900°C/8hrs): 600°C Tempered......175

Figure A–13 Fringe pattern of the carburized 19CrNi5H steel (900°C/13hrs): 180°C Tempered......176

Figure A–14 Fringe pattern of the carburized 19CrNi5H steel (900°C/13hrs): 240°C Tempered......177

Figure A–15 Fringe pattern of the carburized 19CrNi5H steel (900°C/13hrs): 600°C Tempered......178

NOMENCLATURE

ABBREVIATIONS

RS	Residual Stresses
MBN	Magnetic Barkhausen Noise
XRD	X-Ray Diffraction
ESPI	Electronic Speckle Laser Interferometer
BN	Barkhausen Noise
NDT	Non-Destructive Testing
HV	Vickers Hardness
RD	Rolling Direction
ND	Normal Direction
RMS	Root Mean Square
SEM	Scanning Electron Microscopy
OES	Optical Emission Spectrometer
CCD	Charge Coupled Device
CHD	Case Hardened Depth
FWHM	Full-Width Half Maximum
TTT	Time-Transformation Temperature
CCT	Continuous Cooling Transformation
DP	Dew Point

SYMBOLS

N	Normalizing heat treatment
C	Carburizing heat treatment
T	Tempering temperature [°C]
f	Magnetizing frequency [Hz]
V_{pp}	Magnetizing voltage [Volts]

B	Magnetic flux
H	Applied magnetic field
H_c	Coercivity
H_s	Saturation magnetization
B_r	Remanence
M_s	Martensite start temperature [°C]
D_C	Diffusion coefficient of carbon in austenite
C_x	Carbon concentration as a function of distance from the surface
C_o	Initial carbon content of steel [% weight]
C_s	Surface carbon concentration [% weight]
P	Partial pressure of the species
K	Equilibrium constant
L_i	Laboratory coordinates system
S_i	Simple coordinate system
C_{ijkl}	Elastic stiffness coefficients
E	Elastic Modulus [GPa]
hkl	Miller indices
a_c	Activity of carbon
d	Distance between diffracting lattice planes
k	Sensitivity vector
F	Fringe pattern

GREEK LETTERS

μ	Permeability
μ_r	Relative permeability
μ_0	Permeability of vacuum
δ	Penetration depth of Barkhausen noise signal
σ	Conductivity of a material under test
λ	X-ray wavelength
Θ_B	Bragg’s angle

CHAPTER 1

INTRODUCTION

This chapter is devoted to giving information about thermochemical heat treatment process, residual stress formation, and the measurement of residual stress distribution in the heat-treated samples by means of Magnetic Barkhausen Noise, X-Ray Diffraction, and Electronic Speckle Pattern Interferometer assisted hole-drilling method. In the first part of the introductory chapter, particular information about the carburizing processes and residual stress phenomena will be discussed in details. Then, theories of the aforementioned residual stress measurement techniques will also be explained in details by giving some mathematical models. The literature survey conducted is aimed to provide a scientific basis for the understanding of how residual stress induced by the carburizing process can be measured by different techniques. The studies corresponding to the Magnetic Barkhausen Noise technique will be given at the beginning of the literature survey. Then, the studies based on the X-Ray Diffraction will be given and then the studies about the ESPI assisted hole-drilling method will be presented.

1.1 INTRODUCTION TO THE HEAT TREATMENT

Engineering components for some applications must have not only hard and wear resistant surface but also ductile and tough core. The carbon content of the steel should be relatively high to obtain high surface hardness upon quenching, as the hardness of steels is a function of carbon content. Nevertheless, an increase in the carbon content of the steel leads to a decrease in ductility and toughness of the components. Since a combination of high surface hardness and toughness usually cannot be achieved by single quenching and tempering heat treatment operations of the steel parts, such a combination of material properties can be achieved by enriching the surface of the low-carbon steel with carbon up to a certain depth. Thermochemical heat treatment, varying the surface composition of the steel by diffusion of carbon, is one of the techniques utilized to acquire hard and wear resistant outer shell together with ductile and tough inner shell. The fundamentals of thermochemical surface hardening technique, known as carburizing, will be covered in the subsequent chapter.

1.1.1 Theory of Carburizing

Carburizing is described as a heat treatment in which the carbon content of the surface of the low-carbon steel is increased when the surface of the steel is in contact with an environment of high carbon activity at high temperatures in the austenite range. The surface carbon content, in solution in austenite, may increase until carbon activity at the surface becomes equal to that of surrounding environment. Nonetheless, if the activity of carbon at the surrounding is higher than the solubility limit of carbon in the austenite phase at the processing temperature, the maximum surface carbon content is limited to the solubility limit of carbon in austenite. The Iron-Carbon phase diagram indicates that the maximum solubility of carbon in austenite varies from 0.8% at the eutectoid temperature to about 2% at the eutectic temperature. In other words, the solubility limit of carbon is given by A_{CM} line in Iron-Carbon phase diagram shown in Figure 1.1–1. Solubility limits of some carburizing grade steels in austenite can also be seen in Figure 1.1–1. When the carburizing temperature is increased, the more carbon can be dissolved in the austenite so that carbon content of the steel can be increased.

However, an increase in the carbon content of the steel up to about 0.8% has an impact on the hardness of the material. The further increase in the carbon content leads to increase in retained austenite rather than increasing hardness of the sample. Since retained austenite causes lower hardness values and dimensional and microstructural instabilities, the coveted percentage of carbon during carburizing is usually lower than the solubility limit of carbon in austenite at carburizing temperatures.

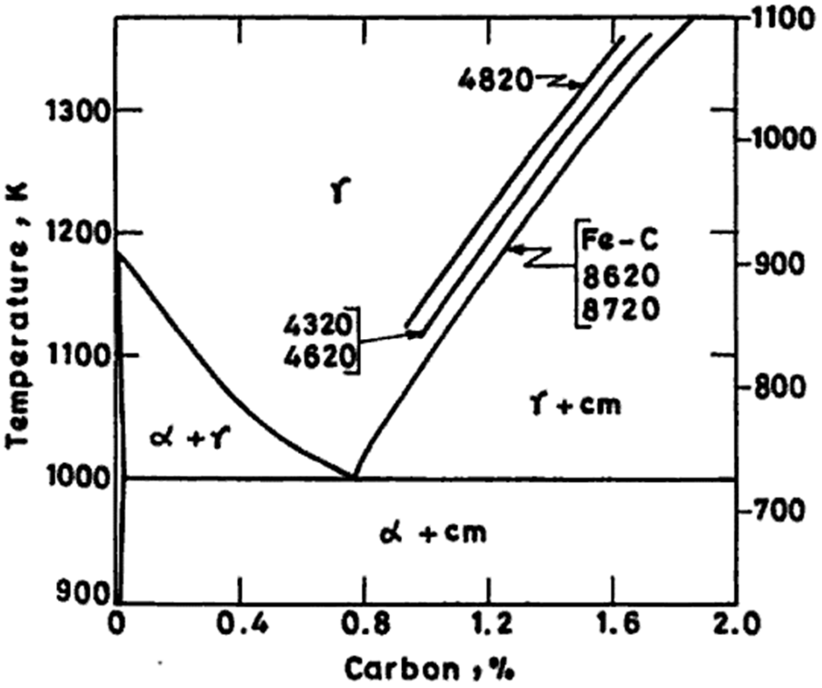

Figure 1.1–1 Solubility of carbon in austenite for some carburizing grade steels [65]

Although carburizing heat treatment is frequently carried out between 850°C and 950°C, the higher temperatures can be used to reduce cycle times. Carburizing treatment may be performed in a gaseous environment, a liquid salt bath, or with solid carbonaceous compounds. In any processes above, the objective is to start carburizing with low-carbon steel and then increase the surface carbon content of the steel by the surface hardening heat treatment. This kind of heat treatment results in gradually decreasing carbon content from surface region to the core region.

The case-hardened depth produced by a given carburizing process as a function of time is determined approximately by the following equation;

$$x = 2\sqrt{D_c t} \tag{1.1-1}$$

where x is the case-depth, D_c is the diffusion coefficient of carbon in austenite phase and t is the carburizing time. The case depth can be calculated more precisely by using Fick's Second Law of diffusion as a function of time and distance;

$$\frac{C_x - C_s}{C_0 - C_s} = erf\left(\frac{x}{2\sqrt{D_c t}}\right) \tag{1.1-2}$$

where C_x is the carbon concentration as a function of distance from the surface, C_s is the surface carbon concentration; C_0 is the initial carbon content of steel and the other terms defined earlier in the Equation 1.1.-1. Carbon concentration calculated as a function of depth x according to the equation 1.1-2 at a given time t is schematically shown in Figure 1.1–2. When a linear line is drawn on the carbon concentration profile illustrated in Figure 1.1–2 in a manner of time t same as in Equation 1.1-2, the distance meeting the C_0 line may be given as;

$$x = \frac{4}{\pi}\sqrt{D_c t} \cong 2.26\sqrt{D_c t} \tag{1.1-3}$$

As seen in Figure 1.1–2, a linear distribution shows a reasonably good approximation for the carbon distribution. Both equations 1.1-2 and 1.1-3 give case-hardened depth as proportional to square root of $D_c t$ with a constant. Thereby, those equations can be used to approximate the **c**ase-**h**ardened **d**epth (CHD).

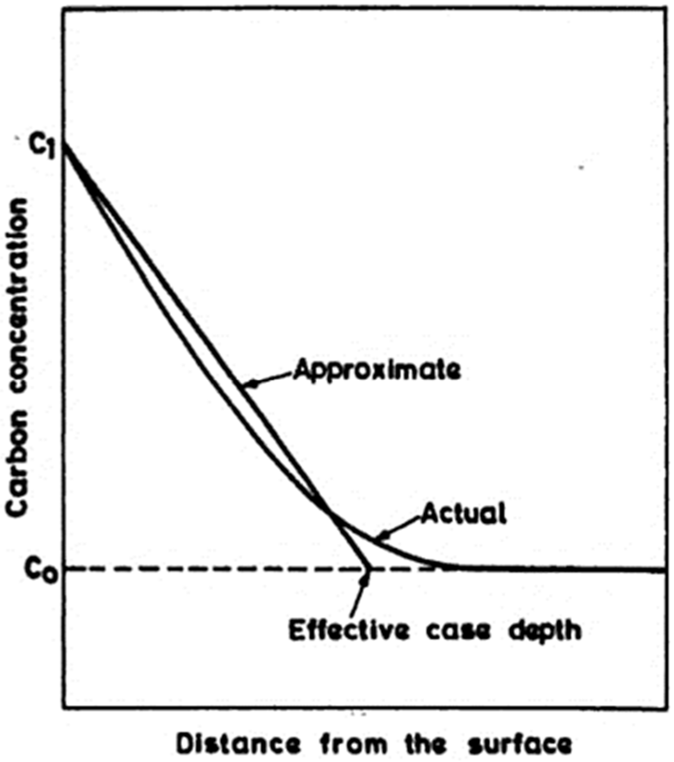

Figure 1.1–2 Actual and approximate carbon content during carburizing [65]

It should be kept in mind that the Equation 1.1-2 and Equation 1.1-3 give approximate CHD during thermochemical heat treatment operation when the surface of the steel is flat so that carbon diffuses perpendicular to the surface from the surface to core. For cylindrical and spherical surfaces, the equations must be calculated by new boundary conditions. Moreover, in actual heat treatment operation, cold pieces are typically loaded into the carburizing furnaces at carburizing temperatures. The time required to reach the carburizing temperature is an important phenomenon since carbon diffusion into the piece is not much during the heating period. Hence, the Equations 1.1-2 and Equation 1.1-3 can only be used at the actual carburizing conditions.

1.1.2 Methods of Carburizing

Three primary methods based on the nature of carburizing atmosphere can be applied for the carburizing heat treatment. Those are categorized as pack carburizing, liquid carburizing and gas carburizing. Workpieces are packed in solid carburizing media in pack carburizing, while they are subjected to liquid and gaseous carburizing atmosphere in liquid and gas carburizing, respectively. Lately, some new methods have been introduced, such as plasma carburizing, vacuum carburizing and fluidized bed carburizing. Pack carburizing, liquid carburizing and the gaseous carburizing will be discussed in details in the following sub-sections. Brief information about the vacuum carburizing and the plasma carburizing will also be given.

1.1.2.1 Pack Carburizing

Pack carburizing method is also known as solid carburizing, and it is the oldest method used as a surface hardening technique. The solid carburizing mixture contains hardwood charcoal, acting as a source of carbon, energizer component which is barium carbonate, and coke increasing the thermal conductivity of the system. Components of the solid mixture are put in a heat resistant container, and then the container is sealed and heated in a furnace preheated to desired carburizing temperature of about 930°C. The typical solid carburizing mixture is given in Table 1.1-1.

Table 1.1-1 Typical composition for a solid carburizing [60]

Component	***Composition (%wt)***
Hardwood charcoal	53 – 55
Coke	30 – 32
Barium Carbonate	10 – 12
Sodium Carbonate	2 – 3
Calcium Carbonate	3 – 4

Though the hardwood charcoal is the primary source of carbon during the carburizing operation, transfer of carbon from carburizing mixture to the surface of the steel sample does not happen directly by the solid-solid reaction. At such a high temperature, air entrapped in the case reacts with the carbon producing carbon monoxide. Then, this carbon monoxide reacts with the steel surface whose carbon content increases according to the reaction;

$$2CO + Fe \rightarrow Fe\underline{C} + CO_2 \qquad [1]$$

CO_2 is produced during the reaction [1], and it further reacts with the charcoal to form CO again to be used in reaction [1];

$$CO_2 + C \rightleftharpoons 2CO \qquad [2]$$

Reaction [2] will always go right when there is enough carbon dioxide in the system at the carburizing temperatures. Barium carbonate in the mixture also decomposes at the high temperatures to give below reaction;

$$BaCO_3 \rightarrow BaO + CO_2 \qquad [3]$$

Reaction [3] supplies the required carbon dioxide for the reaction [2], and so does the enough carbon monoxide for the reaction [1]. This is the reason why barium carbonate and carbon dioxide is called as an energizer. In pack carburizing, the process continues as long as enough carbon exists in the closed system to react with the carbon dioxide.

Operating temperature for the pack carburizing varies from 815°C to 955°C [60]. The carburized case formation rate increases with an increasing operating temperature. By assuming 1.0 as a representative factor of 815°C operating temperature, the factor increases to 1.5 at 870°C operating temperature, and more than 2.0 at 925°C operating temperature. In this carburizing operation, the surface carbon content is approximately equal to the solubility limit of the carbon in austenite at the carburizing temperature (see Figure 1.1–1). The desired carbon level thru the case is directly proportional to the carburizing temperature. When the more carbon is needed in the case region, the temperature should be increased.

Even with the good control of the process, it is difficult to monitor case depths to close tolerances during the operations. The main reason for difficulties in the follow-up to the case depths is because of the variations in the time required for all the mixture to reach the carburizing temperature. Therefore, case depths cannot be assumed by the equation 1.1-1. In addition to this, during the operation, there exist case depths variations of 0.25 mm at the carburizing temperatures of 925°C. When the temperature increases, the differences in the case depth also increases to ±0.8 mm. Due to the changes in the case depths and the cost of packing materials, pack carburization is usually not utilized for the samples requiring case depth less than 0.8 mm [60].

1.1.2.2 Liquid Carburizing

Liquid carburizing is a method of case hardening of ferrous metals by holding them above their transformation temperature in a molten salt bath [64]. The salt in the carburizing mixture decomposes and releases carbon and nitrogen depending on the mixture used. The high level of hardness can be achieved by the diffusion of the released elements into the surfaces of the work metal. Many liquid carburizing baths contain sodium cyanide introducing both carbon and nitrogen into the surface. These baths are divided into two categories as (1) low-temperature bath, (2) high-temperature baths. However, non-cyanide liquid baths using a particular grade of carbon have recently been developed due to the health and environmental risks induced by cyanide baths [64].

Low-temperature baths called as light-case baths are typically functioned in the temperature range varying from 845°C to 925°C. This kind of baths is used to produce shallow case depths varying from 0.13 to 0.25 mm. Typical composition of low-temperature carburizing baths is given in Table 1.1-2. Parts that are produced by low-temperature baths will have a significant amount of nitrogen unless the process is operated with a protective carbon cover of thick enough.

Table 1.1-2 Compositions of liquid carburizing baths in wt% [60]

Constituents	***Low-Temperature Baths (845°C – 900°C)***	***High-Temperature Baths (900°C – 955°C)***
Sodium cyanide	10 – 23	6 – 16
Barium chloride	—	30 – 55
Salts of alkaline earths	0 – 10	0 – 10
Potassium chloride	0 – 25	0 – 20
Sodium chloride	20 – 40	0 – 20
Sodium carbonate	40 maximum	30 maximum
Other accelerators	0 – 5	0 – 2
Sodium cyanate	1.0 maximum	0.5 maximum
Density	1760 kg/m^3 at 900°C	2000 kg/m^3 at 925°C

The chemistry of the carburizing process in low-temperature baths is complicated since several reactions are occurring simultaneously depending upon the bath composition [65]. The main reactions involved during the process are as follows;

$$2NaCN \rightarrow Na_2CN_2 + C \quad [4]$$

$$2NaCN + O_2 \rightarrow 2NaNCO \quad [5]$$

$$NaCN + CO_2 \rightarrow NaNCO + CO \quad [6]$$

The possibility of the cyanate formation is more predominant due to the presence of oxygen. Then, the produced cyanate reacts further to give;

$$NaNCO + C \rightleftharpoons NaCN + CO \quad [7]$$

$$4NaNCO + 2O_2 \rightarrow 2Na_2CO_3 + 2CO + 4N \quad [8]$$

$$4NaNCO + 4CO_2 \rightarrow 2Na_2CO_3 + 6CO + 4N \quad [9]$$

Though the activity of the bath is detracted by the reactions [8] and [9] that cause loss of carburizing effectiveness, all reactions producing carbon monoxide or carbon are effective in providing the desired case depth as;

$$Fe + 2CO \rightarrow Fe\underline{C} + CO_2 \qquad [10]$$

$$C + Fe \rightarrow Fe\underline{C} \qquad [11]$$

The temperature ranges for high-temperature baths, or deep-case baths, are from 900°C to 955°C. Temperature range is critical in the process since the rate of carbon penetration depends upon the temperature. The rapid carbon penetration can be obtained at temperatures between 980°C and 1040°C; yet above the temperatures of 955°C, baths are deteriorated faster. These kinds of baths are used to obtain case depths from 0.5 to 3.0 mm [60]. The typical composition of high-temperature baths is shown in Table 1.1-2. The primary reactions of this type baths are given as;

$$2NaCN + BaCl_2 \rightarrow Ba(CN)_2 + 2NaCl \qquad [12]$$

$$Ba(CN)_2 \rightleftharpoons BaCN_2 + C \qquad [13]$$

The reversible reaction [13] reacts with the surface of the steel further to introduce carbon into as;

$$Ba(CN)_2 + Fe \rightarrow BaCN_2 + Fe\underline{C} \qquad [14]$$

Although the surface of the heat treated steel essentially consists of carbon dissolved in iron, nitrogen present in the system will also dissolve in the steel surface.

Non-cyanide liquid baths contain particular grade of carbon instead of cyanide as a source of carbon in heat treatment process [64]. Operating temperatures are generally in the range from 900°C to 955°C. Deep case depths as in the high-temperature bath can be achieved by this method.

In liquid bath carburizing, the effective case depth depends on the time and temperature as stated earlier in the present study. Surface carbon content is controlled by the salt bath composition since the carbon and/or nitrogen source for the diffusion to the surface is provided from the decomposition of the salt. With liquid carburizing, selective carburizing can be achieved without stop-off applications and variety of samples irrespective of size and shape can be carburized simultaneously [60]. However, the parts are required washing after the heat treatment, and salt that adhere the hot work pieces causes the contamination of the quenching mediums. In addition, cyanide baths are hazardous for both human health and environment [64].

1.1.2.3 Gas Carburizing

During the last few decades, gas carburizing has become the most commonly used method of thermochemical heat treatment process in the industry [68]. Natural gas, or methane (CH_4), is the most used source of carbon for gas carburizing, but other gaseous or liquid hydrocarbons, such as propane (C_3H_8) and butane (C_3H_{10}), may also be used as the carbon source. Since undiluted natural gas or propane is the richer in the carbon, the solubility limit of carbon in austenite is reached at the surface of the steel, and some carbides are formed at the surface of the steel. Therefore, enriching gas should be diluted by the carrier gas before carburizing process. Most commonly used carrier gas, endothermic gas, is obtained by the burning of hydrocarbon in air that the reaction is given as;

$$2C_3H_8 + 3O_2 \rightarrow 6CO + 8H_2 \qquad [15]$$

Then, the endothermic carrier gas consists of the nitrogen remained from air, carbon monoxide, hydrogen as by-products and carbon dioxide, water vapor and unreacted hydrocarbons formed [64]. Typical carrier gas composition may be 40% nitrogen, 20% carbon monoxide, 38% hydrogen and small amounts of carbon dioxide, water vapor by volume. A small amount of enriching gas that is 5 to 20% by volume is diluted by the produced carrier gas [65]. The mixture ratio of the gasses depends on the desired surface carbon content of the low carbon steel.

Specific reaction during the gaseous carburizing process is dependent on the nature of gas mixture; that is, carrier gas and the enriching gas. During the gas carburizing process at carburizing temperatures, various reactions occurred may be assumed thermodynamically in equilibrium [64]. Since the pyrolysis and the reactions from different gaseous atmospheres are out of scope in this study, the chemical reactions with the presence of methane and carrier gasses produced from methane will be discussed in detail in the following. The main constituents of the carburizing atmosphere are carbon monoxide, nitrogen acting as a diluent since it is inert, hydrogen, carbon dioxide, water vapor and the methane. The main carburizing reactions occurring in the presence of the mentioned gasses are as follow;

$$Fe + 2CO \rightleftharpoons Fe\underline{C} + CO_2 \qquad [16]$$

$$Fe + CO + H_2 \rightleftharpoons Fe\underline{C} + H_2O \qquad [17]$$

$$Fe + CH_4 \rightleftharpoons Fe\underline{C} + 2H_2 \qquad [18]$$

When the concentration of carbon dioxide and water vapor in the reactions [16] and [17] increase in the gaseous atmosphere, the reactions occur reversibly that decarburizing process takes places. To annihilate the decarburizing effect of carbon dioxide and water vapor, methane present in the carburizing gas mixture reacts with them to give;

$$CH_4 + CO_2 \rightarrow 2CO + 2H_2 \qquad [19]$$

$$CH_4 + H_2O \rightarrow CO + 3H_2 \qquad [20]$$

During the reactions [19] and [20] that reduce the concentration of carbon dioxide and water vapor, carbon monoxide and hydrogen are regenerated so that the reactions [16] and [17] occur again to increase surface carbon enrichment of the steel. It is seen that the enriching gasses are a major source of the carbon during the carburizing.

The carbon concentration at the surface of the steel part is determined by the carbon potential in the gaseous atmosphere. In the heat treatment practice, the carbon potential can be controlled by (1) carbon dioxide concentration, (2) water vapor concentration and (3) oxygen partial pressure.

The principle of carbon potential control from the carbon dioxide concentration depends on the reaction given;

$$2CO \rightleftharpoons \underline{C} + CO_2$$

The carbon potential can be found from the equilibrium constant, K_1, written for the above-specified reaction by the following relationship;

$$K_1 = \frac{a_C \times P_{CO_2}}{\left(P_{CO}\right)^2} \qquad (1.1.2\text{-}1)$$

where P_{CO_2} and P_{CO} are the partial pressures of the species, a_C is the activity of the carbon and K is the equilibrium constant for the reaction. The equilibrium constant can be calculated from the Gibbs free energy of formation of carbon monoxide and carbon dioxide at the carburizing temperatures [60]. The carbon activity is related to the carbon content of austenite by the relationship [69];

$$\ln a_C = \ln\left(\frac{4.65w}{100-w}\right) + \frac{\left[5093 + 9167 \times \left(\frac{4.65w}{100-w}\right)\right]}{T} - 1.867 \qquad (1.1.2\text{-}2)$$

where T is the temperature in Kelvin, w is the weight percentage of the carbon in austenite. The combination of the Equations (1.1.2-1) and (1.1.2-2) give the relationship between equilibrium carbon content in austenite and carbon dioxide and carbon monoxide content. As long as the assumptions are satisfied, only measuring the carbon dioxide content is enough to define carbon potential, and so does the carbon concentration at the surface. Figure 1.1–3 indicates the relationship between carbon dioxide content and the carbon potential for endothermic gas produced from methane at the different carburizing temperature.

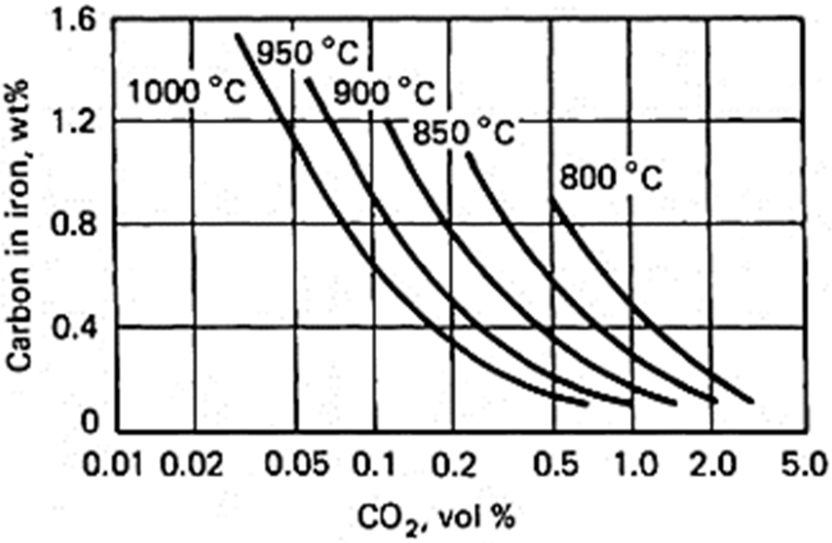

Figure 1.1–3 Relationship carbon dioxide content and carbon potential for endothermic gas from methane [60]

A similar relationship exists for the control of the water vapor by dew point of the atmosphere. The water vapor content of the atmosphere is associated with the carbon potential by the reaction;

$$CH_4 + H_2O \rightleftharpoons CO + 3H_2$$

The equilibrium constant of the reaction is given by the relationship described below;

$$K_2 = \frac{a_C \times P_{H_2O}}{P_{CO} \times P_{H_2}} \tag{1.1.2-3}$$

Since the P_{CO} and P_{H_2} remain constant in the gaseous carburizing atmospheres, the carbon potential can be measured by the dew point. Dew point in degrees Celsius in carburizing atmosphere is given by;

$$D.P. = \frac{5422.18}{14.73 - \ln P_{H_2O}} - 273{,}16 \tag{1.1.2-4}$$

Figure 1.1–4 shows the relationship between dew point in degrees Celsius and the carbon potential for endogas produced from methane at the different carburizing temperature.

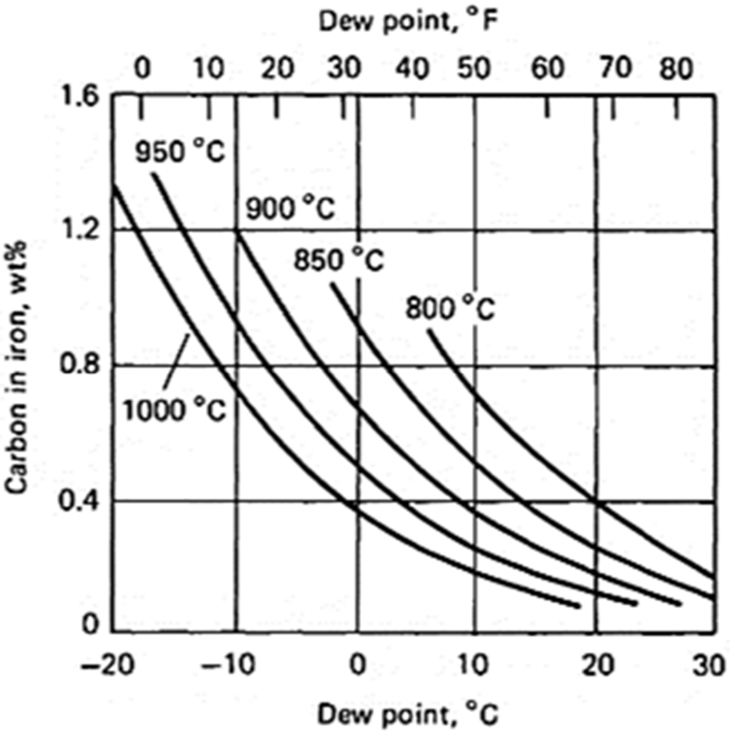

Figure 1.1–4 Relationship dew point and carbon potential for endothermic gas from methane [60]

The partial pressure of oxygen can also be used to control the carbon potential. Under the equilibrium conditions, the partial pressure of oxygen is related to the partial pressure of carbon dioxide by the following reaction;

$$CO + \tfrac{1}{2}O_2 \rightleftharpoons CO_2$$

Then, the equilibrium constant can be given by;

$$K_3 = \frac{P_{CO_2}}{P_{CO} \times \left(P_{O_2}\right)^{1/2}} \qquad (1.1.2\text{-}5)$$

The arrangement of the equations (1.1.2-1) and (1.1.2-5) gives the following relationship;

$$a_C = \frac{K_1 \times P_{CO}}{K_3 \times \left(P_{O_2}\right)^{1/2}} \qquad (1.1.2\text{-}6)$$

Since K_1 and K_3 are the temperature dependent and the partial pressure of carbon monoxide is assumed to remain constant, the carbon potential of the atmosphere can be calculated from the partial pressure of oxygen.

The typical temperature for carburizing is 925°C in the gaseous atmosphere [60]. This temperature allows reasonably fast carburizing rates without the deterioration of furnace equipment. The temperature should be consistent throughout the furnace not to produce various case depths in one batch operation. It also is noted that steel surface is extremely active at carburizing temperatures of 925°C. Therefore, if the carbon content of the atmosphere is higher than that of steel, the steel surface absorbs the carbon to reach the equilibrium. However, when the environment contains less amount of carbon, then the steel surface loses its carbon meaning that decarburizing will occur. With the gas carburizing process, the case depths between 0.5 mm to 2.0 mm can be achieved in a relatively short period of times compared to pack and liquid carburizing.

1.1.2.4 Vacuum Carburizing

In vacuum carburization process, carburizing heat treatment is carried out in vacuum furnaces with the introduction of carburizing gaseous mixture at relatively low pressures. The steel is austenitized under a low vacuum atmosphere and carburized in a partial pressure of enriching gasses. After the enrichment step, diffusion of carbon into the surface is carried out under a low vacuum atmosphere. The process is carried out at temperatures between 980°C and 1050°C [64] and pressures ranging from 6.7 kPa to 40 kPa. Vacuum carburizing provides excellent oxidation and decarburization resistance. Since the vacuum carburizing is a non-equilibrium process, carburizing process is controlled by controlling the process variables, like time, temperature, partial pressure of enriching gasses.

1.1.2.5 Plasma Carburizing

Plasma carburizing is a method of carburizing where the partial heating of the parts and the carburization is carried out in a plasma of low-pressure ionized gasses [65]. The plasma contains ionized gasses and electrons. Positively charged ions, such as CH_3^+, are accelerated towards the cathode where the carbon is introduced into the workpiece while the electrons are accelerated to the anode. Typical temperature range is between 950°C and 1050°C. Since the plasma is insufficient to heat the workpiece, the auxiliary heating source is used.

In plasma carburizing, high rates of carburization are usually obtained. Since the temperature is of the order of 100 times that of the gaseous molecules, some chemical reactions, which cannot occur under normal thermodynamic equilibrium, can occur [65]. With plasma carburizing, uniform carbon introduction to the surface is attained due to the dissociation of the enriching gas and surface oxides removing the barrier to the introduction of carbon. The better case uniformity and lesser distortion in the part are achieved by the plasma carburization. Detailed information can be found in the references [60] and [65].

1.2 RESIDUAL STRESS PHENOMENON

The stresses to which a component is subjected to the service can be estimated with modern analytical and computational techniques [2]. This in itself is not sufficient for the reliable prediction of component performance. Indeed, in many cases, unexpected failure has occurred due to the presence of the residual stresses that seriously shorten the lifetime of the components. It is well known that there exist no materials and/or structures of technical importance with free of residual stresses. In this part of the study, brief information about residual stress and its measurement methods are described.

1.2.1 Background and Definition

Residual **S**tresses (RS) can be defined as the stresses that remain in the material or body after manufacture material processing in the absence of external forces including gravity or thermal gradients [3]. Residual stresses can also be formed during service loading, which causes inhomogeneous plastic deformation in the part of the specimen. The forces acting on the body are self-equilibrating, that is, zero force and moment resultants are produced by the local areas of tensile and compressive stresses within the whole volume of the material or structure. To illustrate, Figure 1.2–1 schematically show how a residual stress distribution through a thickness of a sheet of toughened glass can exist without an external load [4]. Surface compressive residual stresses are balanced with the tensile residual stresses in the central region.

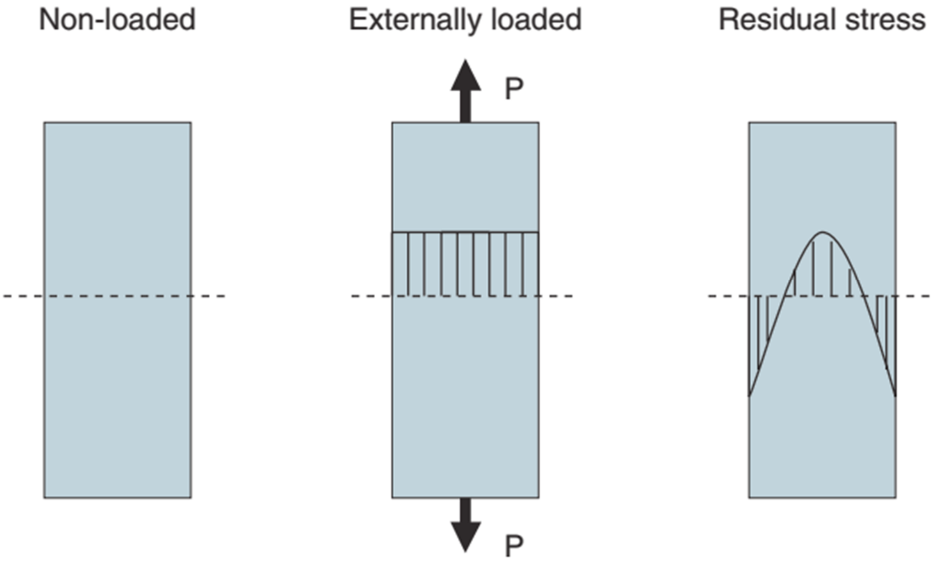

Figure 1.2–1 Schematic diagram of the cross-section of a sheet of toughened glass showing how residual stresses can exist in the absence of an external load [6]

Residual stresses can be defined as either macro or micro stresses, and both stresses can be present in a component at any time. A simple classification can be given as follows:

- ***Type I:*** These are macro residual stresses developing in the body of a component over a scale larger than the grain size of the material. These stresses are equilibrated over the bulk of the material. Dimensions of material will be changed when the equilibrium of forces and moment resultants of a volume containing type I residual stresses are interfered.

- ***Type II:*** This type of residual stresses is nearly homogeneous on the scale of an individual grain and is equilibrated across a sufficient number of grains. Macroscopic changes of the dimensions a volume containing type II stresses may only be observed when distinct disturbances of equilibrium occur.

- ***Type III:*** These are micro residual stresses existing within a grain due to the presence of dislocations and other crystalline defects. No macroscopic dimensional change will happen if this equilibrium is disturbed.

Residual stresses are formed by almost all manufacturing processes. Figure 1.2–2 schematically illustrates some typical ways in which residual stresses are formed in engineering materials. Change in the localized dimension requires elastic deformation of surrounding material to keep the dimensional continuity, so developing residual stresses. Residual stresses can arise from some sources and can be present in the unprocessed raw material, introduced during manufacturing or result from in-service loading. The origins of them in a component can be classified as (1) differential plastic flow, (2) differential cooling rates, and (3) phase transformations with volume changes.

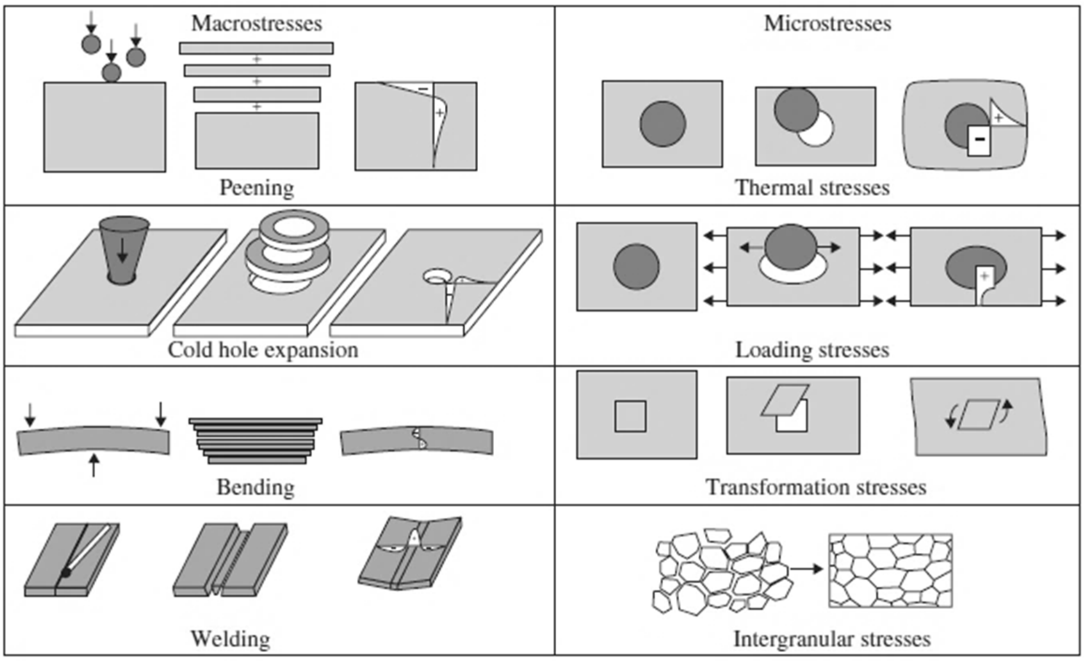

Figure 1.2–2 Residual stresses arise from misfits either between different regions or between phases within material: types of macro and micro residual stress [6]

1.2.2 Residual Stress Formation

The underlying mechanisms of how the temporal and local differences in cooling and phase transformation processes result in thermal shrinking and transformation-induced strains and variation in the microstructural state must be understood when studying the mechanism of stress formation after quenching of carburized steels [1].

In the beginning, the part contracts due to the development of thermal shrinking stresses in all quenched materials. During quenching of hardenable steels, austenite phase transforms into another phase(s) such as ferrite, pearlite, bainite, or martensite. This phase transformation results in so-called transformation stresses superimposing to some extent the thermal stresses caused by pure cooling.

However, *Macherauch and Vöhringer* [45] states that rapid quenching of austenitic steel components to the room temperature gives rise to a hardening residual stress state that cannot be described by a simple superposition of thermal and transformation stresses. During quenching, any austenite to martensite phase transformation is combined with the volume expansion shifting the prevalent stress values to magnitudes that are more negative irrespective of signs. Due to the diffusion based thermochemical process, an inhomogeneous carbon distribution is present within a distinct depth so that the final residual stress state will be affected by this different distribution. Hence, knowledge of time-temperature-transformation (TTT) and continuous-cooling-transformation (CCT) diagrams at each respective surface distance play a paramount role in the development of final residual stress field due to the transformation behavior.

Understanding the influence of varying carbon profile on the kinetics of stress evaluation during the quenching is important to find out whether the core of the component starts phase transformation before or after the carburized surface region. Three theoretical cases can be deduced to understand the sequences of transformations that occur in the case and the core of the carburized component. These cases are as follows:

1. The core region transforms prior to the surface transformation
2. The surface region transformation precedes the core transformation
3. There is no preference concerning the sequence of transformations in the case and the core

During the transformation of the core prior to that of the surface, stress formation during cooling is illustrated schematically in Figure 1.2–3. As can be seen from the CCT diagram in the figure, the phase transformation austenite to ferrite-pearlite phases at the core region starts at time $t_{c,i}$. At this period, compressive stresses formed by the contraction of the part are generated in the core, which is balanced by the corresponding tensile surface stresses. For times between $t_{c,i}$ and $t_{s,i}$, both the surface tensile stresses and the compressive core stresses may plastically deform due to the presence of the relatively high temperatures in both the core region and the surface region. Upon further heat loss, the near-surface regions that possess lower carbon content begin martensitic phase transformation. When the time $t_{s,i}$ is reached, the surface of the component transform to the martensite phase. However, at that time, the expansions caused by martensitic transformations are restricted due to the surface and the near-surface regions that are relatively cool and rigid. As a result, the compressive residual stresses are formed on the outer regions whereas tensile residual stresses are created in the inner regions.

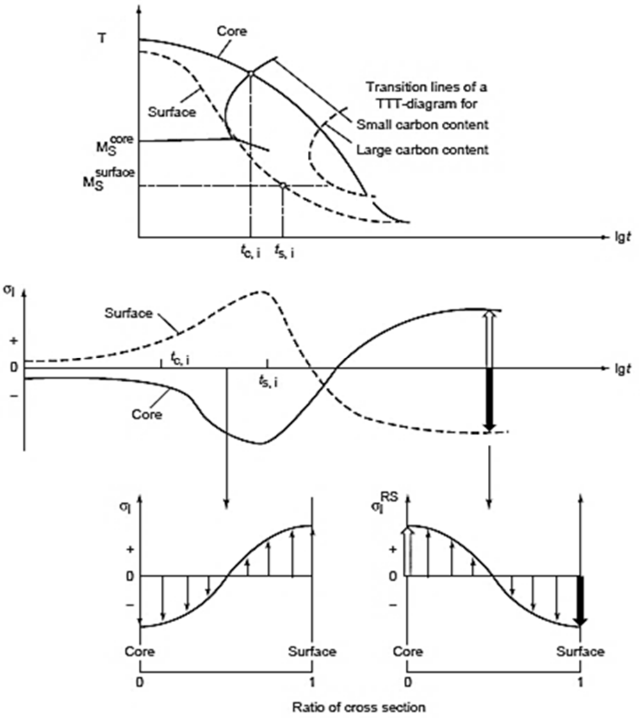

Figure 1.2–3 Temperatures and stresses of surface and core during quenching of carburized steel as a function of log t [1]

In the case II, surface transformation starts before the core transformation, seen in Figure 1.2–4. Before the transformation time $t_{s,i}$, the shrinkage of the surface gives rise to the formation of tensile stresses, which are balanced by compressive stresses present in the inner region. When the surface phase transformation starts at time $t_{s,i}$, the stresses acting on the surface are decreased and turned into the compressive stresses while a similar but a weaker trend is observed in the subsurface region. At this time interval, the core is still austenite and so can be plastically strained. When time is reached to $t_{c,i}$, the core region starts to transform from austenite to ferrite-pearlite phase. Nevertheless, this phase transformation is restricted to the surface regions already transformed so that compressive core stresses are created which are in the balance with the surface tensile stresses. When the temperature compensation is completed, the core regions are subjected to compressive residual stresses whereas tensile residual stresses are generated at the surface regions are.

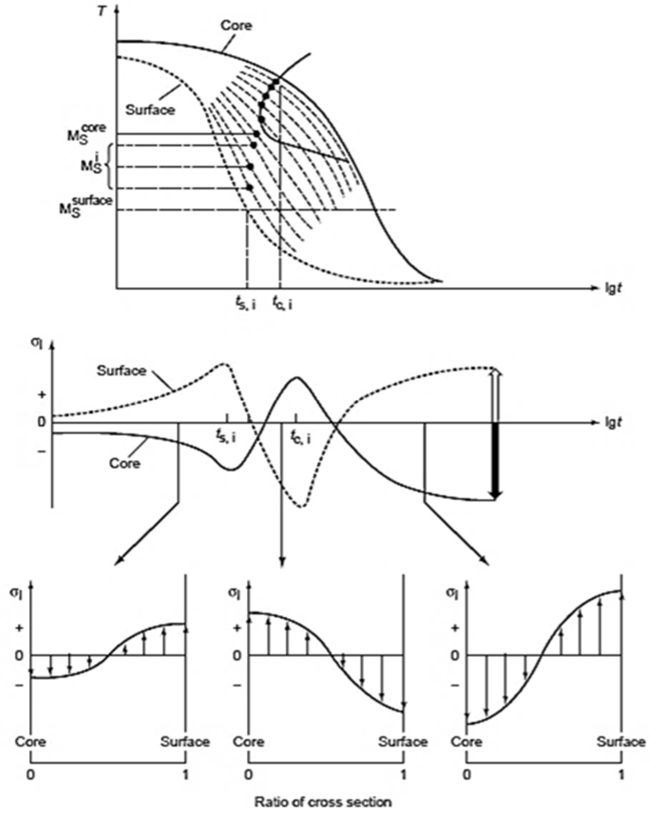

Figure 1.2–4 Temperatures and stresses of surface and core during quenching of carburized steel when martensitic transformations start in the surface [1]

In the third case, there exist several intermediate residual stress distributions. The character of the residual stress is dependent on the extent, which the prevailing conditions deviate from previously assumed cases.

1.2.3 Effects of Residual Stress on the Operating Performance

Because residual stresses have self-equilibrating character, the existence of residual stresses may be disregarded during engineering design. Nevertheless, since they are stresses, they must be taken into account in the same way as stresses due to external loading [5]. Regarding the strength of the material, the main influence of residual stress is an addition to the service loading stresses. In fact, residual stresses are added as a static load in the elastic range while residual stresses are relaxed over the elastic range.

It is well known that compressive residual stress has a beneficial effect on the fatigue life, crack propagation and stress corrosion whereas tensile residual stresses decrease the performance capacity of the materials. If a compressive residual stress, with an applied stress σ_A of the opposite sign, is created, the real stress σ_N in the material is less than σ_A. For example, surface hardening treatment can cause the compressive residual stress to increase the fatigue life of the component.

The performance of the material under loading bases on the residual stress state induced during the fabrication processes of the engineering material. In order to increase the mechanical properties of the sample, it is better to have a sample without residual stress or with compressive residual stress introduced on the surface. Hence, it is imperative to be able to measure and/or predict the residual stress state since the magnitude of residual stress is critical in comparison with the applied load.

1.2.4 Residual Stress Measurement Methods

Over the last few decades, various quantitative and qualitative techniques have been developed and used for the measurement of residual stresses. These techniques are generally classified as either destructive or nondestructive methods.

The destructive methods as implied are based on the destruction of the state of equilibrium of the residual stress in a component. In this way, the residual stress can be measured by relaxing it, and the redistribution of the internal forces causes local strains measured to evaluate the residual stress field. The procedure used can be described as follows:

1. The formation of a new stress state by machining or layer removal
2. The measurement of the strain or displacement caused by the local change in the stress
3. Calculation of the residual stress as a function of the strain by using the elastic theory

The most frequently used destructive, or so-called semi-destructive, methods are the hole-drilling method, the ring core technique, the bending deflection method and the sectioning method. They are all sensitive to the first kind of residual stress, i.e., the macroscopic residual stress [6].

The second sets of methods for the measurement of residual stresses are dependent on the relationship between the physical or crystallographic parameters and residual stress [3]. Since they do not destruct the part, the non-destructive measurement methods can be used for field measurement. The most well-developed techniques are the X-Ray and Neutron Diffraction method, the ultrasonic method, and the magnetic method. The ultrasonic and magnetic methods are sensitive to all three kinds of residual stress while diffraction methods are susceptible to the second and third kind of stresses.

1.3 THEORY OF MAGNETIC BARKHAUSEN NOISE METHOD

Magnetic **B**arkhausen **N**oise (MBN) method is used to characterize materials, materials degradation processes, and internal stresses. MBN method for stress measurement has the great advantage of being rapid, entirely non-destructive and in-situ measurements. However, it has limited use for evaluation of engineering stresses in an unambiguous and robust way due to its complex dependence on material composition, thermos-mechanical treatment, and microstructural condition. In this section of the study, the theoretical background behind Barkhausen noise and its measurement will briefly be presented.

1.3.1 Principles of Magnetism

Prior to giving information about the Magnetic Barkhausen Noise measurement, some fundamental information will be present in this sub-section for a better understanding of the background of BN signal generations.

1.3.1.1 Types of Magnetic Materials

The most common way of classifying the magnetic properties of the materials can be accomplished by their response to an application of magnetic field. Hence, classes of materials can be differentiated by using both relative permeability and relative susceptibility. The two most common kinds of magnetism are diamagnetism and paramagnetism, accounting for the magnetic properties of most of the periodic table of elements at room temperature, which can be seen in Figure 1.3–1. These elements are usually referred to as nonmagnetic, whereas those, which are magnetized to a certain extent by a magnetic field, are called as ferromagnetic.

Diamagnetism, weak form of magnetism, attributes mainly to the orbital motion of electrons creating magnetic moment. In other words, the atoms in a diamagnetic material do not possess magnetic moment during zero applied magnetic field. Magnetization is induced in the opposite direction to that of externally applied magnetic field. Diamagnetic materials have a negative and very weak relative susceptibility and their permeability values are less than one.

The relative permeability of a *paramagnetic* material is only slightly greater than one. Each atom in a paramagnetic material has a magnetic moment randomly oriented as a result of thermal agitation [43]. The application of magnetic field generates a slight alignment of these moments and so a low magnetization in the same direction as the applied field. Thermal agitation increases if the temperature is raised and it will be harder to align the atomic magnetic moments causing a decrease in the susceptibility. This behavior called as Curie law.

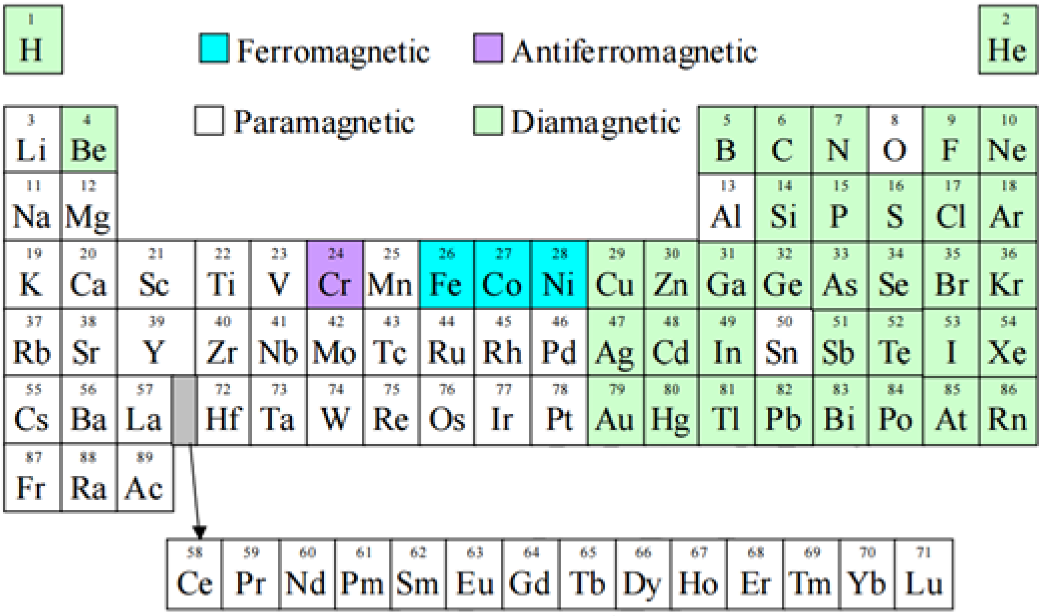

Figure 1.3–1 A periodic table showing the type of magnetic behavior of each element at room temperature [14]

Ferromagnetic materials include spontaneously magnetized magnetic domains in which the magnetization of an individual domain is oriented differently with respect to the magnetization of neighboring domains [43]. The spontaneous domain magnetization is generated by the unpaired electron spins from partially filled shells. Spins are aligned parallel to each other due to a strong exchange interaction. Change in the temperature has an effect on the arrangements of spins so does the spontaneous domain magnetization. The ferromagnetic material is assumed to be *demagnetized* when the total resultant magnetization for all domains is zero. Nevertheless, the application of magnetic field alters the total resultant magnetization from zero to saturation value. If magnetic field is reduced and reversed in sign, the magnetization of the material does not retract its original position and the material exhibits so-called hysteresis. Furthermore, only iron, cobalt, and nickel exhibit ferromagnetic behavior at and above room temperature. The alignment of the atomic moments decreases with increasing temperature. Eventually, the thermal agitation becomes so great that the material becomes paramagnetic at a temperature known as Curie temperature.

1.3.1.2 Magnetostriction

Under the influence of a magnetic field, the shape and the dimensions of the ferromagnetic materials may change very slightly due to a magnetic property named magnetostriction. This type of deformation, which is in the order of about 10^{-5} to 10^{-6} or even smaller, was discovered in 1842 by Joule. It was noticed in the experiment that the length of the iron rod has changed when magnetized in a weak magnetic field as in Figure 1.3–2. Although the dimensions of the material vary upon the application of magnetic field, its volume remains constant, which means that a transverse magnetostriction exists about the half of the value of the longitudinal magnetostriction with opposite sign.

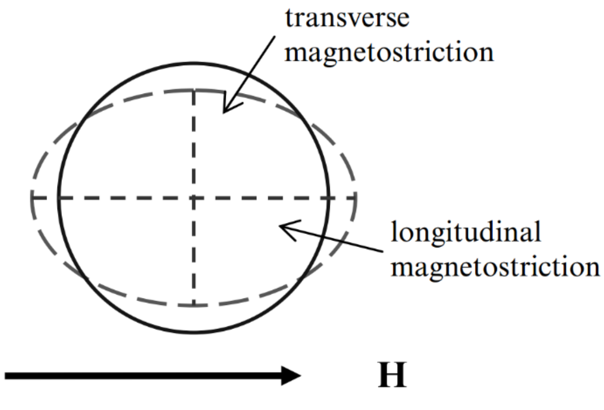

Figure 1.3–2 Elongation of a ferromagnetic object in the direction of an applied magnetic field [14]

Magnetostriction effect occurs due to the spin-orbit coupling of valence electrons in ferromagnets. When the spins change direction to align with domain magnetization, the orbits should change shape to maintain angular momentum. Magnetic field leads to an increase in the strains due to magnetostriction till reaching a saturation value.

1.3.1.3 Division into Domains and Formation of Domain Walls

In materials to be magnetized, individual atomic magnet moments have a tendency to align themselves parallel to each other to decrease the exchange energy that originates from spin-spin interactions responsible for ferromagnetism. Though parallel alignment of the spins decreases the exchange energy, this alignment raises the magnetostatic energy by creating a large external magnetic field seen in Figure 1.3–3a. As a result, to reduce the magnetostatic energy, several magnetic domains are set up with antiparallel magnetizations together with the formation of domain walls (Figure 1.3–3b). Several magnetic domains are formed within the material so that individual magnetic moments sum to a total magnetization in each magnetic domain.

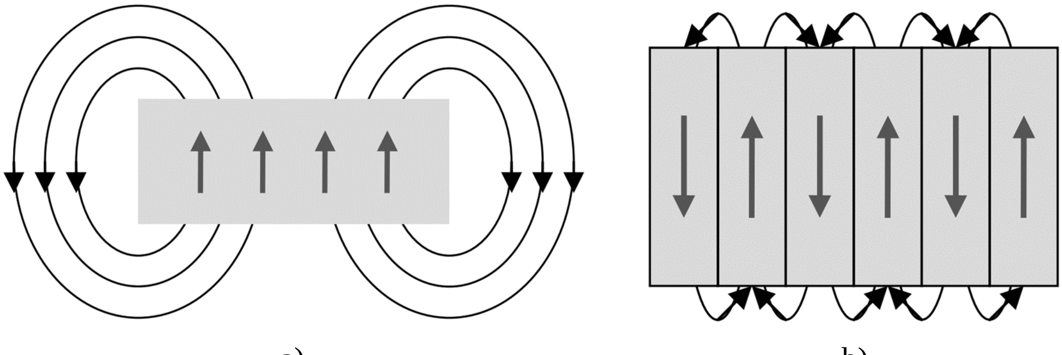
a) b)

Figure 1.3–3 a) Alignment of individual atomic moments, b) Division into magnetic domains with antiparallel domain magnetizations [14]

Further division into magnetic domains decreasing the magnetostatic energy creates the other energies out of balance. Those are magnetocrystalline, magnetoelastic, and wall energy. Hence, there are five basic energies involved in the formation of domains. The sum of these five energies being minimized leads to the formation of a certain magnetic configuration though energies may not be at their minimum. Ferromagnetic materials divide into magnetic domains since five different energies try to minimize its own.

The transition from one magnetization direction to another is sometimes sharp so that the exchange energy is too large to preserve an absolute magnetic domain configuration in equilibrium. Creation of a domain wall of a certain width with magnetic moments of changing orientation step by step helps to have a smoother transition, reducing the exchange energy. This phenomenon can be seen in Figure 1.3–4.

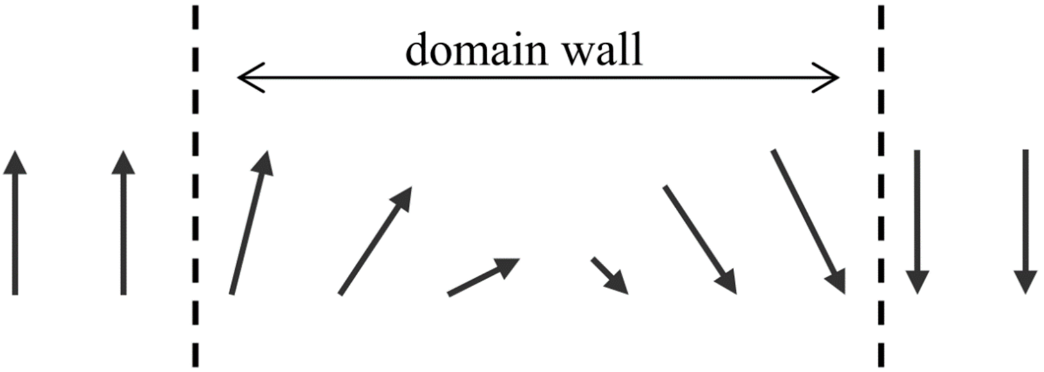

Figure 1.3–4 Magnetic domain walls containing varying orientation of magnetic moment [32]

The domain walls are divided into two types, namely *Bloch wall* in which the atomic magnetic moments rotate outside of the plane of the magnetic moments *and Néel wall* where the atomic moments remain in-plane during the rotation. Since domain magnetizations have a tendency to align with preferred crystallographic axes, domain walls separating domains of different orientations can be classified as 180°, 90° for iron or 109°, 71°for nickel. Different orientation of these walls can occur within closure domains that are created when the material divides into magnetic domains to let the magnetic flux stay in the material, decreasing magnetostriction energy. Furthermore, domain walls are responsible for the extrinsic magnetic properties of the material, such as remanence and coercivity. Magnetic hysteresis curve seen in ferromagnets are also created by those. Magnetic domain configurations show differences with the application of magnetic field or stress through the displacement of domain walls. Therefore, magnetic domains pinning by barriers are magnetic microstructures used in technological applications based on Barkhausen noise.

1.3.2 The Fundamentals of Barkhausen Noise

The **B**arkhausen **N**oise (BN) technique is a non-destructive testing method for ferromagnetic materials. The measurable changes in the magnetization values are generated by the irreversible movement of the magnetic domain walls [31, 32]. Ferromagnetic materials consist of small magnetic regions that are called as domains. It was introduced by Weiss in 1907 that these are small areas in the crystal structure of a ferromagnetic material possessing uniformly oriented magnetic moments in the demagnetized state. In each domain, the magnetic moments align along as easy axis planes that are certain crystallographic axes in the material. The domain walls exist between the magnetic domains in which the magnetic moments are subjected to a reorientation and the adjacent domains are separated by this wall [31]. Magnetic domains that are separating the regions of opposite magnetic moment are called as 180° while the walls lying at 90° to each other are termed as 90° walls for iron-based material presented in Figure 1.3–5. For nickel samples, those are termed as 109° and 71° walls.

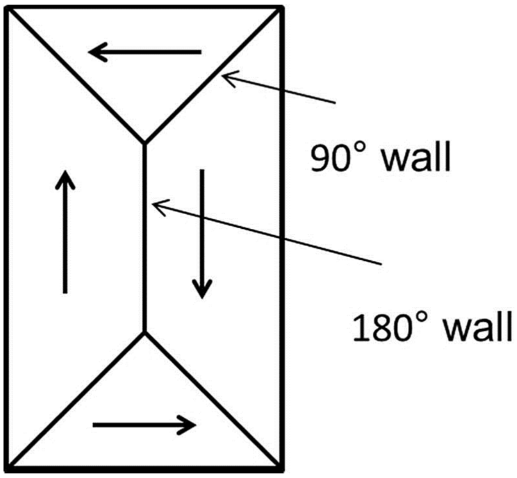

Figure 1.3–5 Diagram showing examples of 90° domain wall and 180° domain wall [35]

The magnetic domains are rearranged and reoriented when the piece of ferromagnetic material is magnetized. The magnetization process results in a hysteresis curve generated by altering the applied magnetic field (**H**) from negative to positive field strength whilst measuring the magnetic flux density (**B**). When the application of the magnetic field strength to a ferromagnetic material is increased slowly, the material becomes magnetized in a series of small steps as illustrated in Figure 1.3–6a. During the magnetization process, discontinuous domain wall motion within the material causes discrete variations in magnetization to be ascertained. These discontinuous variations in the magnetic flux density B are known as the Barkhausen effect [31].

The different changes occurring throughout the magnetization process for a soft magnetic material can be introduced by the hysteresis cycle shown in Figure 1.3–6a. Upon the application of the small magnetic field strength, the domain wall motion is reversible. When a small magnetic field strength is applied, the magnetic domains that are oriented throughout the applied magnetic field can grow at the expense of non-optimally oriented domains by the movement of domain walls. The movements of domain wall originate when the domain located on one side of the wall expands in size whereas one on the opposite side of the domain wall shrinks. The variation in the overall magnetization of the sample is caused by the result of this domain wall motion. The domains can regain their original position when this small-applied magnetic field is removed. Larger applied magnetic field strengths can create irreversible domain wall movement in the ferromagnetic materials. When the applied field increases further, domain rotation occurs and then only one large domain generates when the saturation magnetization ($\mathbf{H_s}$) state is reached. Remanence ($\mathbf{B_r}$) is described as magnetization that remains in the fully magnetized sample without any applied magnetic field. The field required to reduce the magnetization to zero is defined as Coercivity ($\mathbf{H_c}$) after the sample has been fully magnetized.

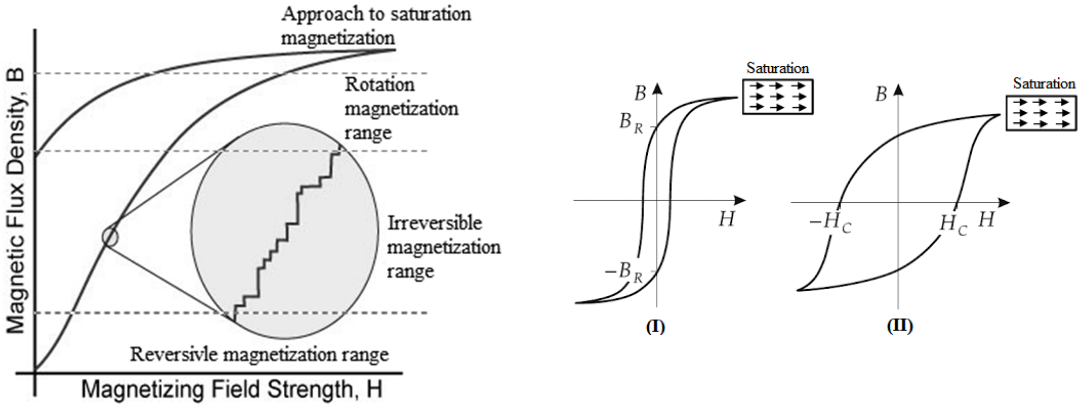

a) b)

Figure 1.3–6 a) Hysteresis curve with large magnification produced by alternating the applied magnetic field as a function of magnetic flux density b) Hysteresis curve for magnetically soft (I) and magnetically hard material (II) [35]

The ferromagnetic material can be characterized by utilizing the magnetic hysteresis curve parameters such as coercivity ($\mathbf{H_c}$) and remanence ($\mathbf{B_r}$) since such parameters are sensitive to the structure of material [33]. For example, coercivity, which is typically related to hardness, may be employed to differentiate hard and soft magnetic materials as seen in Figure 1.3–6b. In addition to this, it is reported in many types research that the coercivity, permeability, and remanence have a linear relationship to stress [34]. However, some studies have shown that a non-linear and monotonic behavior as a function of stress is observed with the remanence.

1.3.2.1 Barkhausen noise measurement system

The fundamental of the Barkhausen Noise analysis is simple. The magnetizing yoke is fed by an alternating current in order to produce an altering magnetic field strength for the repeated magnetization and demagnetization cycles of the ferromagnetic material. The magnetic field induced in the sample is fetched by the search coil. Then, the Barkhausen noise signal is obtained when the signal picked up by the coil is amplified and filtered. A schematic diagram of a typical Barkhausen noise instrument is shown in Figure 1.3–7.

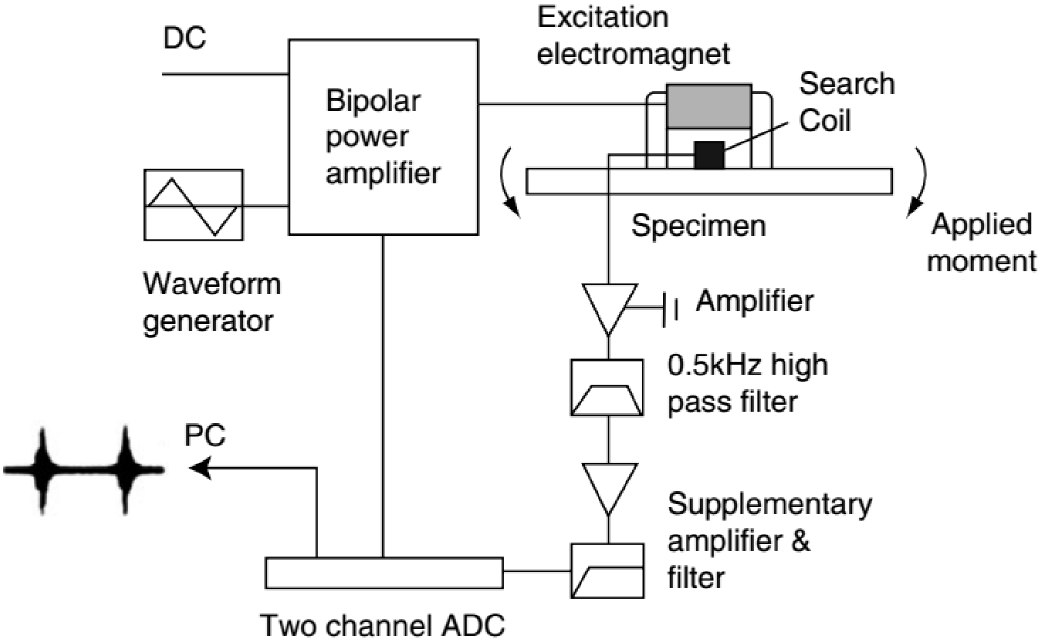

Figure 1.3–7 Schematic diagram of a Barkhausen noise measurement system [41]

The penetration depth of the BN signal bases on the applied magnetizing frequency and the permeability (**μ**) and conductivity of the tested materials [16]. Upon the adjustment of the magnetizing and analyzing frequency, the information depth from which the Barkhausen noise signal comes can be varied. High-frequency Barkhausen noise measurement is utilized to obtain information only from the surface layer of the component. An example of the usage of the high-frequency BN method is to detect grinding burns from hardened and ground components [36]. When high-frequency BN measurement is utilized, the analyzing frequency ranging from 20 to 1000 kHz can be applied to obtain information from penetration depths between 150 to 20 µm beneath the surface. On the other hand, measurements carried out by low-frequencies are defined as possessing a magnetizing excitation frequency of less than 1 Hz [37]. With the typical analyzing frequency range of 0.1 to 100 kHz, measurements with low-frequencies may have a skin depth of 635 µm [37].

1.3.2.2 Barkhausen Noise Signal Analysis

It is deduced that the penetration of the magnetic field into the specimen can be increased by using low-frequency Barkhausen noise measurement. The penetration depth of the BN measurement can be calculated from the following equation [37]:

$$\delta = \sqrt{\frac{1}{\pi \bullet f \bullet \sigma \bullet \mu_r \bullet \mu_0}} \tag{1.3-1}$$

where δ is the penetration depth of the BN signal, f shows the magnetizing frequency of the signal, σ is the conductivity of a material under test, μ_r is the relative permeability while μ_0 is the permeability of vacuum. The BN signal is attenuated exponentially as a function of the distance proceeded within the material owing to the eddy current damping depending on the frequency of the magnetized signal [37, 39]. In addition to the attenuation of the signal, the low-frequency BN measurement depth estimations will be affected by the properties of sensor such as a distance between the magnetizing poles and the sensitivity of the pick-up coil [37]. A typical Barkhausen noise signal generated by the optimum magnetizing voltage and frequency can be seen in Figure 1.3–8.

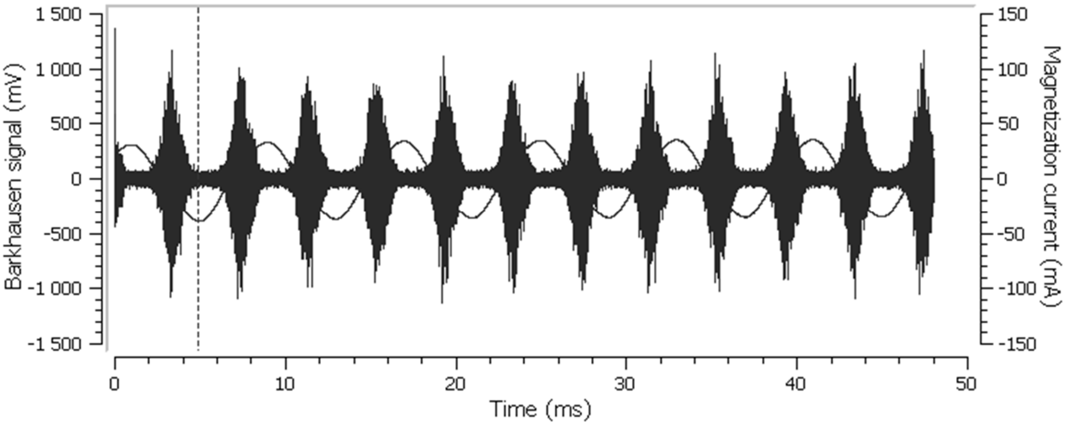

Figure 1.3–8 A typical Barkhausen noise signal with bursts

A collection of voltage pulses of varying amplitude generates the BN signal. Two bursts are formed during an increasing and decreasing magnetization cycle. Although different features can be calculated from the obtained signal affected by various BN events, their magnitude, and duration, the most typical parameter calculated and utilized from the signal is the root mean square (RMS) value of the voltage signal given by;

$$RMS = \sqrt{\frac{1}{N}\sum_{i=1}^{n} x_i^2} \tag{1.3-2}$$

The maximum Barkhausen activity can be obtained from the RMS value. The acquired RMS value is decreased when the hindrance of the domain walls retards the movement of domain walls under a high hardness or compressive stress state as well as the presence of the dislocations, grain boundaries, and precipitates. For one-half of the magnetization cycle, the BN envelope plotted as a function of magnetic field strength or as a function of time can provide information about the peak position and height of the BN signal, and the full-width at half-maximum (FWHM) value of the signal. The obtained envelope can be used to calculate various features of the part under observation. For example, the peak height is decreased with the increasing hardness [40, 41]. In addition, the peak height of the hardened sample increases by over-tempering.

1.3.3 Factors Influencing Barkhausen Noise

Even though it is usually known that **B**arkhausen **N**oise (BN) is simultaneously affected by both the stress state present in the material and the microstructure, the relationship of those is still not totally figured out, and there are contradictory results in the literature. Upon the application of external magnetization, the pinning of domain walls induced by microstructural barriers can affect the signal registered by BN pick-up coil. These obstacles in the microstructure slow down the velocity of the moving domain wall, and reduce the mean free path. Some of the obstacles in the structure can be overcome by the application of a greater magnetic field strength. The further increase in the magnetic field strength leads the domain walls to be relieved abruptly and voltage pulses are generated. The mean free path of the moving domain wall is limited by the interfaces present between the precipitate and the matrix or by the variations in the Type II residual stress state in the material. This, in turn, has an effect on the Barkhausen noise. When there are more obstacles to pin the movement of domain walls, a greater number of individual BN events are created. However, it is observed that these events have smaller amplitude [86]. With less number of hindrances present in the material and smaller resistances to the movement of domain walls, a lesser number of BN events are observed [86], and the Barkhausen noise burst is formed at the relatively low magnetic field strength values. When the density of pinning sites is raised, the application of stronger magnetic field will provide the energy for domain wall to pass through the barriers. In this situation, higher magnetic field values are required for the Barkhausen noise burst to be observed.

Since the various obstacles possess a different pinning power, a distribution of BN signal is generated with variation in amplitude of the pulses (pulse height distribution). The density of the barriers, such as dislocations, has a significant effect on the domain wall movement. Since the dislocation density is increased by the hardness, the harder materials decrease the Barkhausen noise level. As in the microstructural properties affecting the motion of the domain walls, stress state also alters the number of BN signal events and their relative magnitude [15].

Magnetic fields that are required to move and rotate the domains are influenced by the residual stress present in the material. If the tensile stresses are present, an increased magnetic field is necessary to make the domains move. Residual microstresses emerged around the dislocations generate inhomogeneous microstrains on the material. The greater the microstrain in the dislocations, the higher is the resistance to the domain wall movements. The stress-induced variation in the BN signal may be deduced from the basis of the variations in the magnetic domain wall configuration and domain wall motions.

1.3.3.1 The Effect of Stress

The Barkhausen Noise emission is influenced by several microstructural features and by the stress whether applied or residual. The basic relationship between BN and stress are relatively well apprehended as illustrated in Figure 1.3–9. Ferromagnetic materials are subjected to the magnetostriction phenomenon that bases on the magnetic field and stress state. When the magnetostriction coefficient of the material has a positive value, the Barkhausen Noise signal reveals an increasing trend in the direction of the applied elastic tensile stress. On the other hand, the signal decreases with the application of compressive stresses in the materials with positive magnetostriction coefficient [16].

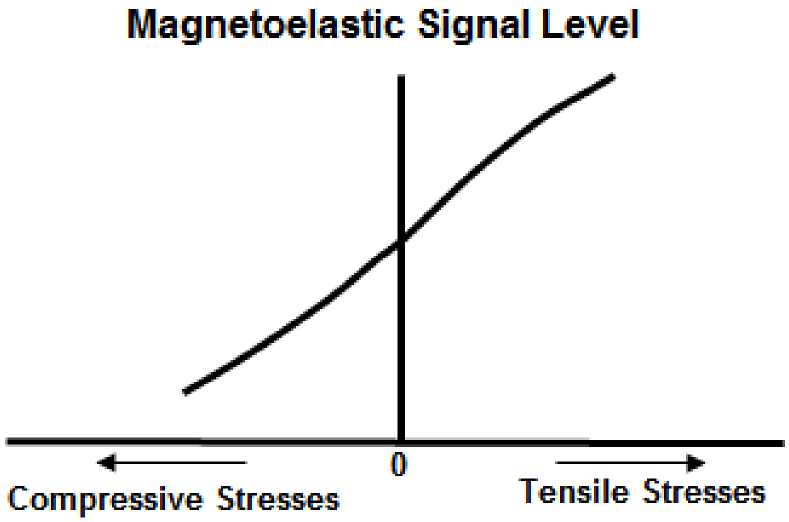

Figure 1.3–9 A change in the magnetoelastic signal level with respect to applied stress [28]

A ferromagnetic piece of steel is slightly converted into the magnet in the direction of the applied load. Without any load, a ferromagnetic material that possesses positive magnetostriction extends along the direction of magnetization order to decrease its magnetoelastic energy [17]. While this behavior is seen in the material with positive magnetostriction, such as iron and cobalt, the ferromagnetic material with negative magnetostriction, like nickel, will show the opposite behavior. Due to the differences in the interactions between magnetostriction, magnetizing, and stress, the behavior of the material that can be magnetized under the application of load is not easily described [16].

1.3.3.1.1 Elastic and plastic deformation

The relative deformation induced by the application of load can generate either elastic strain or plastic strain in the material. Changes in the interatomic spacing of the crystals describe the elastic deformation. When the stresses applied to the material is less than the yield strength, the material behaves elastically so that that the deformation process is reversible [18]. Micro-yielding characterized as dislocation formation in favorably oriented grains may occur before attaining the actual macroscopic elastic limit. Contrary to the elastic deformation, plastic deformation, loading greater than the yield strength, leads to the formation of imperfections such as twins, dislocations, and shear bands [19]. When the part plastically deforms, the number of barriers impeding the domain wall movement increases. It has been monitored that anisotropic behavior with respect to stress direction is created by the plastic deformation. The creation of this anisotropic behavior causes both 180° and 90° domain wall interactions instead of just 180° domain wall interactions [20].

The elastic strain induced by stress has a more pronounced influence on the MBN energy response than the plastic strain. The presence of a plastic deformation in the material only leads to slight variations in the average Barkhausen noise energy [19, 21]. This can be accounted for the dissimilar deformation mechanisms arisen throughout plastic and elastic deformation. The plastic deformation can lead to the variations in the pulse height distribution of the Barkhausen Noise signal amplitudes. The variations of hindrance sites induced by the plastic deformation have an effect of enhancing the number of larger BN pulses.

1.3.3.1.2 Tensile and compressive loading

When the material has a positive magnetostriction coefficient, both the Barkhausen noise emissions and observed RMS value are increased by the tensile stress state present. Nevertheless, the presence of the compressive stress has an opposite effect on them. A magnetic easy axis is generated in the direction of the applied tensile stress to which the domains in the sample attempts to rotate. The magnetic easy axis is created perpendicular to the applied magnetic field if compressive stresses are present in the material. This phenomenon can be seen in Figure 1.3–10. The Barkhausen noise behavior is saturated at some point of applied stress level. Upon the application of high tensile stress after the saturation point, a decrease in the BN amplitude can be observed [22-24]. Hence, the signal saturation of the noise should be taken into consideration when the BN method is used for the residual stress measurement. The main reason for this issue comes from the fact that the magnetostrictive coefficient is varying to negative by the application of tensile stress, so the BN amplitude is influenced.

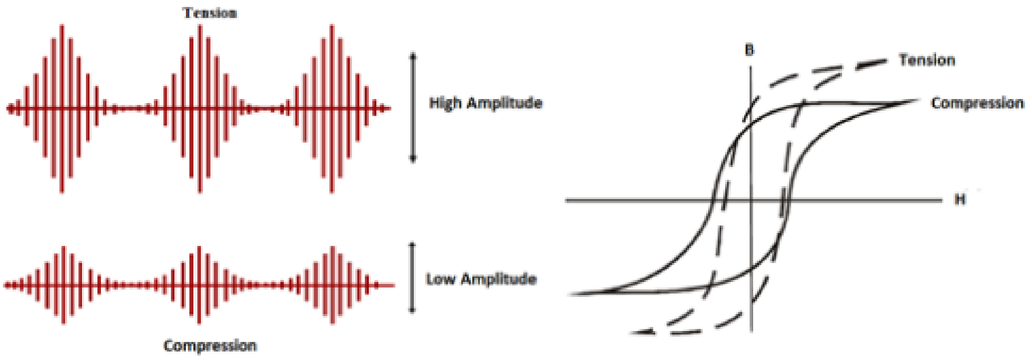

Figure 1.3–10 Barkhausen noise response to tensile and compressive stress [28]

During the magnetization of the ferromagnetic materials, domains firstly try to adjust themselves parallel to the adjoining easy axis corresponding to the stress and magnetic field direction. After the alignment, both of the bulk magnetization and magnetostriction increase. When the load is applied, the further alignment of the domains happens in the exact direction of the applied stresses. Hence, the magnetization is increased while the magnetostriction decreases. Since the alignment of domains has already occurred upon tensile stress with the magnetic field, the magnetostriction increases more slowly and evolves into a decreasing value much earlier. Upon the application of the higher stresses, the increasing magnetization reduces the magnetostriction of the material [25]. As a result, the BN signal dependency on the stress is reversed; that is, the Barkhausen noise signal decreases in the high tensile stress region.

1.3.3.2 The Effect of Microstructure

The magnetic domain configuration and the pinning site distribution are identified by the microstructure of the material. Nevertheless, the magnetic domain size cannot be equalized to the size of the grain, but it is proportional to the square root of the diameter of the grain [26]. Phase boundaries, grain boundaries, and defects can be considered as the hindrance sites for the movement of domain walls. In addition, interface boundaries between the precipitate and the matrix and precipitates having local stress field around can also act as a barrier to the domain wall movement [27]. It is well known that the Barkhausen noise activity in the material is reduced when there is an increase in hardness coming out from enhancement of lattice strain and/or dislocation density [27].

Composition, phase variations, and grain structure affect the sensitivity of the Barkhausen noise. Consequently, changes in these properties are responsible for the BN events obtained during the measurement. Furthermore, different phases have distinct forms of BN envelopes. Thereby, in the following, the effect of the different microstructure to the Barkhausen noise signal is explained.

1.3.3.2.1 Ferrite

When the microstructure of the material contains ferrite phase, the narrower peak is observed in the BN envelope and the peak obtained emerges at lower magnetic field strengths as it can be seen in Figure 1.3–11. In the ferrite structure, the main pinning sites to immobilize the domain walls are the grain boundaries, so the release of the domain walls from the pinning sites requires a lower magnetic field [77]. Because of this, domain walls can move a further distance in the ferritic microstructure before the pinning by obstructions, which are causing larger amplitudes of voltage pulses.

1.3.3.2.2 Pearlite

If the pearlite phase mixture is present in the microstructure, the peak of the MBN envelope is recognized at relatively greater magnetic field values than that of ferrite, as seen in Figure 1.3–11. The hindrance of the domain walls is greatly affected by the pearlite colonies. If the domain walls and the cementite lamellae are aligned parallel to each other, domain walls are more strongly hindered than the lamellae that are aligned normal to the domain walls [29]. The pinning of domain walls becomes stronger by the reducing pearlite spacing. The enhancement in the pearlite spacing that leads to a decrease in the cementite unit volume raises the BN amplitude and reduce the coercivity [29].

1.3.3.2.3 Martensite

The structure of the Martensite is tetragonal forcing the magnetization axis to become parallel to the c-axis in the unit cell of Martensite. Since martensite structure is composed of small needles or packet laths with micro-residual stresses, Barkhausen noise emission is influenced to some extent. The magnetic BN signal is much lower than ferritic and/or pearlitic structure because mobilization of domain walls is impeded due to high dislocation density [28, 30]. The peaks of this phase are also much wider than the other phases as shown in Figure 1.3–11. Due to the residual stresses in the martensite needles and tetragonal structure of the martensite, the differences in the BN envelope occur. The compressive residual stress formation in the martensite structure also has an influence on Barkhausen noise [28].

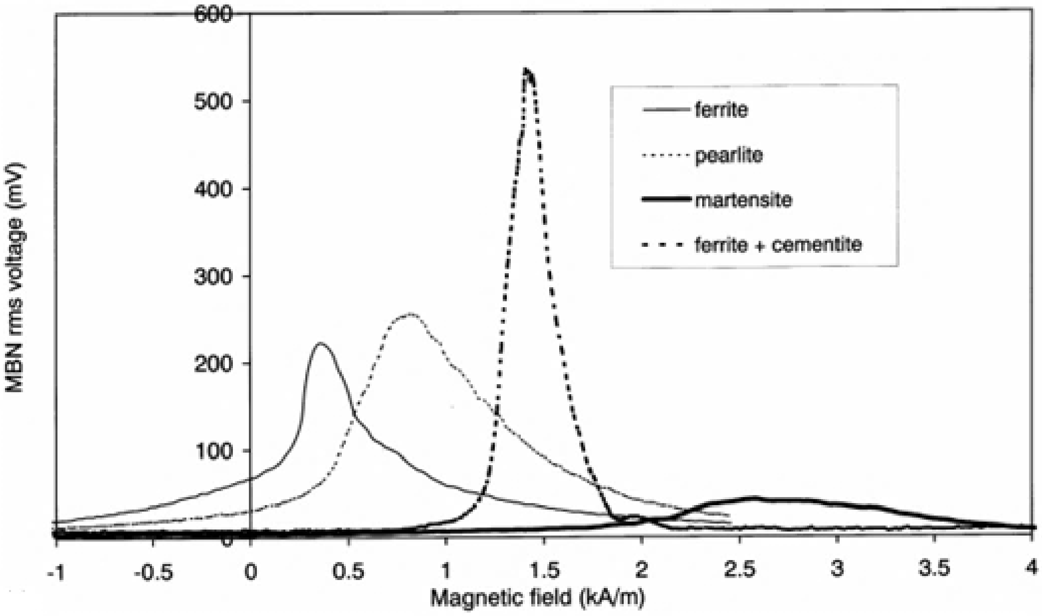

Figure 1.3–11 The RMS value of the BN signal as a function of applied magnetic field with different microstructures [77]

1.3.3.2.4 Retained austenite

Non-magnetic (internal demagnetizing field) areas are generated by retained austenite so that the domain walls cannot overcome these regions. Since the austenite is not ferromagnetic, retained austenite in the phase structure of specimen acts as a strong obstacle for the movements of domain walls even in the presence of high tensile stress [104]. Rautioaho *et al.* showed that the amount of the retained austenite controlled the stress sensitivity of a 9Ni steel [105]. The maximum stress response was observed with the amount of 3 to 5% retained austenite while the higher retained austenite content decreased the stress response of the BN signal [105]. In other words, when the retained austenite content is increased, the corresponding stress response of the Barkhausen Noise decreases. This behavior can be explained in such a way that the austenite remaining in the microstructure creates non-magnetic areas so that it is difficult for domain walls to overcome these areas even in the existence of the high tensile stresses.

1.3.3.2.5 Average Grain Size

It is generally reported that grain boundaries act as active pinning sites for the movements of domain walls. Hence, the grain size is related to BN activity. BN amplitude will decrease in the presence of larger number of grain boundaries that is smaller average grain size [86]. Gatelier-Rothea *et al.* reported that BN signal decreases with the increasing grain size in the iron sample [73]. In contrast, it was observed increasing BN amplitude with increasing grain size at the beginning of the magnetization process [106]. If the grain boundaries are the dominant pinning sites that impeding the domain wall movements, it could be expected an increase in the BN amplitude with increasing grain size since the mean-free-path increases. If it is not the case, the other factors are dominating pinning of the domain walls.

1.4 THEORY OF X-RAY DIFFRACTION STRESS MEASUREMENT METHOD

Of all the residual stress measurement techniques, X-ray diffraction has a particular place as it enables the measurement of surface stresses, essential to estimate the fatigue life of the mechanical component. This method depends on the elastic deformations within a polycrystalline material to measure its internal stress. In this part of the study, the principle of X-Ray Diffraction and stress – strain measurement, radiation selection, stress measurement parameters, measurement uncertainties, advantages, and disadvantages of the technique will be discussed in the following subsections.

1.4.1 X-Ray Diffraction Principles

X-Ray Diffraction occurs when the radiation interacts with atoms or crystallites arranged in a regular array. For a perfect crystalline material, the distance between crystallographic planes is perfectly defined due to the regular atomic packing into a three-dimensional periodic lattice. The intensities of scattered waves sum up into a constructive interference when the condition, called Bragg's Law, $n \bullet \lambda = 2 \bullet d \bullet \sin \Theta_B$ is fulfilled, where d is the distance between diffracting lattice planes, Θ_B is the angle between the incident beam and diffracting planes, λ is the X-ray wavelength, and n is an integer.

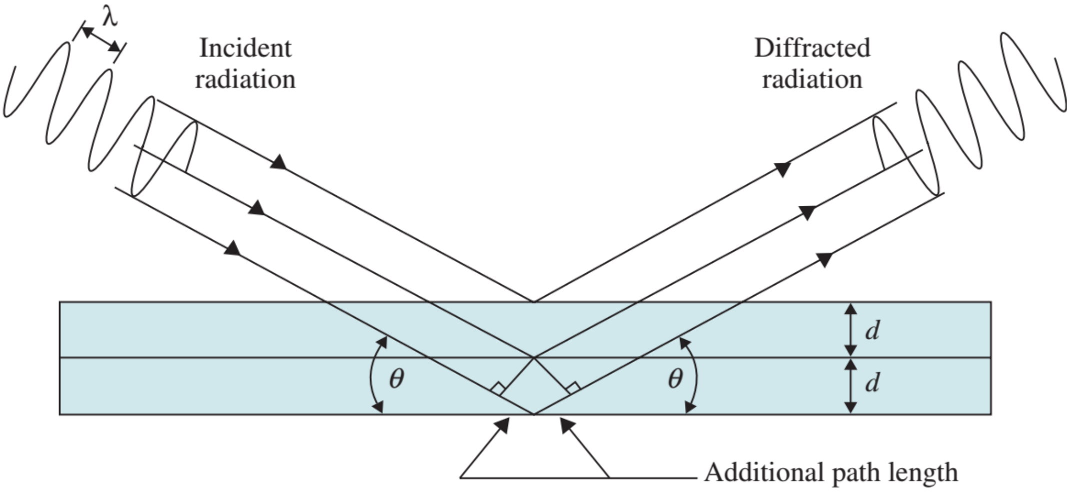

Figure 1.4–1 Radiation diffraction within a crystal structure [4]

Diffraction methods utilize the ability of electromagnetic radiation to evaluate the distance between atomic planes in crystalline or polycrystalline materials. The material will deform in the response to the application of any external mechanical or thermal load or formation of incompatible strains. If the response is in the elastic range, the deformation is linear that atoms in the crystal move to new equilibrium positions, shifting the diffraction peaks (see Figure 1.4–2). With the help of the changes in the positions of diffraction peaks, the strain, and/or stress tensor can be calculated by using the appropriate formulations of solid mechanics. Various formulations with different assumptions may yield very different results depending on information volume from which the displacement data is obtained.

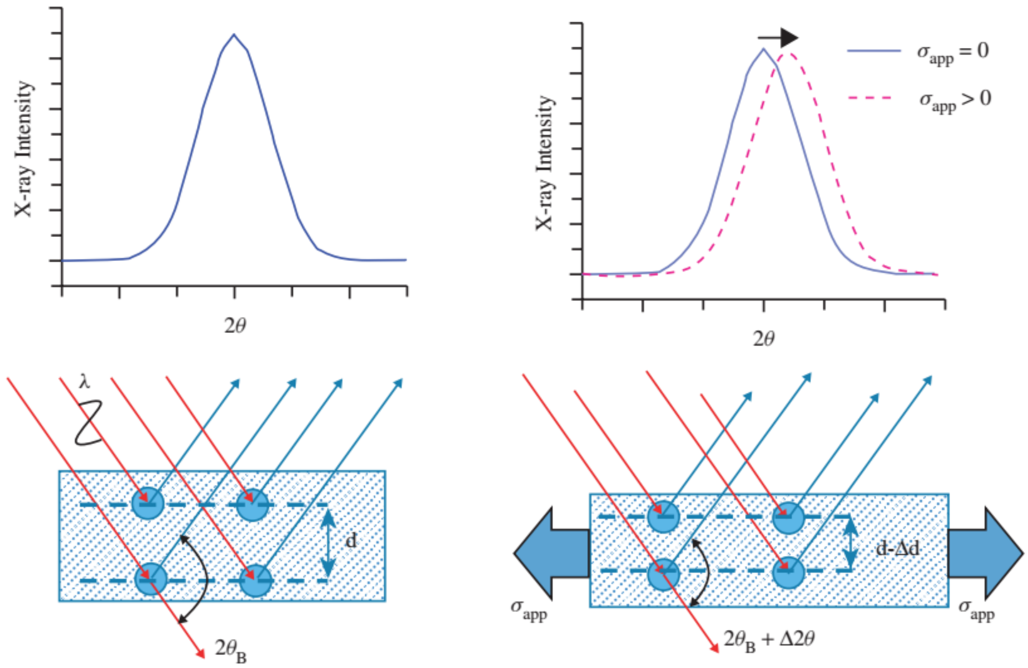

a) b)

Figure 1.4–2 Schematic of diffraction emanating from an atomic array in an (a) unstrained state and (b) under tensile strain due to an applied load [4]

1.4.2 Strain and Stress Measurement

Since the lattice spacing is changed by the elastic strains, only this kind of strains is measured using X-ray diffraction to determine macrostresses. Beyond the elastic limit, further strain causes dislocation motion, disruption of the crystal lattice and the formation of microstresses without any additional macrostresses. In X-ray diffraction measurement, the change in the inter-planar spacing of the {hkl} lattice planes is evaluated and so the strain within the material deduced [7].

Figure 1.4–3 illustrates the coordinate system definition used in the measurement system. The $\overrightarrow{S_i}$ axes define the surface of the specimen that $\overrightarrow{S_1}$ and $\overrightarrow{S_2}$ are on this surface. The laboratory coordinate system $\overrightarrow{L_i}$ is such that the measured plane spacing, $(d_{hkl})_{\phi\psi}$, is along the $\overrightarrow{L_3}$ axis of the laboratory coordinate system. The rotation angles ϕ and ψ, related to the coordinate systems $\overrightarrow{S_i}$ (unprimed tensor quantities) and $\overrightarrow{L_i}$ (primed tensor quantities), follow the convention established by Dölle [8].

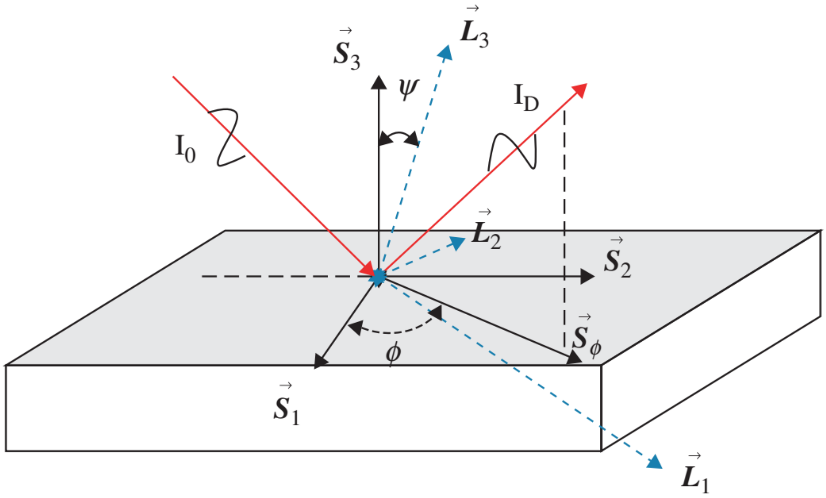

Figure 1.4–3 Definition of the laboratory coordinate system L_i, simple coordinate system S_i, and the angles ϕ, ψ [6]

The interplanar plane spacing $(d_{hkl})_{\phi\psi}$ prevails from the position of the diffraction peak thru Bragg's law. Then, the strain $(\varepsilon_{33}^{'})_{\phi\psi}$ along $\overrightarrow{L_3}$ can be obtained from the following formulae:

$$(\varepsilon_{33}^{'})_{\phi\psi} = \frac{(d_{hkl})_{\phi\psi} - d_0}{d_0} \qquad (1.4\text{-}1)$$

In the equation 1.4-1, d_0 shows the unstressed lattice spacing to be expressed in terms of the strains, ε_{ij} , in the sample coordinate system by the tensor transformation:

$$\varepsilon_{33}^{'} = a_{3k} a_{3l} \varepsilon_{kl} \qquad (1.4\text{-}2)$$

where a_{3k} and a_{3l} are the direction cosines between $\overrightarrow{L_3}$ and $\overrightarrow{S_i}$ axes respectively. The direction cosine matrix for this case can be written as follows:

$$a_{ik} = \begin{vmatrix} \cos\phi\cos\psi & \sin\phi\cos\psi & -\sin\psi \\ -\sin\phi & \cos\phi & 0 \\ \cos\phi\sin\psi & \sin\phi\sin\psi & \cos\psi \end{vmatrix} \qquad (1.4\text{-}3)$$

The angles ϕ and ψ settable on the diffractometer are assumed to be known exactly, so below equation can be obtained from substituting a_{3k} and a_{3l} into the (1.4-2):

$$\frac{(d_{hkl})_{\phi\psi} - d_0}{d_0} = \varepsilon_{11}\cos^2\phi\sin^2\psi + \varepsilon_{12}\sin 2\phi\sin^2\psi + \varepsilon_{22}\sin^2\phi\sin^2\psi$$
$$+\varepsilon_{33}\cos^2\psi + \varepsilon_{13}\cos\phi\sin 2\psi + \varepsilon_{23}\sin\phi\sin 2\psi \qquad (1.4\text{-}4)$$

which is the fundamental equation for X-ray strain determination.

For polycrystalline samples where it is possible to obtain a diffracted beam, three types of $d_{\phi\psi}$ versus $\sin^2\psi$ behavior are observed seen in Figure 1.4–4. When the strain components ε_{13} and/or ε_{23} are equal to zero, a linear variation of $d_{\phi\psi}$ versus $\sin^2\psi$ can be obtained from the equation 1.4-4. However, the strains are non-zero, $d_{\phi\psi}$ measured at positive and negative ψ will be different due to the $\sin 2\psi$ term, which causes a split in $d_{\phi\psi}$ versus $\sin^2\psi$ based on the equation. Equation 1.4-1 is used to analyze the regular behavior of the data. When the oscillatory data is present, other equations are required for the measurement of the strains.

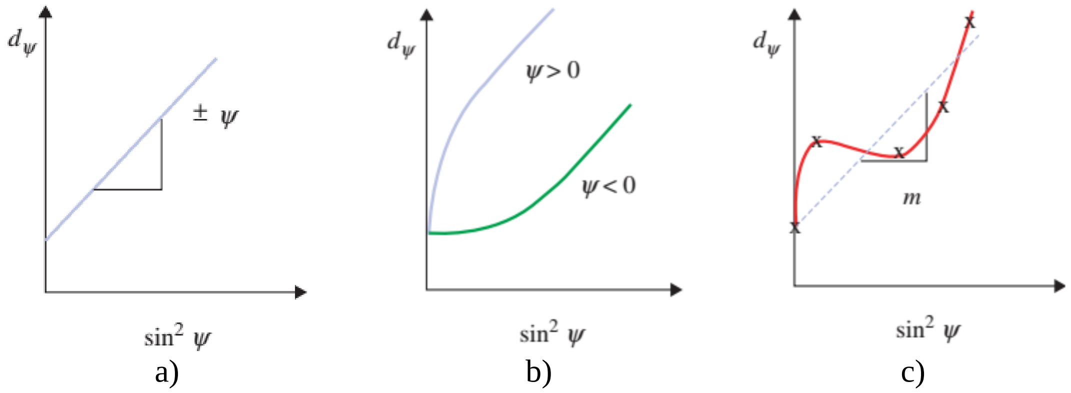

Figure 1.4–4 Plots of regular (a, b) and oscillatory $d_{\phi\psi}$ versus $\sin^2\psi$ data [6]

Equation 1.4-4 is a linear equation with six unknown strains that can be solved exactly if $d_{\phi\psi}$ is measured along six independent directions. There are two techniques, Dölle-Hauk and Winholtz-Cohen Least squares, proposed to analyze such data. In the Dölle-Hauk method, two terms based on the equation 1.4-4 are defined:

$$a_1 = \frac{1}{2}\left[\left(\varepsilon'_{33}\right)_{\phi\psi^+} + \left(\varepsilon'_{33}\right)_{\phi\psi^-}\right] = \left\{\varepsilon_{11} cos^2\phi + \varepsilon_{12}\ sin2\phi + \varepsilon_{22} sin^2\phi - \varepsilon_{33}\right\} sin^2\psi + \varepsilon_{33} \quad (1.4\text{-}5)$$

$$a_2 = \frac{1}{2}\left[\left(\varepsilon'_{33}\right)_{\phi\psi^+} - \left(\varepsilon'_{33}\right)_{\phi\psi^-}\right] = \left\{\varepsilon_{13} cos\phi + \varepsilon_{23} sin\phi\right\} sin\left|2\psi\right| \quad (1.4\text{-}6)$$

A linear variation of a_1 versus $\sin^2\psi$ is predicted by the equation 1.4-5, and the slope and intercept are given by:

$$m_{a1|\phi} = \left\{\varepsilon_{11} cos^2\phi + \varepsilon_{12}\ sin2\phi + \varepsilon_{22} sin^2\phi - \varepsilon_{33}\right\} \quad (1.4\text{-}7)$$

$$I_{a1|\phi} = \varepsilon_{33} \quad (1.4\text{-}8)$$

Similarly, the slope from linear variation of a_2 versus $\sin\left|2\psi\right|$ can be given as:

$$m_{a2|\phi} = \left\{\varepsilon_{13} cos\phi + \varepsilon_{23} sin\phi\right\} \quad (1.4\text{-}9)$$

The unknown strain terms ε_{11}, ε_{12}, ε_{22} can be obtained from the slopes of the a_1 versus $\sin^2\psi$ plots while the strain normal to the surface, ε_{33}, can be obtained from their intercepts If $d_{\phi\psi}$vs. $\sin^2\psi$ data are obtained over a range of $\pm\psi$ at three ϕ rotations (0°, 45° and 90°). This value should be the same for all rotations; this serves as a check of the alignment of the system. The strain terms that are out-of-plane ε_{13}, ε_{23} can be obtained from the slopes of the a_2 versus $\sin|2\psi|$ plots for $\phi=$ 0° and 90° respectively.

When the full strain tensor is, ε_{ij}, is obtained from the diffraction data in the sample coordinate system, the stresses can be calculated from Hooke's law:

$$\sigma_{ij} = C_{ijkl}\varepsilon_{kl} \tag{1.4-10}$$

where the elastic stiffness coefficients, C_{ijkl}, are referred to the $\overrightarrow{S_i}$ coordinate system.

The stresses from any other coordinate system can be determined from the second rank of a tensor transformation rule. The strains in the sample coordinate system can be calculated regarding stresses by the inverse of equation 1.4-10 as follows:

$$\varepsilon_{ij} = S_{ijkl}\sigma_{kl} \tag{1.4-11}$$

where S_{ijkl} indicates the elastic compliances. For and elastically isotropic specimen, the equation 1.4-10 can be rewritten as:

$$\sigma_{ij} = \frac{1}{\frac{1}{2}S_2}\left[\varepsilon_{ij} - \delta_{ij}\frac{S_1}{\frac{1}{2}S_2 + 3S_1}\varepsilon_{kk}\right] \tag{1.4-12}$$

where δ_{ij} is the Kronecker delta. The terms S_1 and $\frac{1}{2}S_2$ are also referred as X-ray elastic constants with the following representative:

$$S_1 = \left(-\frac{\nu}{E}\right)_{hkl}, \qquad \tfrac{1}{2}S_2 = \left(\frac{1+\nu}{E}\right)_{hkl} \tag{1.4-13}$$

In the equation above, *E* represents the elastic modulus; *v* is the Poisson's ratio, and *hkl* shows the Miller indices of the reflection under investigation. For an ideally isotropic material, S_1 and $\frac{1}{2}S_2$ do not depend on the Miller indices but for quasi-isotropic polycrystalline materials, these terms depend on the reflection used.

Instead of the determination of the strain tensor and then calculating the stresses via the appropriate formulation of Hooke’s law, equation 1.4-4 can be rewritten in terms of the stresses for an isotropic material in the sample coordinate system as:

$$\begin{aligned}(\varepsilon'_{33})_{\phi\psi} = \frac{(d_{hkl})_{\phi\psi} - d_0}{d_0} = \frac{1+\upsilon}{E}(\sigma_{11} c\,\mathrm{os}^2\phi + \sigma_{12}\sin 2\phi + \sigma_{22}\sin^2\phi - \sigma_{33})\sin^2\psi \\ + \frac{1+\upsilon}{E}\sigma_{33} - \frac{\upsilon}{E}(\sigma_{11} + \sigma_{22} + \sigma_{33}) \\ + \frac{1+\upsilon}{E}(\sigma_{13}\cos\phi + \sigma_{23}\sin\phi)\sin 2\psi\end{aligned} \tag{1.4-14}$$

When principal stresses σ_1 and σ_2 are present in the plane of surface and no stress is present perpendicular to the surface $\sigma_{3j} = 0$ (biaxial stress state), then the equation 1.4-14 becomes:

$$\frac{d_{\phi\psi} - d_0}{d_0} = \frac{1+\nu}{E}\sigma_\phi \sin^2\psi - \frac{\nu}{E}(\sigma_{11} + \sigma_{22}) \tag{1.4-15}$$

The stress component along the $\vec{S}_\phi$ direction, σ_θ, is given by the equation:

$$\sigma_\phi = \sigma_{11}\cos^2\phi + \sigma_{12}\sin 2\phi + \sigma_{22}\sin^2\phi \tag{1.4-16}$$

Equation 1.4-16 predicts a linear variation between the interplanar spacing and $\sin^2\psi$ with a slope of:

$$m = \frac{1+\nu}{E} d_0 \sigma_\phi \tag{1.4-17}$$

The stress in the $\overrightarrow{S_\phi}$ direction may be obtained directly from the slope of least-square lines that are fitted to the experimental data when measured at various ψ. However, the elastic constant, E, Poisson's ratio, υ, and the unstressed lattice spacing, d_0, must be known for the calculation. The equation 1.4-15 is known as $\sin^2\psi$ a method. In this technique, since d_0 values may not be readily available in practice, the lattice spacing measured at $\psi=0°$ is substituted as unstressed lattice spacing. It is assumed that the elastic strains for most materials may introduce at most 0.1% difference between the actual d_0 and d at any psi angles. Since the multiplier of the slope is related to the unstressed lattice spacing, the total error introduced by this assumption is less than 0.1% in the final stress calculation.

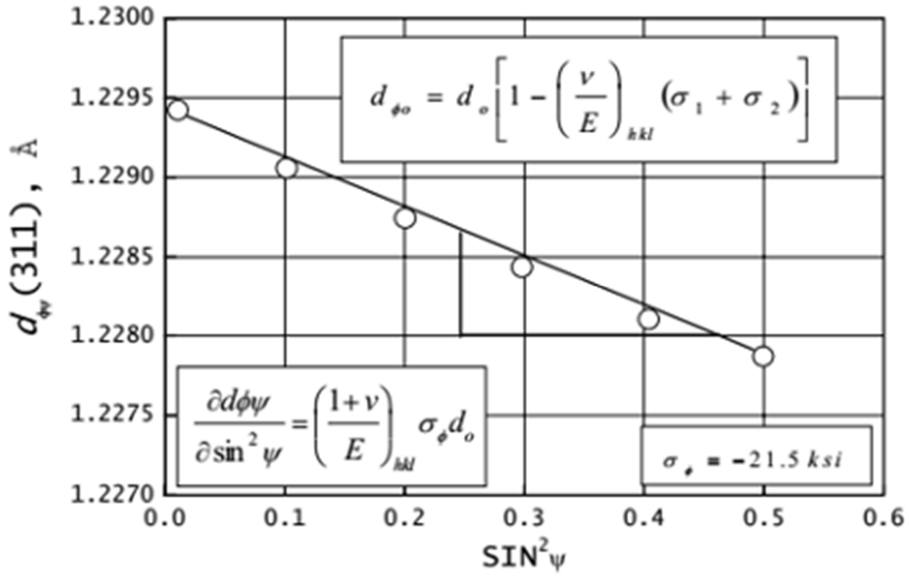

Figure 1.4–5 A d(311) versus $\sin^2\psi$ plot for a shot peened 5056-O aluminum alloy [7]

In traditional residual stress calculation discussed above, the stress components perpendicular to the surface ($\overrightarrow{S_3}$) are neglected in the volume sampled by the X-ray beam. However, it is not always true since ψ-splitting, indicating the $\sigma_{3j} \neq 0$, may be observed in untextured polycrystalline materials.

Stress analysis of *ψ-split* d vs. $\sin^2\psi$ is similar to the that of strains. The a_1 and a_2 are expressed in terms of stresses:

$$\begin{aligned} a_1 &= \left\{ \frac{d_{\phi\psi+} + d_{\phi\psi-}}{2d_0} - 1 \right\} \\ &= \frac{1+\nu}{E}(\sigma_{11}\cos^2\phi + \sigma_{12}\sin 2\phi + \sigma_{22}\sin^2\phi - \sigma_{33})\sin^2\psi \\ &\quad + \frac{1+\upsilon}{E}\sigma_{33} - \frac{\upsilon}{E}(\sigma_{11} + \sigma_{22} + \sigma_{33}) \end{aligned} \qquad (1.4\text{-}18)$$

$$a_2 = \left\{ \frac{d_{\phi\psi+} - d_{\phi\psi-}}{2d_0} \right\} = \frac{1+\nu}{E}(\sigma_{13}\cos\phi + \sigma_{23}\sin\phi)\sin|2\psi| \qquad (1.4\text{-}19)$$

Thus, the stresses σ_{11}, σ_{12} , σ_{22} , σ_{33} may be obtained from the slope and intercept of a_1 vs. $\sin^2\psi$, for Φ=0°, 45°, 90°. The slope of a_2 vs. $\sin|2\psi|$ for Φ=0°,90°, respectively, yields the shear stresses σ_{13} and σ_{23}. When the triaxial stress state is assumed, then the equation 1.4-14 becomes:

$$\begin{aligned} (\varepsilon_{33}^{'})_{\phi\psi} = \frac{(d_{hkl})_{\phi\psi} - d_0}{d_0} &= \frac{1+\upsilon}{E}(\sigma_{11}c\,\mathrm{os}^2\phi + \sigma_{12}\sin 2\phi + \sigma_{22}\sin^2\phi - \sigma_{33})\sin^2\psi \\ &\quad + \frac{1+\upsilon}{E}\sigma_{33} - \frac{\upsilon}{E}(\sigma_{11} + \sigma_{22} + \sigma_{33}) \end{aligned} \qquad (1.4\text{-}20)$$

When the equations 1.4-15 and 1.4-20 are compared, the stress σ_ϕ determined by bi-axial methods from the *$\sin^2\psi$* method will contain an error equal in magnitude to σ_{33}. For such a case, if *d vs. $\sin^2\psi$* data is obtained for two Phi tilts, one can acquire from the slopes of the $(\varepsilon_{33}^{'})_{\phi\psi}$ *vs. $\sin^2\psi$* plots;

$$
\begin{aligned}
m_{\phi_A} &= \frac{1+\upsilon}{E}(\sigma_{11}c\,\mathrm{os}^2\phi+\sigma_{12}\sin 2\phi+\sigma_{22}\sin^2\phi-\sigma_{33}) \\
&= \frac{1+\upsilon}{E}(\sigma_{\phi_A}-\sigma_{33})
\end{aligned}
\tag{1.4-21}
$$

$$
\begin{aligned}
m_{\phi_A+90^o} &= \frac{1+\upsilon}{E}(\sigma_{11}\cos^2(\phi_A+90)+\sigma_{12}\sin(2(\phi_A+90)) \\
&\quad +\sigma_{22}\sin^2(\phi_A+90)-\sigma_{33}) \\
&= \frac{1+\upsilon}{E}(\sigma_{\phi_A+90}-\sigma_{33})
\end{aligned}
\tag{1.4-22}
$$

The sum of the slopes of equations 1.4-21 and 1.4-22 and the interception of $(\varepsilon'_{33})_{\phi\psi}$ *vs.* $\sin^2\psi$ are equal to:

$$
m_{\phi_A}+m_{\phi_A+90}=\frac{1+\upsilon}{E}(\sigma_{11}+\sigma_{22}-2\sigma_{33}) \tag{1.4-23}
$$

$$
I=\frac{1+\upsilon}{E}\sigma_{33}-\frac{\upsilon}{E}(\sigma_{11}+\sigma_{22}+\sigma_{33}) \tag{1.4-24}
$$

where ϕ_A is the angle between $\overrightarrow{S_i}$ and the principle axis $\overrightarrow{P_i}$. Equations 1.4-23 and 1.4-24 may be solved together to calculate the stresses along the surface direction.

1.4.3 Selection of X-ray Radiation

The selection of anode tube to produce X-ray and so the wavelength of the incident radiation plays a major role in the measurement of residual stress. For a precise measurement of the inter-planar spacing d_{hkl} within a crystalline material, anode material has to be selected so that a suitable Bragg reflection can be emitted at sufficiently high 2-theta angles. The radiation is not appropriate for a particular crystalline material when the sample emits its own fluorescent X-rays caused by the Kα component of the incident beam [9]. Fluorescence radiation results in the very high background. Inadequate peak-to-background ratio, therefore, is obtained from the resultant data. This unwanted radiation can be diminished by using a secondary monochromator before entering the X-ray detector. However, the penetration depth is insufficient for representative stress measurement of the bulk due to the absorption of most of the incident X-ray radiation. In order to overcome this problem, anode material should emit the longer wavelength (less energetic) that penetrates further into the sample.

Regardless of the selection of anode material, X-ray should be selected to give a reflection at the highest possible 2-theta angle, as the variations in the d-spacings are minuscule due to the presence of strain. Though the peak shifts are only a few increments of a degree, small variations in the d-spacings can give measurable changes in 2-theta at the high 2-theta angles. As a result, using the reflections at a Bragg angle greater than 130° is sufficient for the measurement of residual stresses.

Different receptions to both elastic (residual stress) and inelastic (line broadening) strain are obtained since the deformation mechanisms vary with different crystallographic planes [8]. Since residual stress measurements conducted on the various crystallographic planes or by different radiations are not comparable, it is important to specify which planes will be used for the measurement. Table 1.4-1 shows recommended test parameters for common steels, which is not same when using different types of anode materials.

Table 1.4-1 Recommended test parameters for steels [8]

Material	*Radiation*	*Wavelength (Å)*	*Peak Plane (hkl)*	*2Θ Angles (degrees)*	*Penetration Depth (μm)*
BCC iron, ferrite and martensite iron base materials	Cr-Kα Cu-Kα	2.289649 1.540501	{211} {222}	156.07 137.13	4.6 – 4.7 1.5 – 1.6
FCC iron, retained austenite austenitic base materials	Cr-Kα Cu-Kα	2.289649 1.540501	{220} {331}	128.84 138.53	3.9 – 4.3 1.5 – 1.9

1.4.4 Measurement Parameters

The X-ray tube should be functioned at its uttermost recommended power output so that the minimum time is attained for the record of diffraction peak. Power settings should be kept as the same for all the measurements for comparison since the variations in the power will result in different depths values for the residual stress measurement. Selected count time should be long enough to assure obtaining a well-defined peak. Optimum count time can be determined by characteristics of both the tube and the sample, the surface preparation method employed, the presence of Kβ filter, etc.

Another measurement parameter is the number of tilt angles, ψ. It is suggested that at least five tilt angles should be employed for both positive and negative psi angle. Upon obtaining an improperly defined diffraction peak, extra psi-tilts can be used to enhance the exactness of the final stress calculation. If psi movement cannot be possible, the opposite sign of psi-value, called pseudo-negative, can be used by rotating the sample by 180° in Phi.

1.4.5 Potential Sources of Measurement Uncertainties

During the residual stress measurement, many factors are contributing to the uncertainty of the measurement. The principle source of error in residual stress measurement by X-ray diffraction is related to the locating the diffraction peak position with high precision. Errors of approximately 0.025 mm in the alignment of the positioning of the sample cause errors approximately 14 MPa in the stress measurement [8]. The alignment of the system should be checked readily using stress-free powder sample.

Systematic error in the measurement can also be caused by roughness or pitting, the curvature of the surface within the irradiated area, or other geometrical factors interfering with the diffracted X-ray beam. In coarse grain size material, the peaks become asymmetrical so that it gives a random inaccuracy in the location of diffraction peak and residual stress measurement.

A major uncertainty emerges from the determination of the X-ray elastic constants $(E/1+\nu)_{hkl}$. The residual stress measured is a function of the value of the X-ray elastic constant. Therefore, the identification of the elastic constant is a necessary for the residual stress measurement.

1.4.6 Advantages and Disadvantages

One of the most commonly used methods for residual stress measurement is X-Ray Diffraction. It is a nondestructive technique used to measure surface residual stresses for quality control. It can also be combined with some form of layer removal techniques so that the stress profile measurement can be done, but then the method becomes destructive. Generally, there is no need for the material preparation for the stress measurement. With the improvement of the detector technology, the measurement times are greatly decreased up to 10 minutes. Residual stresses of a wide range of materials can be measured by this technique.

One of the major disadvantages with XRD is the limitation imposed on the test piece size and geometry [10]. Specimen must have the geometry such that X-ray must be diffracted to the detector without hitting any obstacles after hitting the surface of the specimen. X-ray has shallow penetration depths depending on the materials, so only surface layers are measured. In addition, the sample to be measured should be polycrystalline with reasonable grain size and not be severely textured.

1.5 THEORY OF ESPI HOLE-DRILLING STRESS MEASUREMENT METHOD

An **E**lectronic **S**peckle **P**attern **I**nterferometer, so-called ESPI, is based on the strain gage hole-drilling method. Deformation measured around the hole is converted to a value of in-plane residual stress with the help of ESPI system; therefore, the ESPI system is adapted as a residual stress measurement technique. This relatively new method can provide much better quantification of the preciseness, and a means for future advancements in the science since it applies to a wider range of materials and surfaces, and provides more detailed information about the deformation occurred due to hole-drilling [11]. In the following subsections, single beam ESPI system for the stress measurement, analysis technique, some of the errors quantified, advantages, and disadvantages of the system will be presented.

1.5.1 Principle of ESPI System

The commonly used hole-drilling residual stress measurement technique was first pioneered by *Mathar et al.* in 1933 [12]. It is a destructive technique not because the part is destroyed by drilling a small hole, but because the material is removed, hence the stress support is destroyed. The deformation used to calculate the residual stress occurs due to this removal of the material. The hole can be drilled in several increments, thereby the stress state as a function of depth can be obtained [13]. Though strain gages are employed in the standard method for measuring the relieved strain, optical techniques can be utilized for the measurements of surface displacement around drilled holes, which is proved by *Antonov and McDonach* in the mid-1980’s [102, 103]. Among the optical technologies, ESPI system gathers full field of view data and stores it electronically; hence, the stress analysis is performed rapidly by computer algorithms.

Electronic speckle pattern interferometry assisted hole-drilling measurement can generate data about displacements by shape changes at the surface of the specimen by mathematically combining interferograms registered digitally before and after the deformation caused by drilling a hole on the surface of the sample. In a single beam ESPI system, the object is illuminated with coherent light, which is a green laser in this study. A **C**harge **C**oupled **D**evice (CCD) camera is used to detect the light through a lens system, and a prism is interfering the object light with a reference beam from the laser source. The ESPI measurement system can be seen in Figure 1.5–1.

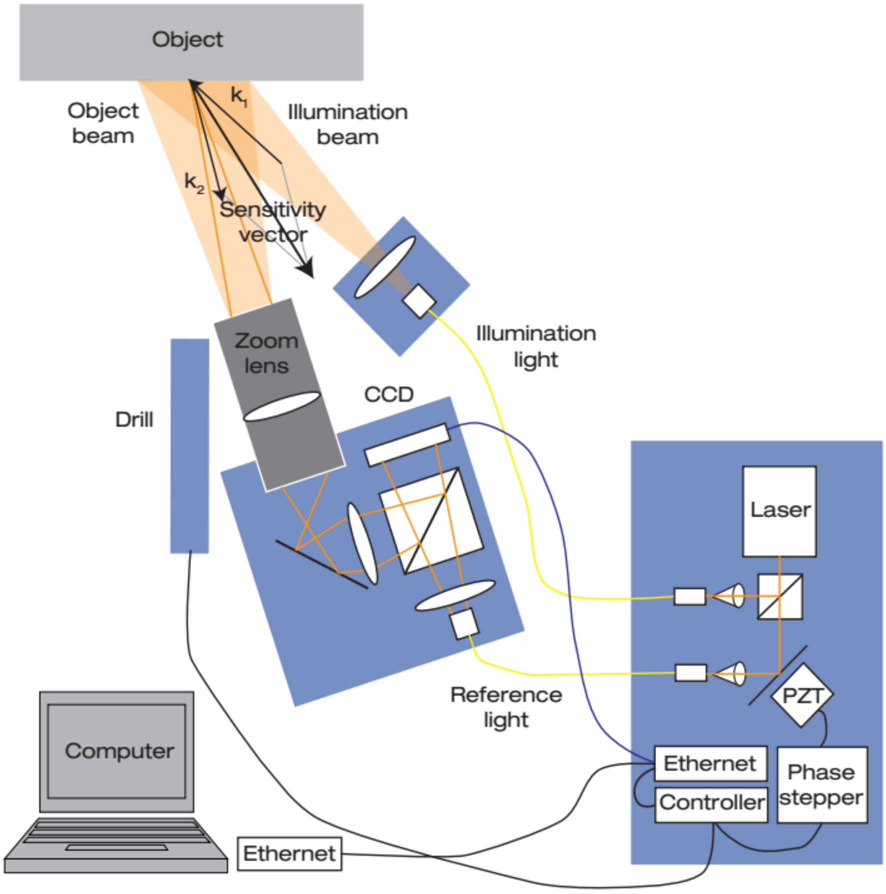

Figure 1.5–1 The ESPI measurement system set-up [7]

The interference images recorded by the CCD camera are stored in a computer for the stress calculation process. Useful information about the measurement cannot be obtained by an unprocessed image by itself. The raw image shows a random-looking fringe pattern of light and dark speckles that is generated by the surface roughness and the optics, seen in Figure 1.5–2. In order to acquire quantitative information from the drilled hole, images taken before and after the deformation process is stored and processed by four-bucket phase-stepped algorithm. This algorithm necessitates two sets of four images each taken before the object deformed (reference set) and after the deformation (deformed set). The reference beam is stepped by 90 degrees between one image and the next with a small mirror bonded to a piezoelectric actuator and driven by electronic circuitry synchronized with the frame grabbing hardware.

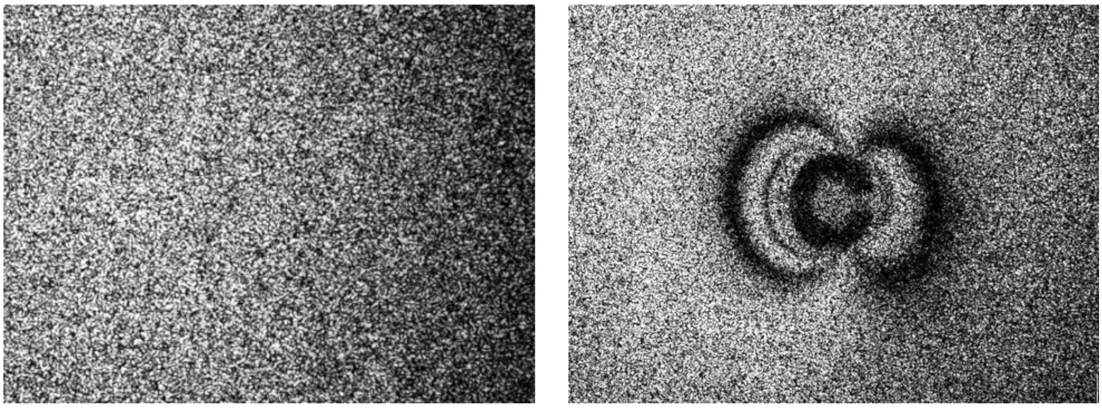

Figure 1.5–2 Example of speckle pattern of unprocessed image (left) and processed image (right) by computer software

1.5.2 Stress Analysis Technique by ESPI System

In Figure 1.5–1, the illumination ($\overrightarrow{k_1}$) and the observation ($\overrightarrow{k_2}$) vector is identified. Those vectors specify in 3-D space the orientation of the incoming laser light and the direction of the observation. The illumination and the observation vectors can be regarded as constant across the image if the field of view of the instrument is narrow enough.

Both vectors are normalized to a magnitude of $2\pi/\lambda$, which is the conversion factor from pathlength variation to phase change (Ω), for the coherent light of wavelength λ. A sensitivity vector, $\vec{k}$, is described as the difference between the observation and illumination vectors. This can be mathematically expressed as:

$$\overrightarrow{k_1} = \frac{2\pi}{\lambda}\overrightarrow{l_{k_1}}, \quad \overrightarrow{k_2} = \frac{2\pi}{\lambda}\overrightarrow{l_{k_2}}, \quad \vec{k} = \overrightarrow{k_1} - \overrightarrow{k_2} \qquad (1.5\text{-}1)$$

$$\Omega = \vec{k} \bullet \vec{d} \qquad (1.5\text{-}2)$$

It can be deduced that the single beam ESPI system of Figure 1.5–1 is only sensitive to surface displacements in the direction of sensitivity vector. The illumination and the observation vectors should be defined by measurable quantities, as they are valuable inputs to the calculation of the sensitivity vector so does the residual stress.

When an interference image is produced, the light intensity that is recorded by the CCD changes according to the following formula;

$$I(p,q) = I_{ref}(p,q) + I_{obj}(p,q) + 2\sqrt{I_{ref}I_{obj}}\cos(\varphi(p,q)) \qquad (1.5\text{-}3)$$

where (p, q) identifies a specific pixel location in the image coordinates and $\varphi(p,q)$ is a random-looking relative phase distribution across the picture. If the surface of the object shifts by a small amount, the phase at every point in the image is further moved by an additional angle $\Omega(p,q)$ that equation 1.5-3 becomes;

$$I(p,q,\vec{d}) = I_{ref}(p,q) + I_{obj}(p,q) + 2\sqrt{I_{ref}I_{obj}}\cos(\varphi(p,q)) + \Omega(p,q) \qquad (1.5\text{-}4)$$

assuming that the optical setup has been left motionless, and the surface displacement of the object is much smaller than the speckle size. The light intensities after the deformation cannot be correlated to the intensities before deformation at various point in the image when the surface displacements go beyond speckle size.

The acquired n images before and n images after the deformation by the ESPI system differ by a fixed step in reference beam phase angle, β. Then, the intensities in the two sets of four images given by;

$$I(p,q) = I_{ref}(p,q) + I_{obj}(p,q) + 2\sqrt{I_{ref}I_{obj}}\cos(\varphi(p,q)) + \Omega(p,q) + i\beta \qquad (1.5\text{-}5)$$

When the four-bucket algorithm is used, the solution of Ω can be expressed as;

$$\Omega = \tan^{-1}\left(\frac{(I_1 - I_3)(I_1^{'} - I_{_3}^{'}) + (I_2 - I_4)(I_{_2}^{'} - I_{_4}^{'})}{(I_1 - I_3)(I_{_2}^{'} - I_{_4}^{'}) - (I_2 - I_4)I_1^{'} - I_{_3}^{'})}\right) \qquad (1.5\text{-}6)$$

An interferogram, ***F***, can be formed quickly by using above equation as;

$$\begin{aligned} F &= \left[(I_1 - I_3) + (I'_1 - I'_3)\right]^2 + \left[(I_2 - I_4) + (I'_2 - I'_4)\right]^2 \\ &= 32 I_{ref} I_{obj} (1 + \cos(\Omega)) \end{aligned} \tag{1.5-7}$$

Equation 1.5-7 is utilized for a real-time display on the computer screen. Displaying the fringes in real time is useful to verify whether a steady data is being acquired. If there exists a vibration that distorts the fringe pattern in the system, this will be seen by the live image on the screen.

The displacements resulting from the release of residual stresses by a blind hole-drilled can be expressed as;

$$\begin{Bmatrix} u_r \\ u_\theta \\ u_z \end{Bmatrix} = \begin{bmatrix} A + B\cos 2\theta & A - B\cos 2\theta & 2B\sin 2\theta \\ C\sin 2\theta & -C\sin 2\theta & -2C\sin 2\theta \\ F + G\cos 2\theta & F - G\cos 2\theta & 2G\sin 2\theta \end{bmatrix} \begin{Bmatrix} \sigma_x \\ \sigma_y \\ \tau_{xy} \end{Bmatrix} \tag{1.5-8}$$

where u_r, u_θ are in-plane displacements in the radial (r) and tangential (θ) directions, u_z is the out-of-plane displacement, σ_x, σ_y and τ_{xy} are the stress components in the material. The coefficients in the above equation can be expressed as;

$$A = \frac{r_0(1+\nu)a}{2E}, \quad B = \frac{r_0 b}{2E}, \quad C = \frac{r_0 c}{2E}, \quad F = \frac{r_0 f}{2E}, \quad G = \frac{4\nu r_0 g}{2E} \tag{1.5-9}$$

where r_0 shows the hole radius, E is the modulus of elasticity, ν are the Poisson's ratio and a, b, c, f, g are the non-dimensional coefficients as a function of radial location normalized by hole radius (r/r_0) and hole depth normalized by hole diameter.

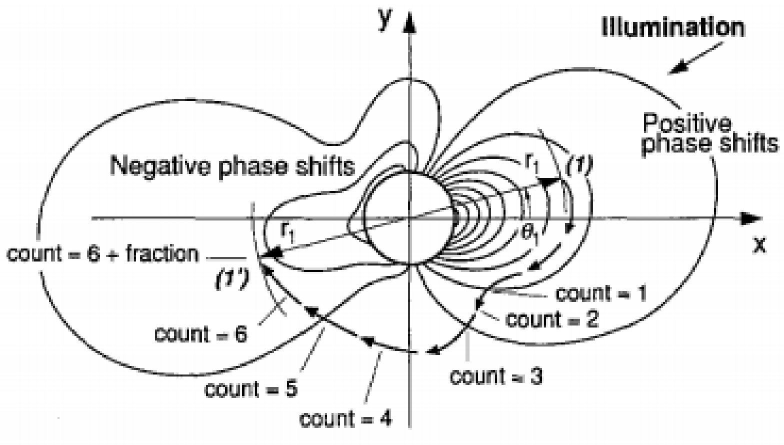

Figure 1.5–3 Typical fringe counting path [11]

The displacements lead to variations in the path length of light that are reflected from the region around the hole. These changes in the path length cause phase variations and a fringe pattern to be composed to gain residual stresses. Once the fringe pattern is obtained by ESPI without the need for phase shifting and unwrapping, a radial location, which is denoted by point (1) and angle θ_1, is selected as seen in Figure 1.5–3. Then, the number of light and dark fringes crossed is counted. With the usage of the same radius as for point (1), similar counts can be made for two other starting points with different angles θ_2 and θ_3. Residual stress components σ_x, σ_y and τ_{xy} can be found when the counts n_1, n_2, and n_3 are put in the following relation;

$$\begin{Bmatrix} \sigma_x \\ \sigma_y \\ \tau_{xy} \end{Bmatrix} = \pi \begin{bmatrix} C_{11} & C_{12} & C_{13} \\ C_{21} & C_{22} & C_{23} \\ C_{31} & C_{32} & C_{33} \end{bmatrix}^{-1} \begin{Bmatrix} n_1 \\ n_2 \\ n_3 \end{Bmatrix} \tag{1.5-10}$$

All fringe counts are taken at the same radius, but at different angles, the coefficient C_{ij} of the equation 1.5-9 can be expressed as;

$$
\begin{aligned}
C_{i1} &= K_x[\cos\theta_i(A+B\cos\theta_i)-C\sin\theta_i\sin 2\theta_i] \\
C_{i2} &= K_x[\cos\theta_i(A-B\cos\theta_i)+C\sin\theta_i\sin 2\theta_i] \\
C_{i3} &= -2K_x[B\cos\theta_i\sin 2\theta_i - C\sin 2\theta_i] \\
K_x &= \frac{2\pi}{\lambda}\cos\gamma
\end{aligned}
\qquad (1.5\text{-}11)
$$

where the horizontal direction is taken in the direction of illumination, γ is the angle between the surface of the sample and the observation light; λ is the wavelength of laser light. Then the principle stress and their directions can be found using the following expressions;

$$\sigma_1,\sigma_2 = \frac{\sigma_{xx}+\sigma_{yy}}{2} + \sqrt{\left(\frac{\sigma_{xx}-\sigma_{yy}}{2}\right)^2 + \tau_{xy}^2} \qquad (1.5\text{-}12)$$

The angle between the illumination direction and principle stress can be calculated as;

$$\beta = 45^o(1-sign[\sigma_{xx}-\sigma_{yy}])(1-\delta(\sigma_{xx}-\sigma_{yy})) + \frac{1}{2}\tan^{-1}(\frac{2\tau_{xy}}{\sigma_{xx}-\sigma_{yy}}) \qquad (1.5\text{-}13)$$

where δ is impulse function.

1.5.3 Potential Errors and Uncertainties of ESPI System

As in the other residual stress measurement techniques, many factors affect the residual stress measurement upon the application of ESPI system. Essentially, the unprocessed ESPI data consist of displacement, from which strains are derived given the image scale. Stress calculation is done indirectly by a user-provided elastic modulus. Thereby, any relative error in the elastic modulus of the material is transmitted 100% into a relative error in the residual stress measurement.

The displacements on the surface are linearly proportional to the depth of the hole drilled on the material as well as hole diameter. Any error in the depth of the hole will produce similar errors in the stress. These errors are a function of the depth so that the change in h/D value will result in a different error. The diameter of the finished hole depends on various parameters like drill chuck wobble, machinability of the material, drilling speed and feed, etc. Variation in the hole diameter results in the difference in the calculated stress values. In addition to these parameters, determination of the location of the hole center is an important in the stress calculation. In ESPI system, the location of the center of the drilled hole is predetermined by the graphical hole-marking tool. The effect of error in the positioning gives rise to miscalculation since surface deformation corresponding to any pixel is calculated wrongly.

When a small hole is drilled into a part possessing residual stresses, the stresses remaining in the part are locally relieved to produce new stress distribution around the drilled hole. Due to the stress concentration effects around the drilled hole, the new stress distribution can exceed the original residual stress values leading to non-elastic deformation around the hole. This non-elastic deformation misleads residual stress calculation. Also, the strains induced by drilling a hole in the material should be kept as low as possible not to affect stress calculation.

Another source of the error in the stress calculation comes from the determination of sensitivity vector described as the average of the illumination and observation vectors. The 3-dimensional orientations of those vectors are guided by the user while setting up the system and those are supplied to the analysis system by the user in the form of angles measured between the CCD camera and the surface of the part. Possible errors in the determination of those angles influences the interpretation of the displacement data caused miscalculation of stress values [12].

Other potential sources of uncertainties and errors in the stress calculation by ESPI system are discussed in details by *Ponslet and Steinzig* in the four-part series in reference 12. Other error sources result from image scale error, cone beams, wavelength and intensity fluctuations of used laser, drill type, ambient light, phase stepping, CCD camera noise, etc.

1.5.4 Advantages and Disadvantages of the ESPI System

The ESPI assisted hole-drilling method has the capability to collect data in a short period in a variety of the materials. The measurement system can be applied to the rough and/or curved surfaces. Contrary to the strain gage hole-drilling method, there is no need to prepare the surface for the strain gage application, so the measurement time is lesser. The technique has the advantage of providing full-filled data useful for data averaging, error checking, and the extraction of detailed information. Hole eccentricity can be modified by this full-filled data since this optical data is like having multi-element strain rosettes with many thousands of available gages.

The measurement system is required more research for establishing the well-proven experimental procedures. Equipment cost can relatively be high compared to other techniques. In addition, the system setup should be interferometric stability for collecting reliable data. The small drilled hole on the sample generally will not significantly impair the structural integrity of the part being tested. Lastly, the calculated stress data can be gigantic due to the need for at least four raw images for each drill step.

1.6 LITERATURE SURVEY

This section of the present study is devoted to the review of the studies conducted about the residual stress measurements in recent years by means of magnetic Barkhausen Noise, X-Ray Diffraction, and Electronic Speckle Pattern Interferometer techniques. The literature survey carried out is aimed to provide a scientific basis for better understanding of residual stress measurement by each technique. To achieve this goal, the present section is divided into three main subsections. In the first subsection, the studies corresponding to Barkhausen noise technique is given. Then, studies by means of X-ray Diffraction will be discussed in the second subsection.

Moreover, in the last subsection, residual stress measurement depending upon ESPI hole-drilling stress measurement system will be discussed.

1.6.1 Studies Based on Magnetic Barkhausen Noise Method

Physical and magnetic properties of the materials are influenced from the microstructure including information about the different phases existing in the material. The number, distribution, shape, volume fraction, and size of the phases are used to define the microstructure of the material [70].

In the literature, many microstructural properties of the materials have been studied with the Barkhausen noise measurements. Such properties are the grain size [71-76], ferrite, pearlite and martensite phases [77-82], and the carbon content of the steel [73, 80, 83-85]. Magnetic domains and domain walls increase when the grain size decreases. Basically, this implies that more Barkhausen jumps occur, but the amplitude of the BN emission will be smaller [86]. The peak height of Barkhausen activity [27] and the maximum Barkhausen noise amplitude [73, 75] was utilized to see the effect of grain size on the Barkhausen activity. *Moorthy et al.* was also noticed that the peak position shifts to lower applied magnetic fields with an increasing grain size [27]. The Barkhausen noise spectra were studied by *Yamaura et al.* Their findings were so significant that an increase in the grain size decreased the ratio between high and low-frequency components and grain misorientation also had a significant effect on the measurement [74].

Quite controversial results are indicated for the influence of the carbon content in the literature. The results were generally showed that an increased carbon content cause increased Barkhausen activity [83, 84]. In a study of *Ranjan et al.*, this situation is explained by the fact that grain size decreased with an increasing carbon content, which leads further to increased Barkhausen activity [71]. The relationship between the carbon content and the three features of Barkhausen noise signal, which are raising slope, FWHM of the profile and RMS value, was studied by *Ng et al.* It had found that all the features are increased when the carbon content increased [83].

Capó-Sánchez et al. also showed that there was a region where similar results could be observed, but the maximum Barkhausen amplitude saturates and begins to decrease with the higher carbon content [84].

The steel microstructures of ferrite, pearlite and martensite have been studied with Barkhausen noise. *Moorthy et al.* and *Kleber et al.* have reported that the amount of ferrite may be detected by the Magnetic Barkhausen Noise measurement [78, 82]. The martensite content was analyzed by *Saquet et al.* and *Kaplan et al.* while the pearlite content was studied by *Koo et al.* [77, 80, 81]. The RMS value or the peak height of the BN emission was sensitive to the microstructure changes. Studies of *Kleber et al., Kaplan et al., and Koo et al.* has showed good correlations between the features of Barkhausen noise and microstructures [80-82]. Tempering of the microstructures has also been studied by *Saquet et al., Moorthy et al., and Davut and Gür* [72, 77, 87].

An increase in the hardness value leads to the generation of more pinning sites since dislocation density increases. The enhancement in the hardness value, also, impedes the domain wall motion. This effect has been observed in the studies reported in the literature. The RMS value of the signal has decreased with increasing hardness [88-90]. The same relationship has been found between hardness, and the peak height of the BN burst [72, 81]. In another study conducted by *Moorthy et al.* and *O'Sullivan et al.*, it has been found a linear relationship between the inverse of BN activity and hardness [72, 89].

Owing to the higher dislocation density induced by hardness, it is expected that the coercivity of the material increase [91]. *O'Sullivan et al.* have reported the inverse of Barkhausen noise was exponentially proportional with the coercivity of the material [89]. *Mészáros and Szabó* found that coercivity was not affected from the hardness of stainless steel samples [92]. The study showed that peak position was proportional with the hardness instead of coercivity. Good correlation between peak position and the hardness have reported in the study of *Davut et al.* [40]. The relationship between coercivity and the peak position has been reported in other studies [87, 93].

In the literature, there have been a lot of results related to between the Barkhausen noise and the stress state of the material. Typical observations have shown that tensile stresses lead to an increase in the Barkhausen activity while the compressive stresses decrease it [90, 94-96]. *Mierczak et al.* have reported that there was a linear relationship between the reciprocal of the peak height and the applied stress [96]. The same relationship has also been reported by *Santa-aho et al.*, but the slope was dependent on the hardness [90]. In studies, it has been observed that both tensile and compressive stresses showed saturating behavior. When increasing the tensile stress after saturation point, Barkhausen noise emission started to decrease [75, 85, 93, 97].

Typically, variations in the stress state have been explained by using the RMS value [73, 95], the Barkhausen noise energy [98, 100], and the peak height [93, 96-99]. It has to be kept in mind that the residual stress measurement by the BN method is challenging since the microstructure, composition, and other parameters affect the Barkhausen signal and the influenced of different properties could not be distinguished from the signal. It has also been indicated that the BN was affected by the direction of measurement, and so the direction must be taken into consideration during Barkhausen noise measurement. To avoid these difficulties, the BN device must be calibrated for each material before the stress measurement [95, 97, 98].

1.6.2 Studies Based on X-ray Diffraction Method

Heat-treated parts with the same hardness profiles may have different microstructures, and so does the residual stress state. Estimation of microstructural transformation and residual stress distribution upon treatment is quite difficult [44]. There are a variety of methods are available to measure the residual stresses; yet, only the X-ray diffraction has the appropriate spatial and volumetric resolution for adequate characterization of residual stress distributions. In the literature, many researchers have attempted to measure residual stress state using X-ray diffraction.

As a result of thermochemical heat treatment, there exists an inhomogeneous carbon and/or alloy distribution within a distinct depth. As seen in Figure 1.6–1, for 26MnCr4 steel plates of 110×15×4 mm in dimensions, distribution of residual stress due to case hardening is different from those formed in the same steel part by quench hardened. The carburizing process was conducted in a gas atmosphere at 930°C. Then, the both plates were subjected to the quenching from a temperature of 840°C. Even though the geometry of components and the quenching conditions are identical, it was observed that resultant residual stress distributions were completely different due to the surface concentration gradient of alloying elements [45].

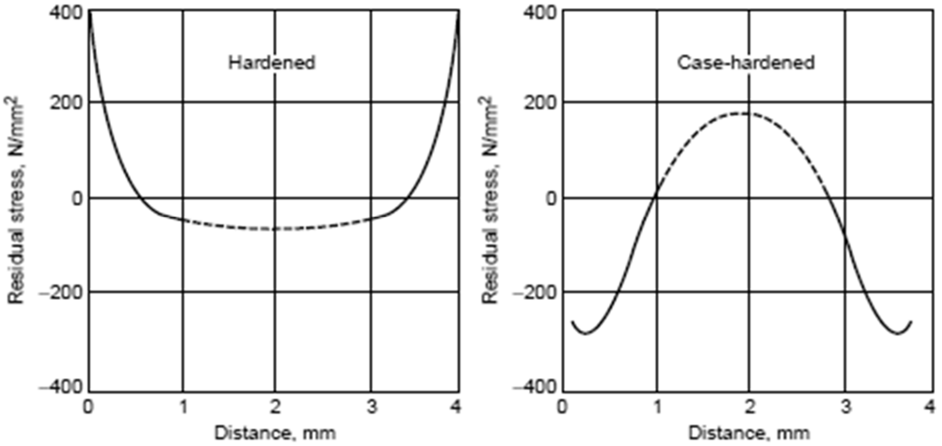

Figure 1.6–1 Residual stress distribution across the thickness of hardened and case-hardened steel plates [45]

In a study carried out by *Macherauch et al., Vöhringer and Stickels*, it has been indicated that the ratio of case and core thickness influenced the magnitude of compressive residual stress state at the surface when the other factors remained same [45, 46]. It was also deduced from the study that compressive residual stresses at the surface would be high when the core was much thicker as seen in Figure 1.6–2a. When the case is thicker, the core tensile stresses would be high. *Schröder* and his colleagues have studied the residual stress measurement at and the below of the carburized cylindrical in shape C22 steels. Steels have been carburized to 0.2, 0.4, and 0.8 mm and quenched from 880°C in water. Figure 1.6–2b shows an increase in the compressive residual stress and the maximum residual stress location shifts towards the core with an increasing case depth [47]. *Parrish and Harper* also have shown that the carburized case depths were encircled by the compressive residual stress zones. In addition, residual stresses were changed their signs generally between the carburized zone and the core region.

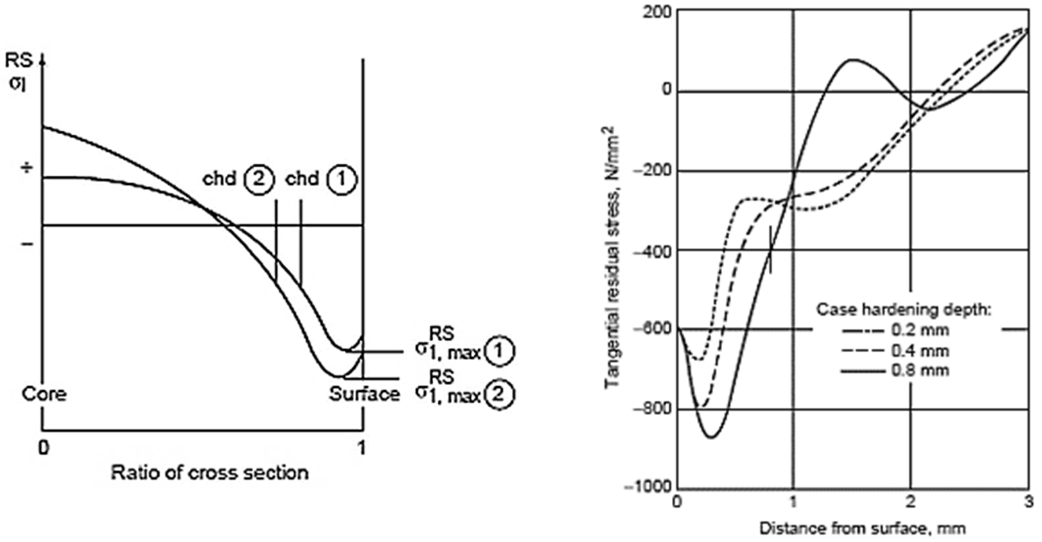

a) b)

Figure 1.6–2 a) Influence of case-hardening depth (CHD) on the distribution of longitudinal residual stresses [45], b) depth profile of tangential residual stress with different case-hardening depths [47]

Another reach about the effect of workpiece size on residual stresses was carried out [50]. It was stated in the study that component geometry together with the heat transfer associated with the quenching had had an effect on the final residual stress state induced by carburizing heat treatment. 20MoCr4 steels were gas carburized for 3 hours at 930°C with a single hardening operation. After tempering operation at 180°C for 2 hours, residual stress distributions measured by means of X-ray diffraction is shown in Figure 1.6–3. While the surface residual stress has remained approximately constant, the tangential compressive residual stress has increased with increasing diameter. As seen in the figure, tripling the diameter of the cylinders creates residual stress state that is approximately the twice of the original sample with a smaller diameter. It was concluded from the study that workpiece shape and geometry has had an indirect effect on the stress state due to the modified cooling conditions during quenching [50].

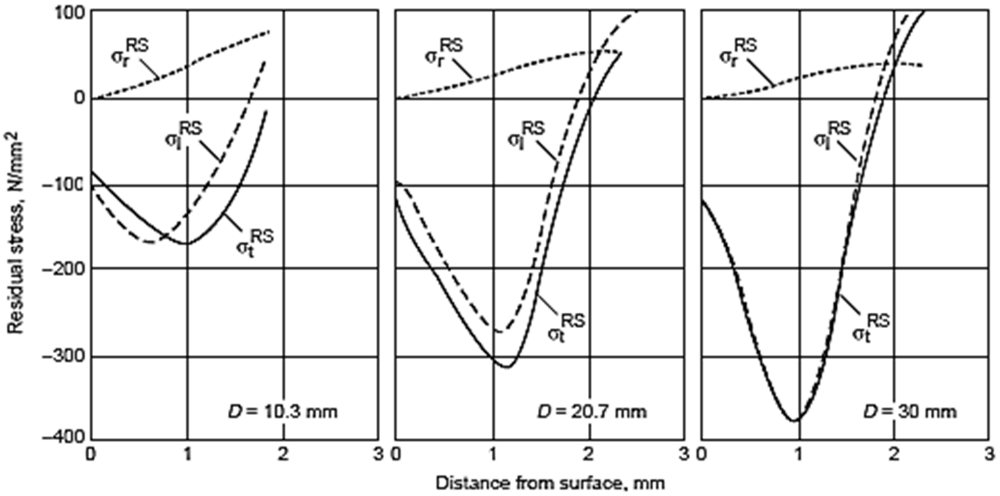

Figure 1.6–3 Residual stress distributions in identical carburized cylinders with different diameters [50]

The effect of quenching and tempering on residual stresses state has been studied by the many researchers [51-57]. Considering the quenchant temperature, an increase in the quenchant temperature has increased the compressive residual stress developed on the sample (see Figure 1.6–4a). With an increased quenchant temperature, the transformation starts temperature was observed to be shifted towards the core, so the core region has transformed prior to the surface [58-59]. Heat-treated samples are usually tempered to transform the unstable martensite to stable tempered martensite. This causes an increase in ductility and so the occurrence of the delayed fracture is minimized. In addition to the increase in the ductility, the retained austenite transformation tends to reduce distortion. Furthermore, residual stress values decrease with the increasing tempering temperature since martensite loses its tetragonality, elastic deformation caused by the distortion in the material reduces. Studies have revealed that tempering operation has decreased the residual stress as seen in Figure 1.6–4b.

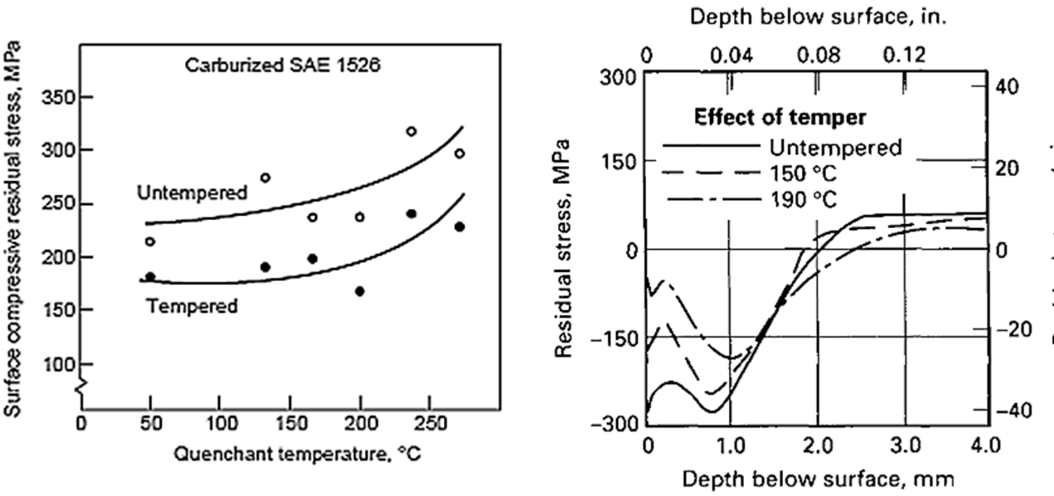

a) b)

Figure 1.6–4 a) Effect of quenchant temperature on the residual stress state, b) Effect of tempering on the residual stress state [58]

1.6.3 Studies Based on ESPI Hole-Drilling Stress Measurement Method

Several types of research have been recently conducted on about whether adopting the optical methods, such as ESPI in combination with hole-drilling, is feasible. Although using this kind of techniques for determination of residual stress state can be advantageous in view of cost and time of measurement, several parameters involved in the measurement process can significantly affect the accuracy of the stress measurement [61].

Barile et al. [62] have studied the effects of process parameters on the accuracy of the stress measurement by ESPI assisted hole-drilling. They have observed that the coordinate of the reference system and that of CCD camera was one of the important factors influencing the residual stress calculation. In the experiment, stress values were recalculated by hypothesizing an error ±2° for the angle defining the x-axis. Figure 1.6–5 shows the percentage of the variations in calculated residual stresses when there is an error ±2°. Numerical results of the study and the percentage of error computed in the stress profile can be seen in Table 1.6-1. From the study carried out by *Barile at al.*, it can be deduced that the error in the angle defining the x-axis plays a important role in calculating the residual stress state [62].

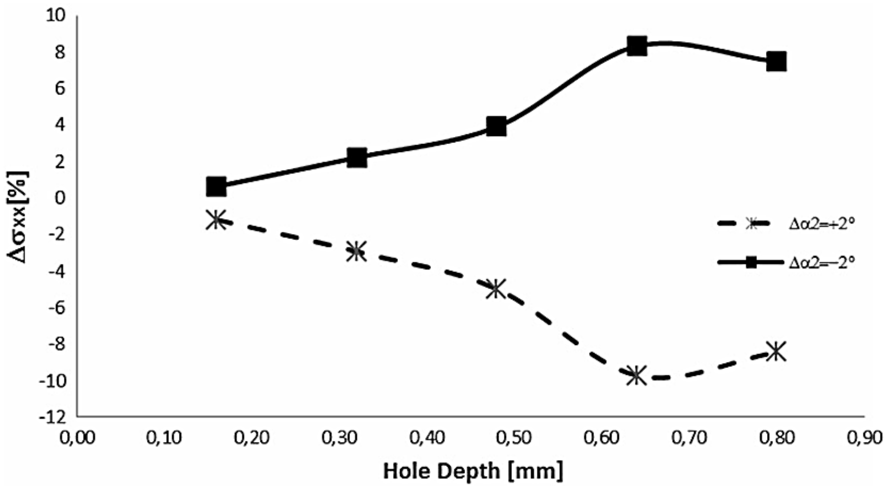

Figure 1.6–5 Variation of the percentage difference in the calculated σ_{XX} with the hole depth in correspondence of an error with respect to measured angle [62]

Table 1.6-1 Calculated stress σ_{xx} for measured α= 24° and percentage error for Δα=±2° [62]

Depth (mm)	σ_{xx} [MPa] (α= 24°)	σ_{xx} [MPa] (α= 22°)	σ_{xx} [MPa] (α= 26°)	$\Delta\sigma_{xx}$ % (Δα=−2°)	$\Delta\sigma_{xx}$ % (Δα=+2°)
0.16	-393	-396	-389	0.6	1.2
0.32	-314	-321	-305	2.2	2.9
0.48	-268	-279	-255	3.9	5.0
0.80	-213	-229	-195	7.5	8.4

The effect of drilling speed on the stress calculation has been studied in the same study [62]. The holes were drilled at three different velocities, 5k, 35k, and 50k rpm. Tested sample has been loaded in the four-point bending frame to create a well-known stress state of 143.6 MPa. Stress results from the ESPI data have shown that the stress calculation was coherent with the expected theoretical value. However, with lower drilling speeds, calculated residual stresses were scattered more than that of maximum speed as seen in Table 1.6-2. They have found that the standard deviation for the stress measurement has been about 20% at 5k rpm, whereas it has been decreased to about 4% at 50k rpm.

Table 1.6-2 Effect of drilling speed on the residual stress measurement [62]

σ_x at 5k rpm **[MPa]**	***σ_x at 30k rpm*** **[MPa]**	***σ_x at 50k rpm*** **[MPa]**	
118.0	153.8	152.6	
152.8	165.2	145.2	
170.2	171.2	150.2	
147.0	***163.4***	***149.3***	***Mean Value***
22.6	***8.8***	***3.8***	***Std. Deviation***

In the study of *Cheng et al.*, residual stresses in heat-treated SUS 304 stainless steel have been measured by using ESPI assisted hole drilling [63]. Results have indicated that the experimental method and the numerical method well agreed to each other so that the ESPI assisted hole-drilling techniques was applicable for the heat treatment induced residual stress measurement [63]. Figure 1.6–6 shows the residual stress distribution; AA’ line in the figure shows the residual stress state at the surface of the sample calculated by FEM while the BB’ is the inner part of the sample.

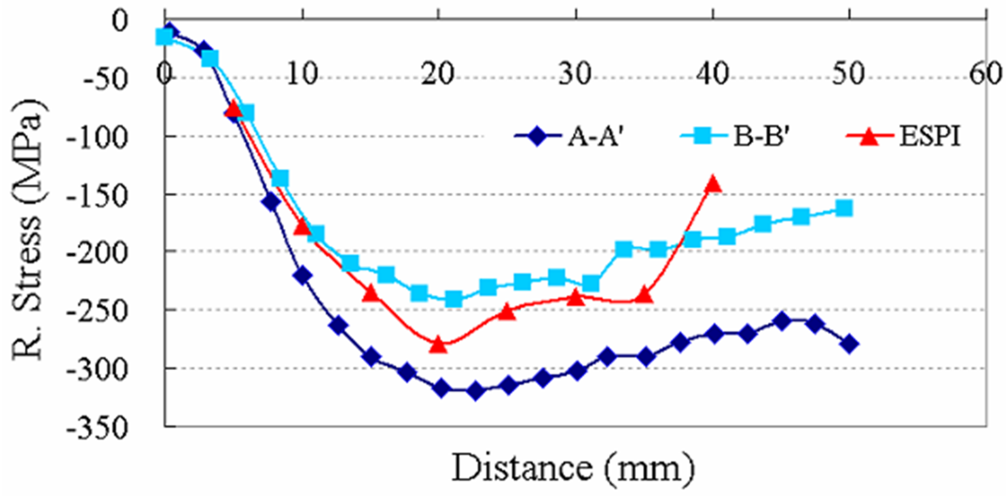

Figure 1.6–6 Comparison of the measured (ESPI) and calculated (FEM) residual stress distribution [63]

It has been shown that the analysis area of the ESPI assisted hole-drilling method has affected the residual stress calculated [66]. When the inner radius of the circle was too small, the experimental error arose due to the plastic deformation around hole and chips deposited near the hole. On the other side, when the outer radius was too large, the error was present since small deformations were considered [66]. The ratio of the radius of inner or outer circle to the radius of the hole defined as 2 and 4, respectively. In the experiment performed in the study, when the inner radius kept constant, changes in the outer radius caused an error in the calculated stress between 2% and 12% depending on the depth. When the outer radius remained same but inner radius changed, the error values varied from 2% to 20% [66].

Rickert et al. [67] have compared the ESPI hole-drilling and X-Ray Diffraction technique. Both methods gave the similar depth profiles as seen in Figure 1.6–7. It has been deduced that the ESPI method has been advantageous over XRD since it was much faster. In addition, ESPI method gathered information about the stress from complete drilling increment, whereas the XRD method was limited to a thin layer. However, zero-depth determination of the ESPI method caused an error in the stress calculation, so the identification of zero-depth as precise as possible was necessary for ESPI method.

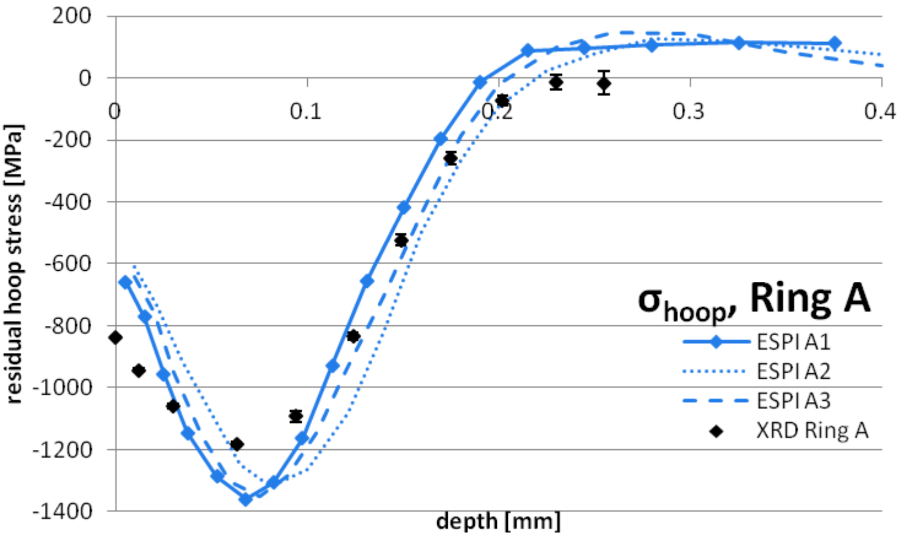

Figure 1.6–7 Comparison of the residual hoop stress measured by ESPI and XRD methods [67]

1.7 THE AIM OF STUDY

Carburizing that is the most widely used industrial thermochemical diffusion process generates a hard and wear resistant surface layer on components primarily produced from low-carbon and/or low-alloy steels. Since it is typically high-temperature process, the microstructure of steel is austenitic at the operating temperature of the thermochemical heat treatment. Because of this, carburizing is always followed by phase transformation after cooling [1].

A major benefit of the process is the formation of compressive residual stresses on the surface of components. In addition, high hardness and strength, which is combined with the beneficial case compressive stress formed by the interaction between case and core, improve both the surface properties and resistance to wear, bending fatigue, and rolling contact fatigue. Even though many carburized parts possess the same hardness profiles, they may have different microstructures and residual stress distributions. Prediction of residual stress state is tough and problematic. During the last decades, there has been a promising breakthrough in calculations based on the computer simulations and measurements of residual stress states in carburized and case-hardened steel samples.

By depending on the size and the type of material to be tested, testing speed, cost of the testing system, residual stress can be measured by either destructive or non-destructive methods. Destructive methods, including strain gage hole-drilling, ring core, sectioning, imply the formation of a new state of stress in a material and the calculation of residual stress as a function of the measured strain developed by the local change in the stress. On the other hand, non-destructive methods, such as X-Ray Diffraction, Ultrasonic, and magnetic methods, measure the stress state without damaging the material. As a magnetic method, Barkhausen Noise technique challenges the commonly used methods with its low cost and fast inspection capacity in the characterization of residual stresses.

The aim of the present study is to monitor the variations in microstructure and residual stress in carburized steels by the use of both destructive and nondestructive methods. The existing research compares three measurement techniques, **M**agnetic **B**arkhausen **N**oise (MBN), **X**-**R**ay **D**iffraction (XRD) and **E**lectronic **S**peckle **P**attern **I**nterferometry (ESPI), in order to measure the residual stress formed by the thermochemical heat treatment process. The first chapter provides theoretical background and overview of thermochemical heat treatments and the methods used in this dissertation. This is followed by the experimental procedure section consisting of material used, heat treatment process information, equipment, and setting, as well as test and measurement parameters. Residual stress measurement results combining with the comparison of obtained measurement results from each technique are dealt with in the third section. In the last chapter of the study, conclusions, and possible future studies are presented.

CHAPTER 2

EXPERIMENTAL PROCEDURE

This chapter is devoted to giving detailed information on experimental procedures that are conducted during each step of residual stress measurement and the other metallurgical measurements, such as microstructural investigation. Various methods are used for the residual stress measurement of the materials varying from destructive to non-destructive methods. In the present study, an incremental hole-drilling method by means of Electronic Speckle Pattern Interferometer (ESPI), X-Ray Diffraction, and Magnetic Barkhausen Noise methods were performed for residual stress measurement. For the sake of simplicity, this section is divided into six sub-sections. Each sub-sections give detailed information about material selection; heat treatment applied and optimized parameters for residual stress measurement methods.

2.1 MATERIAL SELECTION

Carburizing process improving the hardness of case depth by introducing carbon into the surface layer of a component is one of the most widely employed surfaces hardening processes. Carburized steels are composed of a composite material, in which the constituents are the harder carburized surface and ductile unaffected core. Compressive residual stresses are formed in the surface layer of the component when quenched from the carburizing temperature. High wear resistance, fatigue strength, and toughness result from the combination of high hardness and compressive residual stresses.

Since compressive residual stresses are formed depending on carburizing process parameters, analyses were performed by applying three different carburizing procedure flowed by various tempering treatment on 19CrNi5H low carbon steel that is especially used to produce any gears, pins, drive axles, etc.

A total of thirty-nine rectangular in shape samples whose dimensions are 165×36×10 mm (l×w×t) were prepared from 19CrNi5H steel rods by turning and milling operations. Since all samples were machined from the same steel rods, thirty-nine samples possess same mechanical properties and chemical composition given in Table 2.1-1 prior to the heat treatment process.

Table 2.1-1 Mechanical properties and chemical composition of sample

<table>
<tr><th>Material</th><th colspan="11">19CrNi5H / SAE 3120 / En 351 (BS 970) / 20NiCr4</th></tr>
<tr><td>Elastic Modulus (E)</td><td colspan="11">201 – 209 GPa</td></tr>
<tr><td>Poisson’s ratio (υ)</td><td colspan="11">0.27 – 0.29</td></tr>
<tr><td>Yield Strength (YS)</td><td colspan="11">350 – 550 MPa</td></tr>
<tr><td>Ultimate Tensile Strength (UTS)</td><td colspan="11">650 – 850 MPa</td></tr>
<tr><td>% Elongation</td><td colspan="11">8 – 25</td></tr>
<tr><td>Density</td><td colspan="11">7.70 g/cm^3</td></tr>
<tr><td rowspan="2">Chemical Composition (% weight)</td><td><i>C</i></td><td><i>Si</i></td><td><i>Mn</i></td><td><i>P</i></td><td><i>S</i></td><td><i>Cr</i></td><td><i>Ni</i></td><td><i>Mo</i></td><td><i>Al</i></td><td><i>V</i></td><td><i>Fe</i></td></tr>
<tr><td>0.18</td><td>0.26</td><td>0.95</td><td>0.014</td><td>0.026</td><td>1.01</td><td>0.94</td><td>0.05</td><td>0.031</td><td>0.009</td><td>balanced</td></tr>
</table>

2.2 HEAT TREATMENT

Before any heat treatment process, all samples were labeled in accordance with the heat treatment to be applied. To do this, four-digit nomenclature style was applied to samples as seen in Figure 2.2–1. In this labeling, first digit showing heat treatment applied is either normalizing process (N) or carburizing process (C) in the present study. The second digit designates the duration of the heat treatment in hours whilst the third digit refers to the tempering temperature. The last digit shows the measurement point on the surface of the sample.

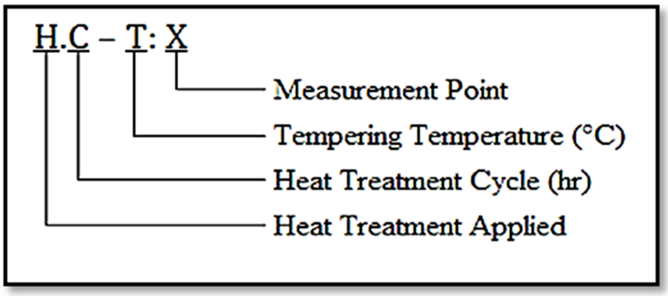

Figure 2.2–1 Nomenclature for coding of the samples

All rectangular samples were subjected to normalizing heat treatment process at the same batch before the application of gas carburizing operations. In the normalizing process, steel samples were uniformly heated to 880°C for the complete transformation to the austenite phase. They were then allowed to cool in still-air. In order to obtain homogenous microstructure throughout the samples, the soaking period is chosen about three hours. Residual stresses induced by turning and milling operations are expected to be relieved by the normalizing processes.

Three of the normalized samples were selected as reference assuming that samples are in stress-free conditions. The rest of the samples is arranged into three groups that consist of twelve identical samples before heat treatment operations. Each group was gas carburized in the batch type furnaces. The first step was heating the steel to the desired carburization temperature of 900°C and soaking at the uniform temperature for 90 minutes. In the heat and soak steps of the process, the carbon potential was set to 0.8 %. After heating and soaking the samples, boost step with the carbon potential of 1.1% was carried out for about 120 minutes. This step results in carbon absorption by the austenite until the limit of carbon solubility in austenite at the process temperature. The boost step was completed by using the mixture of C_3H_8 (g) and the shielding gas (33% H_2, 28% CO, and 0.8% CH_4). Carbon is liberated by the dissociation of the hydrocarbon gas on the surface of the steel samples; then the free carbon is directly absorbed by the austenite. Before quenching operation, steel samples were undergone diffusion step since an extremely abrupt case-core interface would form after the boosting step resulting from carbon gradient. After completion of the diffusion step, a more gradual case-core transition was obtained due to the carbon diffusion inward from the carburized surface. The furnace temperature was then decreased to 860°C with the carbon potential of 0.8%. The typical carburizing cycle can be seen in Figure 2.2–2. Then, the samples were quenched in the oil whose temperature was 60°C. Samples remained in the oil for a duration of 30 minutes. Each group was carburized by different durations, namely 8, 10 and 13 hours to see the effect of carburizing time on residual stress state.

After carburizing operations, samples in the groups were tempered at 180, 240 and 600°C for three hours while some of the samples were held in as-quenched form. The aim of this heat treatment process was to determine whether there is a decrease in residual stress state by tempering operations.

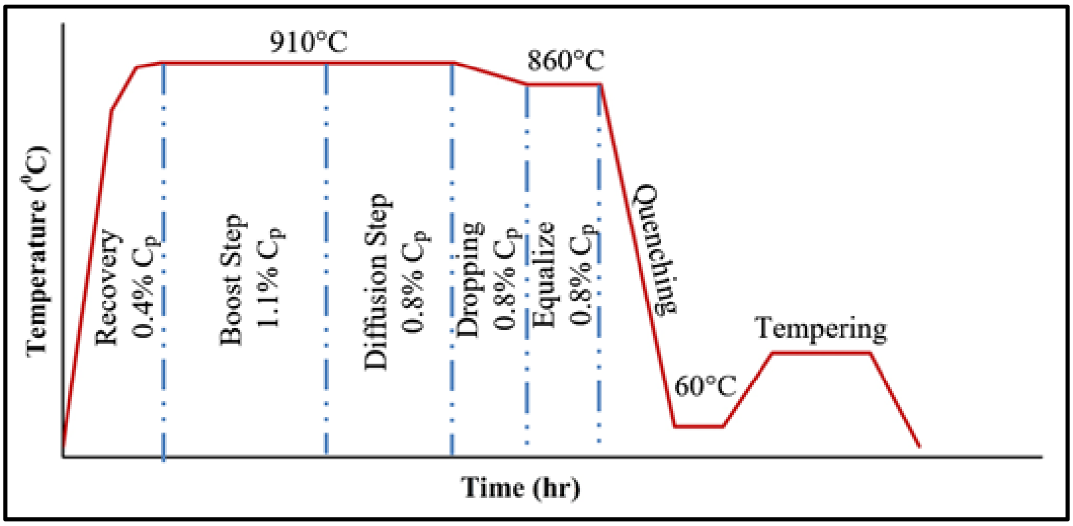

Figure 2.2–2 Typical carburizing cycle for 19CrNi5 steel

2.3 MAGNETIC BARKHAUSEN NOISE METHOD

2.3.1 Specimen Preparation

Since the depth of high-frequency Barkhausen signal is relatively shallow, the surface properties strongly affect the MBN signal. Surface preparation by using chemical and/or electrochemical method is preferred over mechanical methods for high-frequency Barkhausen measurement. Therefore, the surface of the test specimens was prepared chemically not to affect residual stress measurement in a negative way. This chemical cleanup was also used for rest of the residual stress measurement methods since mechanical methods will change the residual stress state of the materials.

In addition to the chemical cleanup of the surfaces, demagnetization of the sample or at least removing the magnetic history by randomizing the domains was necessary at the measurement point, as remanent magnetic fields are likely to influence the measurement. In order to obtain symmetrical magnetization and a corresponding symmetrical MBN signal on the magnetizing cycle, all test pieces were demagnetized by using demagnetizing tunnel used for magnetic particle testing.

2.3.2 Device Information and System Settings

For MBN measurement, specimens with 165×36×10 mm dimensions were used. On these samples, five measurement points were determined at least 2 mm away from the edges not to affect MBN signal acquired. Measurements were made by commercially available Rollscan 300 device together with Microscan 600 software developed by Stresstech Group. In this measurement, the general purpose S1-18-13-01 sensor was used for MBN measurement. A sinusoidal cyclic magnetic field was induced in a small volume of the specimen via a ferrite core with the help of the sensor. The system configuration can be seen in Figure 2.3–1.

Rollscan 300 device utilizes automatic magnetizing voltage and frequency sweeps to find optimum magnetizing parameters. Sine and triangle magnetizing waveform could be applied by this instrument. Rollscan 300 has magnetizing frequency and a peak-to-peak voltage of 0.1 to 100 Hz and 0 to 16 V_{pp}, respectively.

Figure 2.3–1 Magnetic Barkhausen Noise device and the sensor used

2.3.3 Test Parameters

Any residual magnetism in the specimens was eliminated by using demagnetizing tunnel beforehand the measurement. In Rollscan measurement, the magnetizing frequency was 250 Hz and the high-pass, and low-pass filter frequencies were arranged as 0.1 and 1000 kHz, respectively. In the µSCAN measurement, an excitation magnetic field with a frequency of 250 Hz was acquired while the magnetizing voltage, adjusting the magnitude of the magnetizing field applied to the material, was set to 10 V_{pp}. Sampling frequency, which determines how many samples are stored per second for signal analysis, was set as 6.4 MHz Number of magnetizing half cycles stored was fixed to 20 Barkhausen signal bursts during the measurement. During µSCAN analysis, the obtained Barkhausen Noise signals were filtered between 200 and 1000 kHz frequency range to correlate MBN and XRD measurement depths. These parameters were optimized by using two distinct sets of samples according to their residual stress states. By doing this, fully optimized MBN signals for residual stress state could be produced regardless of microstructure and hardness effect. Details of the optimization process can be seen in the next chapter. Five measurements were carried out in three measuring directions, namely 0°, 45°

and 90°. The reliability of MBN measurement was quantified by the R^2 coefficient obtained from the Pearson's correlation.

2.4 X-RAY DIFFRACTION METHOD

2.4.1 Specimen Preparation

Before conducting any residual stress measurement, any soil or grease should be removed from the surface, ideally by washing or by the use of a solvent. Mechanical methods such as the use of wire brush should be avoided since they may introduce additional surface residual stresses into the sample. By keeping this information in mind, as-received samples were cleaned from any residue by ethyl alcohol. Measurement points were also electro polished to about 15 microns to remove any oxide layer affecting residual stress measurement prior to any X-Ray diffraction measurement method.

As a known fact, the main requirement of material for XRD method is that the material should be crystalline or semi-crystalline, and it should have an isolated high angle diffraction peak in the range of 125 to 170° 2Θ. Therefore, a quick X-ray measurement was done to determine whether the samples have separated high angle peak at around 156° 2Θ value. After ensuring the existence of the high angle peak, measurement points were chosen at least 2 mm away from the edge of the flat samples to avoid residual stress relaxation. Whether both the incident and diffracted beams interact with the specimen without blocking was checked by operating the X-ray device for a short time.

2.4.2 Device Information and System Settings

The X-ray diffraction residual stress measurement was performed by using commercially available XStress 3000 G2/G2R manufactured by Stresstech Group seen in Figure 2.4–1. The X-ray source was Chromium radiation with Kα wavelength of 2.289649 Å. Tube voltage and current were set at 30 kV and 6.7 mA, respectively. 3 mm in diameter collimator was used, and the distance between the collimator and the test piece was measured as 10 mm. Before measurements, the device was calibrated by stress-free iron reference sample according to the description in device user's manual. For depth profile measurement of residual stress, MoviPol electro polisher by Struers was used with an A3 acid solution (60 mL perchloric acid + 360 mL ethylene glycol monobutyl ether + 600 mL methanol).

Figure 2.4–1 XStress 3000 G2/G2R residual stress measurement system

After the stress measurement operation, retained austenite in each point was measured by using Seifert XRD 3003 PTS system. Chromium radiation was produced by applying 30 kV and 55 mA. 2 mm collimator was used so as to cover more grains. As stated in ASTM standard, the four-peak method was used to measure retained austenite in the samples. Seifert XRD 3003 PTS system was also utilized to measure the residual stress in the austenite phase if any in the measurement samples.

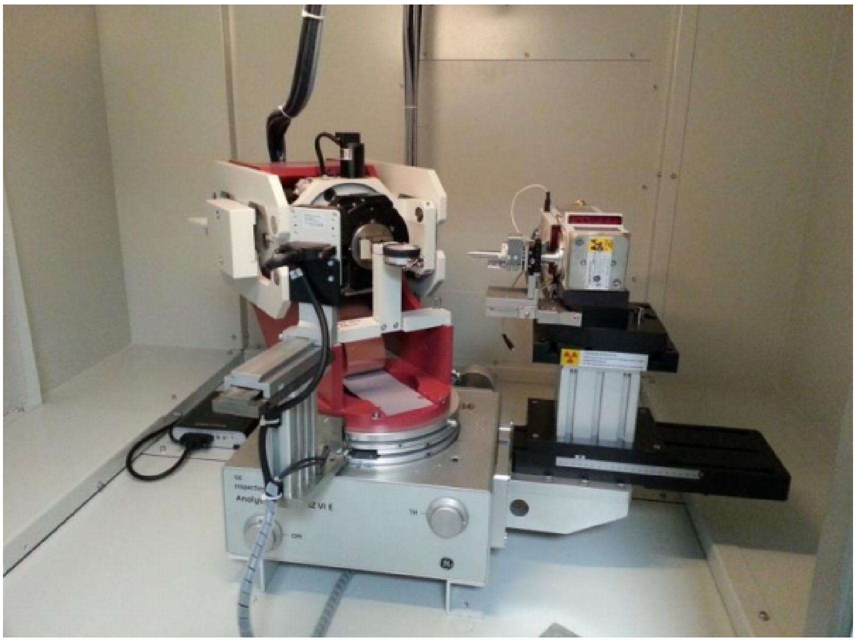

Figure 2.4–2 Seifert XRD 3003 PTS system

2.4.3 Test Parameters

With the XTronic software used for residual stress measurement, Modified χ mode was used as a standard measurement mode since the detector arc is in the position shown in Figure 2.4–3. Cr Kα radiation was employed by focusing on the ferrite {211} planes at $2\Theta \approx 156°$. Five tilts for both positive and negative ψ angle ranging from -40° to 40° were used. As in the MBN measurement, measurement directions for five equally distanced points on the sample surface was 0°, 45°, 90° with respect to the rolling direction. For 3 mm diameter collimator, the exposure time for each tilt was set at 5 seconds, and 10 minutes was required for the completion of the stress measurement. As one of the most important tasks is the accurate determination of the position or shift of the intensity peak in the residual stress measurement by X-ray diffraction, Cross-correlation method was chosen to localize the peak position. With Seifert XRD 3003 PTS system, residual stress measurement on the gamma phase was also conducted by using Cr Kα radiation. In this measurement, gamma phase with lattice plane of {220} was focused at $2\Theta \approx 129°$. Totally forty-five tilts were used between -45° to 45° ψ angle for three Phi (φ) angle. The total amount of time required for the measurement was about 210 minutes for each point on the sample.

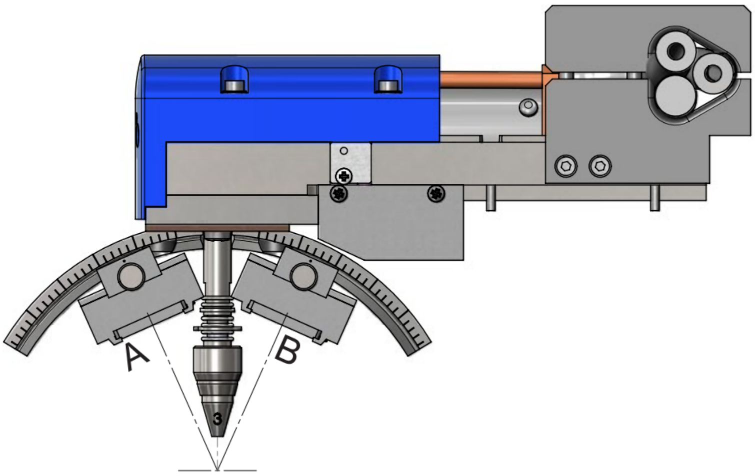

Figure 2.4–3 Detector arc in modified χ mode [7]

During the retained austenite measurement with Seifert XRD system, four diffraction peaks were tried to obtain between 74° and 170° 2Θ values. While two of these diffraction peaks originates from gamma phase with lattice plane of {200} and {220}, the other two comes from ferrite phase of {200} and {211}. Retained austenite content measurement was conducted on the same point used for residual stress and measurement on each point took about 40 minutes.

2.5 ESPI HOLE-DRILLING METHOD

2.5.1 Specimen Preparation

Since **E**lectronic **S**peckle **P**attern **I**nterferometer (ESPI) testing is semi-destructive, incremental residual stress measurement by this method was conducted upon the completion of all nondestructive measurement. Prior to the stress measurement, the measurement surfaces were cleaned from oil and dust or other particles that may affect the measurement. Due to optical measurement of the surface distortion, the sample surface must be optically rough and mirror-like reflected light must be avoided. Accordingly, a thin spray paint coating of matte color was applied to all sample surfaces to improve the measurement conditions.

In ESPI measurement, another important factor affecting the measurement conditions substantially is that the sample should be mounted properly to minimize vibrations. Specimens were positioned by clamps made from aluminum so that the hole is drilled perpendicular to the surface. By doing this, special caution is taken care not to introduce stress in the measurement area by the clamping.

2.5.2 Device Information and System Settings

Prism® that combines the tried-and-true hole-drilling method with digital imaging and ESPI is a new way to measure residual stress in a wide variety of materials. In this technique, minimal specimen preparation is required. A standard Prism system developed by Stresstech Group (Figure 2.5–1) contains a computer for software, type 3R laser light source with a wavelength of 532 nm and the power of 20 mW, illumination and video heads and a high-speed drill. The instrument monitors the stress changes less than 7 MPa.

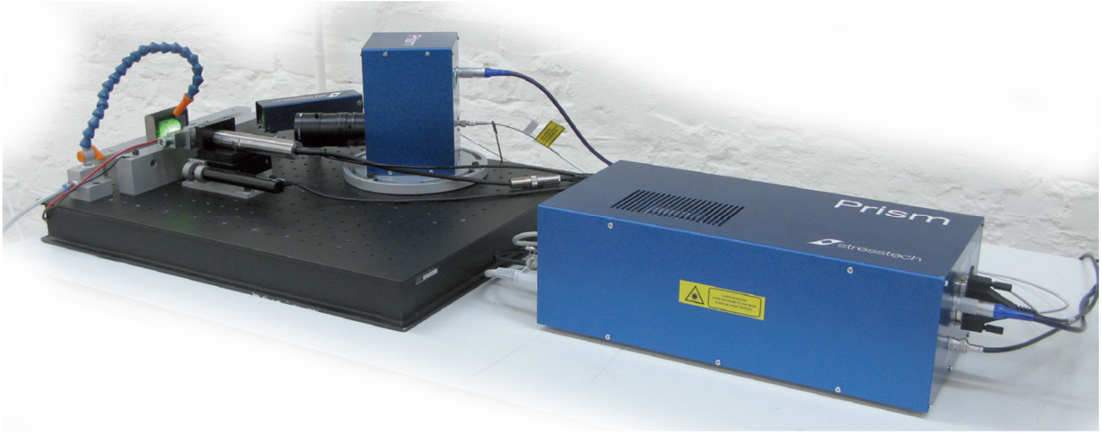

Figure 2.5–1 Prism® residual stress measurement system

During the measurements, two-fluted end mills with a diameter of 1/8” (3.175 mm) and 1/16” (1.5875 mm) were selected for incremental hole-drilling. Due to the difference in the case-hardened depth, two different end mills were used to obtain residual stress data through the hardened layer. All samples were carefully clipped on the aluminum clamp for obtaining a perpendicular drilling on the surfaces.

2.5.3 Test Parameters

Prior to the measurement, proper adjustment of the camera was accomplished so that the camera may properly image the drilled hole. The choice of the hole-depth strictly depends on the chosen end mills diameter. The depth to diameter ratio (D/d) should not exceed the value of 0.6. That is, there is a certain depth limit at which further drilling will not create any response at the surface. Thereby, 1/8” and 1/16” diameter end mills were chosen to obtain stress results from case depth and the core region. Two-fluted end mills were changed with the new one in every five measurements in the steel samples.

To determine the optimum test parameters for carburized materials, trial sets were formed on the dumb case hardened samples by changing drilling speed and drilling feed rates. Drilling speeds varying from 8,000 rpm to 50,000 rpm and feed rates from 0.05 mm/sec to 0.25 mm/sec were tested. After testing on dummy samples, the optimum parameters were determined as 40,000 rpm and 0.15 mm/sec. When determining the drilling speed and the feed rate, important factors are the hole shape, noise formed during measurement and the zig-zag pattern of the analyzed stress values. Desired depth with optimized parameters was reached by 25-micron step-size increment. To reach the depth of 1.0 mm and 1.5 mm was lasted two hours and three hours, respectively. In addition to the determination of the measurement parameters, evaluation parameters were also tried to be found by the series of experiment. Evaluation parameters of ESPI assisted hole-drilling stress measurement system mainly consist of the analysis area and the determination of the sensitivity vector. In-plane direction angle introducing the higher amount of error on the calculated residual stress values was measured as far as possible. Since the analysis is defined as the region between two circles drawn around the drilled hole, the results in terms of residual stresses are influenced by the size of the area. The diameter of the inner circle should not be so small so that the error cannot be arose due to the plastic deformation arisen near the hole region and the bad pixel due to the chips deposited near the edge of the hole. Furthermore, the diameter of the outer circle should not be too large not to consider the region of very small deformations. In the light of these, the analysis area was chosen as such that the inner and outer circles have a diameter of two (2) and four (4) for the stress calculation in the present study.

2.6 MICROSTRUCTURE – HARDNESS – SPECTRAL ANALYSIS

Microstructure and hardness measurement was performed on the samples sectioned from rectangular carburized samples by abrasive cut-off machine. The RD-ND (rolling direction – normal direction) planes of samples were used for these analyses. Specimens were then ground, polished and etched. Since the surface of the bakelite mounted samples were not rough, the grinding operation was performed using 320 and 600 grit SiC papers and polished by using 9 µm, 3 µm, and 1 µm size diamond suspensions followed by 0.04 µm colloidal silica suspension in the final polishing operation.

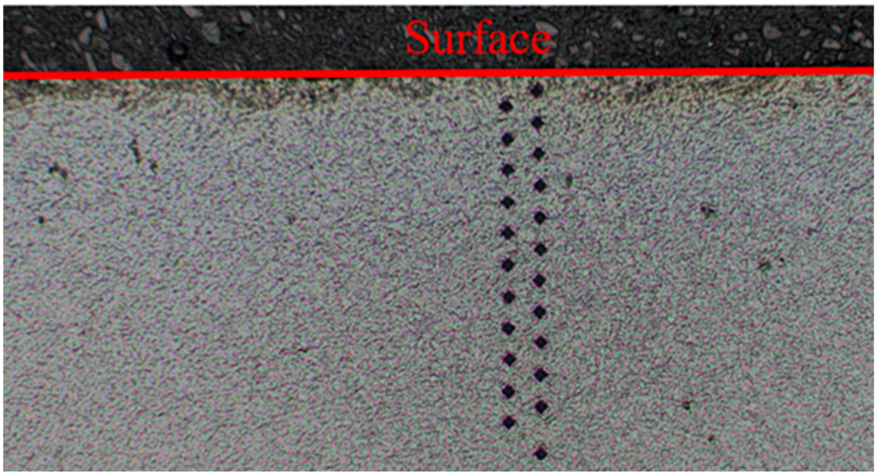

Figure 2.6–1 Zig-zag pattern adopted for hardness measurements

Hardness measurement was made on a cross-section of a part in order to determine case-hardened depth. By this way, case-hardened depth was derived graphically from a curve that represents the variation in hardness as a function of the distance from the surface of the specimen. During the hardness test, the cross-section of the part was polished to allow the correct measurement of the size of the hardness indentation. Hardness measurement was made along four parallel lines normal to the surface within a band of the width of 1.5 mm on each side of the specimens. The total indentations were sixty for each samples. In addition, the distance separating two adjacent indentations were 2.5 times greater than their diagonal and the distance between each indentation from the surface was not greater than the 0.1 mm. Therefore, zig-zag pattern, which can be seen in Figure 2.6–1, was performed on each measurement not to affect hardness values according to *EN ISO 2369* standard. For the hardness measurement in this study, Shimadzu HMV-2T device was utilized with 9.806 N load implemented for 10 seconds. The indentation measurement was done at 100X magnification.

By following hardness measurements, the samples were etched in 4% Picral (4 g Picric acid + 96 mL ethyl alcohol) and 2% Nital (2 mL nitric acid + 98 mL ethyl alcohol) solutions. Microstructural characterization was performed on the same samples after etching. Huvitz HDS-5800 and FEI Nova NanoSEM scanning electron microscopy (SEM) imaging systems were used for microstructural analysis. The magnification level was ranging from 50X to 1000X with the optical system and 1500X to 10,000X with scanning electron microscopy. During SEM analysis, the field-free mode was utilized due to the magnetic characters of the specimens. The high voltage value was 15 kV for 19CrNi5H steel for taking a proper image.

For **O**ptical **E**mission **S**pectrometer (OES) analysis, 80×36×10 mm specimens were sectioned from the carburized samples. OES analysis was performed on at least five points on the surface through case-hardened depth by using Bruker Q4 Tasman optical emission spectrometer. Before each measurement, the surface of the samples was ground by 50 µm under cooling liquids. The OES analysis was performed until reaching the core region which was specified by the carbon content of the normalized sample.

CHAPTER 3

RESULTS AND DISCUSSION

This chapter is devoted to the discussion and the comparison of results obtained from the X-ray Diffraction method, ESPI assisted hole-drilling method and Magnetic Barkhausen Noise method as well as microstructural and optical emission spectrometry analysis and the hardness measurement. It should be noted that all the results are presented for 19CrNi5H steel subjected to the thermochemical heat treatment for a different period of the process. For the sake of convenience, this chapter is divided into five main sections. In the first section, microstructure, hardness, and optical emission spectrometry results are examined. Then, in the next three sections, the results obtained from the X-ray Diffraction method, Magnetic Barkhausen Noise method, and ESPI assisted hole-drilling method are examined in details for the randomly selected carburized and normalized steel samples from the twelve sets of specimens. Moreover, in the last section, these measurement systems are compared with each other in order to decide which technique is best suited for the residual stress measurement of the case-hardened materials.

3.1 MICROSTRUCTURE – HARDNESS – SPECTRAL ANALYSIS RESULTS

In this section of the study, the microstructural characterization of the steel samples will be given at first. Then, the hardness measurement done for the determination of effective case depth will be given prior to the optical emission spectrometer results.

3.1.1 Microstructural Characterization

The **C**ontinuous **C**ooling **T**ransformation (CCT) curve and **T**ime **T**emperature **T**ransformation (TTT) curve for 19CrNi5H steel are shown in Figure 3.1–1. The martensite start temperature is about 400°C. Upon furnace cooling, it is expected to have ferrite and pearlite phases in the microstructure.

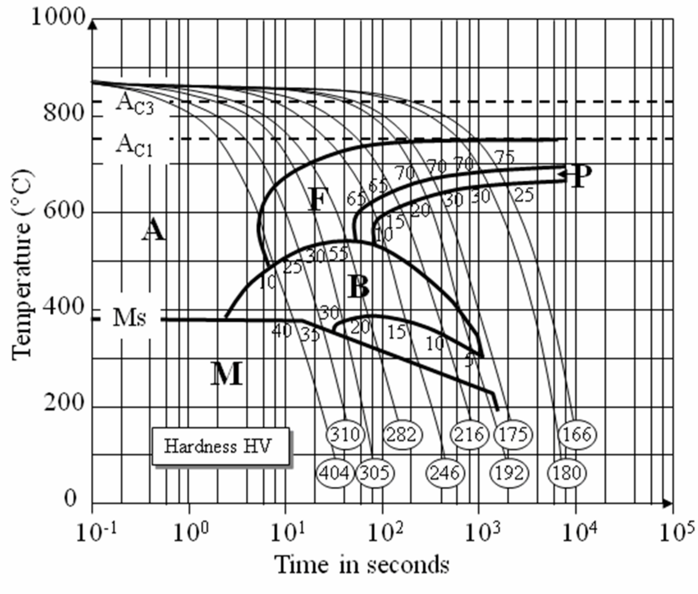

a)

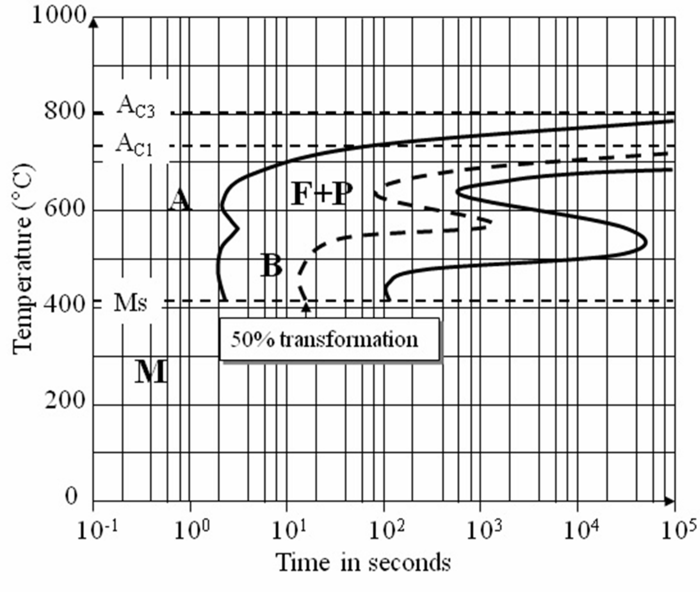

b)

Figure 3.1–1 CCT and TTT (right) diagram for 19CrNi5H steel [100]

As expected from the CCT curve, the normalized sample contains ferrite and degenerated pearlite phases with some possible carbide islands in the microstructure when cooled down to room temperature from austenitization temperature of 880°C, which can be seen in Figure 3.1–2. After the thermochemical treatment and quenching operations, typically martensitic and tempered martensitic structures are obtained for the 19CrNi5H steel specimens. Representative micrographs for 19CrNi5H steel samples subjected to the thermochemical treatment are given in Figure 3.1–3 - Figure 3.1–5.

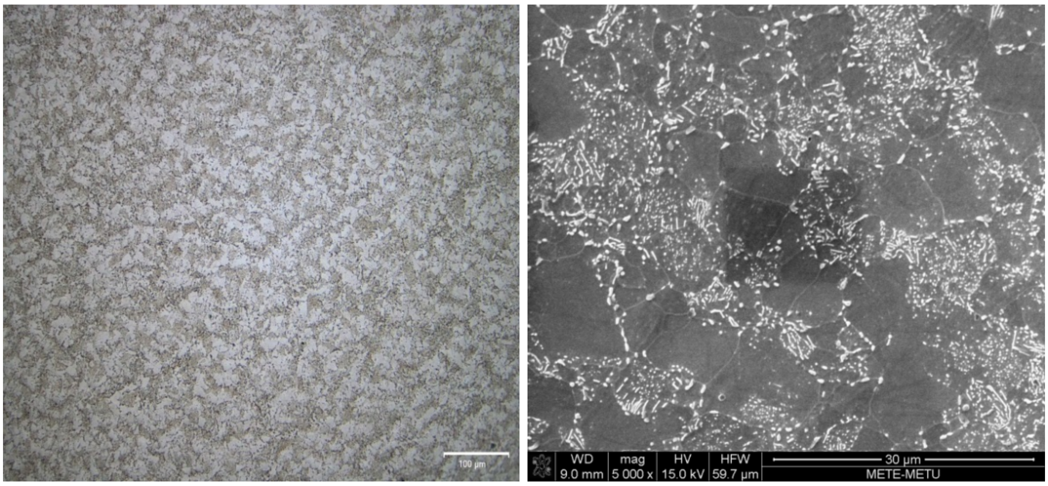

Figure 3.1–2 Optical (left) and SEM (right) micrographs of the normalized 19CrNi5H steel: 500X and 5000X magnification, respectively

A component containing the only virgin or fresh martensite cannot be used in engineering applications as the toughness and ductility of the material is lower with the exception of the maraging and boron steels. Some factors such as lattice distortion, carbide formation, and residual stress lead to the brittleness of martensitic structures. Therefore, materials having martensite formed after quenching is always tempered to (i) relieve internal stresses, (ii) improve the dimensional stability and (iii) increase ductility and toughness of the material.

The 19CrNi5H steel samples are quenched and tempered at various temperatures between 180°C - 600°C in order to differentiate the residual stress caused due to the phase transformation. The SEM micrographs obtained are illustrated in the Appendix A. From optical micrographs; it is seen that the carburized samples have a martensitic structure in both core and the case region. Moreover, the martensitic surface contains retained austenite, which is the white areas in Figure 3.1–3 - Figure 3.1–5. With the tempering at 240°C, the martensite in the core transforms to bainite phase since the martensite start temperature for the carburized 19CrNi5H steel is about 190°C.

The tempering temperatures up to 240°C have no effect on the change of the microstructure. When the tempering process is carried out at 180°C, ε-carbide precipitation occurs, and the martensite phase partially loses its tetragonality. At this temperature, carbon is precipitated as ε-carbide with the hexagonal close-packed crystal structure. These carbide precipitates are of narrow laths or rodlets on the cube planes of the matrix. The epsilon carbide is usually precipitated first since it shows better lattice matching with the matrix so that the coherent nucleation can occur without much strain energy.

Upon tempering operations at 240°C, martensite loses its tetragonality as well cementite replaces the epsilon carbides in the structure. The plate-like structures of cementite appear in the microstructure with dimensions of 200 nm long and about 15 nm thick. When the cementite particles are formed during tempering, they agglomerate and grow until the spheroidized structure is obtained in the microstructure. The cementite is nucleated at the interfaces between ε-carbide and the matrix and ε-carbides gradually disappear during the growth of cementite particles. In addition, the dislocation density is effectively lowered. Further increase in the tempering temperatures up to 600°C, cementite phase in the structure coarsens and spheroidizes due to the decrease in the surface energy. Tempering operations at higher temperatures are expected to cause a decline in the hardness and residual stress state of the material. The microstructural investigations reveal that when the tempering temperature is above the martensite start temperature of the steel, martensite phase starts to transform to obtain more stable phases in the structure.

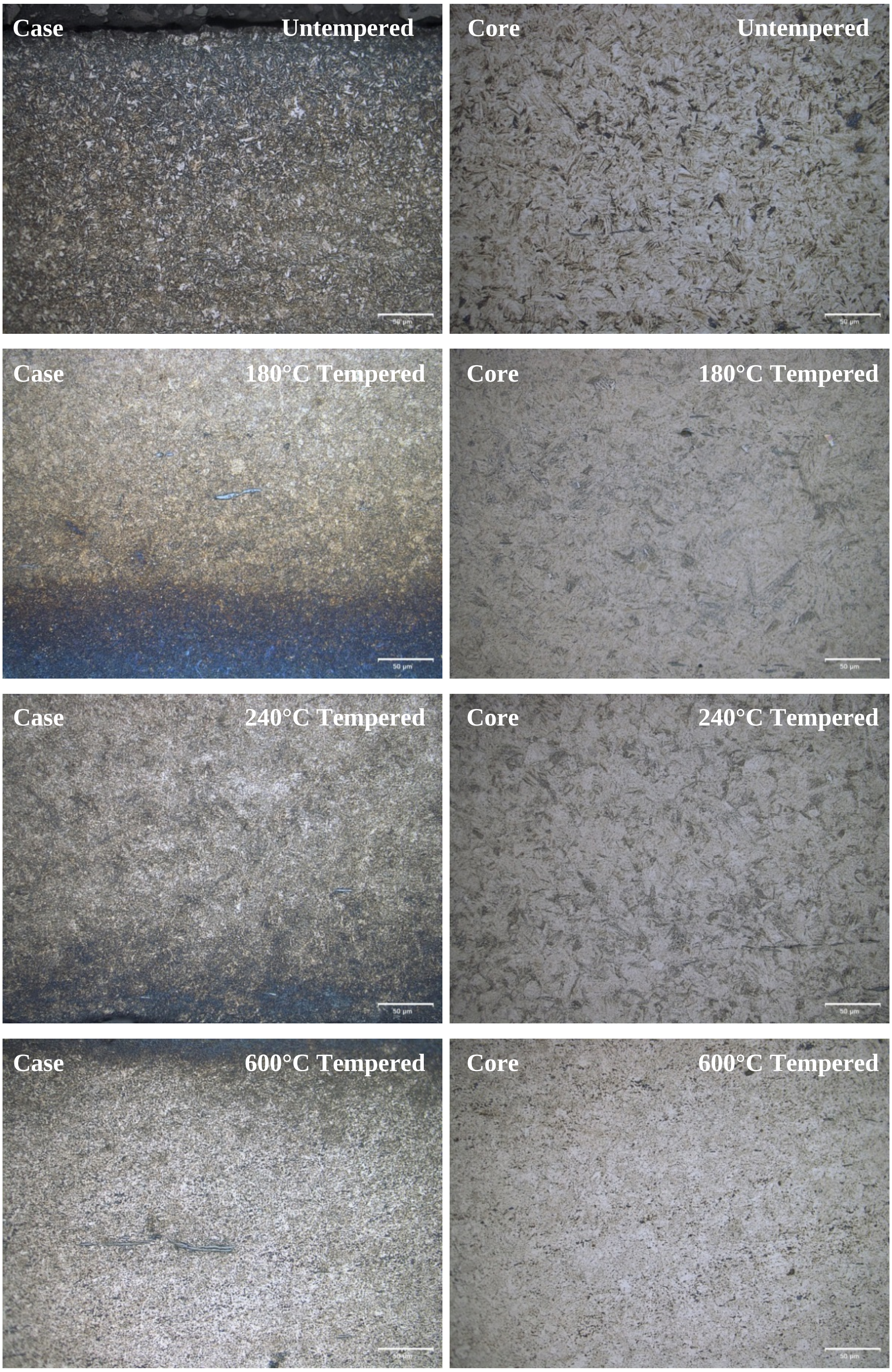

Figure 3.1–3 Optical micrographs for case-hardened 19CrNi5H steel (900°C/8 hrs): 1000X magnification

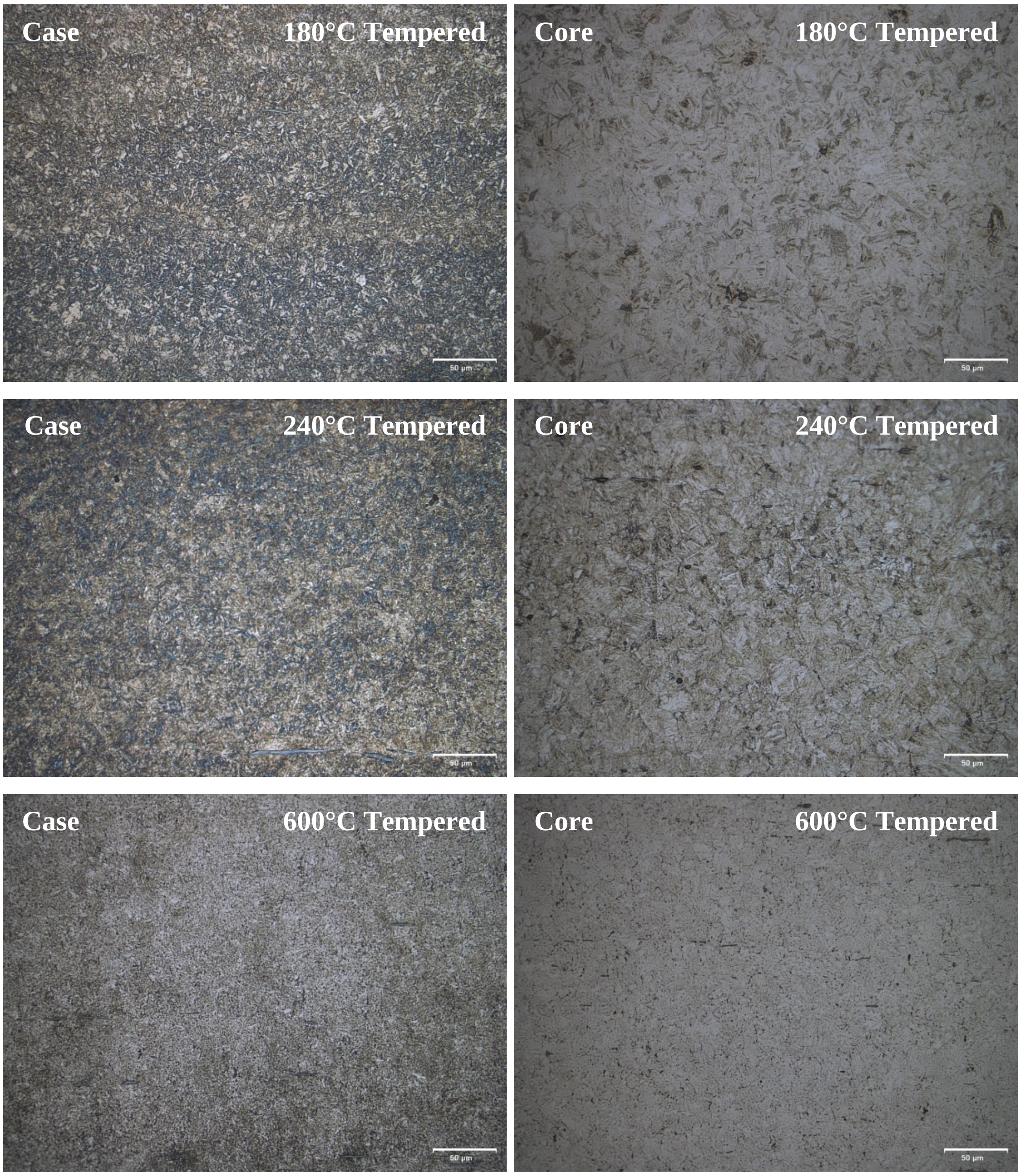

Figure 3.1–4 Optical micrographs for case-hardened 19CrNi5H steel (900°C/10hrs): 1000X magnification

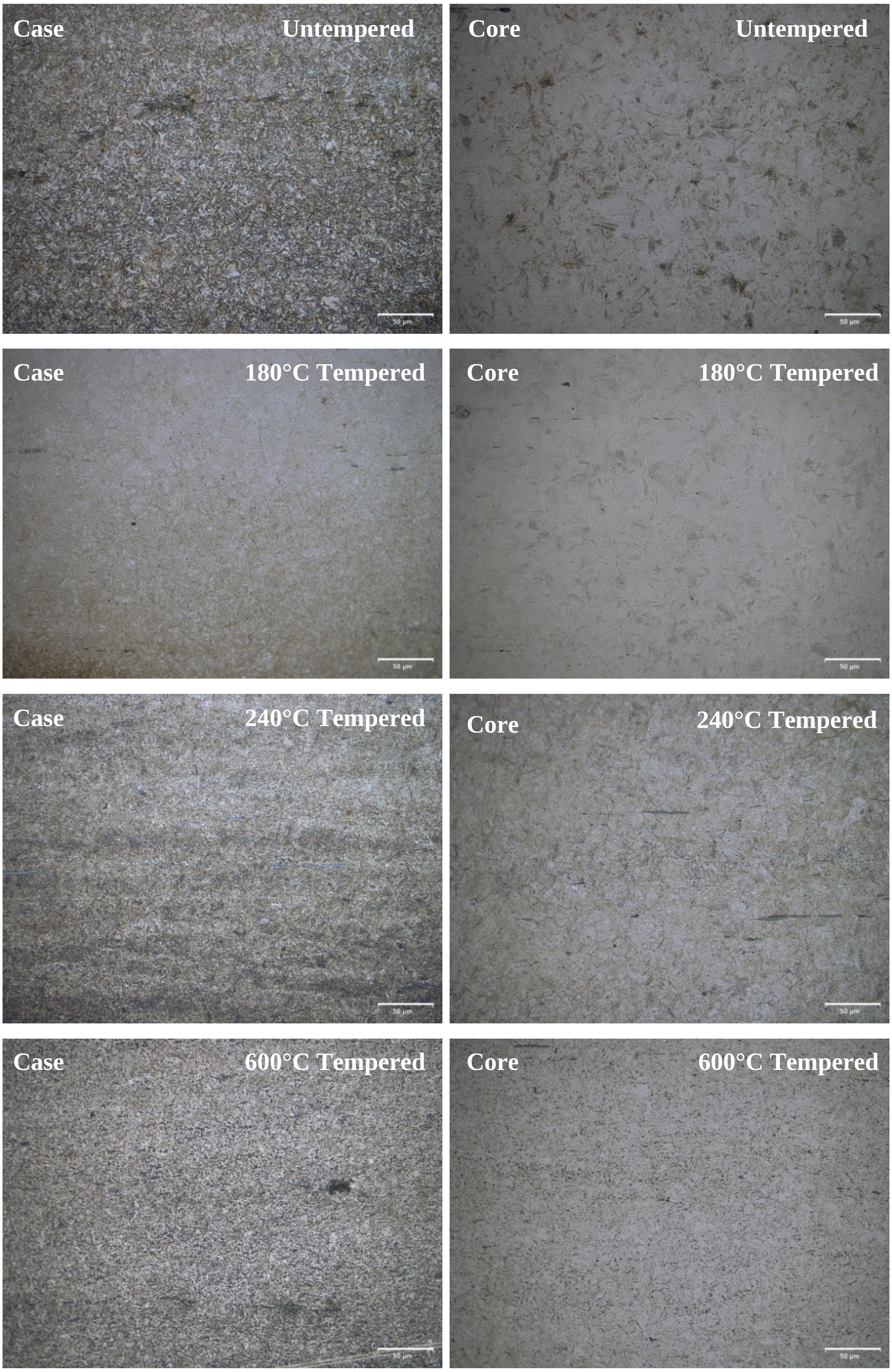

Figure 3.1–5 Optical micrographs for case-hardened 19CrNi5H steel (900°C/13hrs): 1000X magnification

3.1.2 Retained Austenite Measurement

The microstructural and XRD analysis conducted on the samples indicated that the heat-treated 19CrNi5H steel samples contained the only martensite and retained austenite phases, which are randomly oriented. Therefore, quantitative measurements of the relative volume fraction of martensite and austenite can be done by X-ray diffraction as stated in the ASTM E975-13. Standard indicates that the total integrated intensity of diffraction peaks of each phase is proportional to the volume fraction of that phase given by;

$$\frac{I_\alpha}{I_\gamma} = \frac{R_\alpha V_\alpha}{R_\gamma V_\gamma} \tag{3.1-1}$$

where the constant *R* depends on theta, (hkl) and the kind of substance. This ratio is valid only when martensite and austenite are the only phases present in the steel. The volume fraction of austenite for the ratio measured integrated intensities of martensite and austenite peak to R-value is given as;

$$V_\gamma = \frac{I_\gamma / R_\gamma}{(I_\gamma / R_\gamma) + (I_\alpha / R_\alpha)} \tag{3.1-2}$$

During the quenching process of the steel from the carburizing temperature, austenite transforms to martensite with some volume fraction of austenite, which is called as retained austenite.

During the retained austenite measurement, the four-peak method was used to determine the volume percent of retained austenite in the carburized steel sample. As it can be seen in Figure 3.1–6, retained austenite phase is found at 2theta values of about 79° and 128°, whereas martensite phase is found at 105° and 154°. To calculate the volume fraction of the retained austenite, integral intensities and R-values must be calculated.

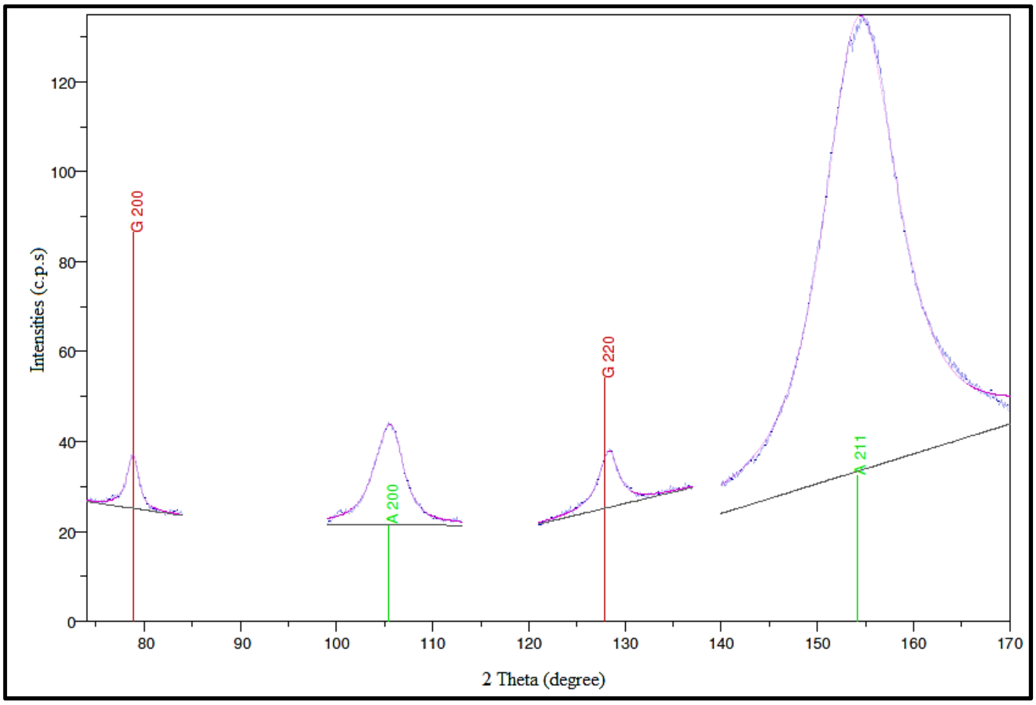

Figure 3.1–6 XRD pattern of the case-hardened 19CrNi5H steel (900°C/13 hrs): as-quenched

Diffraction angle, integral intensities, and R-values of γ-iron and α-iron are summarized in Table 3.1-1. Integral intensities are calculated by the RayFlex software. This software uses constant R-values for Chromium radiation by assuming the lattice parameters are as $a_{\alpha-Fe} = 2.8664\,A^0$ and $a_{\gamma-Fe} = 3.6000\,A^0$ given in ASTM E975-13 standard. In the table, R-values are calculated using the formulae given in the standard by ignoring anomalous scattering factors.

Table 3.1-1 Diffraction angle, integral intensities, and R-values of γ-Fe and α-Fe

Phases	2Theta (Degree)	R	Integral Intensity (cps)
γ -Fe (200)	78.88	36.94	13.6
γ -Fe (220)	128.21	56.20	22.8
α -Fe (200)	105.42	23.34	49.1
α -Fe (211)	154.18	235.43	491.2

After the calculation of the R-values and integrated intensities, the volume fraction of the retained austenite present in the sample was calculated as in Table 3.1-2. Then, the average volume percent of austenite is calculated as 15.6±0.7%.

Table 3.1-2 Calculated volume percent of retained austenite

Ratio of the integral intensities	Percent Volume of γ-Fe
I (γ-200) / I (α-200)	14.9
I (γ-200) / I (α-211)	15.0
I (γ-220) / I (α-200)	16.2
I (γ-220) / I (α-211)	16.3

The same procedure was carried out at five different measurement points for all carburized samples. The results indicated that the amount of retained austenite is the maximum when the carburizing temperature increases. It was also found that the above the tempering temperature of 180°C, retained austenite transforms to the other phases since the martensite start temperature of the 19CrNi5H steel is about 190°C. Calculated retained austenite content for each carburized steels is summarized in Table 3.1-3. C.13-T0 sample contains the highest amount of retained austenite in the case region. Upon tempering temperatures of 180°C, there is no retained austenite in the microstructure of the carburized specimens. For the as-quenched samples that are carburized at 900°C for 8hrs, retained austenite values cannot be measured due to the lower intensities of peaks of austenite phase in the X-ray diffraction pattern.

Table 3.1-3 Calculated retained austenite content in carburized 19CrNi5H samples

Samples #	Measurement Points				
	1	2	3	4	5
C.8h-T0	N/A	N/A	N/A	N/A	N/A
C.8h-T180	6.4 ±1.3%	9.4±2.0%	11.4±3.5%	11.4±2.5%	11.9±2.0%
C.10h-T180	6.9±0.4%	4.4±0.9%	3.2±0.3%	5.2±0.4%	2.7±0.2%
C.13h-T0	15.7±1.9%	16.2±1.9%	15.9±1.8%	14.7±2.2%	14.6±2.6%
C.13h-T180	5.4±1.7%	8.8±2.3%	9.6±2.7%	8.9±3.0%	10.7±3.0%

3.1.3 Hardness Measurement

The only-quenched specimens are the hardest among the all case-hardened steel owing to the tetragonal martensitic structure and higher dislocation density generated by the shear. Martensite is formed by an abrupt diffusionless shear deformation in the austenite lattice. It is also known that martensite phase is a supersaturated solid solution of carbon in the ferritic iron so that the crystal structure turns into the body-centered tetragonal shape. The combined effects of the solid solution and dislocation strengthening and lattice distortion due to internal strain lead quenched specimens to be the hardest. With the tempering operations, the hardness values of the steel specimens are lowered due to the fact that martensite loses its tetragonality, and the phase transformation occurs. The average Vickers hardness values of the core and the case is illustrated in Table 3.1-4. When the tempering is carried out at 600°C, the hardness value is suddenly decreased for all carburized samples due to the presence of spheroidized phases.

Table 3.1-4 Average hardness (HV1) of the carburized samples

Sample #	Case region	Core region
Normalized	N/A	184.3
C.8h-T0	705.7	473.9
C.8h-T180	660.5	460.7
C.8h-T240	633.1	462.3
C.8h-T600	341.3	260.4
C.10h-T180	668.3	475.0
C.10h-T240	624.7	478.3
C.10h-T600	296.8	301.4
C.13h-T0	759.9	496.6
C.13h-T180	688.0	470.4
C.13h-T240	641.2	464.9
C.13h-T600	305.6	316.5

Effective case-depth values was measured by means of microhardness test in accordance with the ISO 2639 test standard. The effective case depth expressed in millimeters is defined as a perpendicular distance between the surface and the layer that has a hardness value of 550 HV1 [101]. The Vickers hardness test is conducted at 100X magnification in accordance with ISO 6507-1. Figure 3.1–7 indicates the Vickers hardness values for the carburized steel samples. From the figure, it can be seen that effective case depth is the lowest in 8hrs carburized specimen as expected. The case-hardened depth determined for three different carburized samples is about 0.7 mm, 0.8 mm and 1.1 mm. These depth values should be verified by the interpolation method since the hardness gradient can be approximated by a straight line in the transition area.

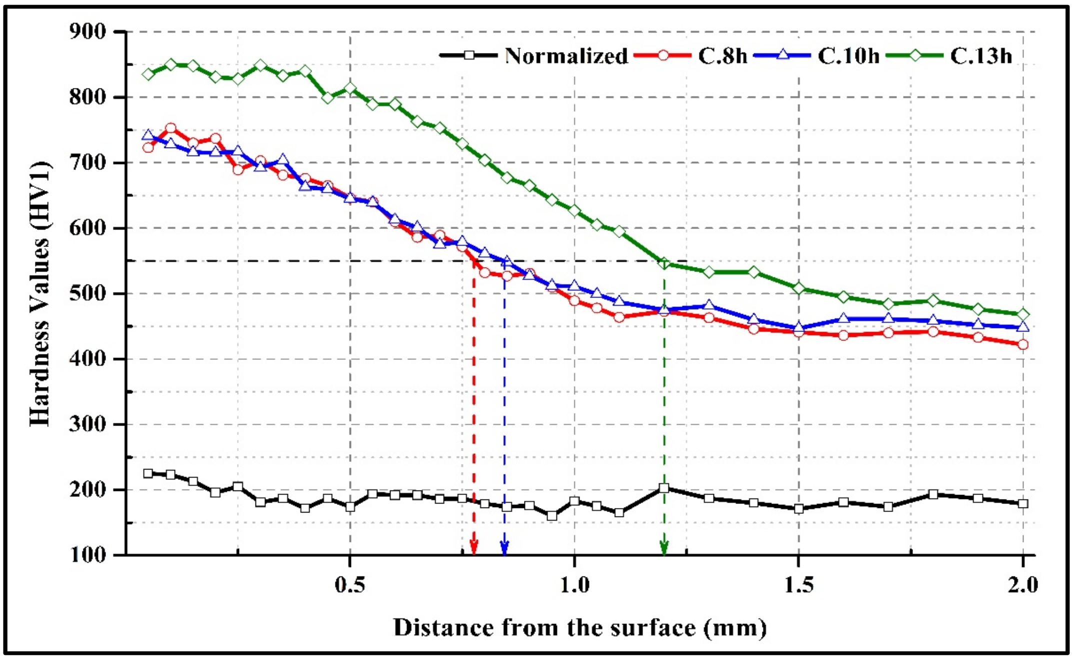

Figure 3.1–7 Effect of the carburizing time at 900°C on the hardness depth profile of the 19CrNi5H steel

The case-hardening depths were verified by the formulae given in ISO 2639;

$$CHD = d_1 + \frac{(d_2 - d_1)\times\left(\overline{H_1} - H_s\right)}{\overline{H_1} - \overline{H_2}} \tag{3.1-3}$$

where H_s is the specified hardness; $\overline{H_1}$ and $\overline{H_2}$ are the arithmetic mean of the measured hardness at distances d_1 and d_2.

The calculated effective case depth values for 8hrs, 10hrs, and 13hrs carburization are 0.78 mm, 0.84 mm and 1.19 mm, respectively. The verification process indicates that the estimated CHD values by the equation 3.1-3 are consistent with those found from the hardness versus depth graph.

3.1.4 Optical Emission Spectrometer Analysis Results

Optical emission spectrometry is carried out to determine the percent of carbon variation from case to the core region. It can be seen from Figure 3.1–8 that the surface carbon content of the carburized steels is about 0.9% and when going from the case region to the core region, the carbon content of the steel approaches to the base carbon content of 0.2%. The 8hrs and 10hrs carburized samples do not show much difference in carbon content, whereas the carbon content of 13hrs carburized sample is higher due to the more carbon diffused into the core region.

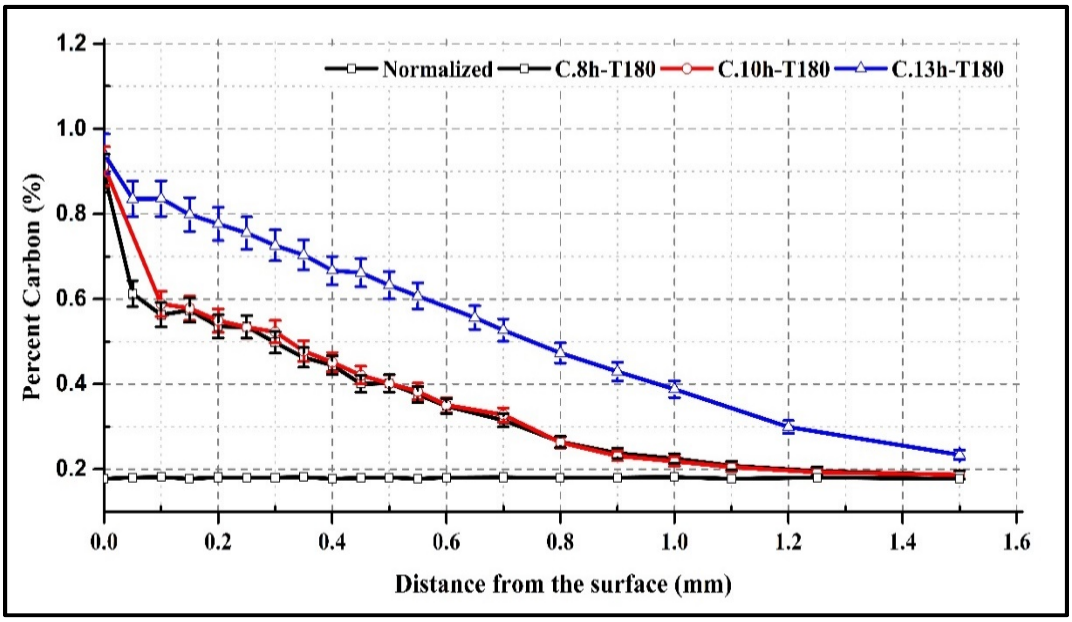

Figure 3.1–8 Effect of the carburizing time at 900°C on the depth profile of the percent carbon in the 19CrNi5H steel

Hardness versus percent carbon content can be seen in Figure 3.1–9 for 13hrs carburized steel sample. It can be deduced from the graph that hardness of the material is proportional to the carbon content of material. The Pearson’s correlation value is obtained as 0.98 in the measurement. This correlation value indicates that there is a very strong linear correlation between the hardness of a part and the carbon content of a part. In addition, most of the data points in the graph lie within the 95% confidence band. This confidence band implies that the hardness of the material can be predicted as 0.95 accurately as possible from the carbon content of the part. This very strong linear correlation level between the hardness and the percent carbon content is also valid for 8hrs and 10hrs carburized steel samples for all tempering condition. The linear correlation found between two properties are approximately 0.97 and 0.98 for the samples carburized at 900°C for 8hrs and 10hrs carburizing.

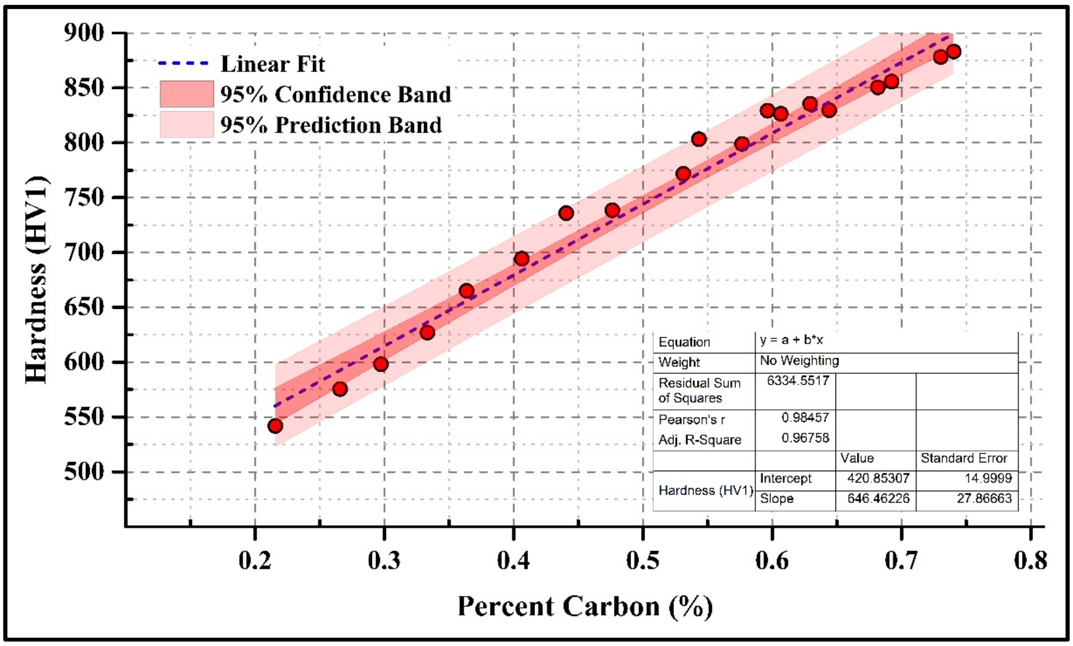

Equation	y = a + b*x		
Weight	No Weighting		
Residual Sum of Squares	6334.5517		
Pearson's r Adj. R-Square	0.98457 0.96758		
		Value	Standard Error
Hardness (HV1)	Intercept	420.85307	14.9999
	Slope	646.46226	27.86663

Figure 3.1–9 Hardness versus percent carbon for carburized 19CrNi5H steel (900°C/13hrs): as-quenched

3.2 X-RAY DIFFRACTION MEASUREMENT RESULTS

Surface residual stress distributions of the carburized and normalized 19CrNi5H steel are calculated by *d* vs. $sin^2\psi$ method described earlier in this study. Biaxial stress state is assumed due to the thickness of the material under investigation.

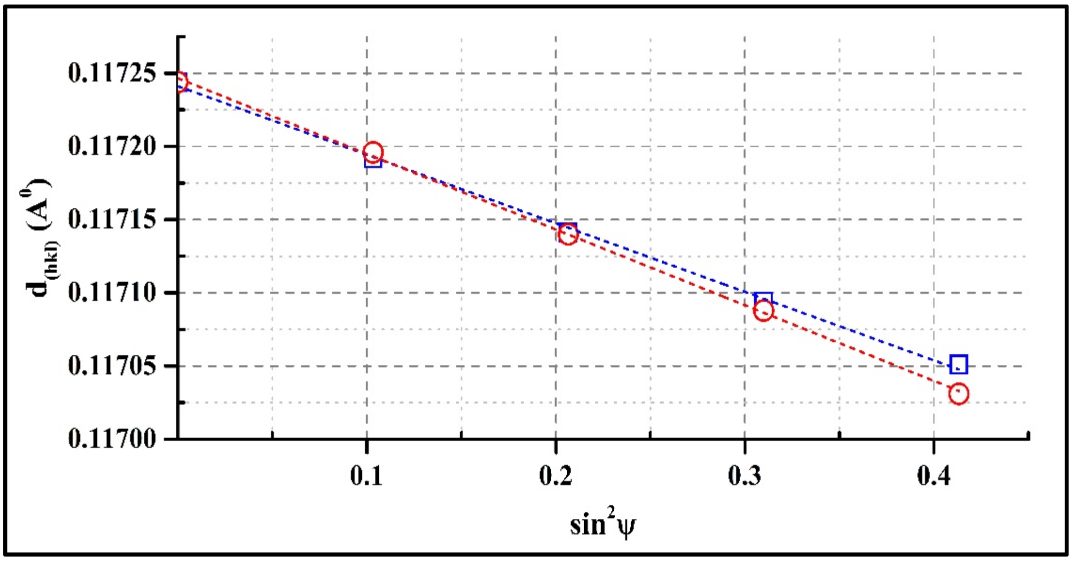

Figure 3.2–1 A linear graph of *d* vs. $sin^2\psi$ fitted to diffraction data of Φ=0° for carburized 19CrNi5H (800°C/8hrs): as-quenched

Each tilt in the experiment yields a point in the coordinates system of *d* vs. $sin^2\psi$ graph. Figure 3.2–1 exhibits a regular *d* vs. $sin^2\psi$ behavior by elliptically fitted line to obtain X-ray diffraction data. This regular shape behavior of the graph suggests the use of equation 1.4-15 for the residual stress calculation. It should be noted from the figure that the strain components ε_{13} and/or ε_{23} acting on the sample is non-zero due to the split in the negative and positive tilts. The residual stress value can be calculated from the slope of the fitted lines, which is discussed in details in Chapter 1 in this study. This basic calculation method is used to calculate all residual stress for each carburized with or without tempered steels. The calculated residual stress distribution for three different phi angles is summarized in Table 3.2-1. It can be seen from the table that compressive residual stress is present for each phi angle in carburized with or without tempering process.

Table 3.2-1 Average residual stress values for martensite phase with the three different phi angle in carburized 19CrNi5H steel sample

	Calculated Residual Stress [MPa]		
Sample #	**Φ=0°**	**Φ=45°**	**Φ=90°**
Normalized	239.7	70.0	-75.9
C.8h-T0	-709.7	-707.4	-706.6
C.8h-T180	-535.6	-553.4	-564.6
C.8h-T240	-341.2	-337.7	-334.6
C.8h-T600	-234.9	-244.3	-247.1
C.10h-T180	-573.2	-563.0	-568.6
C.10h-T240	-409.6	-398.0	-400.6
C.10h-T600	-328.7	-324.8	-329.0
C.13h-T0	-751.1	-729.2	-720.0
C.13h-T180	-626.4	-605.1	-621.6
C.13h-T240	-498.9	-482.9	-471.8
C.13h-T600	-339.4	-344.5	-340.7

Note that the negative sign implies compressive residual stress present

Effect on tempering on the residual stress distribution can be seen in Figure 3.2–2 for 19CrNi5H steel sample that is carburized at 900°C for 8hrs. The X-ray diffraction stress measurement method indicates that the compressive surface residual stresses are present in the as-quenched and the tempered steel specimens. As it is expected, the magnitude of the compressive residual stress is decreasing when the tempering temperature is raised to 600°C. Although the magnitude of the stress is declining in all samples, the compressive residual stress state remains on the surface of the part. When phi angle is changed, the same trend of residual stress state as in the parallel direction was observed. In addition to this, the residual stress values on the surface of the sample did not change much with the variation of the phi angle as seen in Figure 3.2–2.

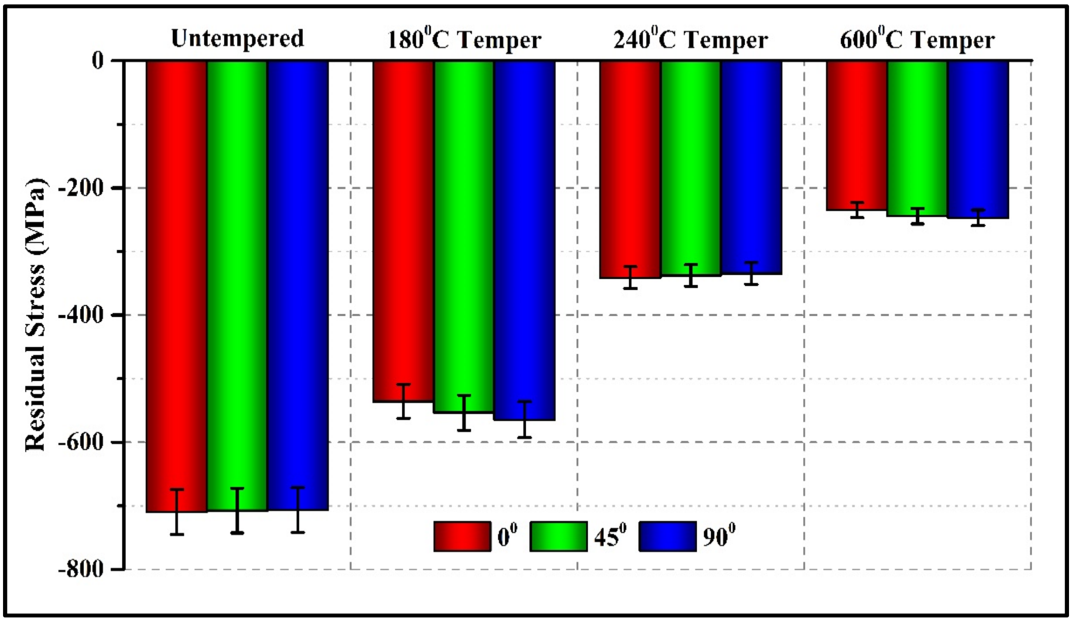

Figure 3.2–2 Effect of tempering on the surface residual stress of the carburized 19CrNi5H steel (900°C/8hrs)

When the steel sample is subjected to 10hrs thermochemical surface heat treatment process at 900°C, compressive residual stress state is generated on the surface of the steel sample. It is seen from Figure 3.2–3 that the magnitude of the compressive residual stress is greater in 10hrs carburized samples than that of the 8hrs carburized specimens as long as the tempering conditions are the same. It is known that the magnitude of the residual stress is dependent on the ratio between the case and core thickness when the other factors are the same. For 8hrs carburized sample, the case to core ratio is about 0.18, and it increases to 0.21 for 10hrs carburized sample. Since the ratio increases with the increasing carburizing time, the more negative compressive stresses are obtained on the surface regions of carburized samples. Even though the magnitude of compressive residual stresses is decreasing with the tempering temperature raised from 180°C to 600°C, compressive residual stresses remain on the surface of the 10hrs carburized steel sample.

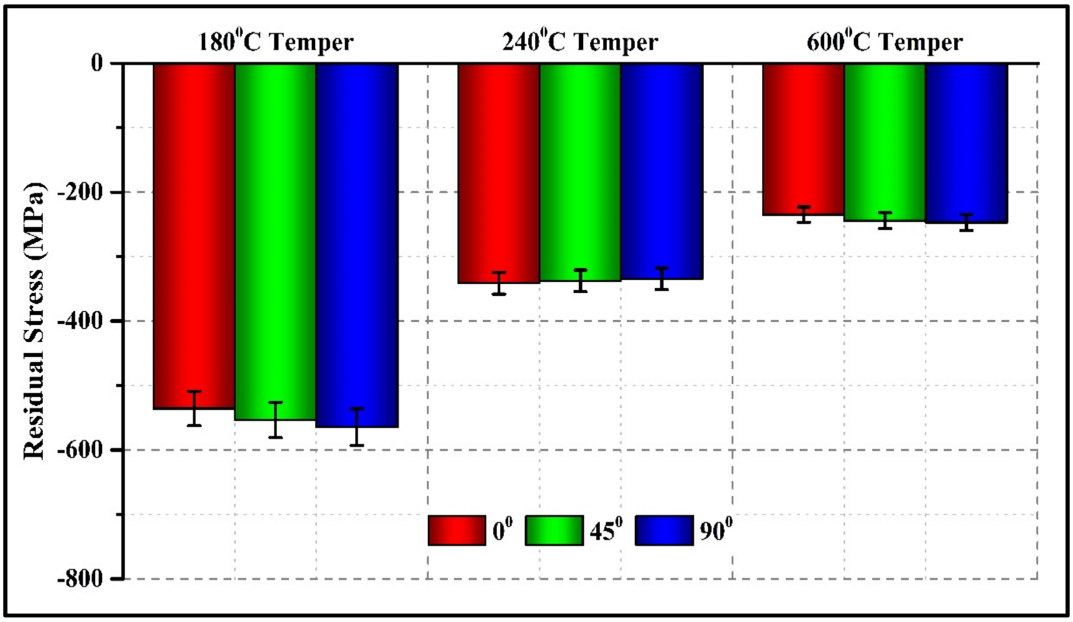

Figure 3.2–3 Effect of tempering on the surface residual stress of the carburized 19CrNi5H steel (900°C/10hrs)

Further increase in the carburizing time leads the ratio between the core and the case thicknesses to increase from 0.18 to 0.32. Therefore, for identical conditions applied to the part, one can expect the formation of more negative surface compressive residual stresses. As seen in Figure 3.2–4, the magnitude of the compressive residual stresses is greater than that of 8hrs and 10hrs carburized samples. For example, the compressive residual stress value is about -750 MPa for 13hrs as-quenched carburized sample, whereas it is about -700 MPa for 8hrs as-quenched carburized sample. Moreover, when tempering temperature varies from 180° to 600°C, surface stress values decrease from about -750 MPa to about -350MPa for 13hrs heat-treated specimen. This trend in lowering compressive residual stresses is valid for three different phi angles. When three different carburized samples are compared, it can be clearly seen that the maximum compressive residual stress is present in the 13hrs carburized 19CrNi5H steel specimens since the ratio between the case and the core thickness is the greatest in those samples.

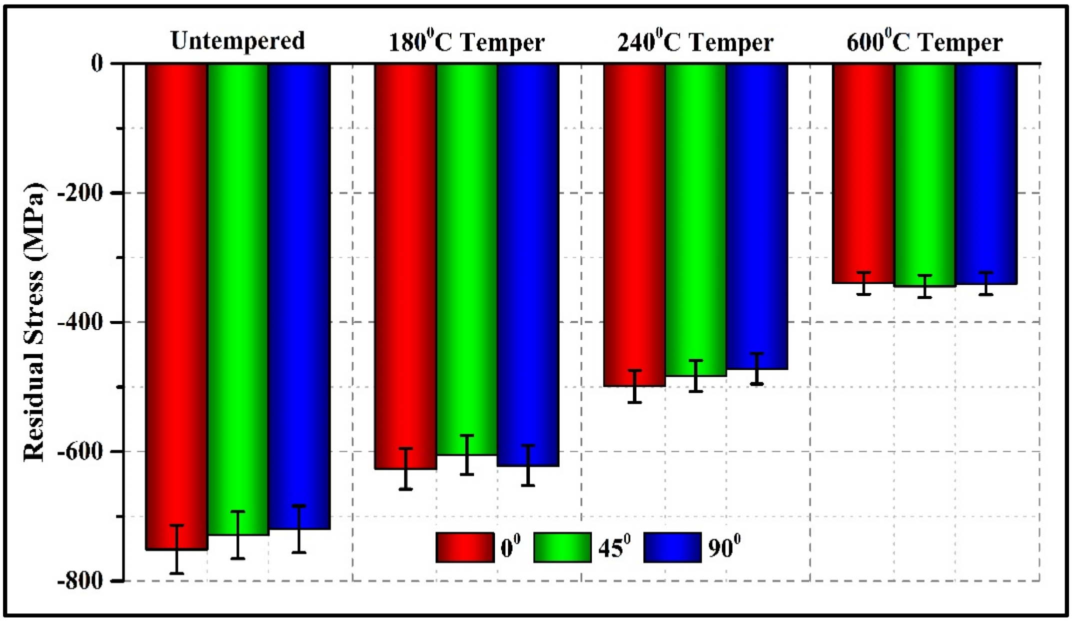

Figure 3.2–4 Effect of tempering on the surface residual stress of the carburized 19CrNi5H steel (900°C/13hrs)

When the carburizing depth increases, the surface compressive stress, also, increases. This is because the magnitude of the compressive residual stress at the surface depends on the ratio between the case and the core thickness. When the other factors are the same, the surface compressive residual stress will be low unless the core is thicker than the case [1]. However, the retained austenite content in the part will be higher due to the thicker case regions. The reason for this is that the area where the retained austenite can form is increased together with the decreasing martensite start temperature. When retained austenite content is considered with the other factors, larger residual compressive stresses are formed when the case hardened depth increases. In the light of this information, when the 19CrNi5H steel is subjected to 13hrs of the carburizing process, the expected compressive residual stress value should be higher than that of 10hrs and 8hrs carburizing process. This effect can be seen from the Figure 3.2–5 that indicates the residual stress measurement parallel to the rolling direction. Although the difference between residual stresses generated in the surface regions is lower for the as-quenched sample, this difference increases when tempering heat treatment is applied.

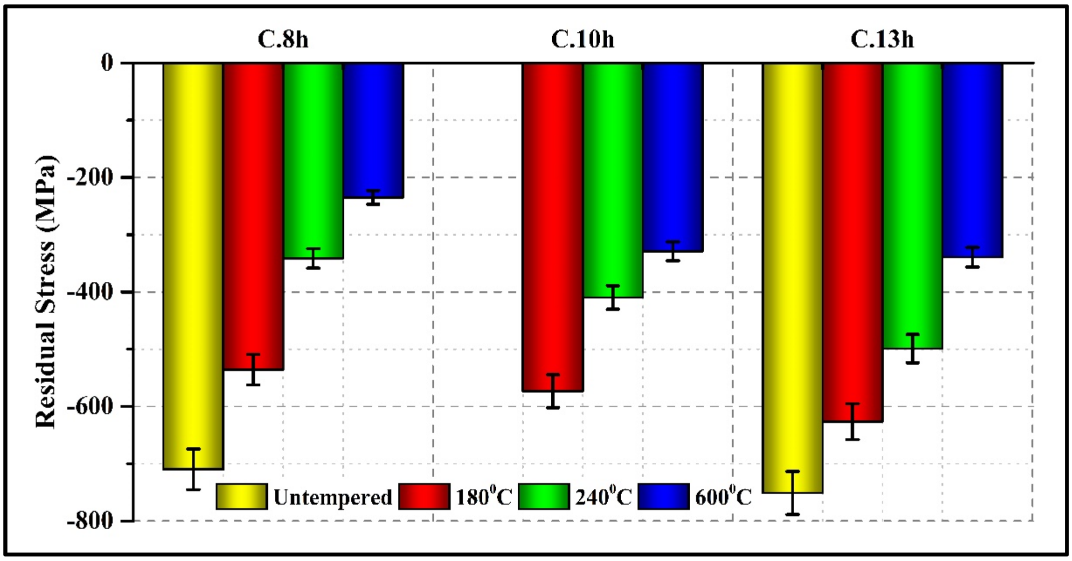

Figure 3.2–5 Effect of tempering on the surface residual stress of the carburized 19CrNi5H steel for 8hrs, 10hrs, and 13hrs

Since retained austenite present in the material after carburizing processes, it is aimed to measure the residual stress induced by this phase. For this measurement, Seifert XRD 3003 PTS system is utilized. By measuring stresses on the gamma phase, out-of-plane stress (σ_{33}) can be determined so that the assumption that is out-of-plane stress is zero will be verified. If the residual stress induced by the retained austenite phase is equal to positive values, then the multiplication of stress by the fraction of retained austenite should be equal to that of the martensite phase. The calculated residual stress on the retained austenite phase is shown in Table 3.2-2.

Table 3.2-2 Average residual stress values for austenite phase in carburized steel sample

	Calculated Residual Stress [MPa]		
Sample #	**Φ=0°**	**Φ=45°**	**Φ=90°**
C.8h-T0	N/A	N/A	N/A
C.8h-T180	-279.3	-364.1	-250.7
C.10h-T180	-382.0	-449.6	-459.3
C.13h-T0	-339.6	-327.4	-352.2
C.13h-T180	-415.1	-451.2	-397.5

Note that the negative sign implies compressive residual stress present

As seen from Table 3.2-2, stress induced by the retained austenite phase is not tensile; hence, assuming the out-of-plane stress as equal zero is not correct. Residual stress measurement in the martensite phase showed ψ-splitting indicating the presence of the strain components ε_{13} and/or ε_{23}. In the light of this information, it is better to keep in mind that the residual stress determined by the bi-axial method from the slope of d vs. $sin^2\psi$ graph contains an error equal in magnitude to out-of-plane stress. For the calculation of the stresses by triaxial stress method, unstressed interplanar spacing should be determined as precise as possible. Since the exact measurement of unstressed lattice placing is not carried out, it is assumed that the out-of-plane stress is equal to zero so that the bi-axial stress method can be utilized to calculate the residual stresses even though there will be an error of the magnitude equal to σ_{33}.

After calculating surface residual stress values for the thermochemical heat-treated steel samples, residual stress depth profile is obtained by removing the layer from the surface by electropolishing for selected steel specimens. Figure 3.2–6 shows how the surface residual stress varies when going from case to core region. It can be clearly seen that the maximum compressive stress state is beneath the surface of the case-hardened steel. This compressive stress state lasts up to depth of 1.3 mm from the surface. By layer removal method, the sample will find a new equilibrium state characterized by a variation in the stress distribution. For X-ray techniques, the change of the stress distribution will affect the determination of the stress depth profile. Therefore, it is important to know true stress depth profile by layer removal. A detailed study has been made by Moore and Evans gives the approximate correction for layer removal if the sample surface electropolished evenly. In addition, the assumption is valid when the layer removal is about 300 µm. Upon further layer removal, a groove may be formed eventually affecting the both layer correlation and stress measurement. In this research, it is seen that residual stress state dramatically alters when the method proposed by Moore and Evans is applied upon 300 µm. Hence, throughout X-ray stress determination in the depth of the sample, layer correction technique is not utilized.

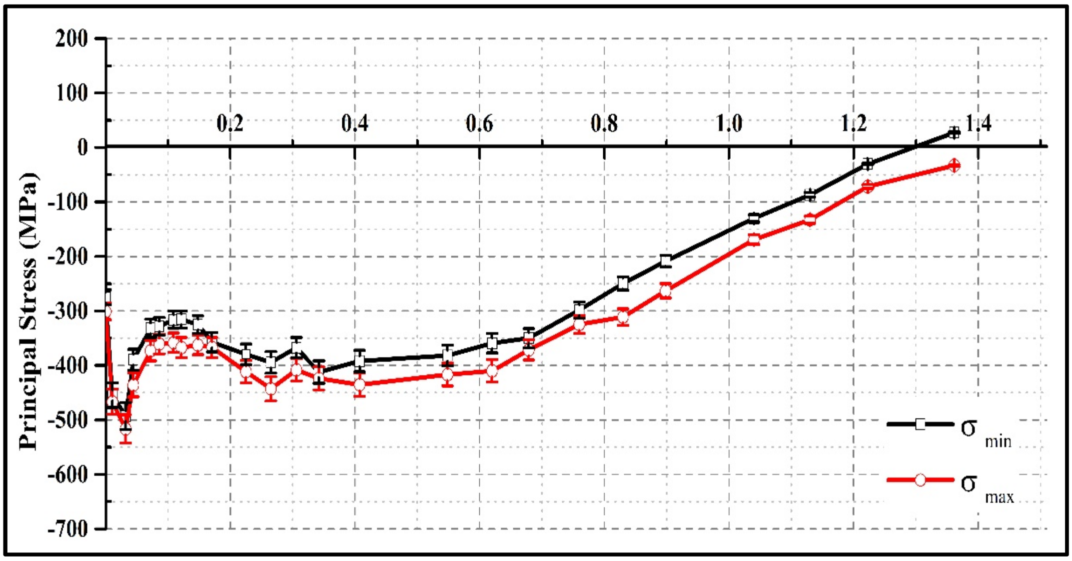

Figure 3.2–6 Residual stress depth profile obtained by XRD method for carburized 19CrNi5H steel (900°C/8hrs): as-quenched

Depth profile analysis is also conducted to 13hrs carburized steel sample, and the acquired results are shown in Figure 3.2–7. In this case, compressive stresses are present beyond the depth of 1.8 mm from the surface of the sample. As compared to previous one (Figure 3.2–6), the maximum stress state is seen at the surface of the sample rather than beneath the surface region.

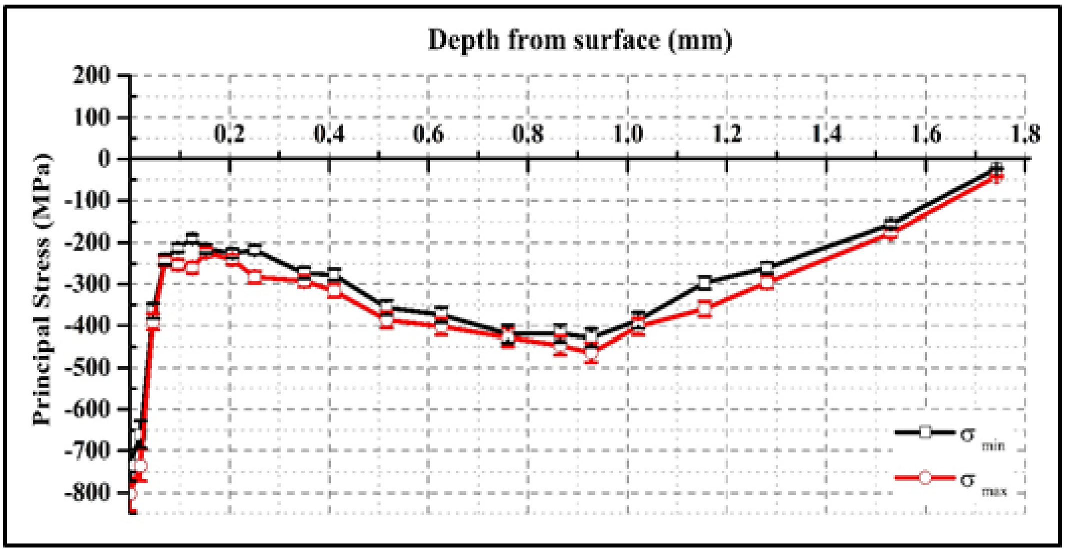

Figure 3.2–7 Residual stress depth profile obtained by XRD method for carburized 19CrNi5H steel (900°C/13hrs): as-quenched

From Figure 3.2–8, it can be seen that the surface residual stresses decrease with the increasing tempering temperatures. It is also seen that the maximum residual stress state exists in the surface region of the as-quenched sample while it is observed in the near surface regions for tempered specimens. Due to the oxide formation and decarburization in tempering operations, the maximum stress states tend to shift towards the core regions.

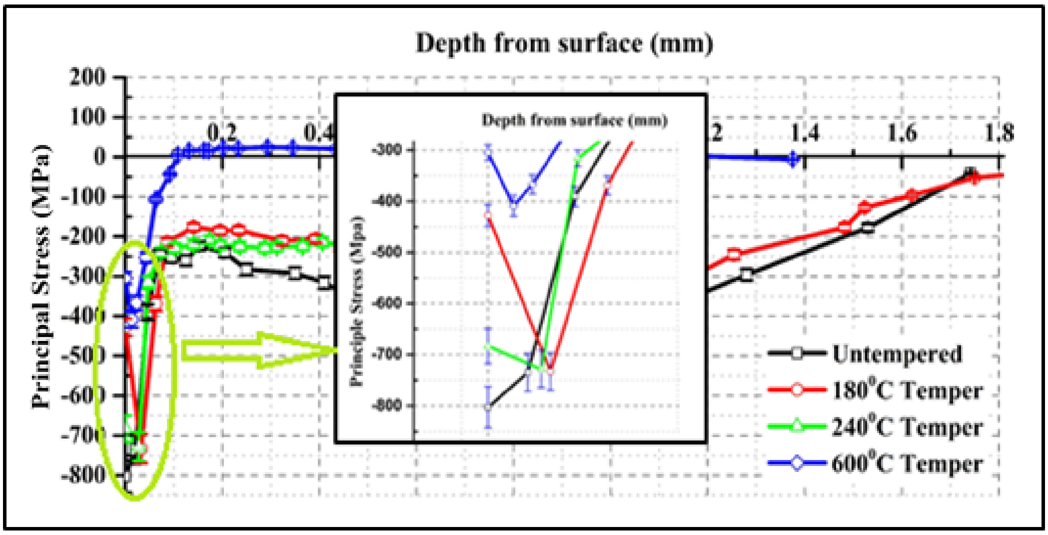

Figure 3.2–8 Effect of the tempering temperature on the depth profile of the residual stresses in the carburized 19CrNi5H steel (900°C/13hrs)

3.3 MAGNETIC BARKHAUSEN NOISE MEASUREMENT RESULTS

3.3.1 Parameter Optimization

Since the Magnetic Barkhausen Noise measurement is sensitive to microstructure, hardness, and the surface residual stress of the sample, parameters used in the BN analysis should be optimized before starting the measurements. The previous studies have shown that there is a relationship between stress state of the material and peak position or RMS of BN signal [90, 96]. Since the residual stress present in the material impedes the domain wall motion, a good linear correlation is expected between the stress state and RMS value.

Figure 3.3–1 shows the Pearson's correlation, known as R2, values of the linear regression analysis executed on all 160 different measurements. The highest values of R^2 are observed for magnetizing frequencies of 150 – 300 Hz and magnetizing voltages of 8 – 16 V_{pp}. Further increase in the magnetizing frequency leads to decrease in the correlation obtained. However, at frequencies of 700 – 900 Hz, higher correlation is again obtained. The magnetizing voltage lower than 8 V_{pp} leads to the lowest R^2 values irrespective of magnetizing frequencies. Hence, it can be deduced that the reliability or the goodness of residual stress correlation of BN emission is greatly affected by the magnetizing voltage used.

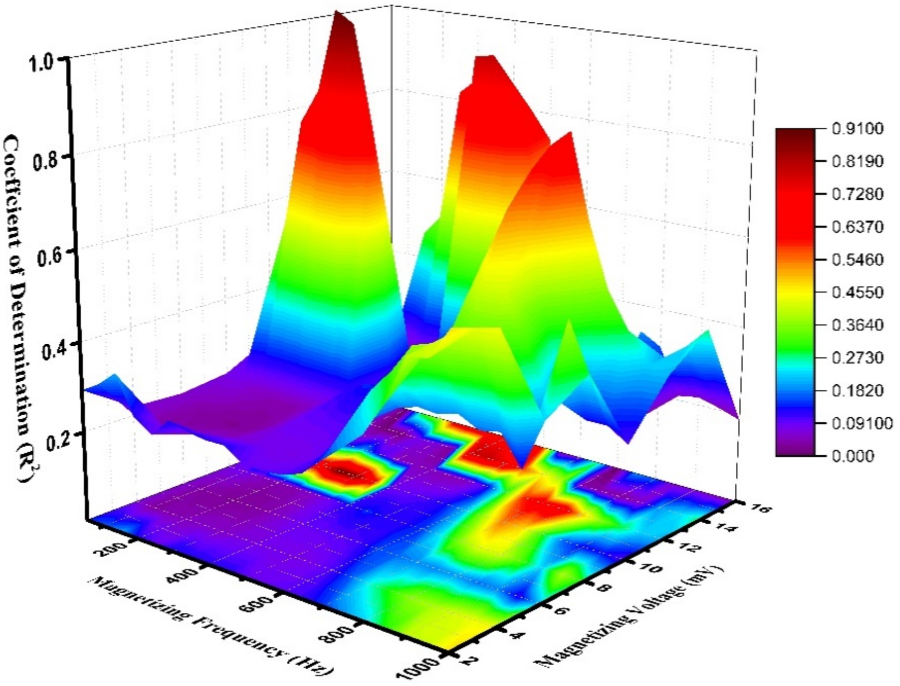

Figure 3.3–1 Pearson's correlation for 160 MBN measurements on the carburized samples

The optimum signal acquired during BN measurement should be so sensitive that the slightest variations in the material properties should be detected. In the present study, the sensitivity index of case-hardened and tempered steel specimens is evaluated using the differences in the BN response to the residual stresses. The 13hrs carburized and only-quenched is chosen as the best response obtained, while the 8hrs carburized and 600°C tempered one is selected as the worst. The sensitivity index, SI, is evaluated by the following equation;

$$SI = 100 \times \frac{\left(RMS_{T600} - RMS_{Quenced}\right)}{RMS_{Quenced}} \tag{3.3-1}$$

The best measurement parameters should maximize the sensitivity index. The calculated sensitivity index can be seen Figure 3.3–2. The highest sensitivity index is acquired between 8 – 10 V_{pp} of magnetizing voltage and 150 – 250 Hz of magnetizing frequency. Then, with voltages of 12 – 16 V_{pp} and with frequencies of 800 – 1000 Hz, sensitivity index is the higher. With these findings, the magnetizing voltage has a pronounced effect on the sensitivity index as in the correlation.

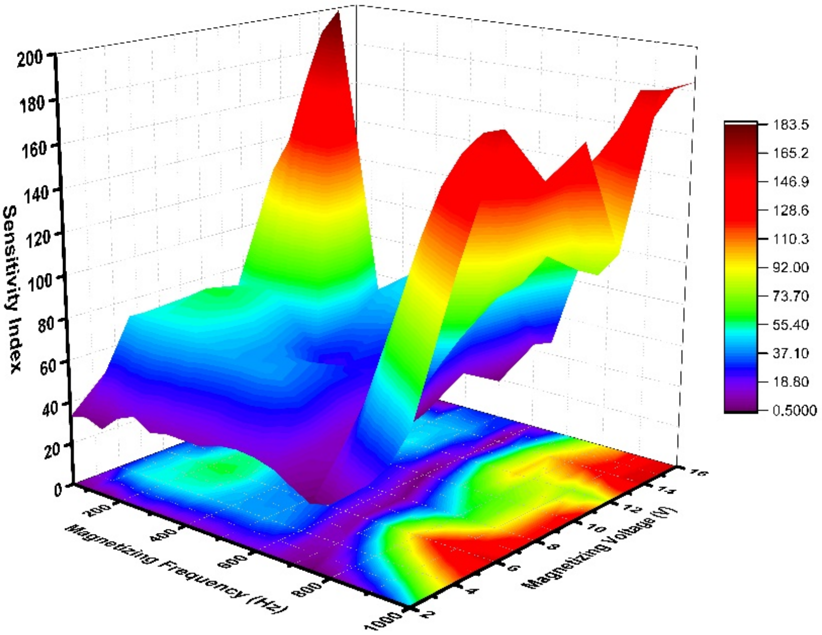

Figure 3.3–2 Sensitivity Index values of 160 MBN measurements on the carburized samples

A valid BN measurement should mainly consist of the noise related to the Barkhausen phenomenon. Therefore, the inherent symmetry of the magnetic hysteresis will be used to evaluate the validity of BN emission. Identical Barkhausen noise should be obtained regardless of externally applied magnetic field due to the inherent symmetry of the magnetic hysteresis. When the process is entirely symmetric, positive and negative values of RMS should be equal to each other. In this study, this inherent symmetry is calculated as validity index;

$$VI = 100 \times \frac{\left| RMS_{positive} - RMS_{negative} \right|}{RMS_{avg}} \tag{3.3-2}$$

The validity index should be zero for an ideally symmetric BN burst that is generated by the correct sets of measurement parameters. Figure 3.3–3 shows the calculated validity index values for 13hrs carburized and only-quenched sample. The lowest index values are observed for magnetizing frequencies of 0 – 250 Hz and 800 – 1000 Hz. When considering the validity index, it is seen that the magnetizing frequency has a significant influence on it rather than the magnetizing voltages.

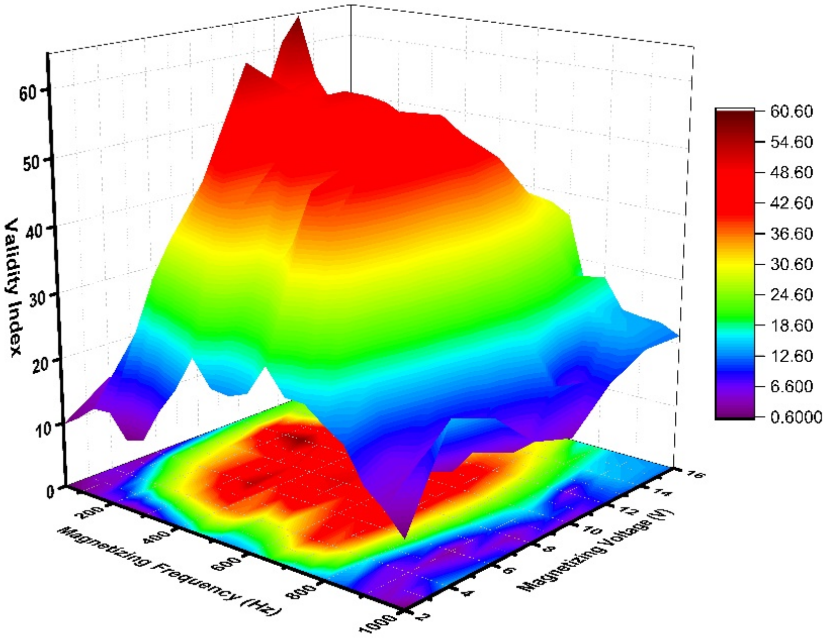

Figure 3.3–3 Validity index values of 160 MBN measurements on the carburized samples

Three different indicators are considered for the parameter optimization of the BN emission. Nevertheless, those indicators cannot be maximized by single sets of measurement parameters at the same time. To select the most optimized measurement parameter, all three indicators are considered together by the voting formulae of the following;

$$Score = 100 \times \frac{\left(aR^2 + b\left(\frac{SI}{SI_{\max}} \right) + c\left(\frac{VI_{\max}}{VI} \right) \right)}{a+b+c} \tag{3.3-3}$$

where SI_{max} and VI_{max} are the maximum obtained value of sensitivity and validity indexes within the carburized steel samples and the constants a, b and c are the weighting coefficient that a is equal to 0.5, b equals to 0.3 and c is 0.2.

The score value is limited to a range between 0 and 100; hence, all datasets can be compared to each other directly irrespective of the three indicators. Figure 3.3–4 shows the calculated score values that can be used in the Magnetic Barkhausen Noise measurement. It can be seen from the illustration that the maximum score value is obtained in the magnetizing frequency range of 150 – 250 Hz and in the magnetizing voltage range of 8 – 10 V_{pp}. The highest score value is obtained for 10 V_{pp} with 250 Hz magnetizing frequency.

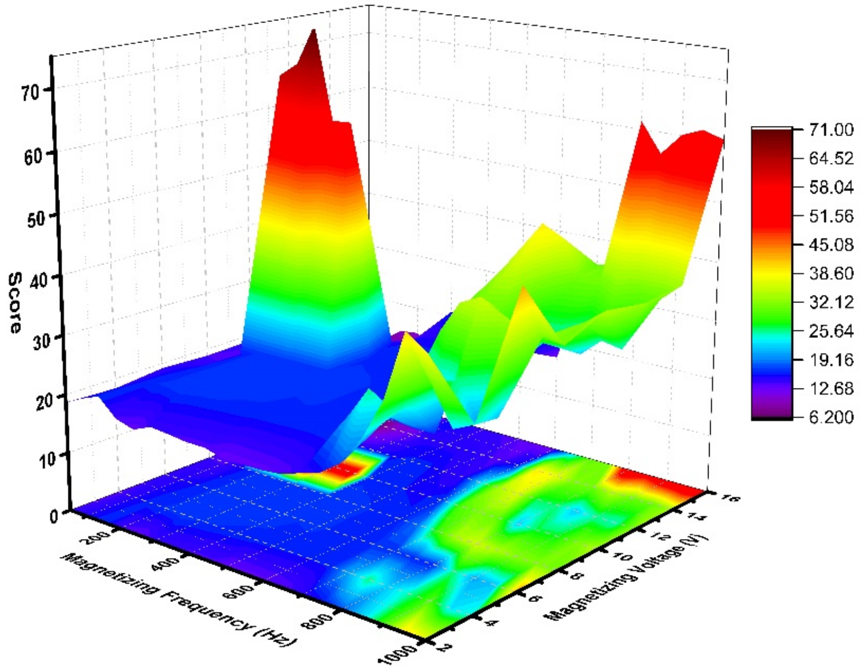

Figure 3.3–4 Calculated score values for parameter optimization of the MBN measurement

The parameter optimization is showed that Magnetic Barkhausen Noise measurement carried out with the magnetizing voltage of 10 millivolts, and the magnetizing frequencies of 250 Hz will give the most reliable results on the carburized steel samples.

After finding the optimum parameter to generate the BN signal, the next aim is to clarify the filtering of the obtained data. In the decision of the filtering range, the main concern is to correlate the residual stress measured by X-Ray Diffraction with the Magnetic Barkhausen Noise measurement. Therefore, it is aimed to collect data with the MBN technique as close as possible to XRD technique. Equation 1.3-1 is used to determine the filtering range by putting μ_r equal to 200 for carburized sample and the electrical resistivity of 34.2 μΩ·cm. By using the equation, it is found that the depth of penetration of BN signal is about 60 µm for 200 kHz and 20 µm for 1000 kHz frequencies. Hence, the filtering of the frequency is chosen from 200 kHz to 1000 kHz.

3.3.2 Rollscan Results

After the optimizing, the measurement parameters, the average root mean square values obtained by using the optimized parameters for different carburized and tempered steel samples can be seen in Table 3.3-1. Tabulated data summarizes the obtained values for RMS for three different measurement directions.

From Table 3.3-1, it can be seen that normalized sample has the greatest RMS value in all direction when compared with the heat-treated samples. Moreover, RMS value of the Barkhausen noise signals changes with the changing angle of direction and with the tempering operations for carburized specimens. Variations in RMS values of each measurement directions were caused by the variations in the residual stress distribution in those directions. Martensite and spheroidized phases also affected the acquired RMS value in the samples compared to a normalized sample having ferritic-pearlitic phases.

Table 3.3-1 Average root mean square values of the MBN measurement

	MBN measurement direction		
Sample #	**0°**	**45°**	**90°**
Normalized	1025.7	830.4	563.0
C.8h-T0	97.2	106.0	110.4
C.8h-T180	185.7	188.6	220.7
C.8h-T240	270.5	248.0	222.6
C.8h-T600	456.0	455.0	453.4
C.10h-T180	168.6	173.6	162.2
C.10h-T240	217.2	236.3	277.6
C.10h-T600	414.2	412.8	385.4
C.13h-T0	90.6	96.68	96.28
C.13h-T180	117.9	118.0	159.2
C.13h-T240	203.2	175.1	331.0
C.13h-T600	376.4	381.1	361.5

As it can be seen in Figure 3.3–8, the minimum RMS value is acquired from the as-quenched 8hrs case hardened steel sample for each measurement directions since the compressive residual stress decreases the BN activity of the sample. When the tempering temperature increases, the BN activity is growing too. With the tempering operations, martensite transforms to tempered martensite and so the hardness of the sample decreases. This decline in the hardness value leads the dislocation density to decrease. When the dislocation density is reduced, the pinning sites that impede the domain wall motion is removed from the system that lower magnetic field is required for domain wall movement. Within the carburized samples, average RMS value is increasing when the tempering temperature is raised from 180°C to 600°C, so the maximum value is obtained by the highest tempering temperature.

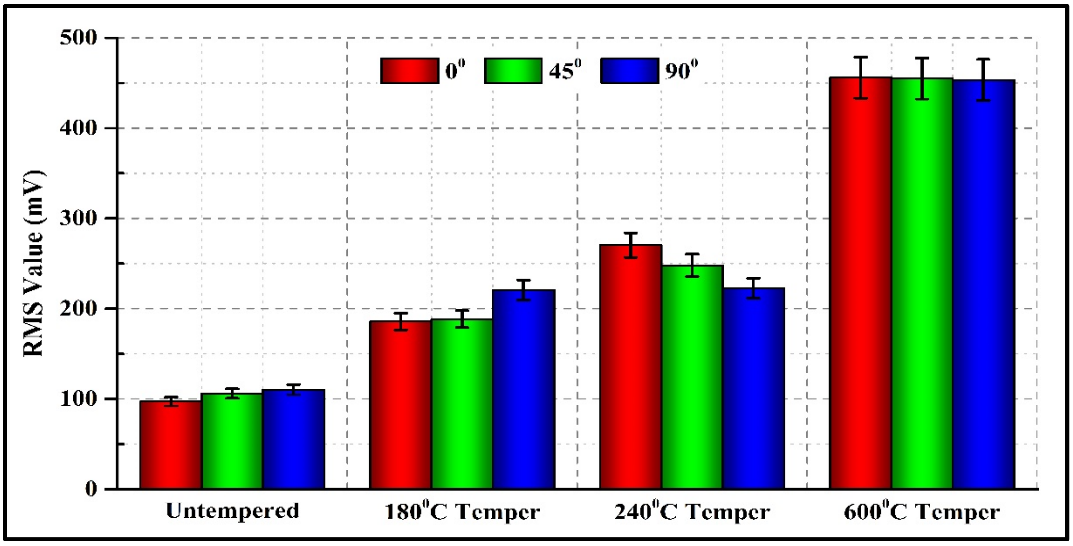

Figure 3.3–5 Effect of tempering temperature on the average RMS values of Barkhausen Noise for carburized 19CrNi5H steel (900°C/8hrs)

When the duration of the carburizing process rose to 10hrs, the relative RMS value obtained in each measurement direction decreased compare with the 8hrs carburized samples, which can be seen in Figure 3.3–6. XRD measurement revealed that compressive residual stresses were more negative for a longer period of carburization process. It is also known that an increase in the compressive stress results in the decrease in the RMS value of the BN signal.

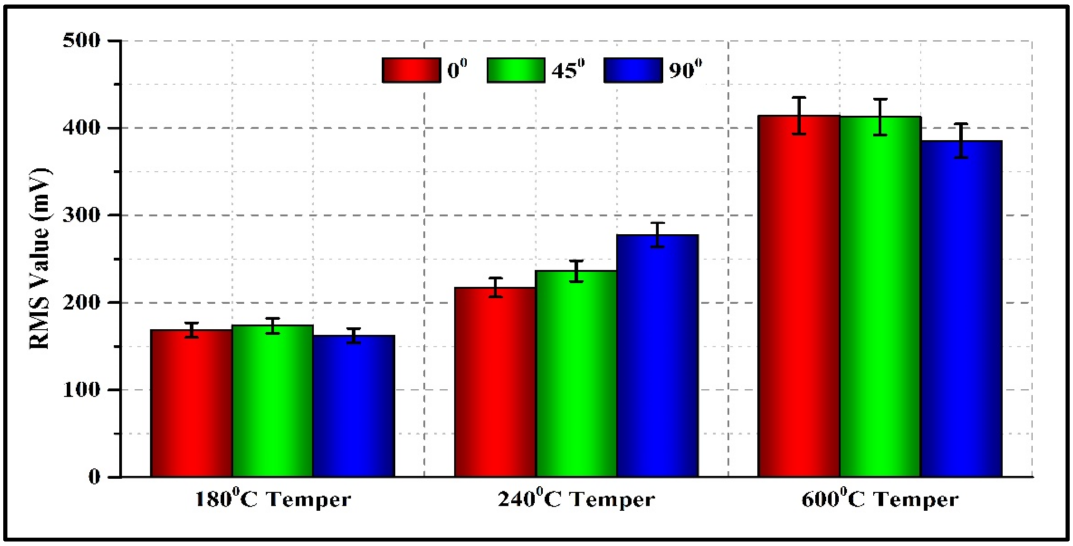

Figure 3.3–6 Effect of tempering on the average RMS values of Barkhausen Noise for carburized 19CrNi5H steel (900°C/10hrs)

Further increase in the duration of the carburization operation led RMS value to decrease as seen in Figure 3.3–7. Since the dislocation density increased with the increasing duration of operation, motion of the domain walls impeded more causing lower RMS value. As in the other samples, RMS values increased upon the tempering operation since martensite lost its tetragonality. The highest RMS value was obtained in the 600°C tempered steel sample.

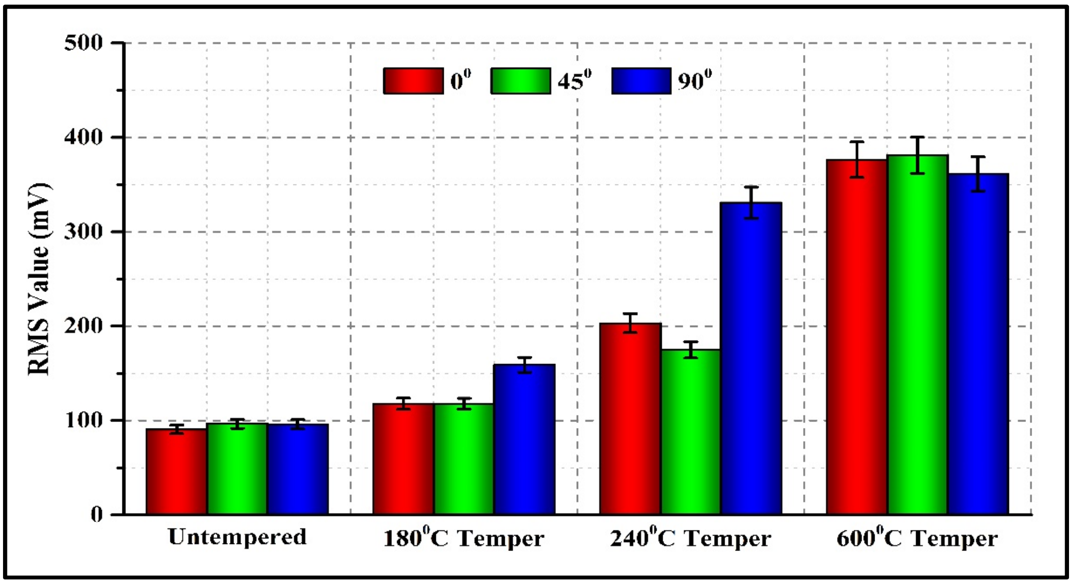

Figure 3.3–7 Effect of tempering on the average RMS values of Barkhausen Noise for carburized 19CrNi5H steel (900°C/13hrs)

When the three different case hardened sample is compared, 13hrs carburized steel sample has the lowest average RMS value among the rest of carburized samples when the tempering condition is kept same (Figure 3.3–8). The reason is that 13hrs carburized sample has the lowest compressive residual stress, as well it is the hardest sample. The combined effect of two properties leads to obtaining the lowest average RMS values in 13hrs carburized specimen. It can be deduced from these results that there exists a correlation between the compressive stress state and the average RMS value of BN signal for these sets of samples.

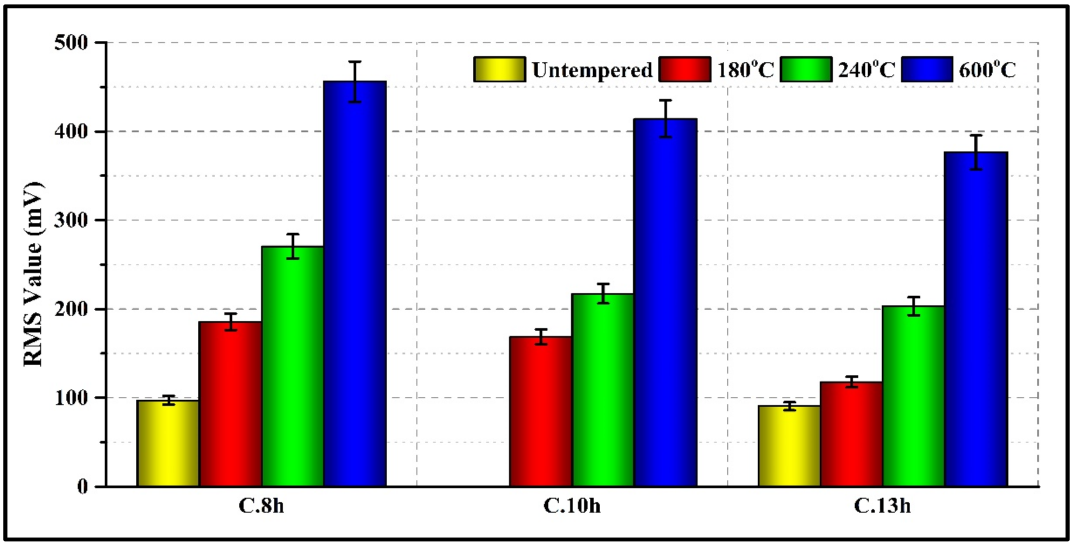

Figure 3.3–8 Effect of tempering and carburizing time on the average RMS values of Barkhausen noise emission of the samples carburized at 900°C for different periods

3.3.3 µScan Measurement Results

3.3.3.1 Barkhausen Noise Signal Envelope

Upon the application of an alternating magnetic field, a magnetic hysteresis loop is generated in the volume of the material due to the energy loss associated with the irreversible magnetization process related to nucleation, annihilation, and growth of domains. Grain or lathe boundaries, dislocations, and precipitates influence this process. As a result, Barkhausen noise peak height is identified by the number of moving domain walls at a given time and the mean free path of the domain wall motion.

Barkhausen noise emissions, which are in the form of voltage pulses, are detected by the pick-up coil positioned close to the surface of the material. The amplitudes of such pulses are dependent on the microstructure and the residual stress state of the material. The root mean square (RMS) value of the signal is the output of the µscan measurements. The average Barkhausen activity is assigned by the RMS voltage acquired by averaging the BN signal over the time required for magnetization reversal.

The relative RMS voltage as a function of relative magnetic field strength obtained for the quenched and tempered after carburizing of 19CrNi5H steel can be seen in Figure 3.3–9. Due to the symmetry with respect to zero magnetic field, only $RMS_{positive}$ curves are plotted. The normalized steel sample has the maximum amplitude, whereas the amplitude is decreasing with an increasing carburization time that the minimum amplitude is obtained in the C.13-0 sample. The lowest peak is positioned at the highest magnetic field strength values due to the high coercivity of martensite. Furthermore, the peak position of the Barkhausen signals shifts to the lower values of magnetic field strength owing to the tempering operations. Upon an increase in the tempering temperatures, the lowest amplitude broad peak of only-quenched carburized steel shifts to the higher amplitude peak positioned at low magnetic field strengths. For example, for 8hrs carburized steel sample, the peak position of the signal is located at the 5.80 percent of the magnetic field for only quenched steel. By increasing of tempering temperature from 180°C to 600°C, the peak position shifts to 5.70%, 5.20% and -14%, respectively. These peak shifts are valid for all other carburized samples whether it is small or large. The results clearly indicate that BN signal is influenced by the tempering operations as dislocation density changes as a function of tempering temperature and the residual stresses are relaxed.

In the as-quenched state, the domain structure is determined by the body centered tetragonal structure of the martensite phase. The relative volume occupied by a domain wall is greater in virtue of minuscule domains in the magnetic structure. In addition, high dislocation density in the martensite phase impedes the domain wall movements. The combination of these two reasons as well as micro residual stress in the martensite leads a strong field to be required for the reversal of magnetization.

Tempering operations at 180°C have a slight effect on the microstructure so that the peak position and the amplitude of the signal do not change significantly. At 240°C, martensite start to lose its tetragonality and the dislocation density is reduced.

Domain nucleation and domain wall movements take place at lower magnetic field strengths. Since the domain wall movements are easier, the peak amplitudes increase. In all samples, when the tempering temperature is raised to 600°C, peak amplitudes increase drastically and shift clearly to lower magnetic field strength values since the morphological changes in the structure and almost complete relaxation of residual stress occurs.

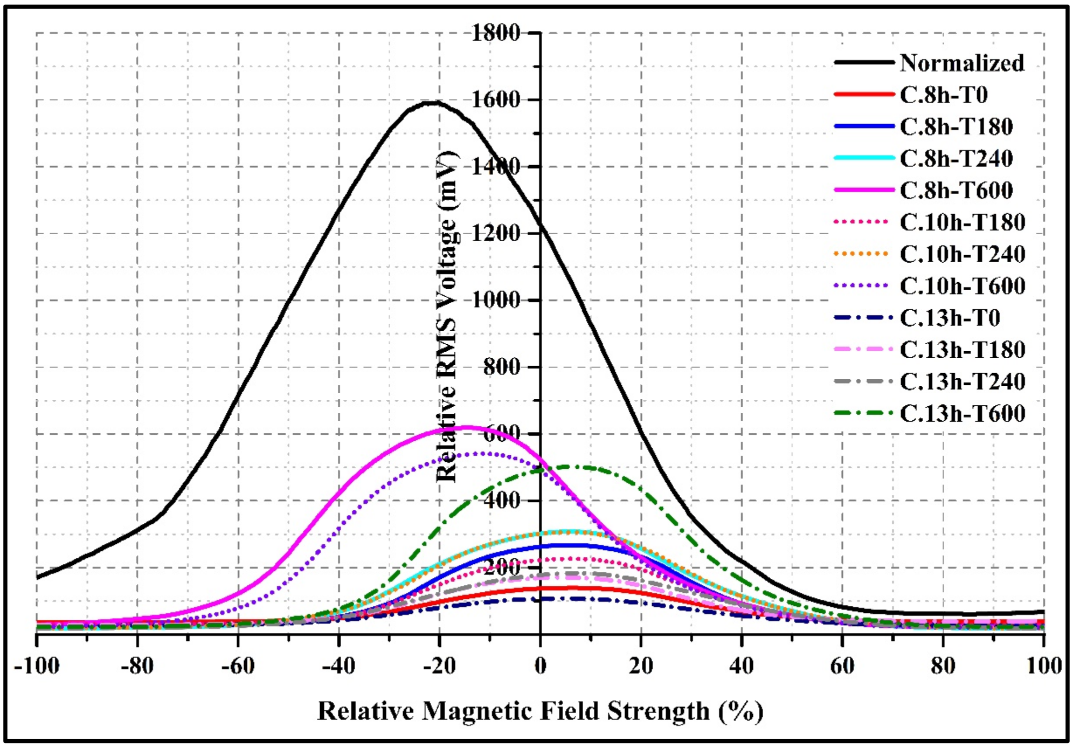

Figure 3.3–9 The relative RMS voltage as a function of relative magnetic field strength for the normalized and carburized 19CrNi5H samples

3.3.3.2 Representative Hysteresis Curve

Stress state and the structural conditions (e.g. precipitations, texture, and dislocation density) of the material have an effect on the magnetic hysteresis curve. Several hysteresis curve properties, such as coercivity in which the maximum Barkhausen activity occurs, remanence, initial permeability, can be obtained from the Barkhausen Noise measurement.

Under constant or zero applied magnetic fields, the domain wall may overcome the pinning site if the internal field is large enough to break away the pinning force. However, for those domain walls that remain pinned by the constant stress, the energy needed to overcome the pinning site depends on the stress state due to the differences in the magnetoelastic energies of the domain walls. Consequently, coercivity and remanence values of the material change with the applied stress. For materials with positive magnetostriction energy such as iron, both the coercivity and the remanence increase with the tension but decrease with the compression. If the magnetostriction energy is negative as in the nickel, magnetic properties exhibit the opposite dependence on the stress. Table 3.3-2 shows the effect of the residual stress on the coercivity and the remanence of the 19CrNi5H steel. Stress dependency of both the coercivity and the remanence is affected by the material showing either soft or hard magnetic behavior. Since 19CrNi5H shows hard magnetic behavior, both properties increase with tension. However, for soft magnetic materials, coercivity decreases with the tension, while remanence increases.

Table 3.3-2 Coercivity and Remanence values obtained from magnetic hysteresis curve of carburized 19CrNi5H steel

Sample #	Coercivity	Remanence
Normalized	0.240	2035.7
C.8h-T0	0.022	29.3
C.8h-T180	0.034	60.4
C.8h-T240	0.050	74.6
C.8h-T600	0.146	460.5
C.10h-T180	0.026	49.4
C.10h-T240	0.038	62.4
C.10h-T600	0.142	391.3
C.13h-T0	0.018	19.9
C.13h-T180	0.026	42.3
C.13h-T240	0.038	62.1
C.13h-T600	0.118	372.4

Magnetic hysteresis loop obtained by µscan measurements for the carburized and tempered steel specimens are given in Figure 3.3–11. As seen in the figure, normalized sample shows hard magnetic behavior so that a significant fraction of the saturation field remains in the material when the magnetic field is removed. The normalized sample has higher coercivity values since the domain wall motion is easier due to the lack of pinning sites.

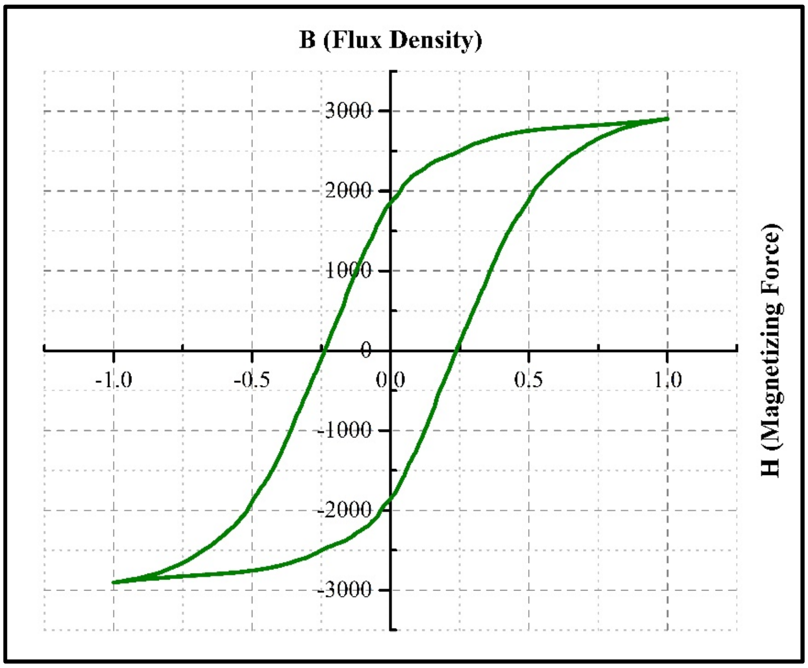

Figure 3.3–10 Magnetic hysteresis curve for the normalized 19CrNi5H steel

In the carburized and tempered samples, coercivity values are lower than that of the normalized specimen due to the pinning of the domain walls in the presence of martensite phase (Figure 3.3–11). Since the differences in coercivity values are not so significant for carburized samples, remanence values may be more suitable to characterize the stress dependency of the magnetic hysteresis curve. From the figure, it is also seen that the decrease in the compressive residual stress shifts the hysteresis curve to the more vertical position.

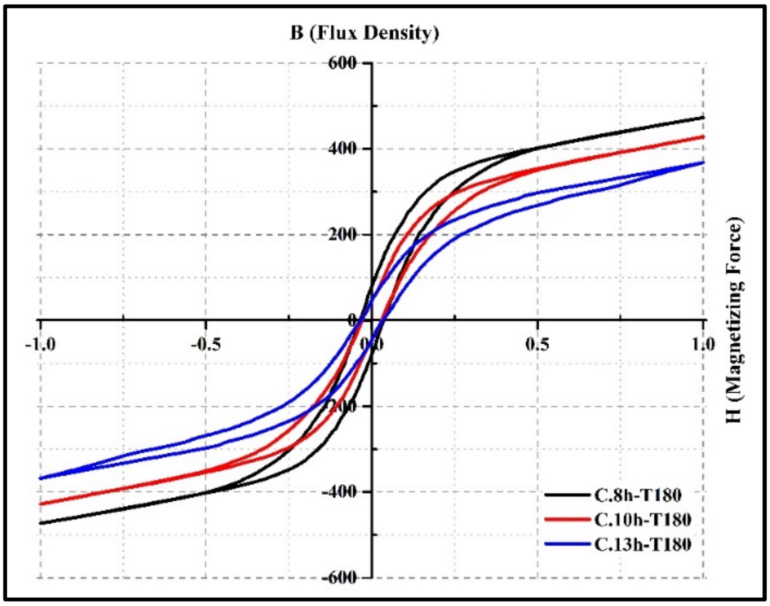

Figure 3.3–11 Magnetic hysteresis curve for the carburized and tempered 19CrNi5H steel

Figure 3.3–12 shows the hysteresis curve of 13hrs carburized specimens. An increase in the tempering temperature results in higher remanence values for 13hrs carburized steel as well as 8hrs and 10hrs carburized ones. The quenched structures consist of large amounts of crystal defects to be eliminated. During tempering, remanence of the steel is increased by getting rid of these defects promoting an atomic rearrangement. It can be seen from the figure that the remanence of the material increases dramatically when the tempering temperature is reached to 600°C.

The differential permeability of the steel is increased with the increasing tempering temperatures. Relative to the other materials, the material has the lower magnetic permeability when the hysteresis loop is wider. When the temperature increases, magnetic softening happens together with the mechanical softening of the microstructure. The increase in the mobilization of the domain walls leads to magnetic softening. It is expected that the easier domain wall movement raises the differential permeability of the tempered structures.

The area enclosed by the hysteresis curve called as hysteresis loss increases with increasing tempering temperatures. The loop area is defined as the magnetic energy dissipated per unit volume when the material is completely cycled around the hysteresis. When the material consists of defects impeding the domain wall movements, these defects induce local energy minima upon the intersection between domain walls and defects. Therefore, the extra energy is needed to overcome the local energy minima that result in hysteresis loss. With the decrease in the tempering temperature, dislocation densities increase so that the hysteresis loss increases. In addition, magnetostriction constant usually very small reduces with the increasing temperature. Although the direct effect of it is small, the shape of the hysteresis curve, and the permeability changes with changing magnetostriction.

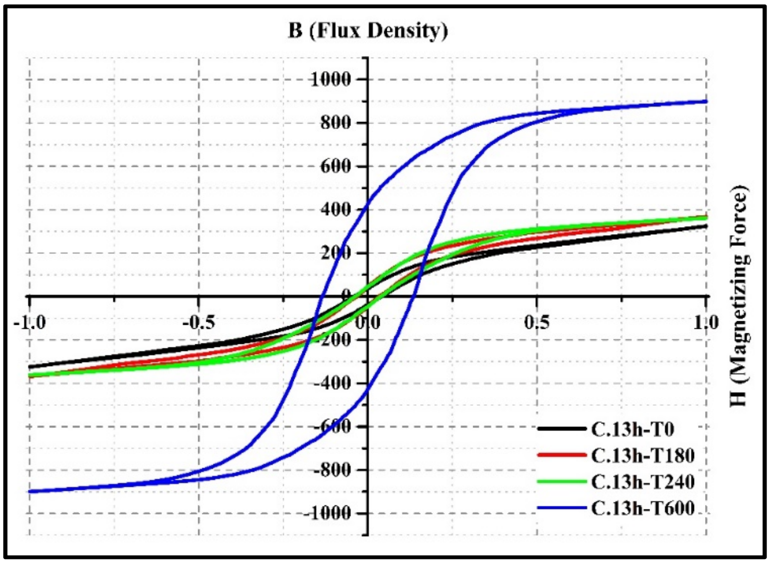

Figure 3.3–12 Magnetic hysteresis curves for the carburized samples (900°C/13hrs)

3.3.3.3 Correlation of the Results Obtained by XRD and MBN Methods

In this part of the study, RMS values obtained from Barkhausen noise measurement will be compared with the residual stress values obtained from the X-Ray Diffraction measurements. If the parameter optimization process is done correctly, BN measurements should give good correlation with the XRD measurement. However, there will be an error in the correlation no matter how good the optimization is as the focused and data obtained areas are different for two methods.

Figure 3.3–13 shows the correlation between BN emission and XRD method for 13hrs carburized steel sample, whereas the correlation for those 8hrs and 10hrs can be seen in Appendix B. The Pearson’s correlation found for the measurements are ranging between 0.92 and 0.94. These values show that there may exist very strong positive linear relationship between the relative root mean square values of MBN and the measured surface residual stress values. In other words, relative RMS values increase when the magnitude of compressive residual stresses is decreasing. However, it is also seen from Figure 3.3–13 that all data used to find linear correlation do not lie within the 95% confidence band. In the light of this information, it can be said that RMS values cannot be directly used for the determination of residual stress state although the linear correlation is very strong between two variables. In addition, the prediction of the residual stress values from measured RMS is only valid within the 95% prediction band. In other words, the residual stress values staying out of this band cannot be predicted. Hence, the here-presented correlation is valid only for the present 8hrs, 10hrs and 13hrs carburized of 19CrNi5H steel at 900°C. When the carburizing conditions and/or steel type changes another correlation has to be found.

Since the correlation is not perfect between the two variables to predict the residual stress, it can be deduced that Barkhausen emission signal is dependent on the other factor and/or factors in the steel specimens. The measurement uncertainty in Barkhausen Noise method can be due to heat treatment applied to the specimens. The retained austenite content in the structure may also affect the Barkhausen noise signal since the austenite phase is not magnetic. The difference between the retained austenite content of specimens used for calibration and measurement may lead to measurement uncertainty in the present study. The measurement uncertainty can result from the heat treatment applied and/or the variations between the specimens used for calibration and measurement. Since carburizing heat treatment is the main consideration in this study, it is needed to be carried out in more controlled way for accurate prediction of the residual stress values

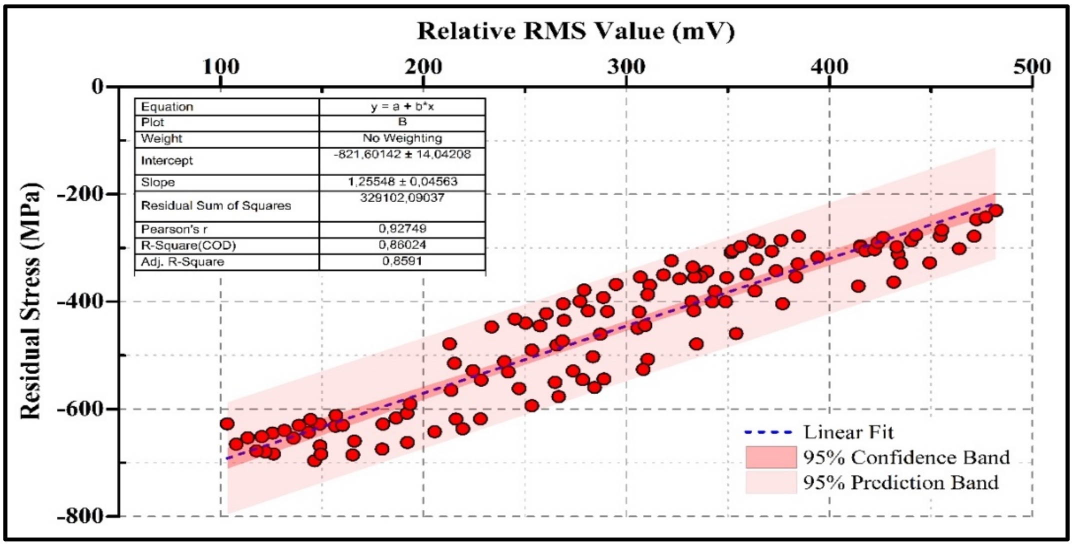

Equation	y = a + b*x
Plot	B
Weight	No Weighting
Intercept	-821,60142 ± 14,04208
Slope	1,25548 ± 0,04563
Residual Sum of Squares	329102,09037
Pearson's r	0,92749
R-Square(COD)	0,86024
Adj. R-Square	0,8591

Figure 3.3–13 Correlation between residual stress and RMS values for carburized 19CrNi5H (900°/13hrs)

3.4 ESPI HOLE-DRILLING MEASUREMENT RESULTS

All ESPI assisted hole-drilling measurements are taken along the centerline of each carburized sample. Measurement points are taken at a distance of 20 mm away from edges of a rectangular in shaped sample, which is the same location used in another residual stress measurement. They, also, are at least 50 mm apart from each other not to affect the area of deformation used in the residual stress calculation. Figure 3.4–1 indicates the measurement point location. More than one measurement are performed in each sample in order to check whether the results are consistent throughout the sample, and the differences in surface condition around the point of interest affect the stress results. As seen in Figure 3.4–1, the surface of the sample is spray-painted with matte white to get rid of reflective sample surfaces.

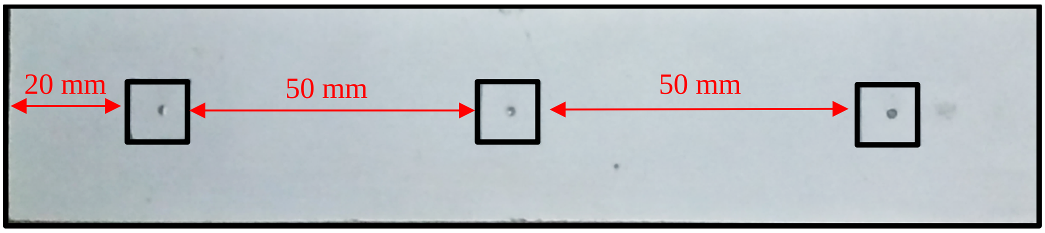

Figure 3.4–1 ESPI assisted hole-drilling measurement points

Residual stresses are calculated from the deformation data, known as the interferograms, by using the *PRISMS*® software, which is developed by Stresstech Group. The residual stress analysis method is based on the method developed by Nelson *et al.* and Steinzig *et al.*, as described in the Section 1.5.2 in the present study. When the residual stress state is calculated for each measurement, the graphs of residual stress versus drilled depth are plotted. During the ESPI assisted hole-drilling measurement, one sample was chosen from carburized and tempered steel groups so that thirteen samples were hole-drilled with ESPI system since the measurement takes long hours.

Fringe patterns obtained at various hole depth increments for the 8hrs carburized sample can be seen in Figure 3.4–4. Since single ESPI system is used, fringe patterns acquired during the hole-drilling are formed on the horizontal x-axis plane around the hole. The inclination of the sensitivity vector in the positive x-direction leads to the unsymmetrical fringe shapes in the measurement. The brighter fringes indicate the half-wavelength increments in the component of the measured surface displacements in the sensitivity direction. The pixels adjacent to the hole within the inner dashed circle, seen in Figure 3.4–2 (100µm depth), are excluded from the stress calculation since the plastic deformation around the hole causes de-correlation between pre- and post-dole images. Furthermore, the shapes beyond the outer dashed circle are not considered in the calculation since they are far away from the hole with low data content. Therefore, defining the inner and outer circle is crucial in the residual stress measurement. To stay in the safe zone, inner radius is defined as two, while the outer radius is chosen as four because of the calculation area. Moreover, interferograms indicate that there are not errors related to unwrapping in the patterns. As seen in Figure 3.4–2, fringe patterns do not form in the vertical direction of the drilled hole since the system used in the experiment is sensitive only to the horizontal direction. In addition, interferograms are smaller in diameter and single pattern forms in each hole depth increments.

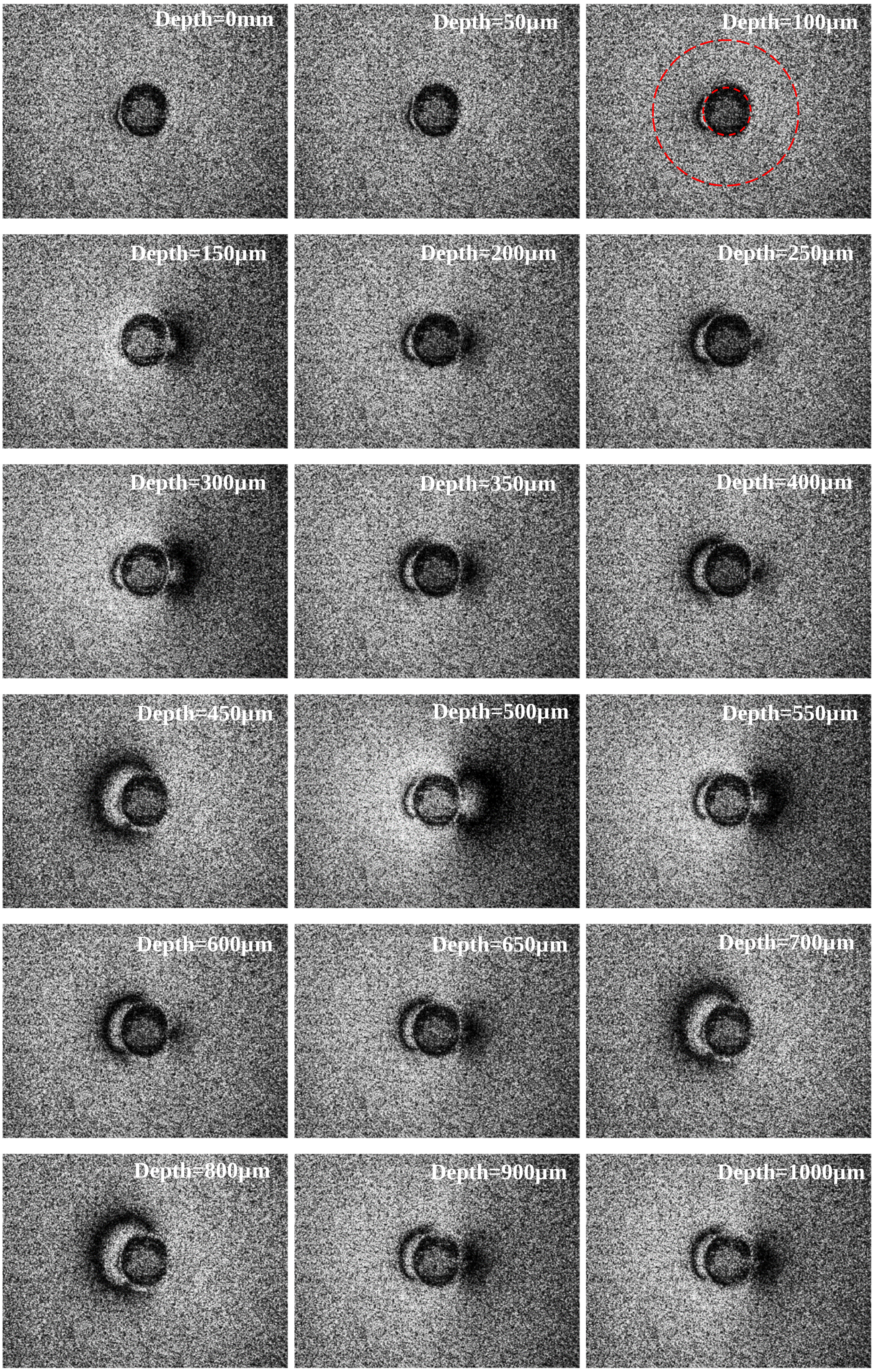

Figure 3.4–2 Fringe pattern of normalized 19CrNi5H steel (880°C/3 hrs)

Figure 3.4–3 shows the calculated stresses for normalized 19CrNi5H steel heated to 880°C for three hours. Tikhonov regularization as in the strain gauged hole-drilling method is used in the ESPI system to correct the zig-zag pattern of the residual stress pattern. Non-uniform stress state due to the variations in the cooling rates of the interior and surface of the steel is generated by the thermal contraction. During the cooling of the steel samples from elevated temperatures, the outer part of the sample cools prior to the inner surface. This cooling causes contraction of the surface and compressing the inner region. When thermal compensation between the inner and the outer region is ensured, inner region tries to contract, but this contraction impedes by already transformed the surface region. Therefore, tensile residual stresses formed on the outer region, while compressive residual stresses are created in the inner regions.

As it can be seen Figure 3.4–3, tensile residual stresses are present in the surface of the sample. These tensile stresses are compensated by the compressive residual stresses in the core regions. Tensile to compressive stress transition point is about 0.4 mm away from the surface of the sample. It should be noted that the ESPI assisted hole-drilling method is sensitive to the stress in the horizontal axis though there is a good correlation between σ_{xx} and σ_{yy} stress state.

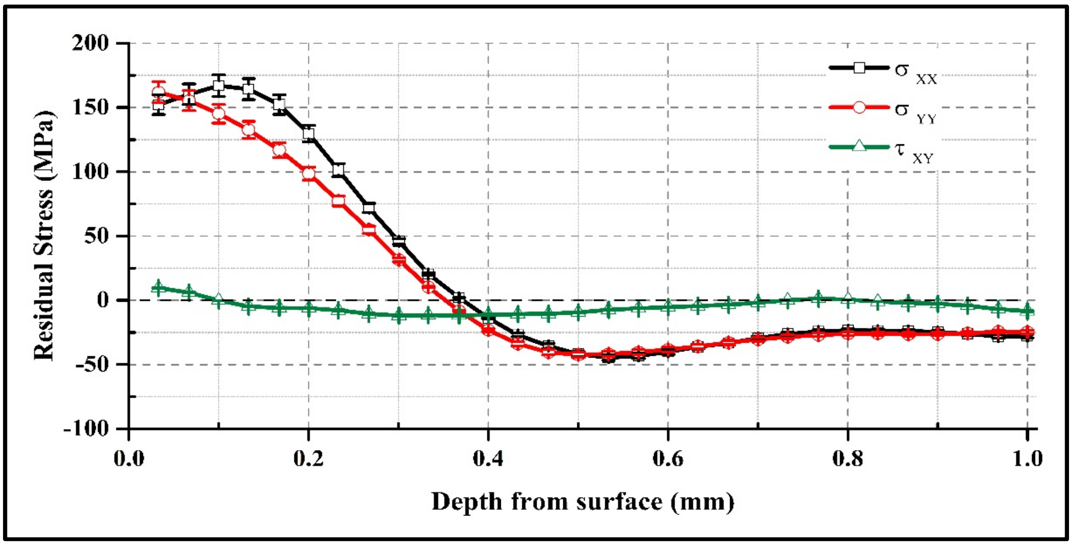

Figure 3.4–3 Depth profile of the residual stress state obtained by ESPI assisted hole-drilling (after normalizing)

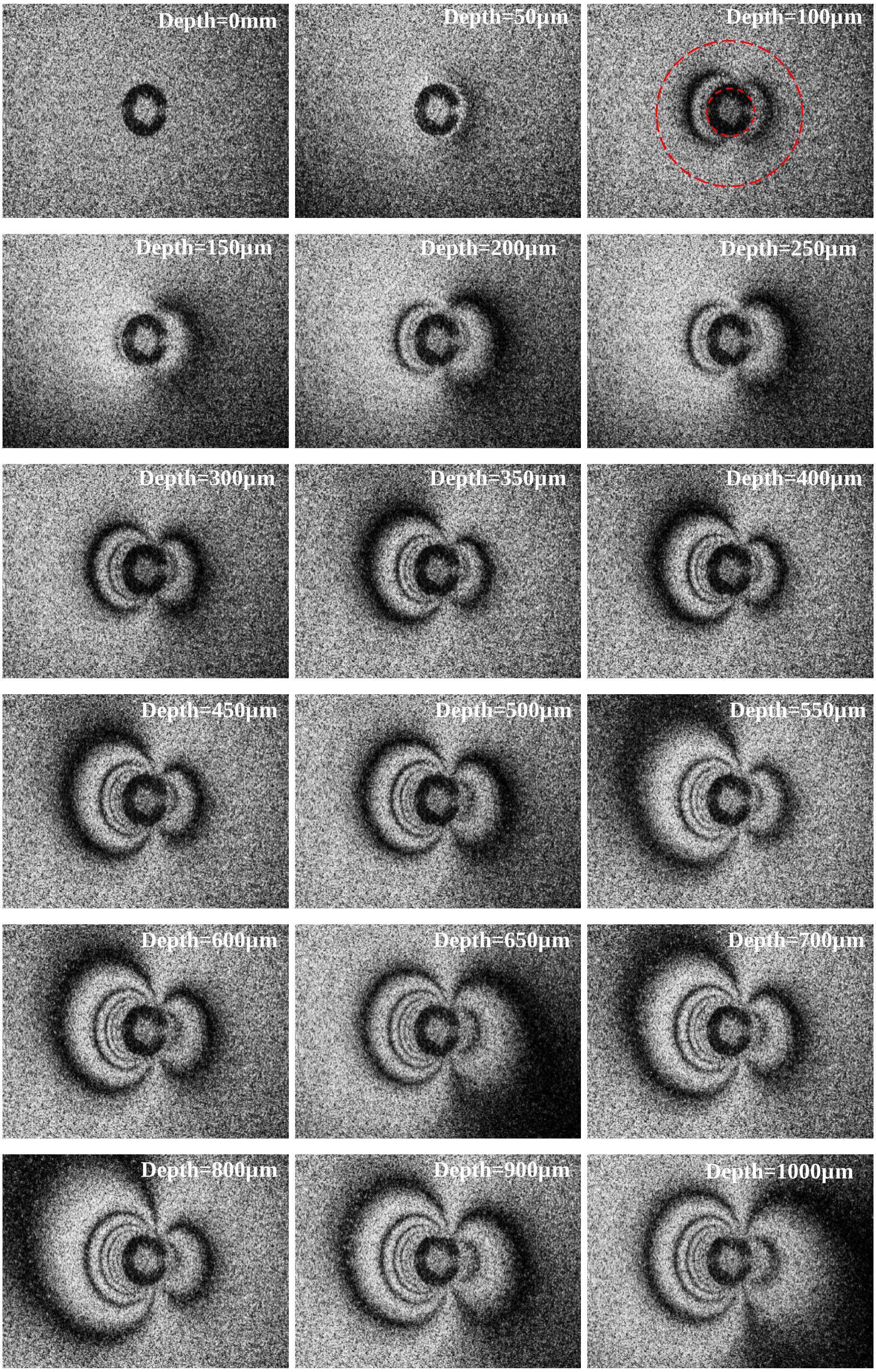

Figure 3.4–4 Fringe pattern of the carburized 19CrNi5H steel (900°C/8hrs): as-quenched

Different fringe pattern compared to normalized sample is obtained after the thermochemical heat treatment operation of 19CrNi5H steel. Fringe pattern induced by the residual stresses can be seen in Figure 3.4–4 for 8hrs carburized steel sample. When the hole depth increases, the acquired fringe images also increase. Residual stress induced by the carburizing process can be seen in Figure 3.4–5. Tikhonov regularization is again utilized to calculate the residual stress values of the sample. The figure indicates that the tangential stress acting on the carburized steel sample is zero as in the normalized sample. However, normal stresses in the x- and y-direction are compressive with the maximum value of about -700 MPa.

As stated earlier in the present study, compressive residual stresses are generated by the carburizing heat treatment while tensile residual stress in the core region compensates these compressive surface stresses. Upon quenching from carburizing temperatures, austenite to martensite transformation starts at the interface created between the case and the core regions. When the cooling is completed, compressive stresses are formed on the case region and the stresses in the interface transform from compressive to tensile stresses. This situation can be clearly seen in Figure 3.4–5. The maximum compressive residual stress arises about 0.2 mm away from the surface and when the distance from the surface increases compressive stresses diminishes due to the tensile residual stresses present in the core and the interface. Within the 1.0 mm depth from the surface, compressive residual stress is almost transformed to tensile stresses in the material.

Steel specimens subjected to thermochemical surface heat treatment for 8hrs is tempered at three different temperatures for three hours. It is known that the tempering operation leads residual stress to decrease. As seen in Figure 3.4–6, the maximum compressive residual stress is present when the sample is in the only quenched state. When the tempering temperature increases, the residual stress at the surface of the sample diminishes. Beneficial compressive residual stresses are still present in the tempered samples except for the sample tempered at 600°C. 180°C and 240°C tempered samples have stress values of -600 MPa and -500 MPa on the surface region, respectively. However, at 0.2 mm inside the surface, these compressive stresses decrease to about -100 MPa, and they almost turn to detrimental tensile stresses when the distance from the surface reaches to 0.6 mm. When the tempering temperature is increased to 600°C, compressive stresses are acting on the shallow case regions that tensile stresses are formed at 0.1 mm depth. Though the tensile stress formed on the surface is about 50 MPa, they will negatively affect the fatigue life of the sample.

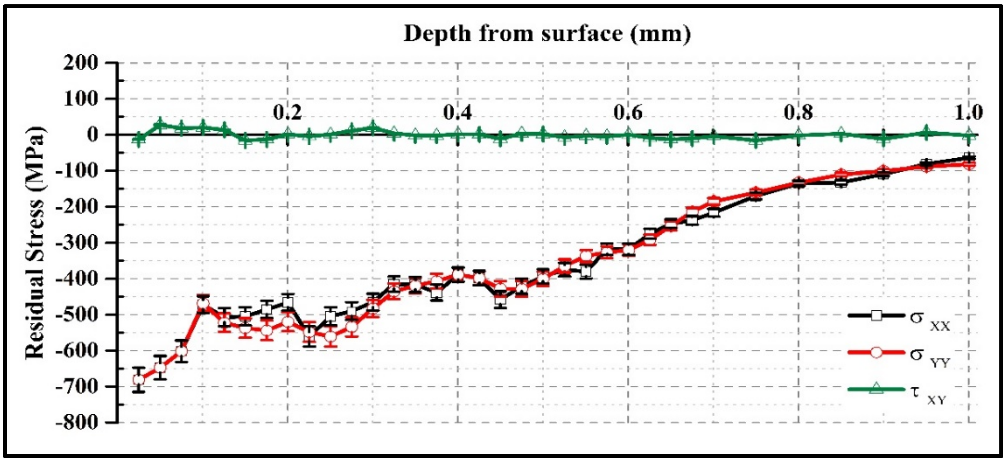

Figure 3.4–5 Depth profile of the residual stress state obtained by ESPI assisted hole-drilling (900°C/8hrs carburizing): as-quenched

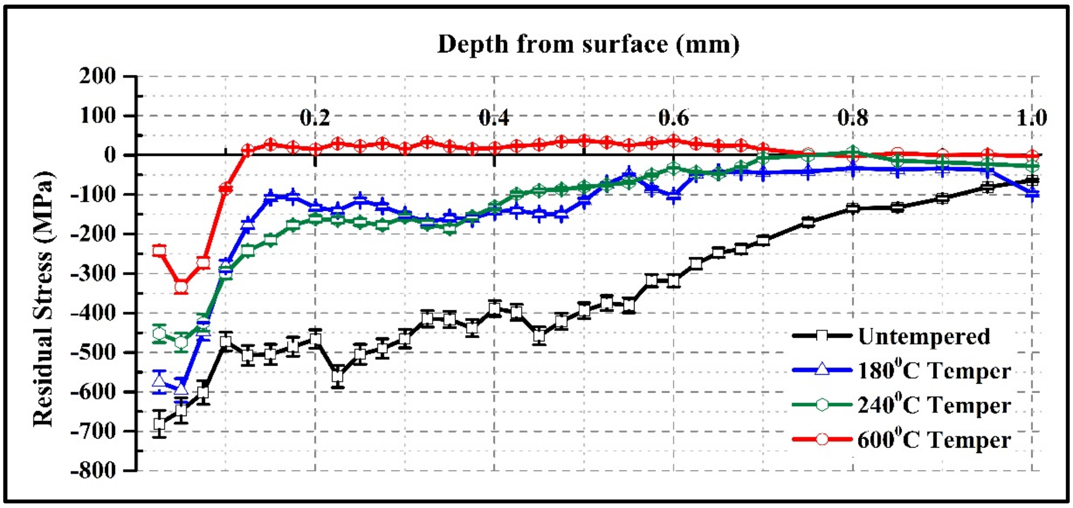

Figure 3.4–6 Effect of the tempering temperature on the depth profile of the residual stress state obtained by ESPI assisted hole-drilling (900°C/8hrs carburizing)

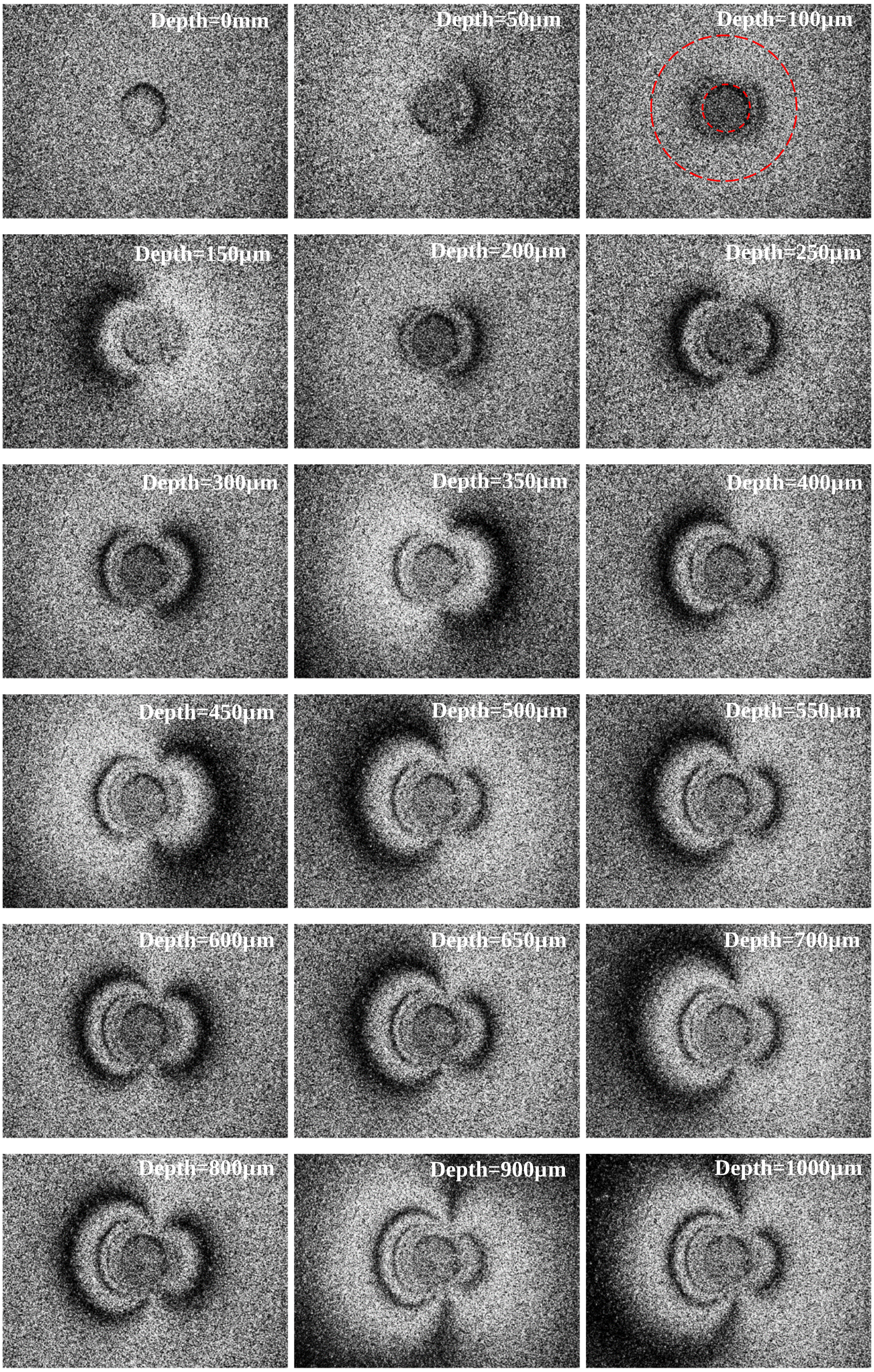

Figure 3.4–7 Fringe pattern of the carburized 19CrNi5H steel (900°C/10hrs): T180

Figure 3.4–7 shows the interferograms obtained during the ESPI hole-drilling measurement of 10hrs carburized steel sample. Compared to the fringe pattern obtained from the tensile stresses, more than one deformation circle is present around the drilled hole. The diameter of the interferograms is smaller when compared with the as-quenched steel sample shown in Figure 3.4–4.

When the carburizing time increases to 10hrs, compressive residual stresses arise at the case region, which is compensated by tensile residual stress at the core region. Upon tempering operations at 180°C, 240°C and 600°C for three hours, surface stresses are -550 MPa, -500 MPa and -400 MPa, respectively. As in the 8hrs carburized steel sample (Figure 3.4–6), when the tempering temperature is increased to 600°C, compressive case stresses transform to the tensile stresses at a distance of 0.1 from the case hardened surface, which can be seen in Figure 3.4–8. It can be deduced that the transformation of martensite to other phases, such as bainite, may occur during the tempering operation at 600°C, so the tensile stresses are developed due to the volume difference induced by phase transformation. The maximum compressive stresses are lower when compared with the 8hrs carburized 19CrNi5H steel sample. This is because ESPI assisted hole-drilling is not sensitive to the stresses in the near surface regions that there is an experimental error in the calculation of stresses at the surface zones.

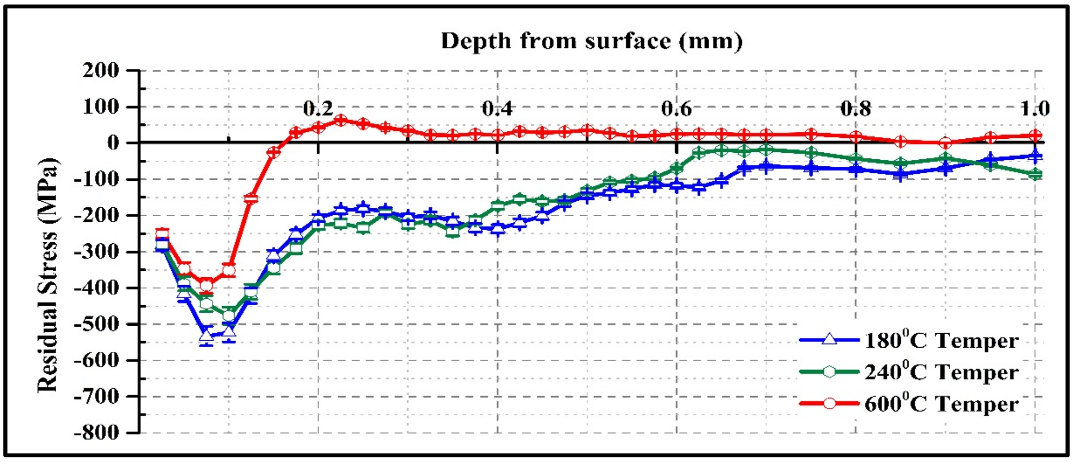

Figure 3.4–8 Effect of the tempering temperature on the depth profile of the residual stress state obtained by ESPI assisted hole-drilling (900°C/10hrs)

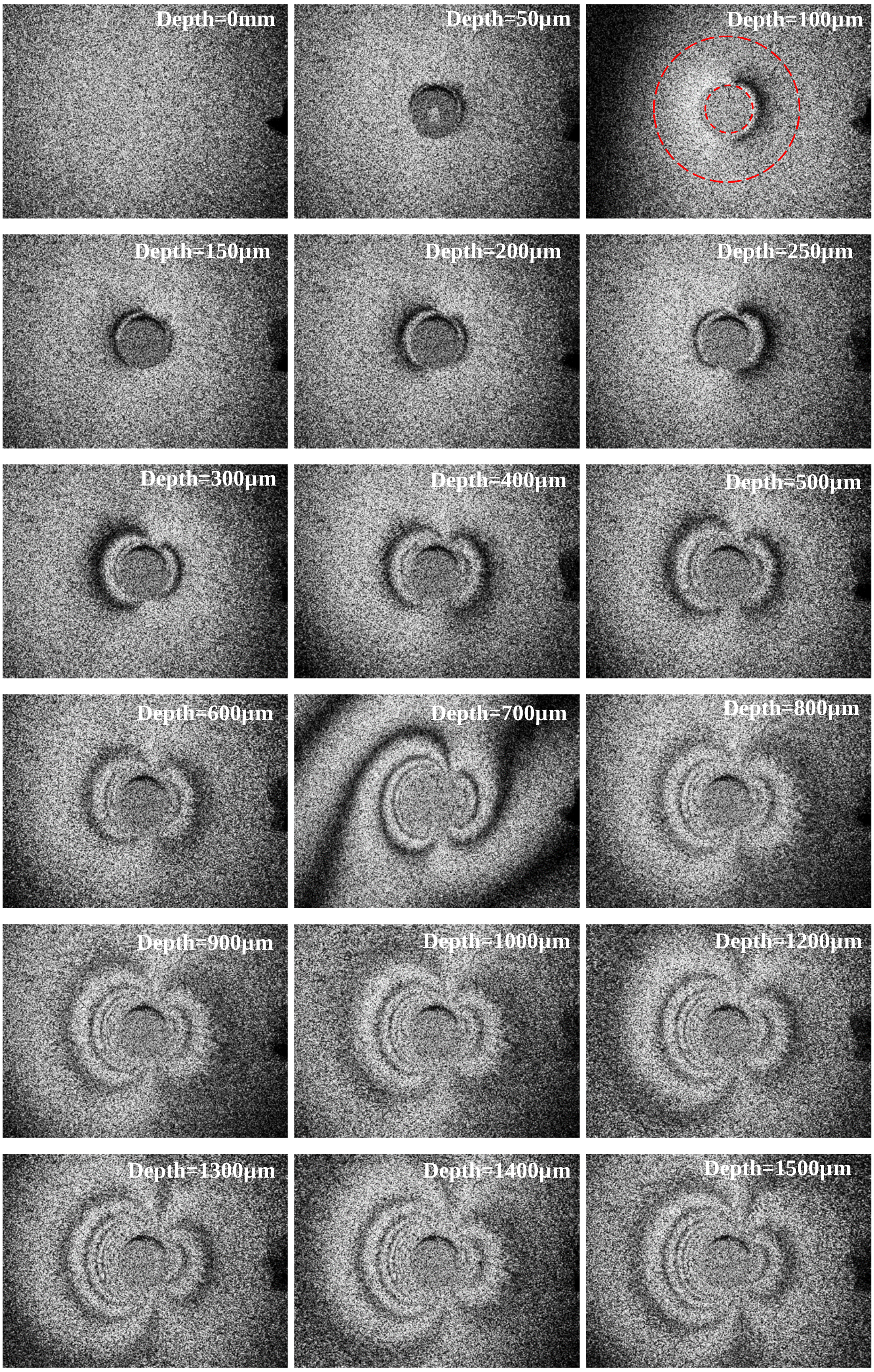

Figure 3.4–9 Fringe pattern of the carburized 19CrNi5H steel (900°C/13hrs): as-quenched

Figure 3.4–9 shows the interferograms obtained during the ESPI hole-drilling measurement of 10hrs carburized steel sample. Compared to the fringe pattern obtained from the tensile stresses, more than one deformation circle is again present around the drilled hole. The diameter of the interferograms is larger compared with the as-quenched steel sample shown in Figure 3.4–4. This may imply that the more negative compressive stresses are present in the sample.

Same situation as in the 8hrs and 10hrs carburized steel sample remains same for the 13hrs carburized steel sample (Figure 3.4–10). Carburized and only-quenched sample has the maximum compressive stress values at the surface whereas this maximum stress decreases with increasing tempering temperature. When tempering temperature reaches to 600°C, compressive to tensile stress transformation occurs at a distance of 0.2 mm while the compressive stresses are still present up to 1.2 mm for other operations.

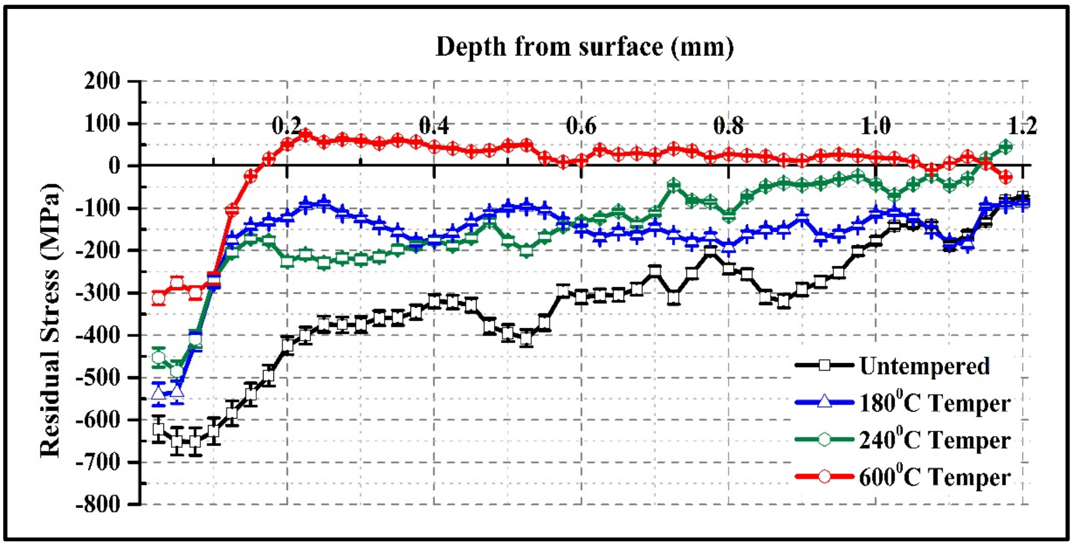

Figure 3.4–10 Effect of the tempering temperature on the depth profile of the residual stress state obtained by ESPI assisted hole-drilling (900°C/13hrs)

When the carburized depth increases, the maximum compressive stress shifts towards the core region as seen in Figure 3.4–11. When time is increase which implies an increase in case-depth, the maximum stress shifts from 0.05 mm to 0.10

mm from the surface. For a better understanding of this situation, X-Ray Diffraction with layer removal can be utilized since the ESPI hole-drilling method is not effective for the precise measurement of surface residual stress distributions.

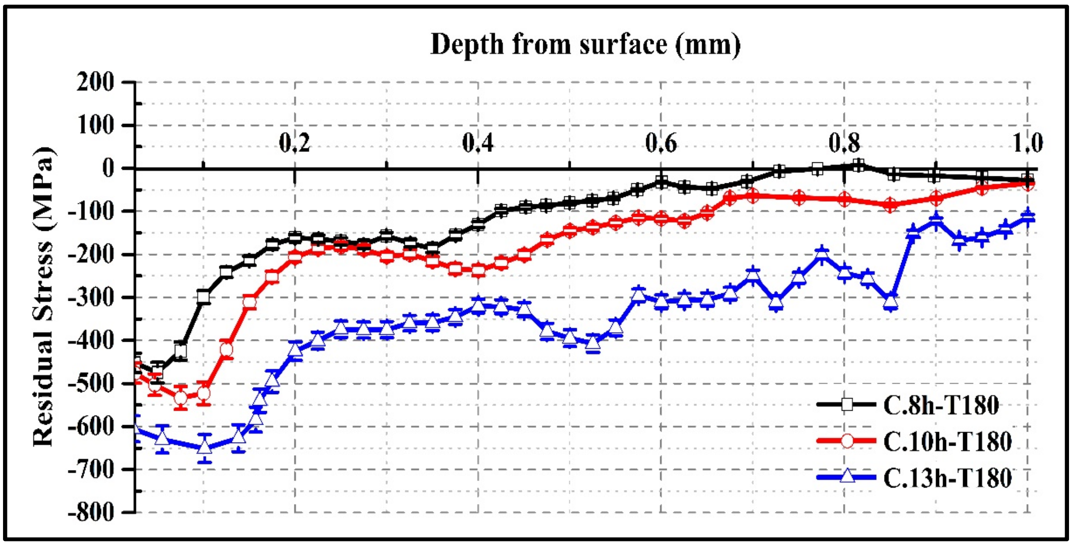

Figure 3.4–11 Effect of the carburizing time on the residual stress state of the 19CrNi5H steel

3.5 COMPARISON OF THE THREE RESIDUAL STRESS MEASUREMENT METHODS

The residual stress states obtained by the three different measurement methods show a good correlation with each other. The quantitative residual stress values may be directly obtained from the X-ray Diffraction software and ESPI assisted hole-drilling measurement software, whereas residual stress state is estimated by means of RMS values from magnetic Barkhausen noise system.

The stress depth profile obtained by ESPI assisted hole-drilling for 13hrs carburized steel samples shows the same trend with the those obtained by X-ray diffraction as seen in Figure 3.5–1. The depth profiles obtained by XRD and ESPI techniques are shifted against each other. This situation results from the differences in the stress measurement techniques of two methods. Stress data acquired by ESPI comes from the relatively larger volume compared to the XRD method. Therefore, residual stress values converge to the lower values in the ESPI assisted hole-drilling method. In addition to this, electropolishing creates groove at the measurement point. Due to the hollow shape of the measurement point, interplanar spacing used for residual stress measurement in the XRD technique is miscalculated so does the residual stress value of the significant depth. That may be another reason for the differences in the stress values. Nevertheless, considering the similar residual stress trend obtained by XRD and ESPI techniques, the ESPI system has an advantage over the XRD in this study since the residual stress depth profiles are obtained much faster with the ESPI system. The XRD data originates from a relatively thin layer, whereas the hole-drilling analyzes the changes resultant from each complete drilling step. Therefore, it is important to drill hole with a small increment to compare it with the XRD stress result.

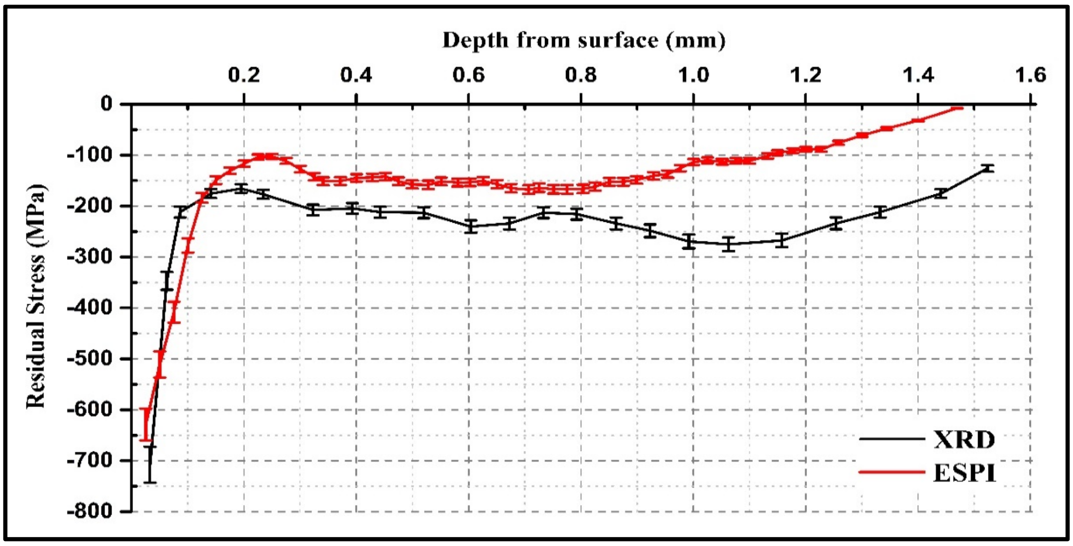

Figure 3.5–1 Comparison of the residual stress depth profiles obtained by XRD and ESPI techniques for the carburized 19CrNi5H steel (900°C/13hrs): 180°C tempered

The Barkhausen noise can be compared with the XRD since they gather residual stress data from a relatively shallow area and ESPI assisted hole-drilling method has a higher error at low depths. With the tensile residual stress, the amplitude of the BN signal is greater than those with compressive residual stress as seen in Figure 3.5–2.

Although it is difficult to predict residual stress by looking at the BN burst since it is also affected by the hardness value of the sample, the amplitude of the signal may be used for the prediction of the residual stress state in this study as a proper calibration process is applied to the samples. Moreover, the shape of the characteristic magnetic hysteresis curve depends on the stress state of the material. Experiments reveal that the hysteresis curve becomes wider with the presence of the tensile residual stresses, and the hysteresis loss, or area of the curve, increases.

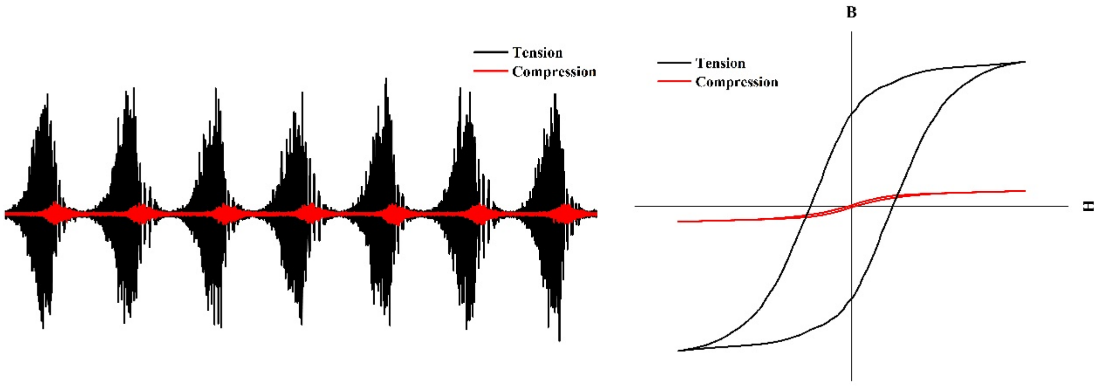

Figure 3.5–2 Barkhausen Noise response to the residual stress

In addition to the amplitude of the BN activity, the root-mean-square of the BN signal decreases with the increasing compressive stress, irrespective of the sign. Furthermore, the peak position shifts to the lower magnetic field strength values with the tensile stress present. With a proper calibration operation, MBN technique can be used to predict the residual stress induced in the material although the confidence of the method is not so perfect. Among the other residual stress measurement methods, the fastest method is the MBN method.

CHAPTER 4

CONCLUSION

4.1 GENERAL CONCLUSIONS

The purpose of the present dissertation is to monitor the variations in microstructure and residual stress distributions in carburized steels by the use of both destructive and nondestructive methods. Four different groups of specimens were prepared from the low alloy low-carbon 19CrNi5H steel to evaluate the residual stress distribution caused by heat treatment operations. One of the groups was subjected to the normalizing heat treatment, whereas the other three groups have been submitted to the thermochemical surface hardening heat treatment for three different process periods and four different tempering operations. The microstructures in the materials structure, hardness and percent carbon content of the steel were determined by the conventional optical metallography and Scanning Electron Microscopy, conventional hardness testing and the optical emission spectrometer. In this research, three different residual stress measurement techniques are utilized for the determination of the stress state. Those are Magnetic Barkhausen Noise (MBN), X-Ray Diffraction (XRD) and Electronic Speckle Pattern Interferometry (ESPI) assisted hole-drilling.

For each semi-destructive and/or non-destructive measurement, a specific calibration procedure was carried out to measure the stress state as precise as possible. The calibration procedure was done by using unstressed iron powder for X-ray diffraction technique, while it was carried out by series of experiments for the Magnetic Barkhausen Noise and ESPI assisted hole-drilling methods. In the determination of the optimized measurement parameters, the main consideration for the XRD measurement was the intensity of the diffracted beam that should be high enough and the background noise. Optimization operation included feed rate, drilling speed and the analyzing area for the ESPI assisted hole-drilling technique. For the MBN measurement, magnetizing voltage and frequency and the filtering range were the main considerations.

The following conclusions can be drawn from the results of the thesis work.

- The martensitic structure in the core and the case region is present in the steel specimens subjected to the thermochemical heat treatment process since the critical cooling rate to form martensite was reached in both regions of thin rectangular in shaped samples.
- The hardness value reduces gradually from the case region to the core region for quenched and tempered steel samples.
- Spectrometer measurement shows that the carbon content of the material after carburization operation decreases gradually from 0.9% to 0.2%.
- X-Ray Diffraction stress measurement reveals that the tensile residual stresses are present in the normalized 19CrNi5H steel, whereas the compressive residual stresses are present in the thermochemical heat treated samples.
- An increase in the tempering temperature causes a decrease in the compressive residual stress state (irrespective of sign) of the samples. In addition, the maximum attainable residual stress state shifts towards the core region as the duration of carburizing increases.

- Magnetic Barkhausen Noise measurement with the optimized parameter sets indicates that the relative MBN root mean square value of carburized samples decreases with increased carburizing time at 900°C. However, it increases with increasing tempering temperature.

- MBN peak positions shifts to higher magnetic field strengths when the martensite content of the sample increases. The maximum peak height of the specimens decreases with the increasing tempering temperature.

- Representative magnetic hysteresis curve indicates that the shape of the curve and the magnetic parameters depend strictly on the residual stress present in the material. Coercivity and remanence values decrease due to the presence of compressive residual stresses.

- The ESPI assisted hole-drilling technique shows that compressive residual stress states are present on the surface and the core regions of the carburized steel samples.

- The residual stress values obtained by ESPI and XRD techniques show the similar stress distribution trend in the materials.

- The ESPI assisted hole-drilling method is proven to be used in the evaluation of the residual stress state induced by the thermochemical heat treatment.

- Three different residual stress measurement methods show a very strong correlation between each other. Among them, MBN technique is the fastest way to predict the surface residual stress state of the part.

4.2 RECOMMENDATIONS FOR FURTHER STUDIES

It is suggested that carburizing operation should be carried out by thicker samples in order to distinguish case to the core region. By optimized and better carburizing process, residual stress distribution can be evaluated in a better way.

Interplanar space lattice parameter for unstressed specimen may be measured more precisely so that the stress tensor that contains stress in all direction can be calculated. In the present research, the out-of-plane stress state was assumed as zero. However, d vs. $sin^2\psi$ graph used for the stress calculation showed ψ-splitting in the material, which indicates that there exist strains induced by out-of-plane stress. By determining the interplanar spacing as exact as possible, three stress tensor can be calculated by using triaxial stress state.

It is known that BN signal is influenced by the microstructure of the material, the hardness of the material, residual stress state of the material, etc. Nevertheless, it is not known which factor has the greatest effect on the BN. As a result, it is also recommended that all individual factors affecting the Barkhausen noise activity should differentiate clearly.

ESPI assisted hole-drilling method differs from the strain gage hole-drilling method. Therefore, it is important to find optimized parameter for residual stress evaluation in the material. By series of the experiment prior to the calculation of the residual stress state, feed rate, drilling speed, etc. must be clearly determined for each material under investigation.

REFERENCES

[1] Totten, G., Howes, M., & Inoue, T. (2002). *Handbook of residual stress and deformation of steel* (pp. 189-208). Materials Park, OH: ASM International.

[2] Withers, P. & Bhadeshia, H. (2001). Residual stress. Part 1 – Measurement techniques. *Materials Science And Technology*, *17*(4), 355-365.

[3] Kudryavtsev, Y. (2008). Residual Stress. In W. Sharpe, *Springer handbook of experimental solid mechanics* (1st ed., pp. 371-387). Boston MA.: Springer Science+Business Media.

[4] Schajer, G. (2001). *Practical residual stress measurement methods* (pp. 152-174). A John Wiley & Sons, Ltd., Publication.

[5] Withers, P. (2007). Residual stress and its role in failure. *Rep. Prog. Phys.*, *70*(12), 2211-2264.

[6] Lu, J. (1996). *Handbook of measurement of residual stresses*. Lilburn, GA: Fairmont Press.

[7] Prevey, P. S. (2016). *X-ray Diffraction Residual Stress Techniques*. Lambda Technologies

[8] Dölle, H. (1979). The influence of multiaxial stress states, stress gradients and elastic anisotropy on the evaluation of (Residual) stresses by X-rays. *J Appl Cryst*, *12*(6), 489-501.

[9] Fitzpatrick, M.E., A.T. Fry, P. Holdway, F.A. Kandil, J. Shackleton, and L. Suominen. March 2002. Measurement Good Practice Guide No. 52: Determination of Residual Stresses by X-ray Diffraction. *The National Physical Laboratory*, Teddington, Middlesex, United Kingdom

[10] Kandil, F., Lord, J., Fry, A., & Grant, P. (2001). A Review of Residual Stress Measurement Methods - A Guide to Technique Selection. *NFL Report MATC(A)O4*.

[11] Steinzig, M. & Ponslet, E. (2003). Residual Stress Measurement Using The Hole Drilling Method And Laser Speckle Interferometry: Part I-IV. *Experimental Techniques*, *27*(3), 43-46.

[12] Mathar, J. (1934) Determination of Initial Stresses by Measuring the Deformations Around Drilled Holes. *Trans. ASME, Iron Steel, 56 (2),* 249–254.

[13] Makino, A. & Nelson, D. (1994). Residual-stress determination by single-axis holographic interferometry and hole drilling—Part I: Theory. *Experimental Mechanics*, *34*(1), 66-78.

[14] Stefanita, C. (2012). *Magnetism* (pp. 39-67). Heidelberg: Springer-Verlag Berlin Heidelberg.

[15] Jagadish, C., Clapham, L., & Atherton, D. (1990). The effect of stress and magnetic field orientation on surface Barkhausen noise in pipeline steel. *IEEE Trans. Magn.*, *26*(1), 262-265.

[16] Cullity, B. & Graham, C. (2009). *Introduction to magnetic materials*. Hoboken, N.J.: IEEE/Wiley.

[17] Stefenita, C. (1999). *Surface Magnetic Barkhausen Noise Response to Plastic Yield of Steel* (Ph.D). Queen's University at Kingston.

[18] Courtney, T. (1999). *Mechanical behavior of materials* (2nd ed.). New York: McGraw-Hill.

[19] Stefanita, C., Atherton, D., & Clapham, L. (2000). Plastic versus elastic deformation effects on magnetic Barkhausen noise in steel. *Acta Materialia*, *48*(13), 3545-3551.

[20] Makar, J. & Tanner, B. (2000). The effect of plastic deformation and residual stress on the permeability and magnetostriction of steels. *Journal Of Magnetism And Magnetic Materials*, *222*(3), 291-304.

[21] Stefanita, C., Atherton, D., & Clapham, L. (2000). Subtle changes in magnetic Barkhausen noise before the macroscopic elastic limit, *Journal of Materials Science, 35*, 2675-2681

[22] Stewart, D., Stevens, K., & Kaiser, A. (2004). Magnetic Barkhausen noise analysis of stress in steel. *Current Applied Physics*, *4*(2-4), 308-311.

[23] Kleber, X. & Vincent, A. (2004). On the role of residual internal stresses and dislocations on Barkhausen noise in plastically deformed steel. *NDT & E International*, *37*(6), 439-445.

[24] Anglada-Rivera, J., Padovese, L., & Capó-Sánchez, J. (2001). Magnetic Barkhausen Noise and hysteresis loop in commercial carbon steel: influence of applied tensile stress and grain size. *Journal Of Magnetism And Magnetic Materials, 231*(2-3), 299-306.

[25] Stevens, K. (2000). Stress dependence of ferromagnetic hysteresis loops for two grades of steel. *NDT & E International*, *33*(2), 111-121.

[26] Degauque, J. & Astie, B. (1982). Evolution of the Configuration of Magnetic Domains Interacting with Structural Defects in High Purity Iron. *Phys. Stat. Sol. (A), 74*(1), 201-210.

[27] Moorthy, V., Vaidyanathan, S., Jayakumar, T., & Raj, B. (1997). Microstructural characterization of quenched and tempered 0.2% carbon steel using magnetic Barkhausen noise analysis. *Journal Of Magnetism And Magnetic Materials*, *171*(1-2), 179-189.

[28] Mix P. (2005). *Introduction to Nondestructive Testing: A Training Guide (2nd ed.),* John Wiley & Sons.

[29] Lo, C., Scruby, C., & Smith, G. (2004). Dependences of magnetic Barkhausen emission and magnetoacoustic emission on the microstructure of pearlitic steel. *Philosophical Magazine*, *84*(18), 1821-1839.

[30] Davis, J. (2002). *Surface hardening of steels* (pp. 17-90). Materials Park, OH: ASM International.

[31] Bozorth, R. (1968). *Ferromagnetism* (pp. 225-265). Princeton, NJ: Van Nostrand.

[32] Chikazumi, S., Graham, C., & Chikazumi, S. (1997). *Physics of ferromagnetism*. Oxford: Oxford University Press.

[33] Jiles, D. (2003). Recent advances and future directions in magnetic materials. *Acta Materialia*, *51*(19), 5907-5939.

[34] J. M. Makar, B.K. Tanner, The effect of plastic deformation and residual stress on the permeability and magnetostriction of steels, Journal of Magnetism and Magnetic Materials, 222 (2000) 291-304.

[35] Santo-aho S. (2012). *Barkhausen Noise Method for Hardened Steel Surface Characterization – The Effect of Heat Treatments, Thermal Damages and Stresses* (Ph.D). Tampere University of Technology

[36] Wojtas A., Suominen L., Shaw B., & Evans J. (1998). Detection of thermal damage in steel components after grinding using the Magnetic Barkhausen Noise method, *NDT.net, 3(9)*

[37] Moorthy, V., Shaw, B., & Hopkins, P. (2006). Surface and subsurface stress evaluation in case-carburised steel using high and low frequency Magnetic Barkhausen emission measurements. *Journal Of Magnetism And Magnetic Materials*, *299*(2), 362-375.

[38] Dossett, J. & Boyer, H. (2006). *Practical heat treating*. Materials Park, Ohio: ASM International.

[39] Cizeau, P., Zapperi, S., Durin, G., & Stanley, H. (1997). Dynamics of a Ferromagnetic Domain Wall and the Barkhausen Effect. *Phys. Rev. Lett.*, *79*(23), 4669-4672.

[40] Davut, K. & Hakan Gür, C. (2007). Monitoring the Microstructural Changes During Tempering of Quenched SAE 5140 steel by Magnetic Barkhausen Noise. *Journal Of Nondestructive Evaluation*, *26*(2-4), 107-113.

[41] Moorthy, V., Vaidyanathan, S., Laha, K., Jayakumar, T., Bhanu Sankara Rao, K., & Raj, B. (1997). Evaluation of microstructures in 2.25Cr-1Mo and 9Cr-1Mo

steel weldments using magnetic Barkhausen noise. *Materials Science And Engineering: A*, *231*(1-2), 98-104.

[42] Volkers, J. (2008). *The influence of dislocations on magnetic properties in steel: Magnetisation curve and magnetic Barkhausen effect in relation to deformation and recovery in C-Mn and IF steel* (Master). Delft University of Technology.

[43] Miyazaki, T. & Jin, H. (2012). *The physics of ferromagnetism* (pp. 100-102). Berlin: Springer.

[44] Hızlı H., Gür C. (2015). Nondestructive Monitoring of the Effects of Carburizing on 19CrNi5H Steel by Magnetic Barkhausen Noise Method, *11th International Conference on Barkhausen Noise & Micromagnetic Testing*, Kuşadası, CD Proc., No. 19.

[45] Macherauch, E. & Vöhringer, O. (1992). Residual Stresses After Quenching. *Theory And Technology Of Quenching*, 117-181.

[46] Stickels C. (1991). Gas Carburizing. In Dossett, J. *Steel heat treating fundamentals and processes* (pp. 312-324). Materials Park, OH: ASM International.

[47] Schroder R., Scholtes B., & Macherauch E. (1984). Rechnerische und rontgenographische Analyse der Eigenspannungsbildung in abgeschreckten Stahlzylindern. *Hart.-Tech. Mitt., Vol 39,* 280–292

[48] Parrish, G. & Harper, G. (1985). *Production gas carburising* (pp. 86-187). Oxford a.o: Pergamon Press.

[49] Danke, M. & Worzala, F. (1992). The Structure and Properties of Ion Nitrided 410 Stainless. *Materials Science Forum*, *102-104*, 259-270.

[50] Kim C. (1984). Fracture of Case-Hardened Steels and Residual Stress Effects. In Diesburg, D. *Case-hardened Steels: microstructural and residual stress effects* (pp. 59-87). Warrendale, Pa.

[51] Krauss G. (1993). Microstructure, Residual Stresses and Fatigue of Carburized Steels. In Quenching and Carburizing, Proc. 3rd Int. Sem. Int. Fed. Heat Treat. Surface Eng. (pp. 205-225). Alden Press, Oxford.

[52] Jatzak C. & Rice S. (1978). Surface Hardening with Carbon and Nitrogen. In Davis, J. (1990). *ASM handbook* (pp. 533-542). Materials Park: ASM International.

[53] Wisti M. and Hingwe M. (2014) Tempering of Steel, in Dossett, J. *Steel heat treating fundamentals and processes* (pp. 122-136). Materials Park, OH: ASM International.

[54] Parrish, G. (1980). *The influence of microstructure on the properties of case-carburized components* (pp. 73-80). Metals Park, Ohio: American Society for Metals.

[55] Grosch J. (1997). Heat Treatment with Gaseous Atmospheres. In Totten, G. & Howes, M. *Steel heat treatment handbook* (pp. 663-719). New York: Marcel Dekker.

[56] Krauss G. (1991). Microstructures and Properties of Carburized Steels, in ASM Handbook, Vol 4, Heat Treating, *ASM International*, 363–375

[57] R.C. Rice, Ed., Fatigue Design Handbook, AE-10, 2nd ed., Society of Automotive Engineers, 1988

[58] Shea, M. (1980). Residual stress and microstructure in quenched and tempered and hot oil quenched carburized gears. *Journal Of Heat Treating*, *1*(4), 29-36.

[59] Shea, M. (1983). Influence of quenchant temperature on the surface residual stress and impact fracture of carburized steel. *Journal Of Heat Treating*, *3*(1), 38-47.

[60] Dossett, J. (2014). *Steel heat treating fundamentals and processes* (pp. 528-580). Materials Park, OH: ASM International.

[61] Krempaszky, C., Šedivý, O., & Werner, E. (2016). ESPI assisted Hole Drilling Method. *Dantecdynamics*.

[62] Barile, C., Casavola, C., Pappalettere, G., & Pappalettere, C. (2016). Overview of the Effects of Process Parameters on the Accuracy in Residual Stress Measurements by Using HD and ESPI. In S. Bossuyt, G. Schajer & A. Carpinteri, *Residual Stress, Thermomechanics & Infrared Imaging, Hybrid Techniques and Inverse Problems, Volume 9* (1st ed., pp. 113-118). Cham: Springer International Publishing.

[63] Cheng, J., Kwak, S., & Choi, J. (2008). ESPI combined with hole drilling method to evaluate heat treatment induced residual stresses. *Fourth International Symposium On Precision Mechanical Measurements*.

[64] Dossett, J. & Boyer, H. (2006). *Practical heat treating* (pp. 141-158). Materials Park, Ohio: ASM International.

[65] Sharma, R. (1996). *Principles of heat treatment of steels* (pp. 211-216). New Delhi: New Age International.

[66] Barile, C., Casavola, C., Pappalettera, G., & Pappalettere, C. (2014). Considerations on the choice of experimental parameters in residual stress measurements by hole-drilling and ESPI. *Fracture and Structural Integrity, 0*(30), pages 211-219.

[67] Rickert, T., Thomas, J., & Suominen, L. (2014). Residual Stress Measurement of Shot-Peened Steel Rings by Barkhausen Noise, ESPI Hole-Drilling and X-Ray Diffraction. *AMR, 996*, 380-385.

[68] Thelning, K. (2002). *Steel and its heat treatment* (pp. 17-90). London: Butterworths.

[69] Bradley D., Leitnaker J., & Horne F. (1980). *High Temp. Sci., Vol 12*, 1–10

[70] Anderson J., Leaver K., Rawlings R. & Alexander J. (1990). *Materials Science,* (4th ed.). London, Chapman & Hall.

[71] Ranjan R., Jiles D. & Rastogi P. (1987). Magnetic properties of decarburized steels: An investigation of the effects of grain size and carbon content. *IEEE Transactions on Magnetics 23*, 1869–1876.

[72] Kypris, O., Nlebedim, I., & Jiles, D. (2014). A model for the Barkhausen frequency spectrum as a function of applied stress. *J. Appl. Phys.*, *115*(8), 083906.

[73] Gatelier-Rothea C., Chicois J., Fourgeres R. & Fleischmann P. (1998). Characterization of pure iron and (130 PPM.) carbon-iron binary alloy by Barkhausen noise measurements: Study of the influence of stress and microstructure. *Acta Materialia 46*, 4873–4882.

[74] Yamaura S., Furuya Y. & Watanabe T. (2001). The effect of grain boundary microstructure on Barkhausen noise in ferromagnetic materials. *Acta Materialia 49,* 3019–3027.

[75] Anglada-Rivera, J., Padovese, L., & Capó-Sánchez, J. (2001). Magnetic Barkhausen Noise and hysteresis loop in commercial carbon steel: influence of applied tensile stress and grain size. *Journal Of Magnetism And Magnetic Materials*, *231*(2-3), 299-306.

[76] Kim D-W. & Kwon D. (2003). Quantification of the Barkhausen noise method for the evaluation of time-dependent degradation. *Journal of Magnetism and Magnetic Materials 257*, 175–183.

[77] Saquet O, Chicois J & Vincent A (1999) Barkhausen noise from plain carbon steels: analysis of the influence of microstructure. *Materials Science and Engineering A 269*: 73–82.

[78] Moorthy V., Vaidyanathan S., Raj B., Jayakumar T. & Kashyap B. (2000). Insight into the microstructural characterization of ferritic steels using micromagnetic parameters. *Metallurgical and Materials Transactions A 31*, 1053–1065.

[79] D'Amato C., Verdu C., Kleber X., Regheere G. & Vincent A. (2003). Characterization of Austempered Ductile Iron Through Barkhausen Noise Measurements. *Journal of Nondestructive Evaluation 22*, 127–139

[80] Koo K., Yau M., Ng D. & Lo C. (2003). Characterization of pearlite grains in plain carbon steel by Barkhausen emission. *Materials Science and Engineering A 351*, 310–315.

[81] Kaplan M., Gür C. & Erdogan M. (2007). Characterization of Dual-Phase Steels Using Magnetic Barkhausen Noise Technique. *Journal of Nondestructive Evaluation 26*, 79–87.

[82] Kleber X., Hug-Amalric A. & Merlin J. (2008). Evaluation of the Proportion of Phases and Mechanical Strength of Two-Phase Steels Using Barkhausen Noise Measurements: *Application to Commercial Dual-Phase Steel. Metallurgical and Materials Transactions A 39*, 1308–1318.

[83] Ng D., Cheng K., Cho K., Ren Z., Ma X. & Chan S. (2001) Nondestructive Evaluation of Carbon Contents and Microstructures in Plain Carbon Steel Bars by Barkhausen Emission. *IEEE Transactions on Magnetics 37*, 2734–2736.

[84] Capó-Sánchez J., Pérez-Benitez J., Padovese L. & Serna-Giraldo C. (2004). Dependence of the magnetic Barkhausen emission with carbon content in commercial steels. *Journal of Materials Science 39*, 1367–1370.

[85] Pérez-Benitez J., Capó-Sánchez J., Anglada-Rivera J. & Padovese L. (2005). A model for the influence of microstructural defects on magnetic Barkhausen noise in plain steels. *Journal of Magnetism and Magnetic Materials 288*, 433–442.

[86] Jiles D. (2000). Dynamics of domain magnetization and Barkhausen effect. *Czechoslovak Journal of Physics 50*, 893–924.

[87] Sipahi L. (1994). Effects of creep damage, shot peening, and case hardening on magnetic Barkhausen noise analysis. *IEEE Transactions on Magnetics 30*, 4830–4832.

[88] O'Sullivan D., Cotterell M., Tanner D. & Mészáros I. (2004). Characterisation of ferritic stainless steel by Barkhausen techniques. *NDT & E International 37*, 489–496.

[89] Santa-aho S., Vippola M., Lepistö T. & Lindgren M. (2009). Characterization of case hardened gear steel by multiparameter Barkhausen noise measurements. *Insight - Non-Destructive Testing and Condition Monitoring 51*, 212–216.

[90] Kinser E., Lo C., Barsic A. & Jiles D. (2005). Modeling microstructural effects on Barkhausen emission in surface-modified magnetic materials. *IEEE Transactions on Magnetics 41*, 3292–3294.

[91] Mészáros I. & Szabó P. (2005). Complex magnetic and microstructural investigation of duplex stainless steel. *NDT & E International 38*, 517–521.

[92] Stewart D., Stevens K. & Kaiser A. (2004). Magnetic Barkhausen noise analysis of stress in steel. *Current Applied Physics 4*, 308–311.

[93] Jagadish C., Clapham L. & Atherton D. (1990). Influence of uniaxial elastic stress on power spectrum and pulse height distribution of surface Barkhausen noise in pipeline steel. *IEEE Transactions on Magnetics 26,* 1160–1163.

[94] Lindgren M. & Lepistö T. (2002). Application of Barkhausen noise to biaxial residual stress measurements in welded steel tubes. *Materials Science and Technology 18,* 1369– 1376.

[95] Mierczak L., Jiles D. & Fantoni G. (2011). A New Method for Evaluation of Mechanical Stress Using the Reciprocal Amplitude of Magnetic Barkhausen Noise. *IEEE Transactions on Magnetics 47,* 459–465.

[96] Blaow M., Evans J. & Shaw B. (2007). The effect of microstructure and applied stress on magnetic Barkhausen emission in induction hardened steel. *Journal of Materials Science 42,* 4364–4371.

[97] Gauthier J., Krause T. & Atherton D. (1998). Measurement of residual stress in steel using the magnetic Barkhausen technique. *NDT&E International 31,* 23–31.

[98] Moorthy V., Shaw B. & Day S. (2004). Evaluation of applied and residual stresses in case-carburised En36 steel subjected to bending using the magnetic Barkhausen emission technique. *Acta Materialia 52,* 1927–1936.

[99] Iordache V., Hug E. & Buiron N. (2003). Magnetic behaviour versus tensile deformation mechanisms in a non-oriented Fe–(3 wt.%) Si steel. *Materials Science and Engineering A 359,* 62–74.

[100] Retrieved from https://www.totalmateria.com on Jun 16, 2016

[101] ISO 2639 - Standard Test Method for Determination and Verification of Case Depth by Microhardness Test

[102] McDonach, A., McKelvie, J., MacKenzie, P., & Walker, C. (1983). Improved Moiré Interferometry and Applications in Fracture Mechanics, Residual Stress and Damaged Composites. *Experimental Techniques, 7(6),* 20-24.

[103] Antonov, A. (1983). Development of the Method and Equipment for Holographic Inspection of Residual Stresses in Welded Structures. *Weld Prod 30(12)*, 41-43.

[104] Moorthy, V., Vaidyanathan, S., Laha, K., Jayakumar, T., Bhanu Sankara Rao, K., & Raj, B. (1997). Evaluation of microstructures in 2.25Cr-1Mo and 9Cr-1Mo steel weldments using magnetic Barkhausen noise. *Materials Science And Engineering: A, 231(1-2)*, 98-104.

[105] Rautioaho, R., Karjalainen, P., & Moilanen, M. (1991). Stress response of Barkhausen noise and coercive force in 9Ni steel. *NDT & E International*, *24*(1), 46.

APPENDIX A

SCANNING ELECTRON MICROSCOPE IMAGES

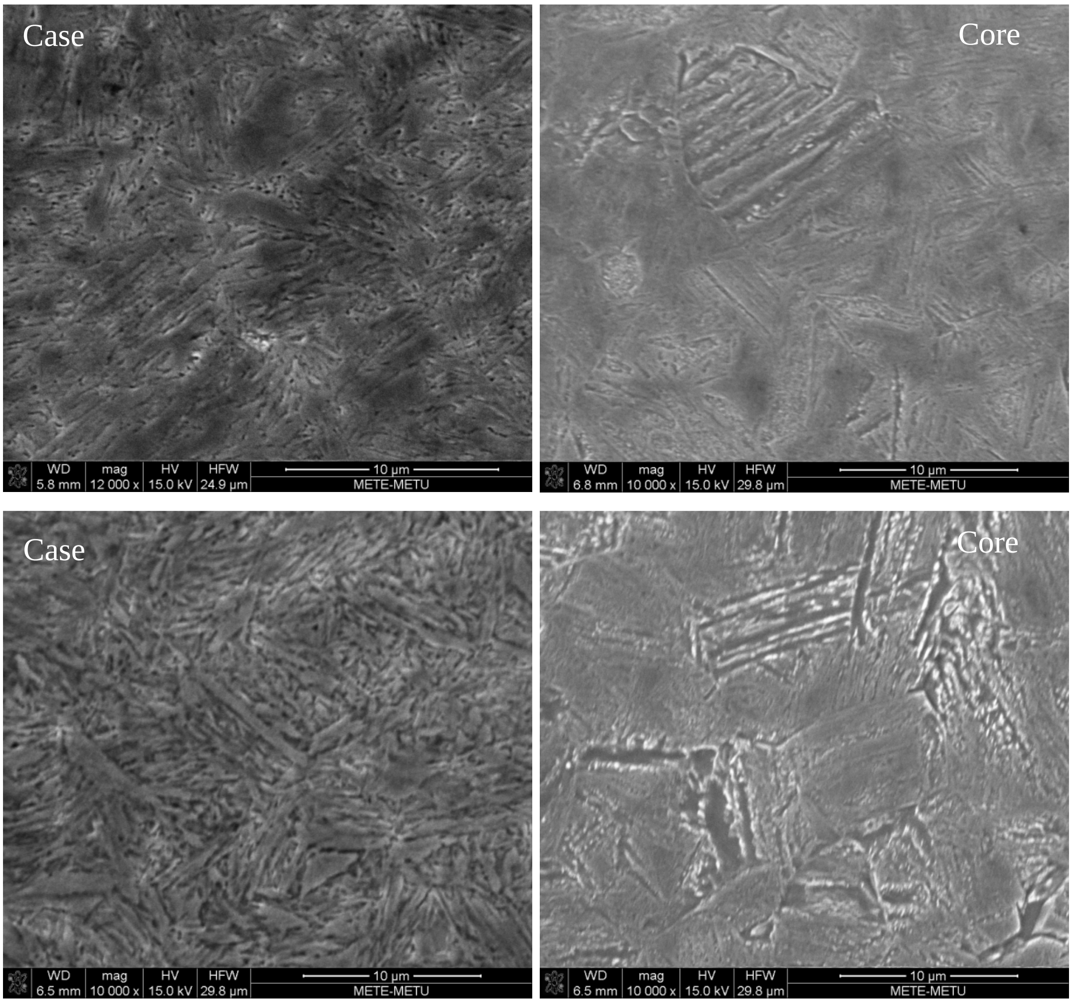

Figure A–1 SEM micrographs of carburized steel sample (900°C/8hrs): as-quenched core (upper left), as-quenched core (upper right) and 180°C tempered case (below left) and core (below right)

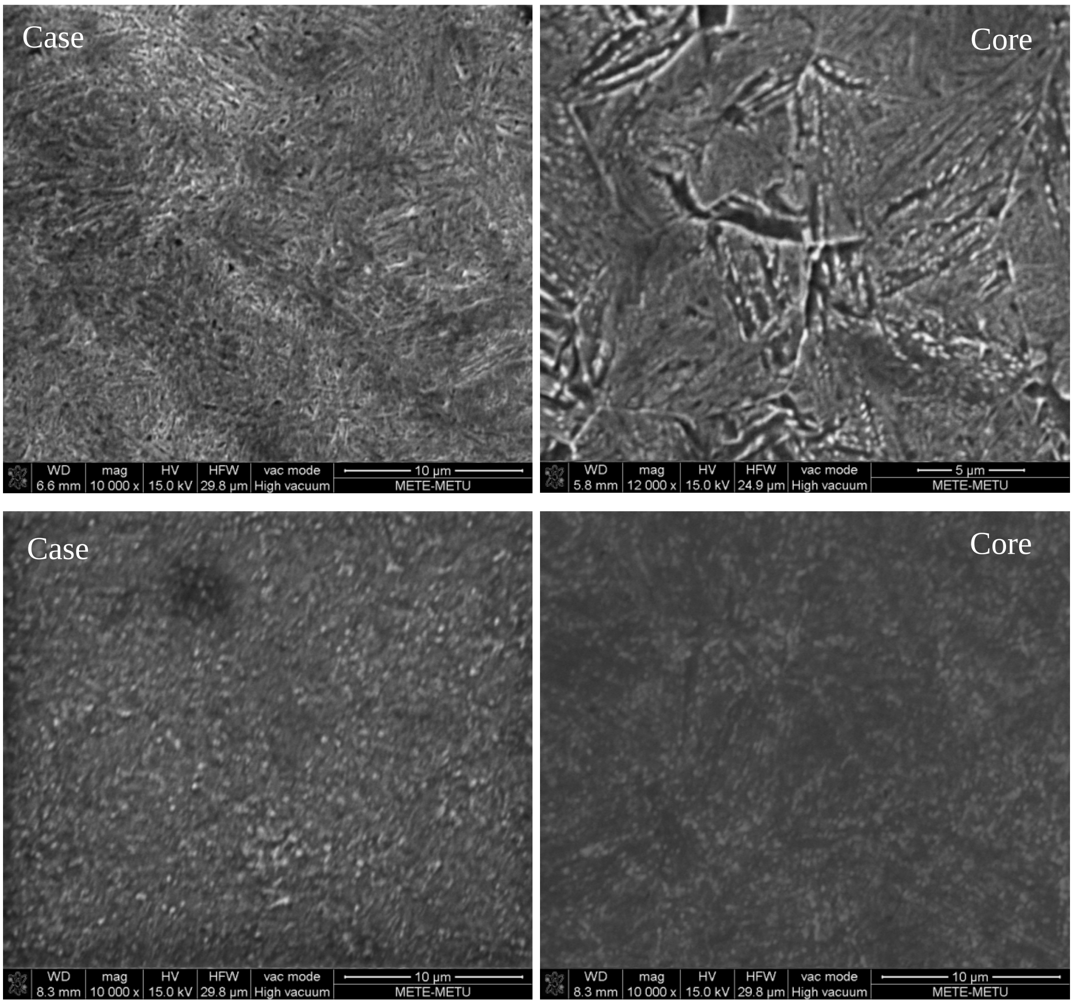

Figure A–2 SEM micrographs of carburized steel sample (900°C/8hrs): 240°C tempered core (upper left), as-quenched core (upper right) and 600°C tempered case (below left) and core (below right)

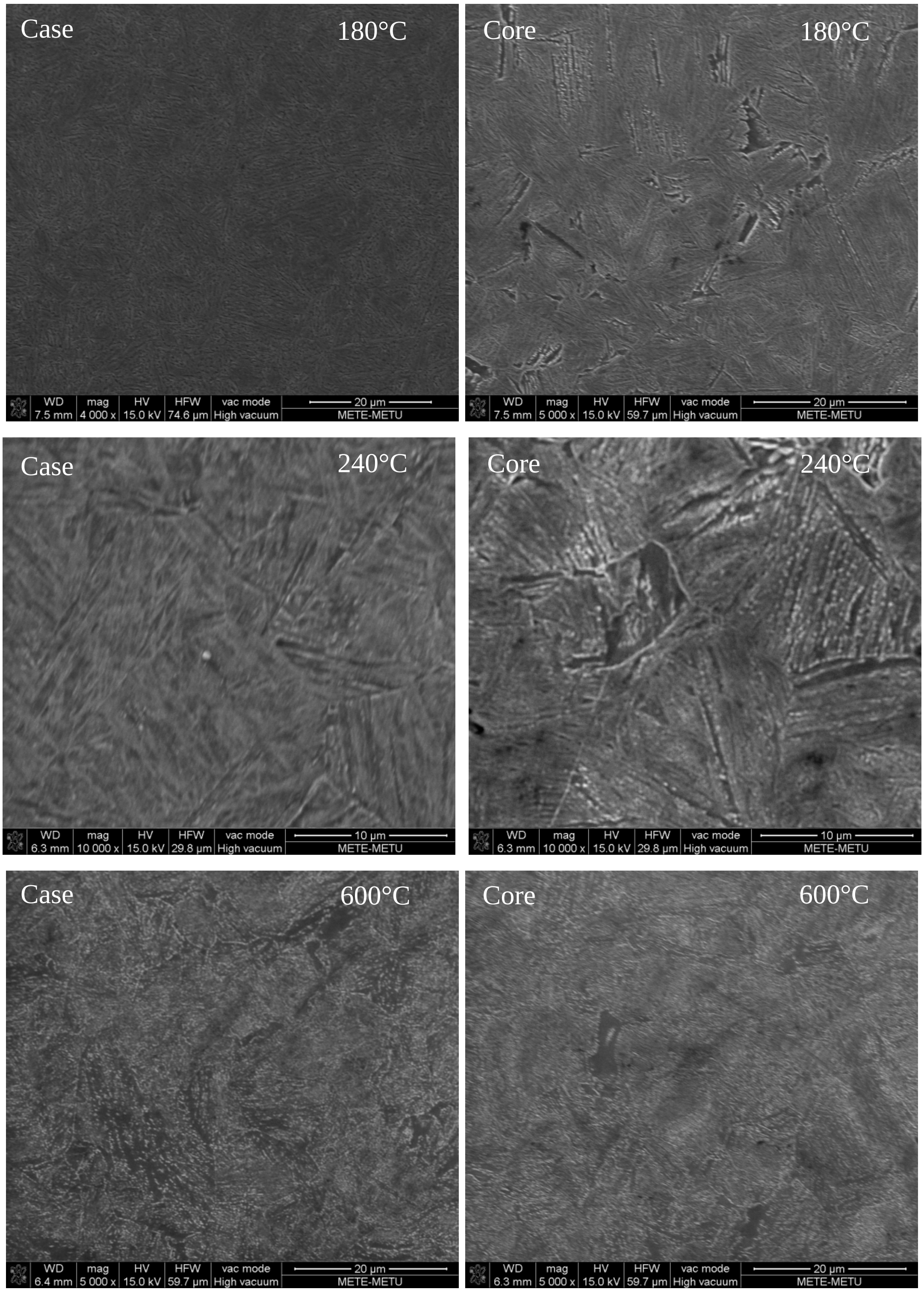

Figure A–3 SEM micrographs of carburized steel sample (900°C/10hrs)

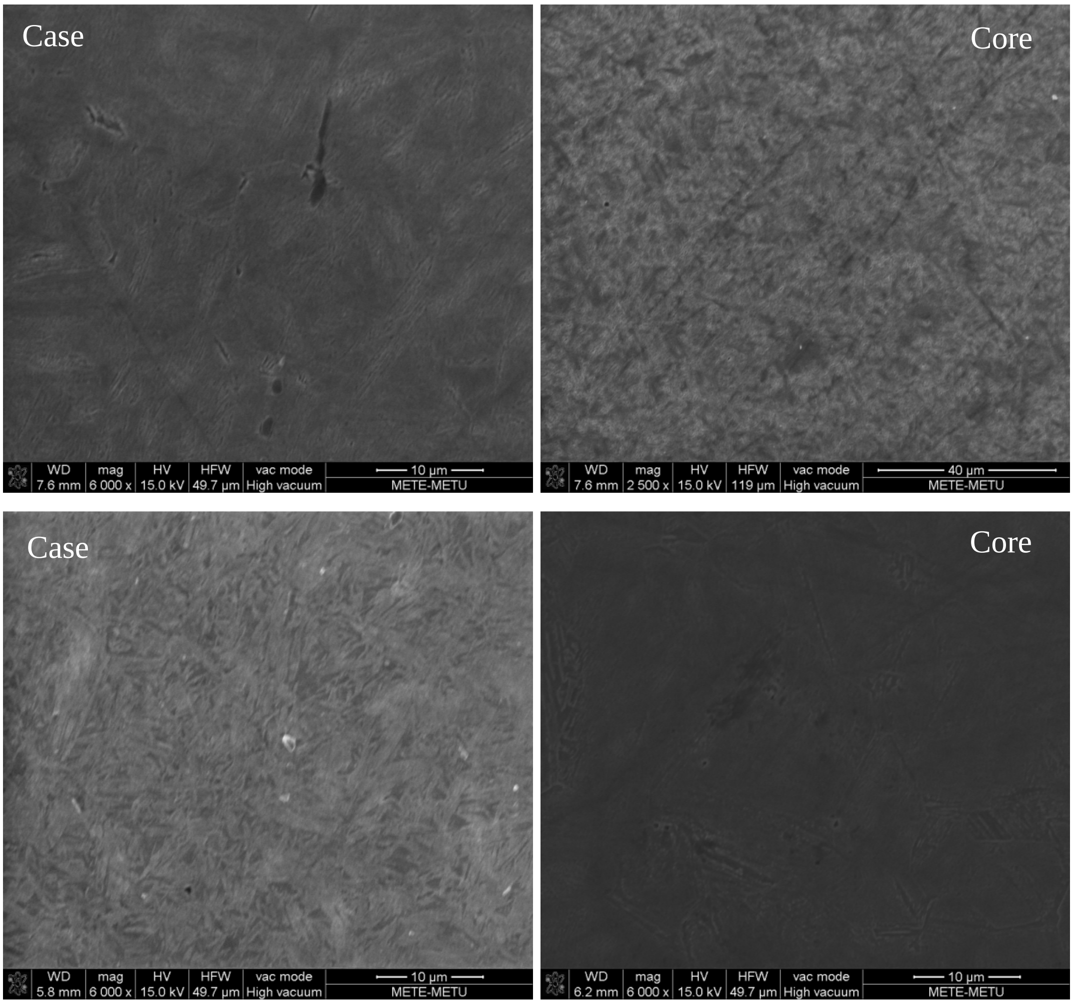

Figure A–4 SEM micrographs of carburized steel sample (900°C/13hrs): as-quenched core (upper left), as-quenched core (upper right) and 180°C tempered case (below left) and core (below right)

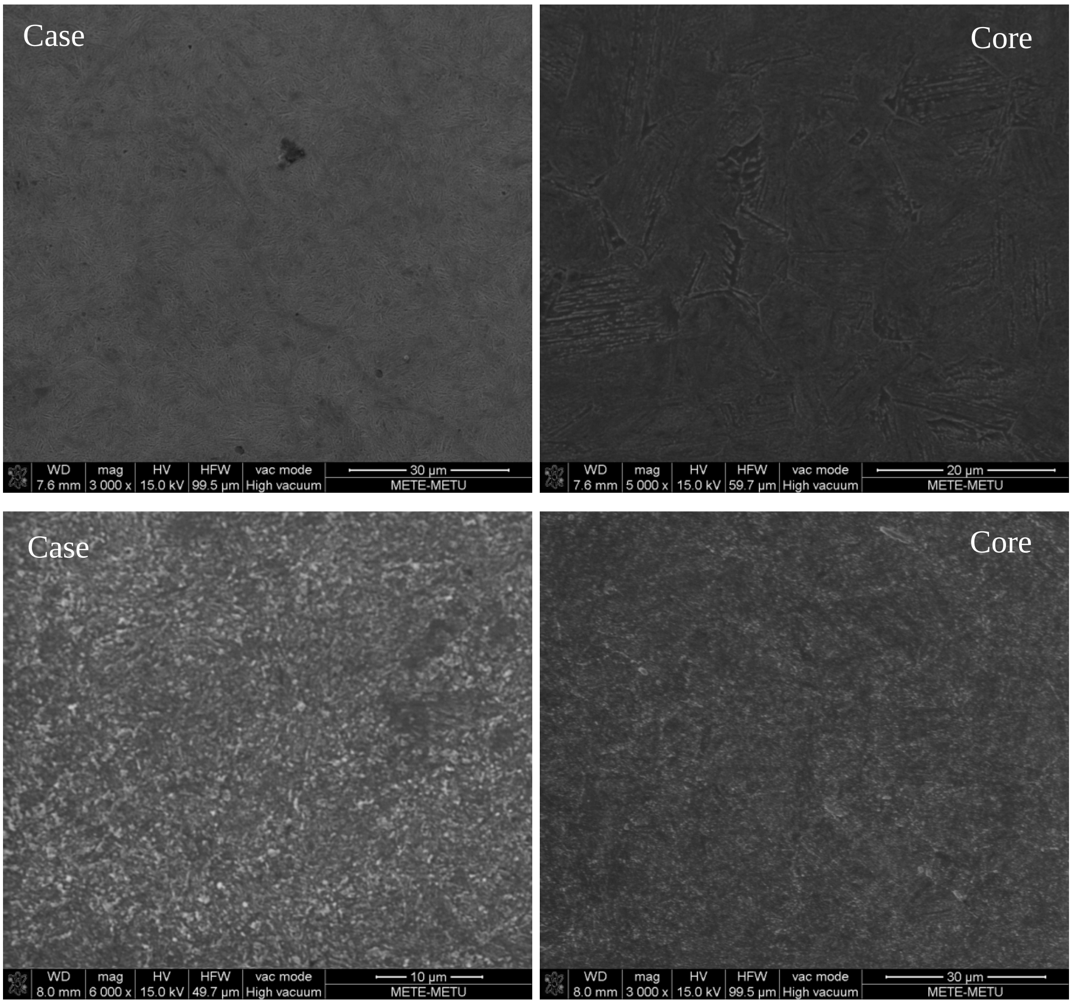

Figure A–5 SEM micrographs of carburized steel sample (900°C/13hrs): 240°C tempered core (upper left), as-quenched core (upper right) and 600°C tempered case (below left) and core (below right)

APPENDIX B

CORRELATION BETWEEN XRD and MBN METHODS

B.1 8HRS CARBURIZED STEEL SAMPLES

The correlation between the XRD and the MBN method shows Pearson's correlation of 0.94 for 8hrs carburized 19CrNi5H steel. The correlation is calculated by using the all data points obtained from the three different measurement points. The acquired correlation is higher when each measurement angle is correlated separately. While the Pearson's goodness is about 0.99 and 0.97 for parallel and perpendicular direction, it is about 0.93 for 45° measurements.

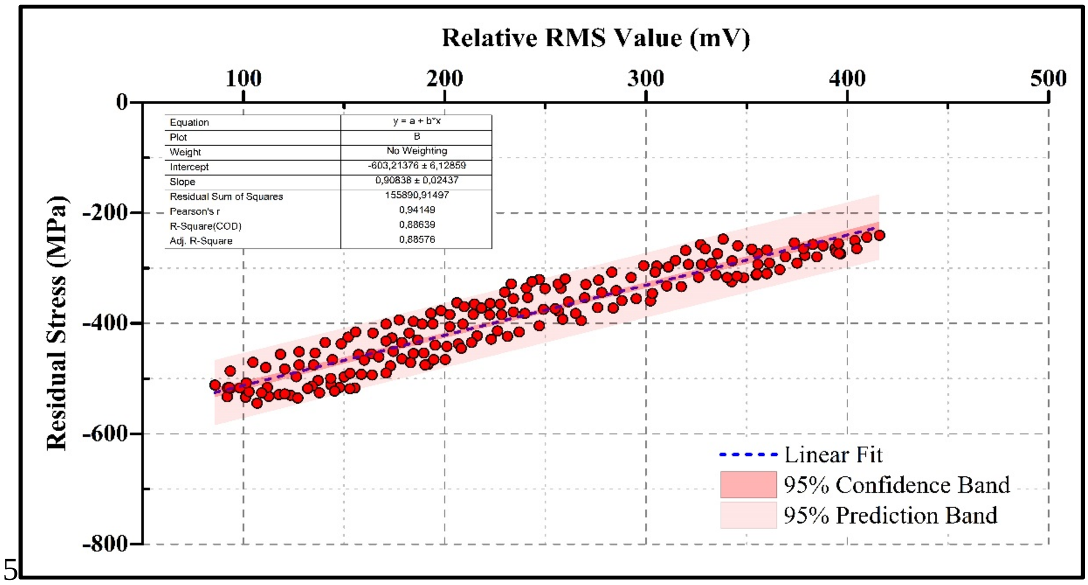

Figure A–6 Correlation between residual stress and RMS values for carburized 19CrNi5H (900°/8hrs)

B.2 10HRS CARBURIZED STEEL SAMPLES

The Pearson's goodness between the XRD and the MBN methods is about 0.92 for 10hrs carburized samples. As in the 8hrs carburized samples, the 45° measurements direction gives the lower goodness, 0.90, value when compared with the other two directions, 0.99 and 0.96.

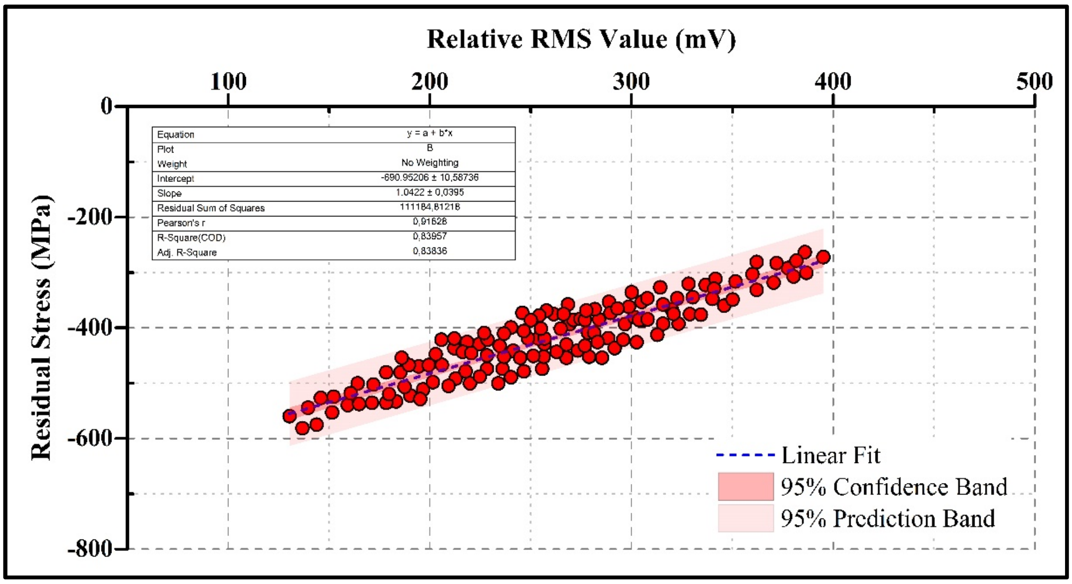

Figure A–7 Correlation between residual stress and RMS values for carburized 19CrNi5H (900°/10hrs)

As seen in the 13hrs carburized steel samples, the linear correlation between residual stress and RMS values is very strong for 8hrs and 10hrs carburized sample. However, a few data points are present within the 95% confidence band regions, but all the data points lie within the 95% prediction band. This two bands indicates that residual stress value can be predicted between upper and lower bad regions even if there will be an error in the predicted stress values; that is, the predicted stress value from RMS is not confident.

APPENDIX C

ESPI FRINGE PATTERNS

C.1 FRINGE PATTERNS OF THE 8HRS CARBURIZED SAMPLE

C.1.1 180°C Tempered Sample

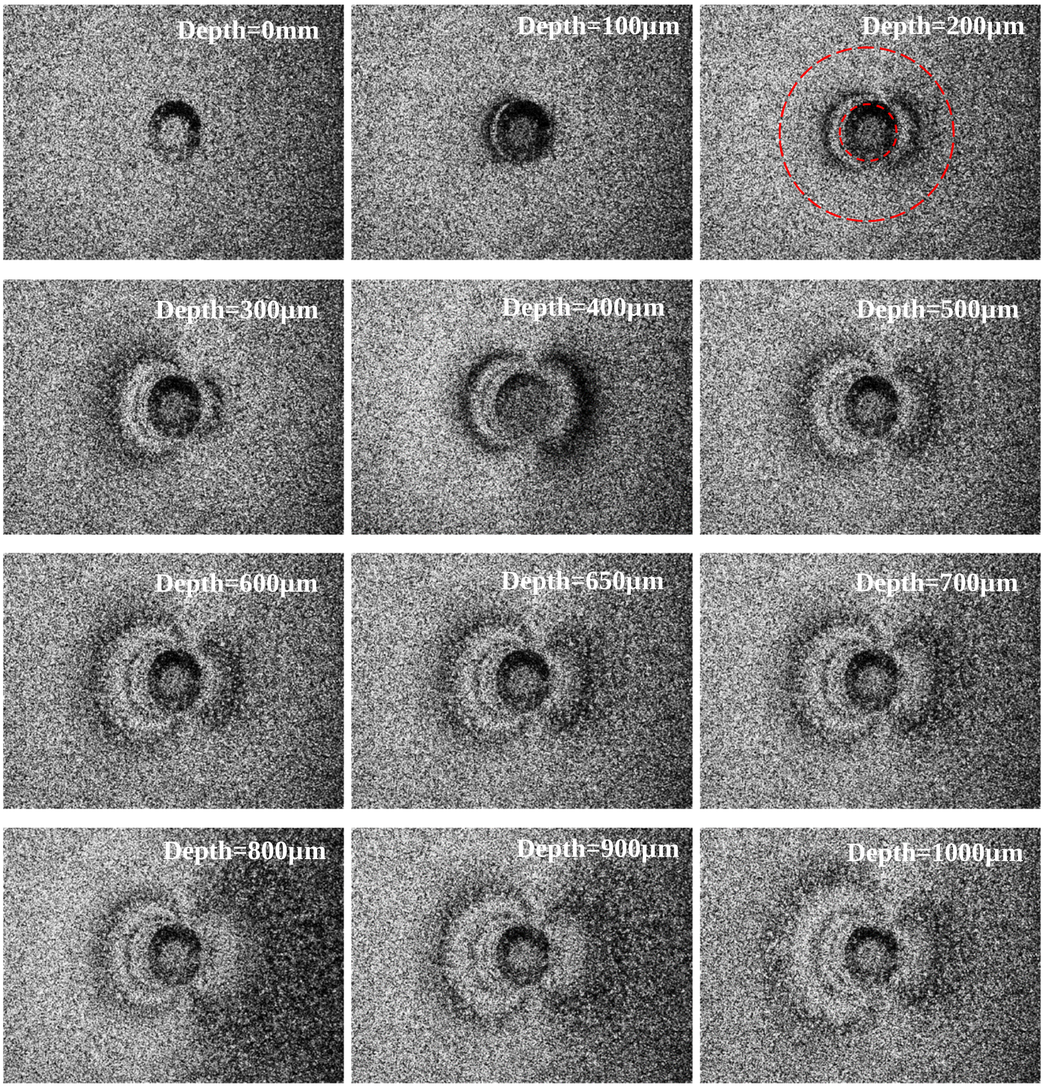

Figure A–8 Fringe pattern of the carburized 19CrNi5H steel (900°C/8hrs): 180°C Tempered

C.1.2 240°C Tempered Sample

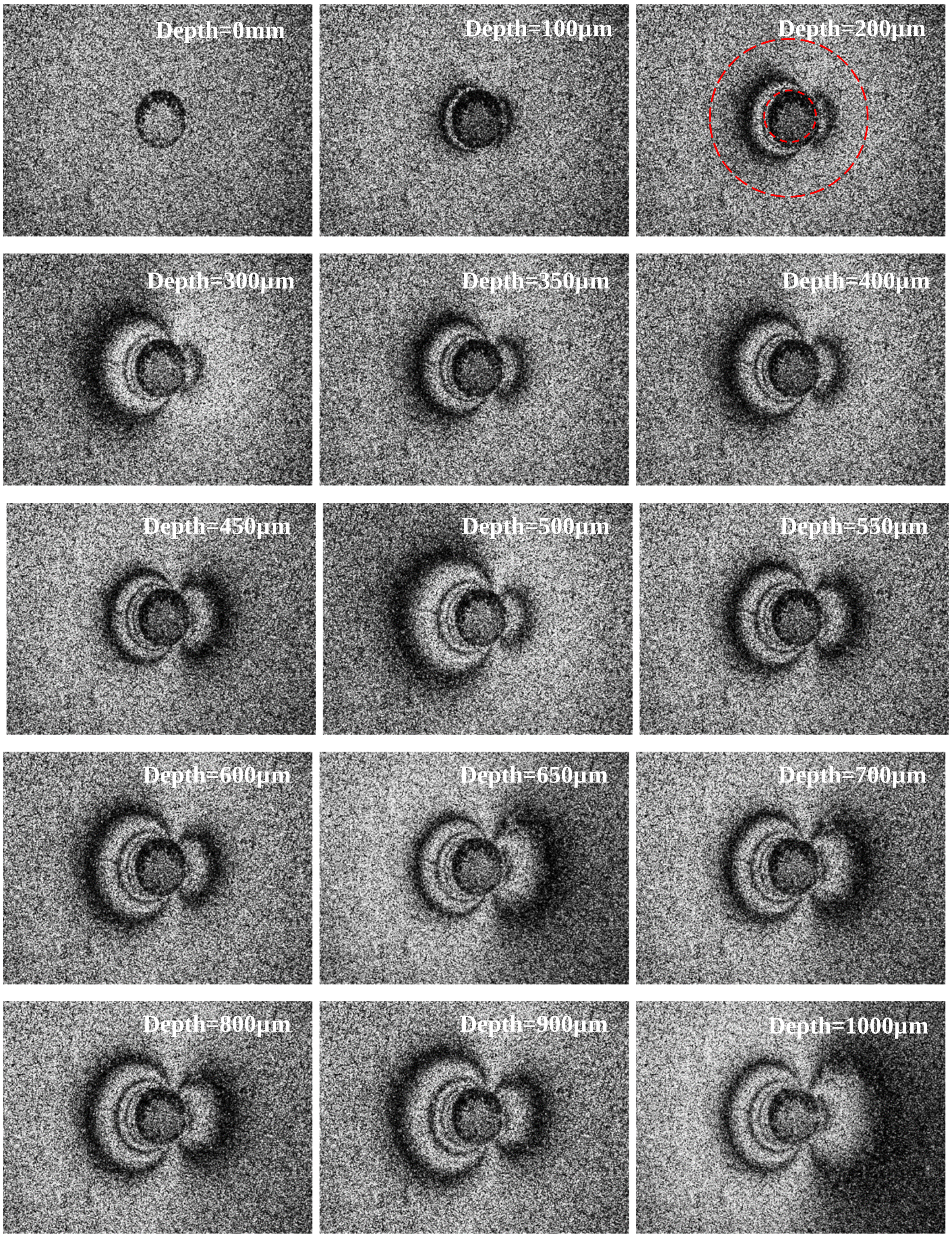

Figure A–9 Fringe pattern of the carburized 19CrNi5H steel (900°C/8hrs): 240°C Tempered

C.1.3 600°C Tempered Sample

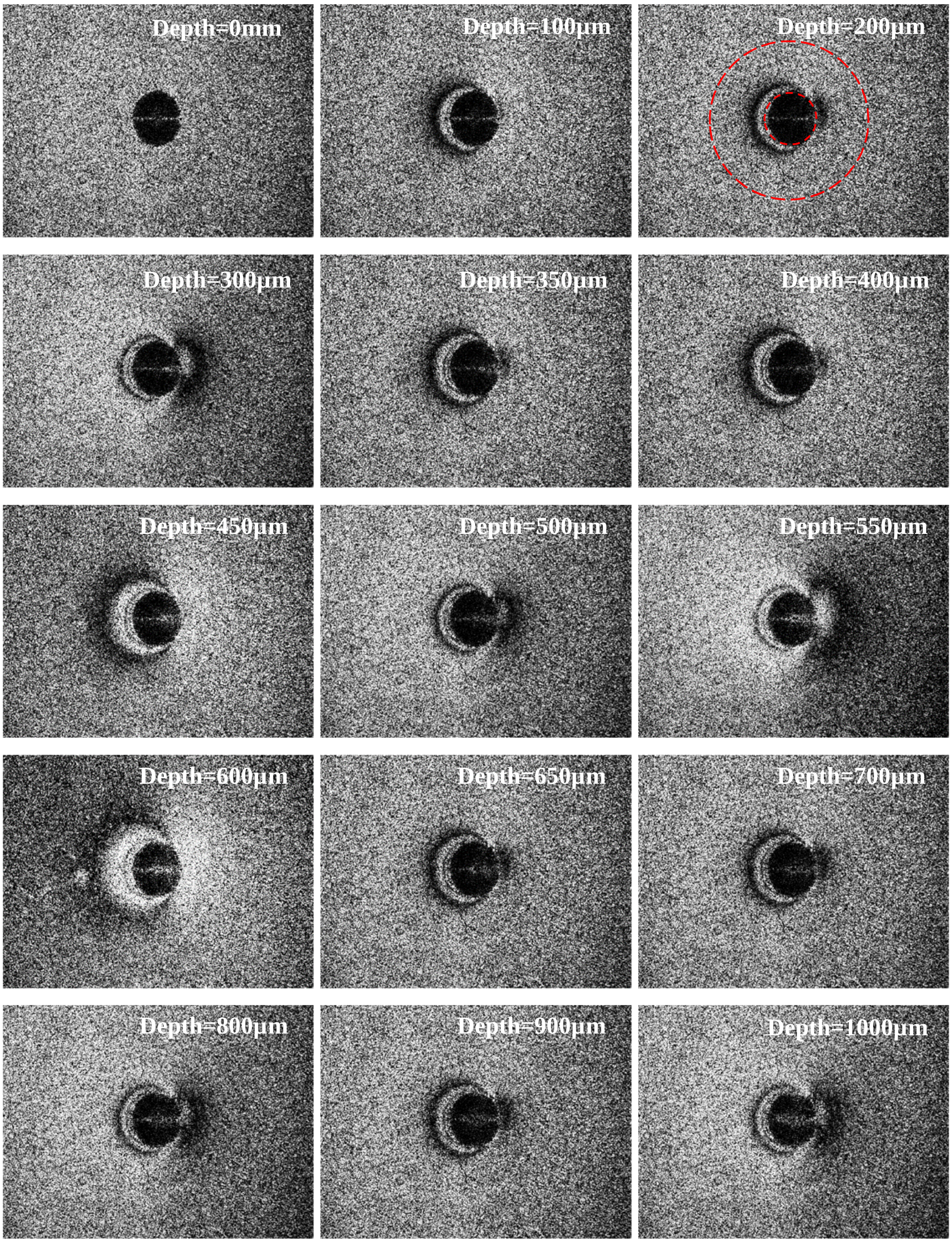

Figure A–10 Fringe pattern of the carburized 19CrNi5H steel (900°C/8hrs): 600°C Tempered

C.2 Fringe Patterns of the 10hrs Carburized Sample

C.2.1 240°C Tempered Sample

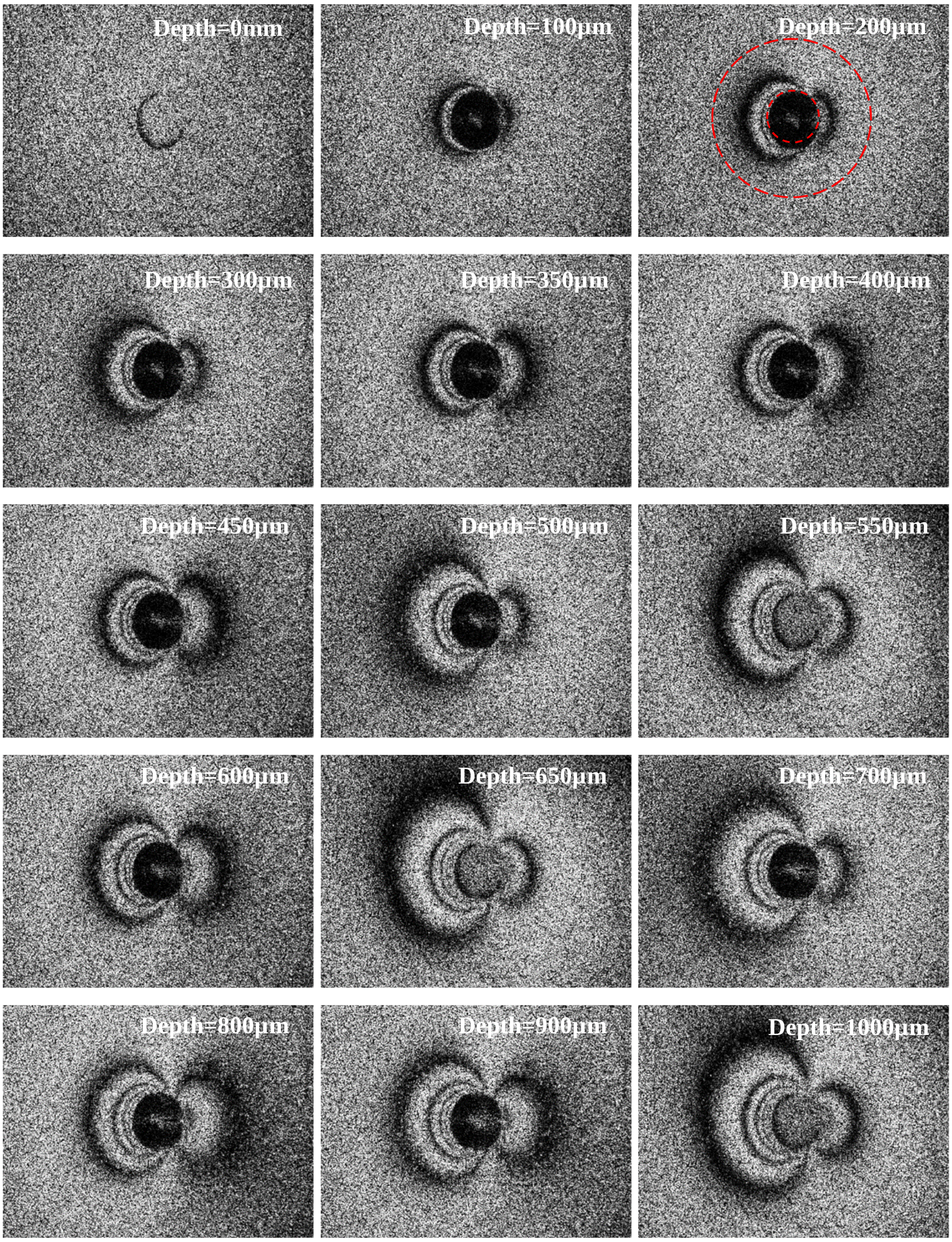

Figure A–11 Fringe pattern of the carburized 19CrNi5H steel (900°C/10hrs): 240°C Tempered

C.2.2 600°C Tempered Sample

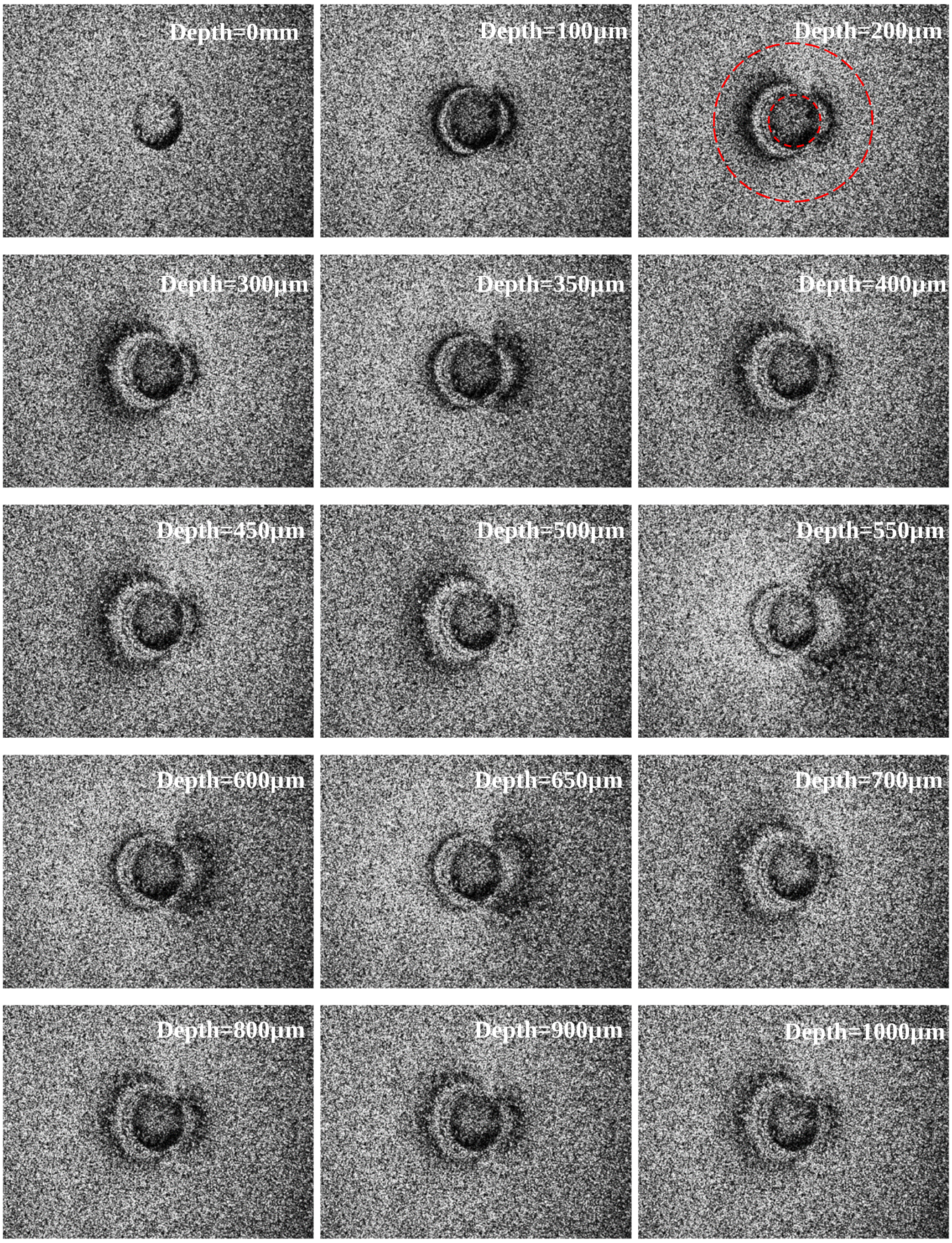

Figure A–12 Fringe pattern of the carburized 19CrNi5H steel (900°C/8hrs): 600°C Tempered

C.3 FRINGE PATTERNS OF THE 13HRS CARBURIZED SAMPLE

C.3.1 180°C Tempered Sample

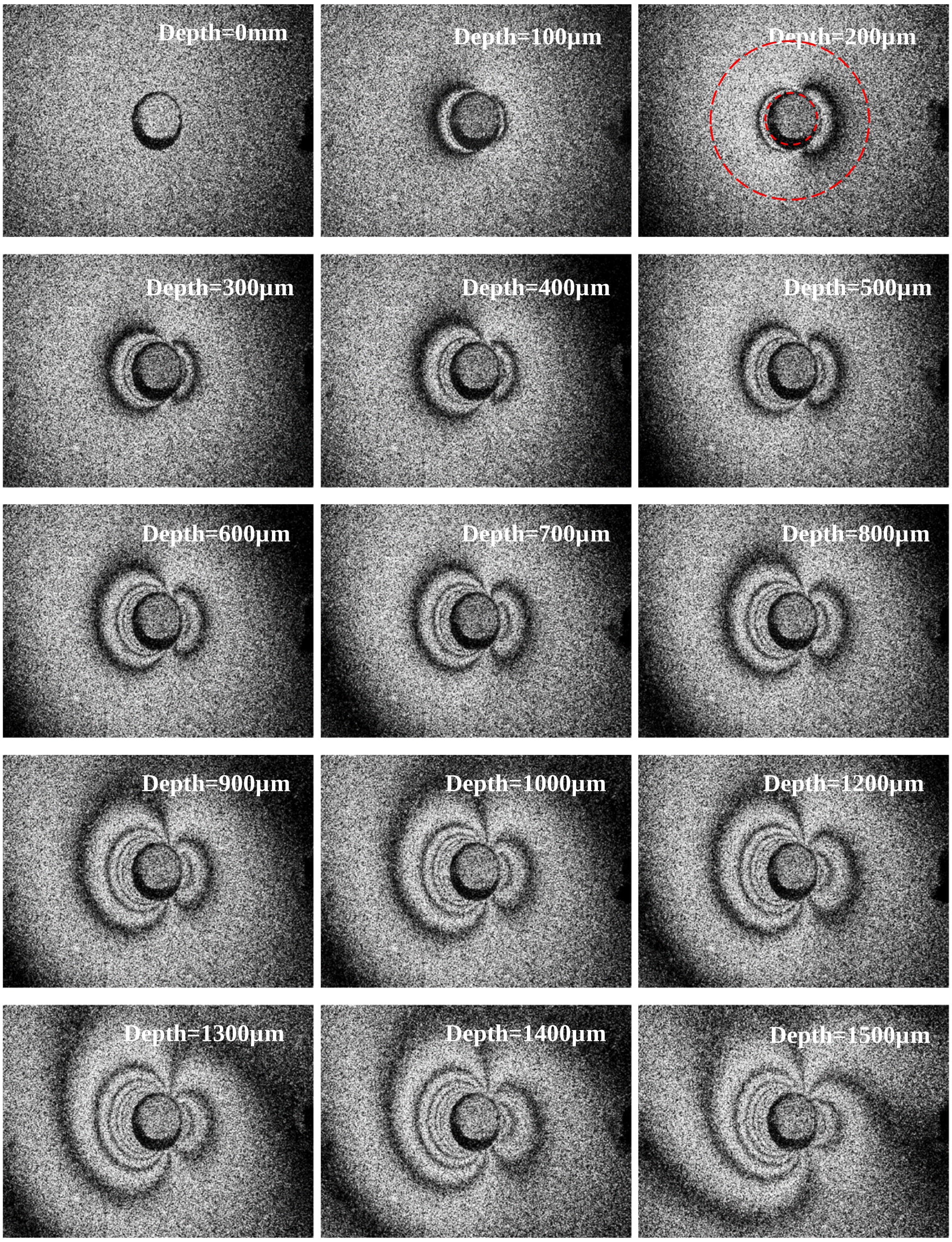

Figure A–13 Fringe pattern of the carburized 19CrNi5H steel (900°C/13hrs): 180°C Tempered

C.3.2 240°C Tempered Sample

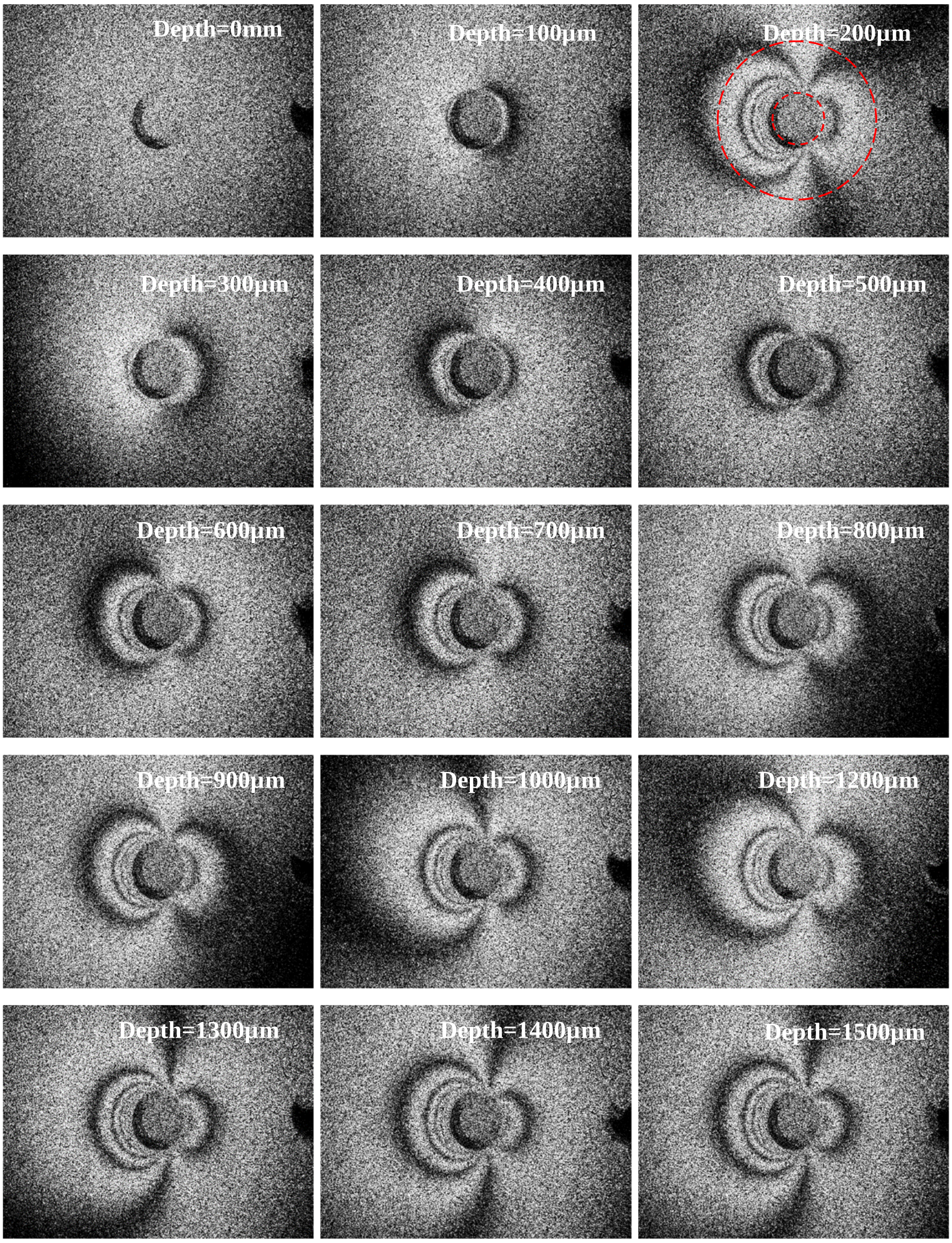

Figure A–14 Fringe pattern of the carburized 19CrNi5H steel (900°C/13hrs): 240°C Tempered

C.3.3 600°C Tempered Sample

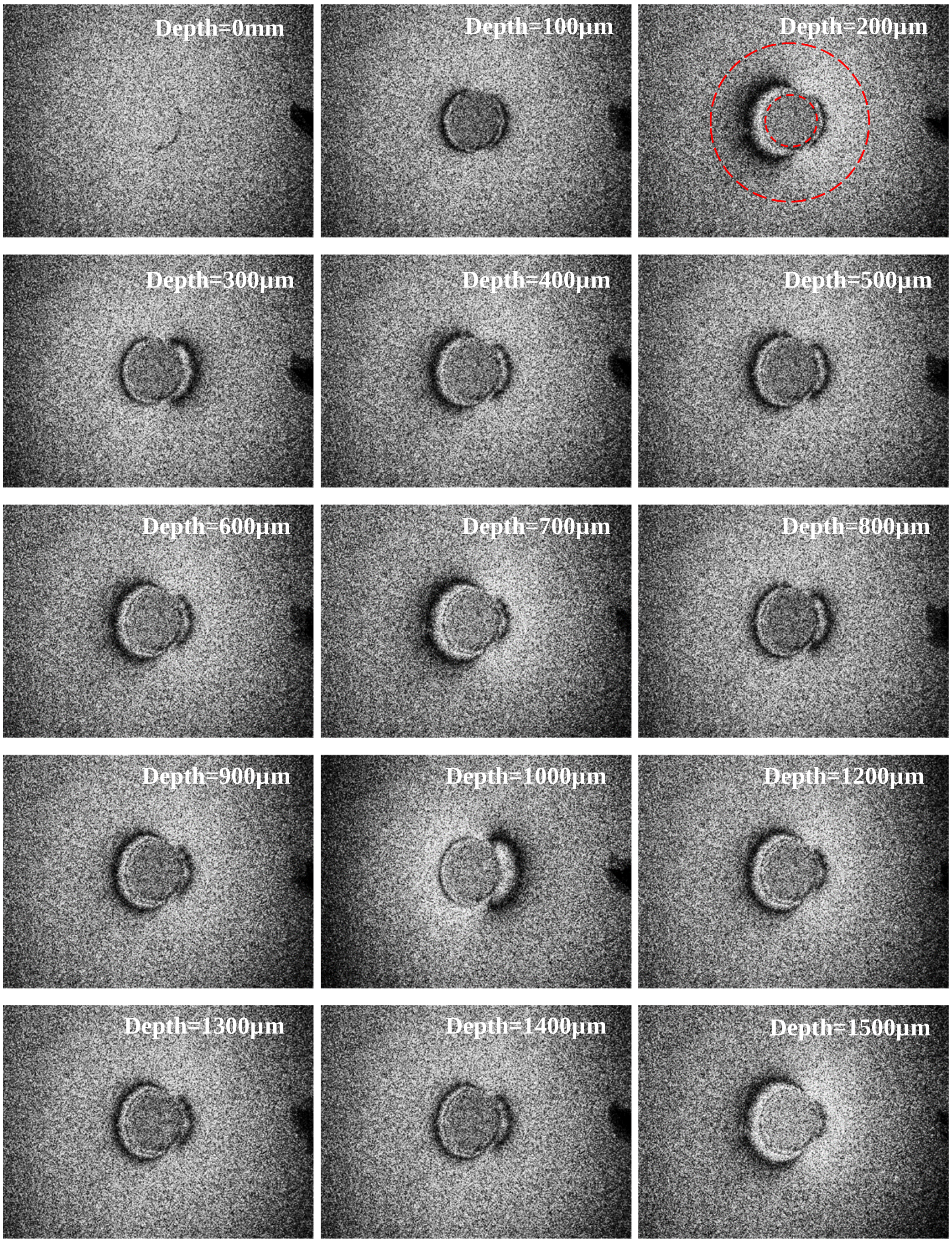

Figure A–15 Fringe pattern of the carburized 19CrNi5H steel (900°C/13hrs): 600°C Tempered